OTOTOXIC HEARING LOSS AND BALANCE DISORDERS: CHALLENGES AND TREATMENT

EDITED BY: Vikrant Borse, Pranav Mathur, Leonard Rybak and Peter S. Steyger

PUBLISHED IN: Frontiers in Molecular Neuroscience

frontiers Research Topics

ISSN 1664-8714
ISBN 978-2-83250-432-1
DOI 10.3389/978-2-83250-432-1

About Frontiers

Frontiers is more than just an open-access publisher of scholarly articles: it is a pioneering approach to the world of academia, radically improving the way scholarly research is managed. The grand vision of Frontiers is a world where all people have an equal opportunity to seek, share and generate knowledge. Frontiers provides immediate and permanent online open access to all its publications, but this alone is not enough to realize our grand goals.

Frontiers Journal Series

The Frontiers Journal Series is a multi-tier and interdisciplinary set of open-access, online journals, promising a paradigm shift from the current review, selection and dissemination processes in academic publishing. All Frontiers journals are driven by researchers for researchers; therefore, they constitute a service to the scholarly community. At the same time, the Frontiers Journal Series operates on a revolutionary invention, the tiered publishing system, initially addressing specific communities of scholars, and gradually climbing up to broader public understanding, thus serving the interests of the lay society, too.

Dedication to Quality

Each Frontiers article is a landmark of the highest quality, thanks to genuinely collaborative interactions between authors and review editors, who include some of the world's best academicians. Research must be certified by peers before entering a stream of knowledge that may eventually reach the public - and shape society; therefore, Frontiers only applies the most rigorous and unbiased reviews.
Frontiers revolutionizes research publishing by freely delivering the most outstanding research, evaluated with no bias from both the academic and social point of view. By applying the most advanced information technologies, Frontiers is catapulting scholarly publishing into a new generation.

What are Frontiers Research Topics?

Frontiers Research Topics are very popular trademarks of the Frontiers Journals Series: they are collections of at least ten articles, all centered on a particular subject. With their unique mix of varied contributions from Original Research to Review Articles, Frontiers Research Topics unify the most influential researchers, the latest key findings and historical advances in a hot research area! Find out more on how to host your own Frontiers Research Topic or contribute to one as an author by contacting the Frontiers Editorial Office: frontiersin.org/about/contact

OTOTOXIC HEARING LOSS AND BALANCE DISORDERS: CHALLENGES AND TREATMENT

Topic Editors:
Vikrant Borse, Otonomy Inc, United States
Pranav Mathur, Otonomy Inc, United States
Leonard Rybak, Southern Illinois University Carbondale, United States
Peter S. Steyger, Creighton University, United States

Citation: Borse, V., Mathur, P., Rybak, L., Steyger, P. S., eds. (2022). Ototoxic Hearing Loss and Balance Disorders: Challenges and Treatment. Lausanne: Frontiers Media SA. doi: 10.3389/978-2-83250-432-1

Table of Contents

frontiers in Molecular Neuroscience

ORIGINAL RESEARCH
published: 01 September 2021
doi: 10.3389/fnmol.2021.715952

Development of Tinnitus and Hyperacusis in a Mouse Model of Tobramycin Cochleotoxicity

Ryan J. Longenecker, Rende Gu, Jennifer Homan and Jonathan Kil*

Sound Pharmaceuticals Inc., Seattle, WA, United States

Aminoglycosides (AG) antibiotics are a common treatment for recurrent infections in cystic fibrosis (CF) patients. AGs are highly ototoxic, resulting in a range of auditory dysfunctions. It was recently shown that the acoustic startle reflex (ASR) can assess behavioral evidence of hyperacusis and tinnitus in an amikacin cochleotoxicity mouse model. The goal of this study was to establish if tobramycin treatment led to similar changes in ASR behavior and to establish whether ebselen can prevent the development of these maladaptive neuroplastic symptoms. CBA/Ca mice were divided into three groups: Group 1 served as a control and did not receive tobramycin or ebselen, Group 2 received tobramycin (200 mg/kg/s.c.) and the vehicle (DMSO/saline/i.p.) daily for 14 continuous days, and Group 3 received the same dose/schedule of tobramycin as Group 2 and ebselen at (20 mg/kg/i.p.). Auditory brainstem response (ABR) and ASR hearing assessments were collected at baseline and 2, 6, 10, 14, and 18 weeks from the start of treatment. ASR tests included input/output (I/O) functions which assess general hearing and hyperacusis, and Gap-induced prepulse inhibition of the acoustic startle (GPIAS) to assess tinnitus. At 18 weeks, histologic analysis showed predominantly normal appearing hair cells and spiral ganglion neuron (SGN) synapses. Following 14 days of tobramycin injections, 16 kHz thresholds increased from baseline and fluctuated over the 18-week recovery period. I/O functions revealed exaggerated startle response magnitudes in 50% of mice over the same period. Gap detection deficits, representing behavioral evidence of tinnitus, were observed in a smaller subset (36%) of animals. Interestingly, increases in ABR wave III/wave I amplitude ratios were observed. These tobramycin data corroborate previous findings that AGs can result in hearing dysfunctions. We show that a 14-day course of tobramycin treatment can cause similar levels of hearing loss and tinnitus, when compared to a 14-day course of amikacin, but less hyperacusis. Evidence suggests that tinnitus and hyperacusis might be common side effects of AG antibiotics.

Keywords: hearing loss, tobramycin, hyperacusis, tinnitus, ebselen, aminoglycoside – ototoxicity

OPEN ACCESS

Edited by:
Leonard Rybak,
Southern Illinois University
Carbondale, United States

Reviewed by:
Lorenz S. Neuwirth,
SUNY Old Westbury, United States
Sangyong Jung,
*Institute of Molecular and Cell Biology (A*STAR), Singapore*

****Correspondence:***
Ryan J. Longenecker
rlongenecker@soundpharma.com

Specialty section:
This article was submitted to Brain Disease Mechanisms, a section of the journal Frontiers in Molecular Neuroscience

Received: *27 May 2021*
Accepted: *10 August 2021*
Published: *01 September 2021*

Citation:
Longenecker RJ, Gu R, Homan J and Kil J (2021) Development of Tinnitus and Hyperacusis in a Mouse Model of Tobramycin Cochleotoxicity. Front. Mol. Neurosci. 14:715952. doi: 10.3389/fnmol.2021.715952

Abbreviations: AG, aminoglycosides; CF, cystic fibrosis; SGN, spiral ganglion neurons; ABR, auditory brainstem response; ASR, acoustic startle reflex; kHz, kilohertz; DMSO, dimethyl sulfoxide; GPIAS, gap-induced prepulse inhibition of the acoustic startle reflex; GAP, trial with gap preceding startle SO, trial with startle only; ANOVA, analysis of variance; IO, input/output; CMD, center of mass displacement.

INTRODUCTION

Aminoglycosides (AG) such as tobramycin are commonly used to treat cystic fibrosis (CF) patients with recurrent pulmonary infections and those infected with multi-drug resistant tuberculosis (Flume et al., 2009). Unfortunately, AGs are ototoxic and can often result in permanent hearing loss (Staecker, 2021). Recent prospective clinical studies demonstrated that a single course of tobramycin can lead to hearing threshold shifts, word-in-noise deficits, and tinnitus, or sound perception in the absence of a sound source (Garinis et al., 2020; Harruff et al., 2020). For those being treated with AGs for chronic conditions, the cumulative ototoxic effects present an enhanced risk of cochleotoxicity (American Speech-Language-Hearing Association, 1994; Garinis et al., 2017; Elson et al., 2020; Hong et al., 2020). While AG-induced hearing loss is now beginning to be well-documented, little is known about the auditory dysfunctions that often accompany hearing loss. However, more research into the prevalence of tinnitus and hyperacusis should be examined in animal models and clinically (Baguley and Andersson, 2007; Hammill and Campbell, 2018).

In vivo assessments of hearing functionality via auditory brainstem response (ABR) and postmortem cochlear histology are common in AG animal models, albeit with methodological inconsistency and variable reports of hearing dysfunction (Huth et al., 2011; Ogier et al., 2020). Longenecker et al. (2020) recently expanded on these traditional hearing assessments by showing that the acoustic startle reflex (ASR), a reflexed-based behavioral assay (Davis, 1984; Gómez-Nieto et al., 2020), can identify potential AG-induced changes to the central auditory system. Amikacin was also shown to induce behavioral evidence of hyperacusis, a sensitivity to loud sounds, and tinnitus, a ringing or buzzing in the ears (Longenecker et al., 2020), which has been observed in noise-induced (Auerbach et al., 2014; Shore and Wu, 2019) and salicylate-induced tinnitus animal models (Salvi et al., 2021). It is unknown if these auditory dysfunctions are specific to amikacin treatment or if they are a general side effect of AG antibiotics. Tinnitus is a prevalent side effect of many classes of drugs which include non-steroidal anti-inflammatory drugs, antibiotics, cancer drugs, diuretics, antimalarial drugs, and antidepressants. Indeed, a recent meta-analysis of clinical reports from the Cochrane library shows that tinnitus is one of the more common side effects for CF patients with recurrent AG treatments (Smith et al., 2018). Hyperacusis is under-reported clinically but is known to be debilitating and comorbid with tinnitus (Pienkowski et al., 2014), increasing with the number of years a patient has experienced tinnitus (Raj-Koziak et al., 2021; Refat et al., 2021). Thus, it is important for AG-induced auditory dysfunctions to be further investigated in animal models to develop potential therapeutics for these diseases of maladaptive plastic change.

Ebselen, a novel anti-inflammatory and anti-oxidant drug, has shown clinical efficacy for ameliorating hearing loss caused by acute noise exposure, and chronic Meniere's disease, and is now investigating therapeutic interventions for tobramycin-induced ototoxicity (Kil et al., 2021). Less is known as to whether the anti-inflammatory properties of ebselen can prevent or treat diseases of the brain (Martini et al., 2019; Sharpley et al., 2020), but it is likely that inflammation plays an important role in AG-induced auditory dysfunctions (Jiang et al., 2017b; Wood and Zuo, 2017). Encouragingly, recent work in mice has demonstrated that ebselen can reduce suprathreshold ABR wave fluctuations and hyperacusis caused by amikacin treatment (Longenecker et al., 2020). Therefore, ebselen, with its variety of proposed anti-oxidant/anti-inflammatory mechanisms of action (Wang et al., 2020), is a good candidate to investigate as a potential therapy for both peripheral and central sensory diseases.

Here we show the effects of a 14-day course of tobramycin in CBA/Ca mice. Small magnitude temporary threshold shifts were observed in many mice. The prevalence of tobramycin-induced hyperacusis and tinnitus as assessed by ASR was highest 2 weeks after treatment and observed to decrease over time. This corresponded to an increase in brain activity as measured by ABR amplitudes. In an amikacin model, ebselen provided statistically significant protection against tobramycin-induced threshold shifts and demonstrated some efficacy for protecting against tobramycin-induced tinnitus (Longenecker et al., 2020). Finally, we suggest potential mechanisms that could explain the AG-induced auditory dysfunctions we have observed in tobramycin and amikacin treated mice.

MATERIALS AND METHODS

Subjects

A total of 36 male and female CBA/Ca mice 3-6 months of age (at the start of experiments) were used in this study. Mice were born in house from parents obtained from Jackson Laboratories. Mice were housed 3 - 5 to a cage within a colony room with a 12-h light-dark cycle at 23°C. Hearing sensitivity and behavior was tracked longitudinally for each animal in a repeated measures design and animals were sacrificed for cochlear histology 18 weeks after the start of dosing following the final behavioral tests (see **Figure 1**).

Drug Formulation, Dosing, and Schedule

Stock ebselen powder was dissolved in pure dimethylsulfoxide (DMSO) at 20 mg/ml and stock tobramycin was dissolved in distilled water at 50 mg/ml and both were stored at minus 20°C. Mice were divided into three groups: Group 1 (n = 8) served as a control and did not receive tobramycin or ebselen. Group 2 (n = 14) received the vehicle i.p. and tobramycin (200 mg/kg body weight diluted in 0.2 ml saline) s.c. thirty minutes later. Group 3 (n = 14) received ebselen i.p. (20 mg/ml in DMSO at 20 mg/kg body weight was diluted in fresh 0.5 ml sterile saline) and tobramycin at s.c. thirty minutes later. The daily dosing schedules for Groups 2 and 3 was identical and was continued for 14 days. During the dosing period, the health and condition of animals were monitored by body weight, which is known to decrease during AG treatments.

Auditory Brainstem Response

Mice were anesthetized with isoflurane. Basal body temperature was maintained using a Gaymar T-pump warming pad set to 37°C and the animals' health was monitored by observation of respiration and circulation. Each ear was otoscopically inspected prior to insertion of ear tips (Nicolet Biomedical, Inc.) for

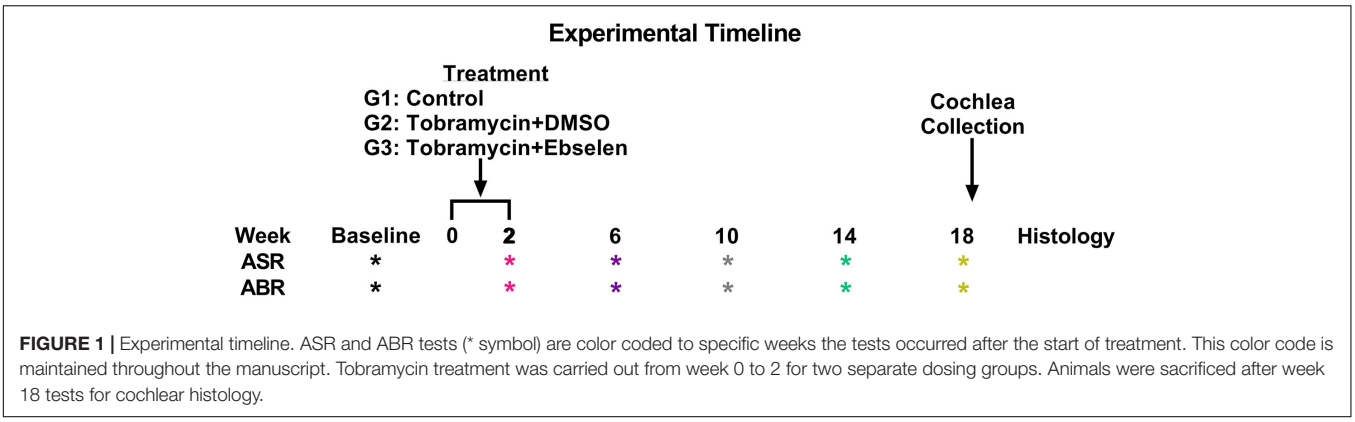

FIGURE 1 | Experimental timeline. ASR and ABR tests (* symbol) are color coded to specific weeks the tests occurred after the start of treatment. This color code is maintained throughout the manuscript. Tobramycin treatment was carried out from week 0 to 2 for two separate dosing groups. Animals were sacrificed after week 18 tests for cochlear histology.

sound delivery. Monaural closed field ABRs (Intelligent Hearing Systems) were collected before (baseline), as well as at weeks 2, 6, 10, 14, and 18 from the start of AG treatment. Subdermal platinum needle electrodes (Grass Telefactor, Inc.) were placed with the active electrode at the vertex and the reference electrode to the test ear, and the ground to the contralateral ear. Each ear was tested independently. Stimuli consisted of pure tone pips (5 ms duration, rectangular envelope) at 4, 8, 16, and 20 kHz presented for 800 repetitions (19.3 r/s) at sound levels from 80 dB SPL to 0 dB SPL (initially 20 dB steps until near threshold, then 5 dB steps) calibrated with a 0.25-inch microphone (Brüel and Kjaer, 4939). Thresholds were measured in 5 dB increments and defined visually by the presence of the most robust peak (I or III) that was reliable within 0.1 ms. Thresholds were analyzed by a scientist blind to treatment and isolated from data collection.

Behavioral Assessments of Hyperacusis, Tinnitus

Acoustic Startle Hardware/Software

Startle Reflex Hardware was purchased from Proxima Centauri Technologies (Julian, California). Each startle cabinet was lined with Sonex anechoic foam to minimize sound reflection and wave canceling sound echoes (Longenecker and Galazyuk, 2012). Sound levels from each cabinet's speakers was calibrated with a 0.5-inch microphone (Brüel and Kjaer 4939). Startle Waveforms were recorded using load-cell platforms and calibrated with 100 g weights. Offline data processing with code written in visual basic was used to evaluate whether each trial was a startle or non-startle via template matching and startle magnitude data was converted from force to center of mass displacement (CMD) (Grimsley et al., 2015). Only legitimate startles were included and used in the final data analyses (Longenecker et al., 2018).

Input/Output Functions for Hyperacusis Assessments

Startle stimuli were pseudorandomly presented between 60- and 100-dB SPL in 5 dB steps. Intertrial intervals were randomized between 4 and 6 s. Each input/output (I/O) session lasted roughly 12 min and consisted of 135 total trials in which each startle intensity was presented 15 times. I/O assessments were collected before (baseline), as well as at weeks 2, 6, 10, 14, and 18 from the start of AG treatment. For each individual animal, hyperacusis was defined by a significant increase in startle magnitude (two-way ANOVA) between baseline and any time point after dosing.

GPIAS for Tinnitus Assessment

Gap prepulse inhibition of the acoustic startle reflex was used to assess behavioral evidence of tinnitus (Longenecker and Galazyuk, 2011; Longenecker and Galazyuk, 2016). The ability of mice to detect a gap of silence preceding a startle stimulus was determined by comparing the startle magnitude in response to a startle stimulus (white noise; 100 dB SPL) presented alone (SO) and a startle stimulus paired with a preceding (100 ms before) gap (20 ms long) of silence (GAP). Both trials were presented in a continuous narrowband noise carrier presented at 5 different frequencies (4, 8, 12.5, 16, 20 kHz) at a constant intensity of 65 dB SPL. Additionally, 15 startles presented in silence were used to monitor startle habituation. Intertrial intervals were randomized between 4 and 6 s. Eight mice were excluded from GPIAS analysis because their baseline gap detection ratios did not meet criterion.

A testing session was comprised of 15 blocks comprising 150 trials, lasting roughly 15 min. A block was defined by 10 trials containing 5 pseudorandom SO and GAP trials presented in a uniform carrier frequency. Throughout the session, each carrier frequency block was represented 3 times for a total of 45 trials. On each testing day, 3 GPIAS sessions were run on each mouse lasting roughly 45 min. The best performance ratio was used to determine an individual animal's daily gap detection performance (Longenecker et al., 2018). GPIAS assessments were collected before (baseline), as well as at weeks 2, 6, 10, 14, and 18 from the start of AG treatment. For each individual animal, tinnitus was defined by a significant increase in the gap ratio (less inhibition) between baseline and any time point after dosing.

Cochlear Histology

Following the final ABR and behavioral assessments, mice (∼6-12 months old) in three different groups (untreated control n = 8; tobramycin/DMSO n = 14; tobramycin/ebselen n = 14) were sacrificed with CO_2. Cochlea were collected, fixed in 4% PFA overnight, then processed for whole mount immunostaining. After the bony wall was removed carefully, the intact membranous cochlea was isolated from the modiolus. After decalcification in 0.5 M EDTA for 1 h, the membranous cochlea

was permeabilized and blocked in 0.2% Triton X-100, 1% BSA and 5% donkey serum in PBS. To assess damage to inner and outer hair cells, tissue of one cochlea from each group were incubated with primary antibody: Rabbit anti-Myosin VIIa (1:200 dilution) overnight at 4°C, rinsed in PBS, and incubated with secondary antibody: Alexa Fluor 594 Donkey anti-Rabbit IgG (1:500 dilution) for 2 h at room temperature. Then the tissue was stained with FITC-Phalloidin (1:1000 dilution) for 10 min. For ribbon synapse observation, tissue of the cochlea (untreated control n = 14; tobramycin/DMSO n = 25; tobramycin/ebselen n = 25) were incubated with two primary antibodies: Rabbit anti-GluR2 (1:500 dilution) and Mouse anti-CtBP2 (1:500 dilution) overnight at 4°C, rinsed in PBS, and incubated with two secondary antibodies: Alexa Fluor 594 Donkey anti-Rabbit IgG (1:500 dilution), Alexa Fluor 488 Donkey anti-mouse IgG (1:500 dilution) for 2 h at room temperature. After the immunostaining was finished, the membranous cochlea was cut at the apical turn and the basal turn, then further dissected, embedded in mounting media with DAPI. Samples were examined via an epi-fluorescent microscope (Nikon Eclipse Ti), images were captured via a charge-coupled device camera (Hamamatsu C11440). Hair cells were observed as row images of the cochlea and were captured under 20X plain lens, then single images were assembled to form the whole cochlea image by using Adobe Photoshop CC 2018. For ribbon synapse observation, raw images at 16 kHz region were captured under 60X oil optical lens with a Z-stack range at 6 – 10 μm (based on the distribution of ribbon synapse / inner hair cell), in 0.2 μm steps; raw images then deconvoluted and processed with maximum intensity project.

Data Analysis

GraphPad Prism 9 was used for statistical analysis. One-way and two-way ANOVAs were used in data sets with normally distributed and equal sample sizes. Mixed models analyzed data that did not meet these assumptions. Sidak's multiple comparison or Fisher's LSD tests were used to discover individual differences at specific timepoints in the in vivo dosing study. Greyscale statistical symbols represent significance differences between dosing groups, while colored symbols represent specific significant differences between baseline and specific after dosing epochs. For each figure, the level of statistical significance is represented as: one symbol, $p \leq 0.05$; two symbols, $p \leq 0.01$; three symbols, $p \leq 0.001$; four symbols, $p \leq 0.0001$. Fisher's exact test were used to analyze clinically relevant ABR threshold, hyperacusis, and tinnitus changes. To develop clinically relevant ABR threshold shift criterion, we modified ASHA guidelines for ototoxic change using pure tone audiometry (American Speech-Language-Hearing Association, 1994; Gu et al., 2020; Longenecker et al., 2020). Here, we identified ototoxic change using the following three criteria: (1) A $\geq$ 10 dB shift at three adjacent tested frequencies (4, 8, 16, 20 kHz). (2) A $\geq$ 15 dB shift at two adjacent tested frequencies. (3) A $\geq$ 20 dB shift at any one tested frequency. Each ear was tested and analyzed independently. The percentage of ears which met the threshold shift criteria was calculated for each time point (weeks 2, 6, 10, 14, and 18).

RESULTS

Tobramycin Causes Temporary Threshold Shifts Without Permanent Cochlear Damage

To examine the effects of tobramycin on hearing sensitivity, we documented ABR thresholds up to 18 weeks from the start of AG treatment. Following a standard 14-day tobramycin regimen, mean ABR thresholds were elevated 10-15 dB at 16 kHz from baseline levels (**Figure 2**). ABR traces from baseline and 2 weeks following the start of dosing are shown from an untreated control (**Figure 2A**), a tobramycin/DMSO treated (**Figure 2B**, and a tobramycin/ebselen treated mouse (**Figure 2C**). A two-way ANOVA found a significant effect of dosing between subjects at 2 weeks [$F_{(2,265)} = 9.724$, $p < 0.001$] and 6 weeks [$F_{(2,264)} = 11.40$, $p < 0.001$] after the start of dosing (**Figures 2D,E**). Significant effects for frequency were also found at 2 weeks [$F_{(3,265)} = 5.363$, $p = 0.001$], 6 weeks [$F_{(3,264)} = 3.172$, $p = 0.025$], 10 weeks [$F_{(3,262)} = 3.499$, $p = 0.016$] and 14 weeks [$F_{(3,257)} = 2.820$, $p = 0.040$] after dosing. Interactions between dosing and frequency were seen at 2 weeks [$F_{(6,265)} = 3.118$, $p = 0.006$] and 6 weeks [$F_{(6,264)} = 2.660$, $p = 0.016$]. Šidák's multiple comparison tests showed highly significant differences between control and tobramycin/DMSO groups at 16 kHz during the 2-week (**Figure 2D**, $p = 0.001$) and 6-week (**Figure 2E**, $p = 0.001$) epochs. Specific differences at 16 kHz were also seen between tobramycin/DMSO and tobramycin/ebselen groups at week 2 ($p < 0.001$), week 6 ($p < 0.001$), week 10 ($p = 0.014$), and week 14 ($p = 0.021$), as well as at 20 kHz at the 6-week epoch ($p = 0.036$) (**Figures 2D-G**). Tobramycin-induced threshold shifts were resolved by week 18 after the start of dosing (**Figure 2H**). To evaluate if these ABR deficits were significant on a per ear level, we applied the recently developed clinically relevant change criteria (**Figure 2I**; Gu et al., 2020; Longenecker et al., 2020). When evaluated with the Fisher's exact test, these responder criteria revealed a significant difference between tobramycin/DMSO and tobramycin/ebselen treated ears at week 2 (39.3% vs 7.7%, $p = 0.010$) and week 6 (35.7% vs. 0%, $p < 0.001$), but not at later timepoints after dosing. These data suggest that although the mean threshold shifts were relatively mild after tobramycin treatment, a sizeable minority of mice experienced noticeable hearing impairment via a clinically relevant hearing assessment.

To investigate if the central auditory system became more reactive following tobramycin treatment, we assessed ABR wave III/wave I amplitude ratios (**Supplementary Figure 1**). We found that for most frequencies and amplitudes that there was a general increase in the wave III/wave I amplitude ratio (**Supplementary Figures 1A-F**) in tobramycin treated animals. While a significant effect of time was not found, a trend towards increased ratios over time was observed at some frequencies (reference to 100% dashed line). A between subjects mixed-effects analysis found an effect of dose for 16 kHz 40 dB ratios [$F_{(2,69)} = 3.295$, $p = 0.043$], in which subjects of the tobramycin/DMSO group ratio was higher at most epochs than the subjects of the control or tobramycin/ebselen groups

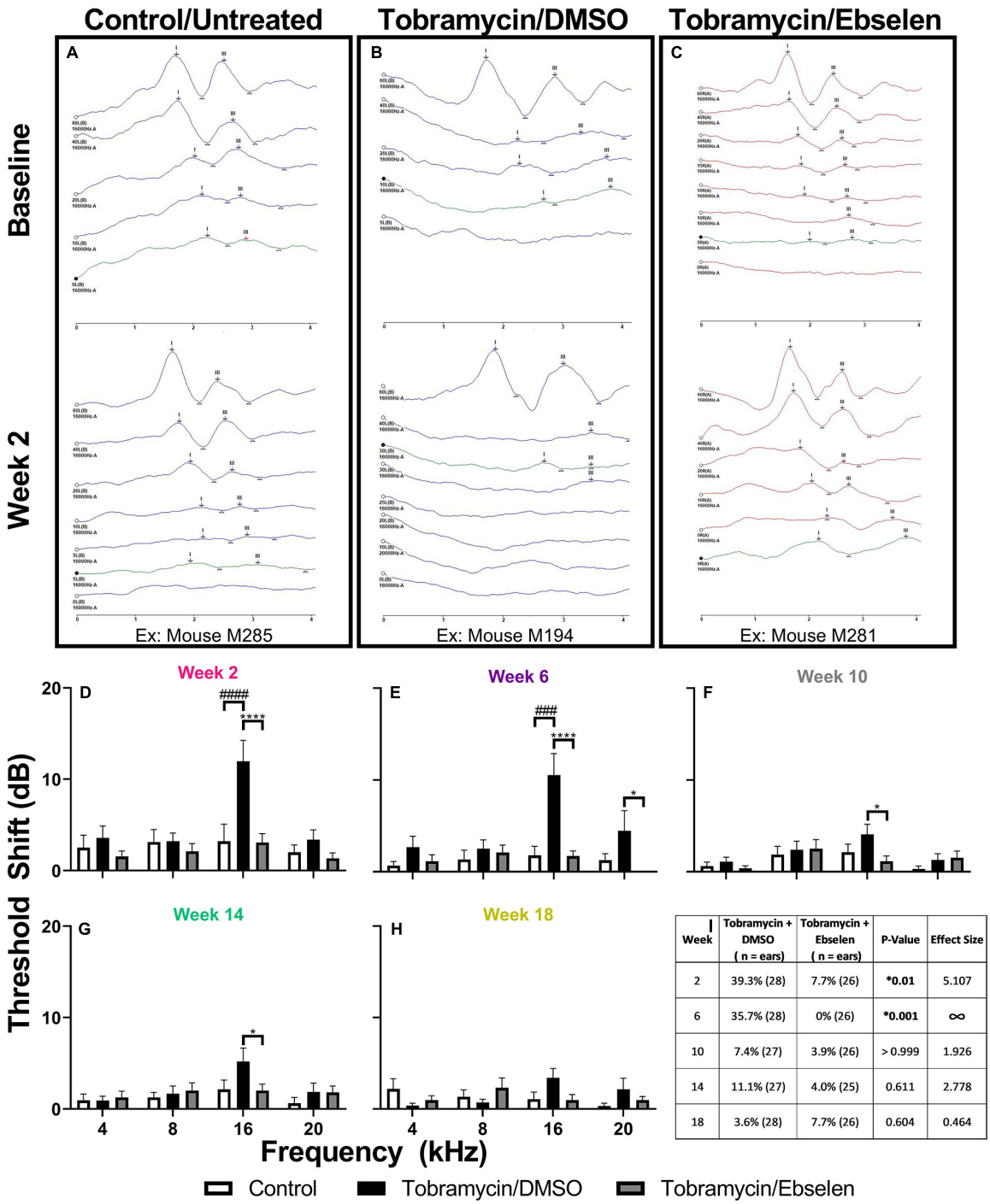

Week	Tobramycin + DMSO (n = ears)	Tobramycin + Ebselen (n = ears)	P-Value	Effect Size
2	39.3% (28)	7.7% (26)	*0.01	5.107
6	35.7% (28)	0% (26)	*0.001	∞
10	7.4% (27)	3.9% (26)	> 0.999	1.926
14	11.1% (27)	4.0% (25)	0.611	2.778
18	3.6% (28)	7.7% (26)	0.604	0.464

FIGURE 2 | Evaluation of hearing loss caused by tobramycin. ABR traces from 16 kHz stimuli collected at baseline and 2 weeks after the start of treatment showing impact of tobramycin on hearing thresholds (**(A)**: untreated control, **(B)**: tobramycin/DMSO, **(C)**: tobramycin/ebselen). Blue and red traces show ABRs from left and right ears, respectively. Green trace in each panel represents threshold. Averaged tobramycin-induced ABR threshold shifts comparing testing groups at different epochs (**(D):** week 2, **(E):** week 6, **(F):** week 10, **(G):** week 14, **(H):** week 18) after the start of treatment. ABRs were collected for 4, 8, 16, and 20 kHz. Shifts represent the specific epoch minus the baseline ABR value for each group. Data is represented by threshold shift means and standard errors. Post hoc tests determined significant differences between testing groups, which are indicated as follows: # (black), between control and DMSO treated animals; # (gray), between control and ebselen treated animals; *, between DMSO and ebselen treated animals. **(I):** Clinically relevant change criteria table. (1) Criterion for CRC: A ≥ 20 dB shift at one frequency. (2) A ≥ 15 dB shift at two adjacent frequencies. (3) A ≥ 10 dB shift at three adjacent frequencies. Each ear was analyzed independently. The percentage of ears which met the ABR threshold shift criteria was calculated for each time point (weeks 2, 6, 10, 14, 18). Two-sided Fisher's exact tests were used statistically evaluate differences between testing groups. The effect size represents relative risk (Koopman asymptotic score).

(**Supplementary Figure 1F**). Specific Fisher's LSD post hoc significance values can be seen in **Supplementary Table 1**. The trends observed here closely resemble those seen in amikacin treated mice (Longenecker et al., 2020). Such changes in ratios could be explained by increases in wave III amplitudes or decreases in wave I amplitudes from baseline levels. We found that wave I amplitudes were mainly decreased, especially at higher frequencies (**Supplementary Figures 2**, **3**). Additionally, some wave III amplitudes for 40 dB stimuli did increase (**Supplementary Figure 2**).

Such changes electrophysiological changes were not readily explained by damage to cochlear sensory cells. In representative cochlear whole mounts, inner and outer hair cells remained intact from the base to the apex in untreated controls (**Figure 3A**), tobramycin/DMSO treated (**Figure 3B**), and tobramycin/ebselen treated animals (**Figure 3C**). At the region representative of 16 kHz hearing, no observable differences were seen in pre- (CtBP2 green) and post- (GluR2 red) synaptic densities between untreated controls (**Figure 3D**), tobramycin/DMSO treated (**Figure 3E**), and tobramycin/ebselen treated animals (**Figure 3F**). This was true throughout all the cochlea regions we analyzed which spanned all frequencies we examined in this study.

Tobramycin Treatment Can Induce Hyperacusis and Tinnitus-Like Behavior

To investigate if tobramycin treatment resulted in amplified startle responses to loud acoustic stimuli as it did with amikacin treatment (Longenecker et al., 2020), we conducted ASR input/output assessments (**Figures 4**, **5**). Following tobramycin treatment startle responses were greatly exaggerated in some mice, examples of which are seen in **Figure 4**. A two-way repeated measures ANOVA showed significance of time after treatment for mouse M94 [$F_{(3.715,467.4)} = 9.624$, $p < 0.001$] and mouse F305 [$F_{(4.061,441.0)} = 34.84$] (**Figures 4A,B**). For these mice, Dunnett's multiple comparison tests revealed that startle responses were significantly elevated at week 2 ($p < 0.001$), week 6 ($p = 0.037$), week 10 ($p < 0.001$), and week 18 ($p = 0.011$) for mouse M94, as well as week 2 ($p < 0.001$) and week 10 ($p < 0.001$) for mouse F305. Such significant elevations in startle were not observed for example mouse F301 (**Figure 4C**). Time after dosing was also a significant factor for Mouse F301 [$F_{(4.526,415.5)} = 12.96$, $p < 0.001$), but startle magnitudes significantly decreased over time, following the normal habituation to the startle stimulus. To tabulate the incidence of hyperacusis-like behavior following tobramycin treatment, the percentage of individual mice that demonstrated statistically significant increases in startle response for each epoch after dosing were evaluated with responder criteria (**Figure 4D**). At the week 2 epoch roughly 40% of mice experienced hyperacusis-like behavior, which fell to less than 10% by week 14. This responder analysis is important because it can elucidate that the symptoms of individual mice, which can be missed by group mean averages as seen in **Figure 5**. Between subject group analysis revealed very little hyperacusis-like behavior, as IO functions for each dosing group were below the baseline (below 0) startle magnitude at most epochs, representative of habituation (**Figure 5**). This was not surprising, because the majority of mice did not show hyperacusis-like behavior (**Figure 4D**). Two-way ANOVAs revealed that significant effect of treatment at week 2 [$F_{(2,367)} = 3.139$, $p = 0.045$], week 6 [$F_{(2, 311)} = 4.758$, $p = 0.009$], and week 10 [$F_{(2, 304)} = 11.11$, $p < 0.001$] (**Figures 5A-C**). Animals treated with tobramycin showed less habituation as a group, because a subset of these animals developed hyperacusis, while control animals did not (**Figure 5**). Šidák's multiple comparison tests revealed that the tobramycin/ebselen treated group maintaining significantly higher levels of startle than the untreated control group at week 6 ($p = 0.007$) and the control group ($p = 0.002$) and DMSO group ($p = 0.003$) at week 10. By week 14 and 18 after the start of dosing, no significant differences were seen between groups with startle responses trending well below baseline startle reactivity (**Figures 5D,E**). To evaluate if increases in hyperacusis-like behavior were significantly different between treatment groups we conducted a Fisher's exact test. Based on relatively similar mean startle response magnitude averages between groups (**Figures 5A-E**), it was unsurprising to see no significant difference between tobramycin/DMSO and tobramycin/ebselen groups (**Figure 5F**). Based on this dataset, ebselen did not play a major role in preventing the development of tobramycin-induced hyperacusis.

To evaluate tobramycin-induced behavioral evidence of tinnitus, we used the GPIAS methodology which has been used to assess drug- and noise- induced tinnitus (**Figure 6**; Longenecker and Galazyuk, 2016; Longenecker et al., 2020). Individual examples of a mice that did and did not develop gap detection deficits following tobramycin treatment demonstrate the variability between mice (**Figures 6A,B**). A repeated measures mixed-effects model showed an effect of time after dosing on gap detection for mouse F305 [$F_{(3.749,263.9)} = 3.859$, $p = 0.006$], but not mouse M089 [$F_{(4.553,321.4)} = 0.5342$, $p = 0.734$]. Fisher's LSD tests revealed frequency specific gap detection deficits (20 kHz) at week 2 ($p = 0.018$) and week 6 ($p = 0.028$) when compared to baseline gap detection for mouse F305 (**Figure 6A**). These sorts of deficits were not observed in example mouse M89 which was also treated with tobramycin (**Figure 6B**), nor mouse M90 which served as an untreated control (**Figure 6C**). To further investigate the overall effect of tobramycin on gap detection we examined the grand mean average of animals that developed tinnitus or those which did not (**Figures 6D,F**). In the tinnitus positive group, a two-way repeated measures ANOVA found an effect of time after tobramycin dosing ($F_{(4.110,164.4)} = 2.943$, $p = 0.021$), but not in the tinnitus negative group ($F_{(4.346,325.9)} = 1.199$, $p = 0.311$), or the untreated controls ($F_{(2.799,27.99)} = 0.8964$, $p = 0.449$). Fisher's LSD tests revealed frequency specific deficits at 8 kHz (week 18: $p = 0.038$), 12.5 kHz (week 14: $p = 0.041$), 16 kHz (week 2: $p = 0.026$), and 20 kHz (week 2: $p = 0.001$, week 6: $p = 0.014$, week 14: $p = 0.048$) in the tinnitus positive group (**Figure 6D**). Interestingly, the tinnitus negative group also demonstrated one significant frequency at 16 kHz (week 6: $p = 0.386$). The incidence of tinnitus-like behavior (**Figure 6G**) demonstrated a similar

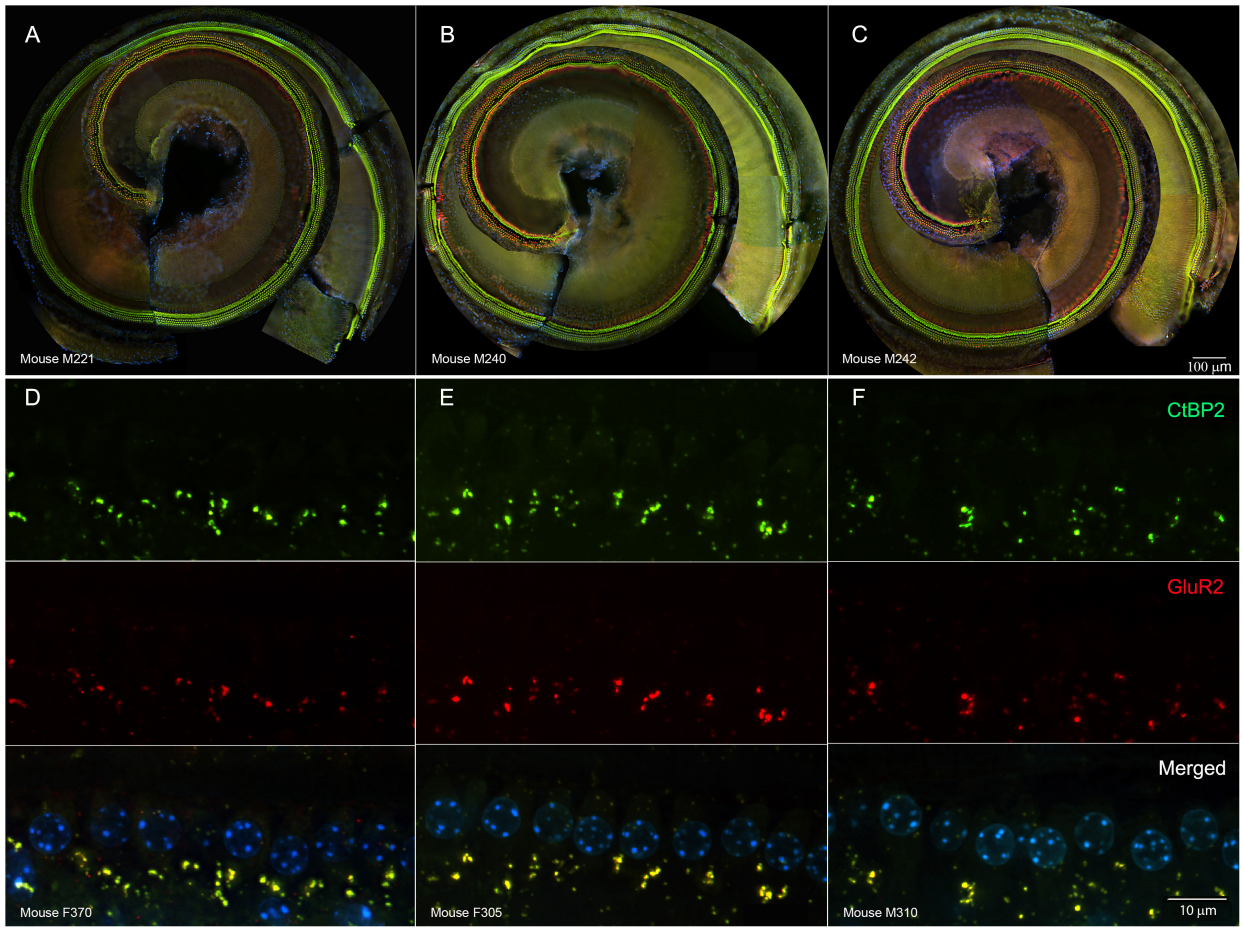

FIGURE 3 | Representative whole mount cochlear images displaying cochlear hair cells for each treatment group (**(A):** untreated control, **(B):** tobramycin/DMSO, **(C):** tobramycin/ebselen [Scale bar = 100 µm]). No observable evidence of tobramycin-induced outer hair cell or inner hair cell loss. Outer hair cells were stained with anti-myosin VIIa antibody (red) and inner hair cells were stained with FITC phalloidin (green). Representative micrographs showing pre and post synaptic densities in the 16 kHz region for each treatment group (**(D):** untreated control, **(E):** tobramycin/DMSO, **(F):** tobramycin/ebselen [Scale bar = 10 µm]). When comparing treatment groups, no observable differences were apparent when examining the immunolabeled presynaptic marker CtBP2 (green), postsynaptic marker GluR2 (red), or the merged images (yellow), which include hair cell nucleus marker DAPI (blue).

pattern as hyperacusis-like behavior (**Figure 4D**), as it was highest at 2 weeks after tobramycin dosing and gradually decreased over time. When examining if ebselen had an effect on preventing tinnitus-like behavior (**Figure 6H**), a Fisher's exact test did not find a significant effect ($p = 0.248$) but was more impactful than in hyperacusis-like behavior (**Figure 5F**).

DISCUSSION

In this study we demonstrated that a 14-day course of tobramycin can lead to hearing deficits, hyperacusis, and tinnitus in CBA/Ca mice, that may be clinically relevant. Ebselen was shown to be effective at preventing hearing loss and demonstrated non-significant evidence of preventing the development of tinnitus or hyperacusis in tobramycin treated mice. These deficits were observed in the absence of obvious cochlear hair cell loss or ribbon synapse degradation. These results are further discussed in context of previous preclinical and clinical studies investigating aminoglycoside-induced auditory dysfunction.

Tobramycin-Induced Temporary Threshold Shifts Can Occur Without Permanent Cochlear Damage

Tobramycin has been known to cause variable magnitudes of temporary and permanent threshold shift following a single course in animal models (Gu et al., 2020; Ogier et al., 2020) and humans (Garinis et al., 2020; Harruff et al., 2020). Here we confirmed that a standard course of tobramycin treatment caused consistent, yet small significant mean threshold shifts of roughly 10-15 dB SPL at 16 kHz in a CBA/Ca animal model (**Figure 2**). After 18 weeks after dosing, these hearing deficits decreased and returned to near baseline levels (**Figures 2D-H**). The responder criteria for hearing loss demonstrated a similar pattern, in which the percentage of mice with a relevant shift

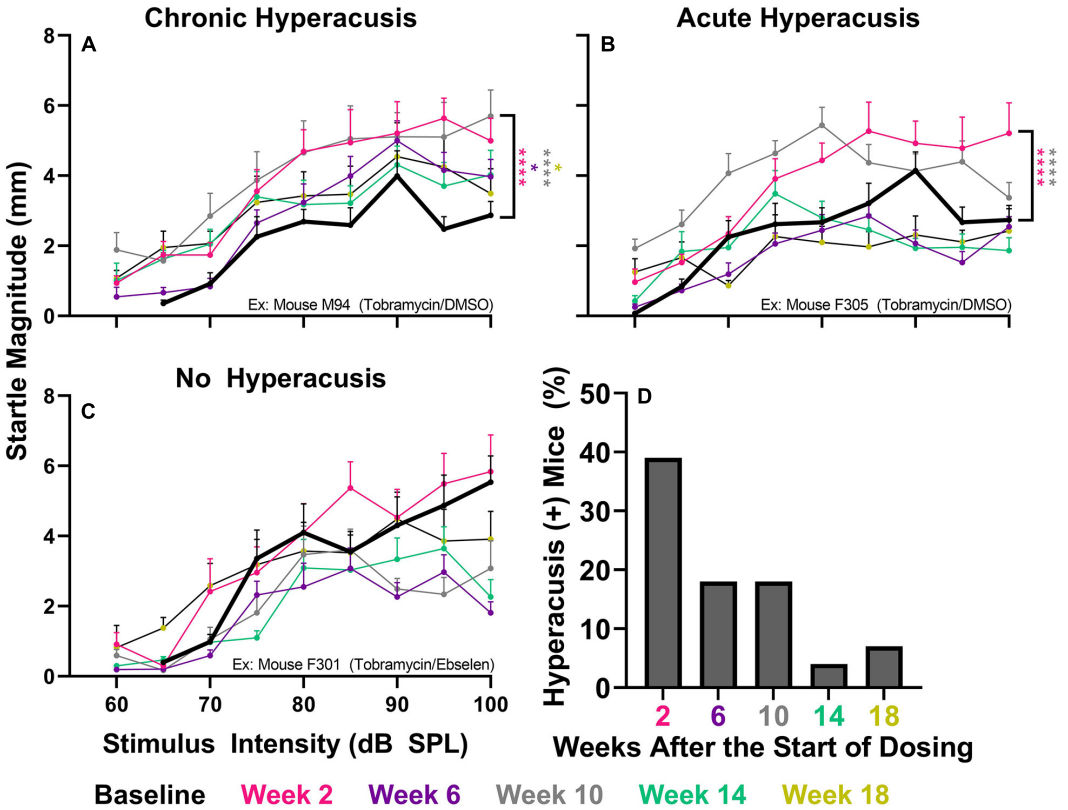

FIGURE 4 | Evaluation of behavioral evidence of hyperacusis for individual animals. IO Startle stimulus/response functions recorded from 3 representative tobramycin-treated mice. **(A):** Example of a tobramycin-treated mouse with chronic hyperacusis, **(B):** Acute hyperacusis, and **(C):** no hyperacusis. Startle response magnitude CMD (mm) as a function of stimulus intensity (60 to 100 dB SPL) represent each specific epoch (color coded) compared to baseline (bolded black line). Data is represented by means and standard errors. *Post hoc* significant differences between specific epochs (color coded) and baseline are indicated as follows: $^{*}p \leq 0.05$; $^{**}p \leq 0.01$; $^{***}p \leq 0.001$; $^{****}p \leq 0.0001$. **(D):** Histogram representing the % of all tobramycin treated mice which showed statistically significant increases in startle IO functions at each epoch after dosing.

decreased over time (**Figure 2I**). When comparing the effect size dosing factors, ebselen demonstrated protection against tobramycin-induced threshold shifts for the first 2 epochs after the start of dosing, but not at later time periods because threshold shifts were non-significant after this point (**Figure 2**). A similar finding was observed with the clinically modified or adopted responder criteria (American Speech-Language-Hearing Association, 1994). This finding was comparable to the effect of ebselen on amikacin treated mice (Longenecker et al., 2020), and provides evidence that ebselen or other otoprotective drugs might work at ameliorating AG-induced hearing loss in clinic (Avci et al., 2016; Fox et al., 2016; Dogan et al., 2017; El-Anwar et al., 2018; Apaydin et al., 2021). However, the threshold shifts seen here were drastically different than those found with a similar tobramycin dosing experiment in Swiss-Webster mice (Gu et al., 2020). While little is reported on the susceptibility of ototoxicity for most strains of mice, the CBA/Ca is well known for its relative resistance to noise- (Davis et al., 2001), and age- (Zheng et al., 1999; Peguero and Tempel, 2015; Liu et al., 2019), related hearing loss. When comparing these studies, it seems the CBA/Ca mouse has more resistant to AG-ototoxicity. However, the commercially available tobramycin used in each experiment could have differed by specific strain. This possibility was highlighted by an important recent finding which demonstrated that specific strains of gentamycin can have differential cochleotoxic effects (O'Sullivan et al., 2020). This could create a major confound in ototoxicity studies due to the variability of strain-induced damage and partially explains the variability of published results in the literature (Ogier et al., 2020). Nevertheless, a future study should investigate a tobramycin ototoxicity/dose response curve for CBA/Ca mice.

Just as we and others have discovered, aminoglycosides are not acutely ototoxic after one course of using non-lethal doses in most species and strains of laboratory animals (Longenecker et al., 2020; Ogier et al., 2020). In fact, cochlear hair cell loss was minimal or absent following one 14-day course of tobramycin (**Figures 3A-C**). It was also shown that spiral ganglion neurons and their synapses remain intact, at least after a recovery period of 16-18 weeks after tobramycin treatment (**Figures 3D-F**) or amikacin treatment (Longenecker et al., 2020). It is possible that immediate or early changes in synapse integrity following tobramycin treatment could explain the temporary auditory dysfunction documented in this study (Liu et al., 2015; Hong et al., 2018). Indeed, potentially relevant but largely

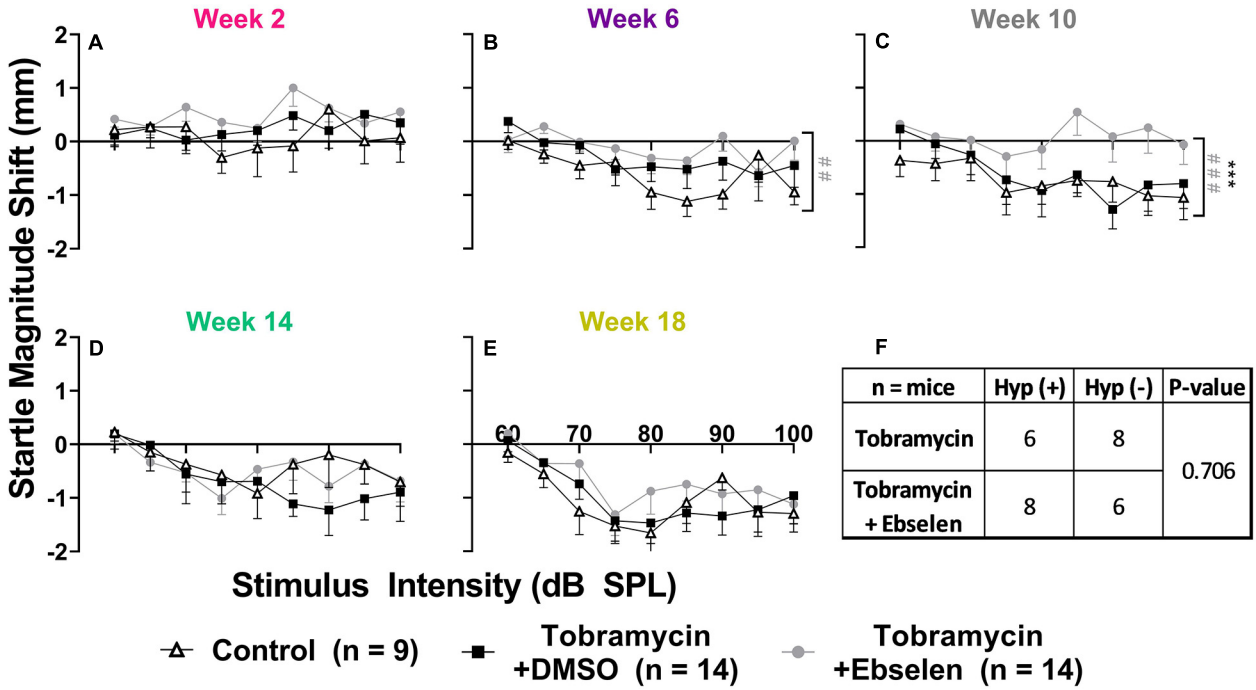

FIGURE 5 | Evaluation of behavioral evidence of hyperacusis by dosing group. Averaged tobramycin-induced IO stimulus/response functions shifts comparing testing groups at different epochs (**(A):** week 2, **(B):** week 6, **(C):** week 10, **(D):** week 14, **(E):** week 18) after the start of treatment. Startle response magnitude CMD (mm) as a function of stimulus intensity (60 to 100 dB SPL) represent each specific epoch minus baseline. The value 0 on the y-axis represents no change from baseline startle reactivity. Data is represented by means and standard errors. Post hoc tests determined significant differences between testing groups, which are indicated as follows: # (black), between control and DMSO treated animals; # (gray), between control and ebselen treated animals; *, between DMSO and ebselen treated animals. **(F):** Contingency table for the development of hyperacusis which shows the number of mice which met or did not meet the criteria for hyperacusis (significant increase in startle IO function at any epoch when compared to baseline). Each animal was analyzed independently. Two-sided Fisher's exact tests were used statistically evaluate differences between tobramycin dosed groups.

non-significant increases in ABR wave III/wave I amplitude ratios (**Supplementary Figure 1**) suggest either central compensation from altered peripheral input (Gold and Bajo, 2014), or direct effects of AGs on the central nervous system (Segal et al., 1999; Abd-Elhakim et al., 2021).

Hyperacusis and Tinnitus Appear After Tobramycin Treatment

The most important finding of this study is that tobramycin can cause behavioral signs of hyperacusis and tinnitus in mice (**Figures 4**, **5**, **6**). Additionally, these abnormal behaviors occur in the presence of only a mild loss of hearing sensitivity. These new findings are consistent with prior findings that amikacin can cause these behavioral symptoms following a mild threshold shift, although the mechanism will need to be elucidated (Longenecker et al., 2020; **Figure 7**). The largest difference between the two studies was that tobramycin treated mice demonstrated less startle magnitude increases after treatment than amikacin treated mice (**Figure 5** vs. **Figure 6** from Longenecker et al., 2020). This was especially true at the early epochs following treatment (**Figures 5A-C**). Tobramycin led to 50% and amikacin led to 82.3% of mice developing behavioral signs of hyperacusis. In both studies, hyperacusis-like symptoms were highest at epochs tested near the start of dosing and decreased thereafter (**Figure 4D**). The majority of mice treated with amikacin showed drastic increases in startle magnitude in contrast to a minority of mice treated with tobramycin. However, it is important to note that hyperacusis manifested differently between mice. Increased input/output startle functions such as the presented example of tobramycin treated mouse M94 (**Figure 4A**) was more commonly observed in amikacin treated mice (Longenecker et al., 2020). M94 demonstrated consistent hyperacusis throughout the testing period while F305 only experienced hyperacusis at weeks 2 and 10 after the start of dosing followed with clear habituation the rest of the epochs (**Figures 4A,B**). This temporal fluctuation disparity explains the dramatic difference in effect size between these mice which were both treated with tobramycin. Due to the lower incidence and startle magnitude shifts in tobramycin treated animals, it is not surprising that there was a non-significant effect of ebselen in preventing tobramycin-treated hyperacusis (**Figure 5F**). The effect sizes of dosing between epochs remained low throughout the study. The likely explanation of this phenomenon is that hyperacusis can be observed despite the natural response for mice to habituate to the startle reflex over time (**Figures 4B,C**, **5**). Long-term habituation of the ASR is a universal phenomenon across multiple species and testing conditions (Davis, 1984) and has been specifically observed

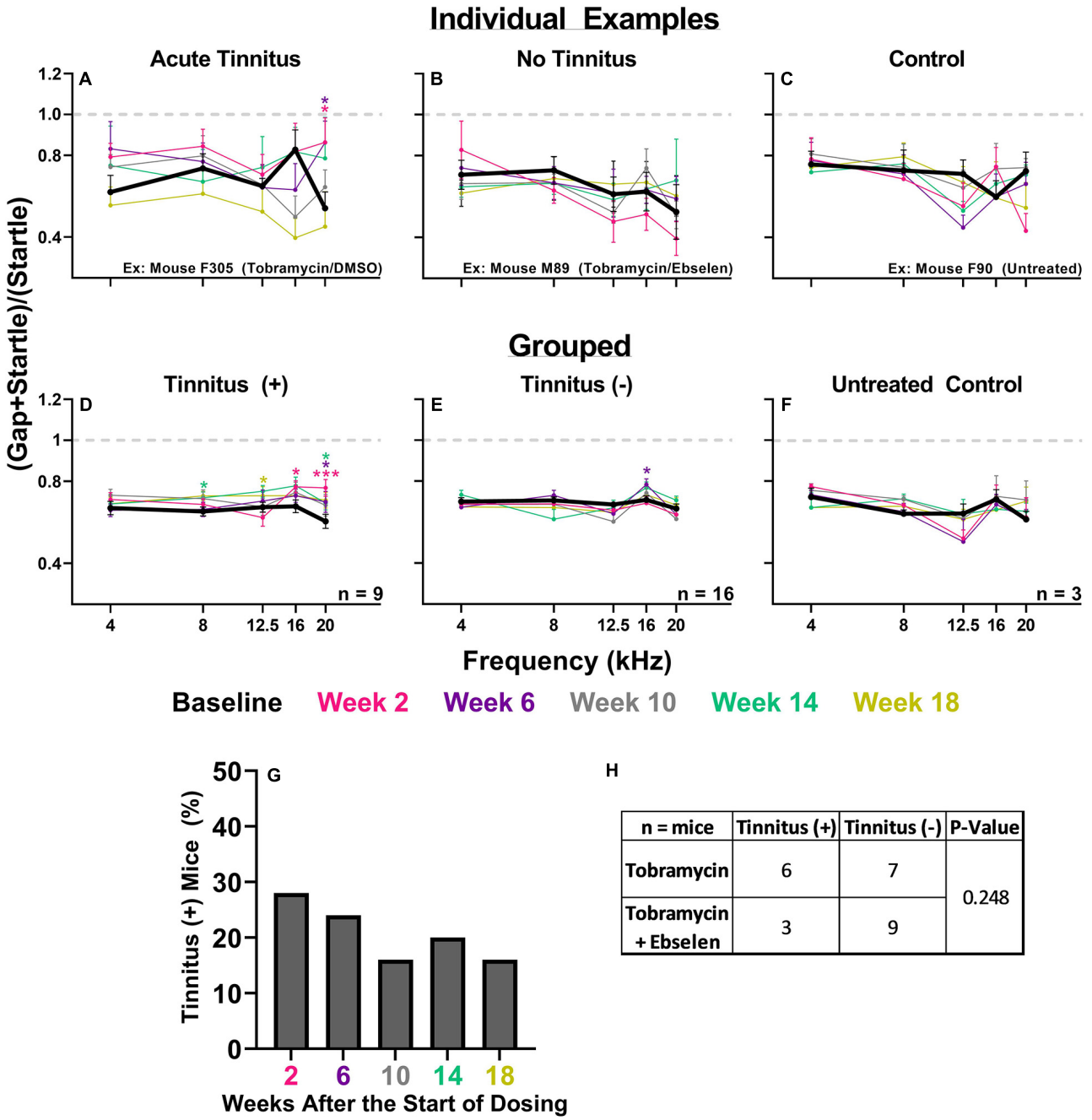

n = mice	Tinnitus (+)	Tinnitus (-)	P-Value
Tobramycin	6	7	0.248
Tobramycin + Ebselen	3	9	

FIGURE 6 | Evaluation of behavioral evidence of tinnitus for individual animals and dosing groups. **(A):** Example GPIAS functions for a tobramycin treated mouse with behavioral evidence of acute tinnitus, **(B):** a treated mouse with no tinnitus, and **(C):** an untreated control mouse. **(D):** GPIAS functions for the group mean averages of tinnitus mice, **(E):** tinnitus negative mice, and **(F):** untreated control mice. Tinnitus was defined as a significant GPIAS deficit at 1 or 2 adjacent frequencies at any epoch (color coded) compared to baseline (bolded black line). Data is represented by ratio means and standard errors. Post hoc significant differences between specific epochs (color coded) and baseline are indicated as follows: $^{*}p \leq 0.05$; $^{**}p \leq 0.01$; ***. **(G):** Histogram representing the % of all tobramycin treated mice which showed statistically significant gap detection deficits as described above at each epoch after dosing. **(H):** Contingency table for the development of tinnitus which shows the number of mice which met or did not meet the criteria for tinnitus. Each animal was analyzed independently. Two-sided Fisher's exact tests were used statistically evaluate differences between tobramycin dosed groups.

several strains of mice (Bullock et al., 1997; Pilz et al., 2014; Longenecker et al., 2018). This fact amplifies the importance of the odd behavioral shift towards dramatic increases in startle magnitude seen in some tobramycin (**Figures 4A,B**), and amikacin treated mice (Longenecker et al., 2020). The main reason hyperacusis was not observed in group averages

of tobramycin treated mice (**Figure 5**) is because most mice did not develop hyperacusis and habituated to the startle (**Figures 4D**, **5F**), which therefore decreased the average startle magnitude (**Figures 5A-E**). Amikacin treatment led to a higher incidence and magnitude of startle response shift, which explains the more elevated treatment group averages previously seen (Longenecker et al., 2020). Taken together, data from these studies suggest that aminoglycosides can dramatically increase startle responses in some animals despite habituation.

Behavioral evidence of tinnitus was also observed in tobramycin treated animals (**Figure 6**), although it is important to note the limitations of the GPIAS method in the context of AG-cochleotoxic experiments which were discussed in detail previously (Longenecker et al., 2020). We found that 9 out of 25 mice (36%) experienced gap detection deficits indicative of tinnitus at some point during the 18 weeks of testing after treatment, and similar to hyperacusis and hearing loss (**Figures 2**, **4D**), the incidence decreased over time (**Figure 6G**). AG-induced tinnitus is thought to have an incidence rate between 12 and 37.5% in CF or tuberculosis patients (Daud et al., 2014; Harruff et al., 2020; Sabur et al., 2021). The other interesting point to note is that tobramycin treatment caused consistent gap detection deficits. When tinnitus-positive animals were grouped together, a significant broad-frequency deficit in gap detection was observed at multiple epochs (**Figure 6D**). The greatest deficits were seen at high frequencies (i.e. 20 kHz), which is higher than the frequency with the greatest threshold deficits (16 kHz), a common report following noise exposure in animal studies (Turner et al., 2012; Coomber et al., 2014; Longenecker and Galazyuk, 2016). Importantly, when averaged together, animals determined to be tinnitus negative had a gap detection deficit at 16 kHz at week 6 (**Figure 6E**). This deficit might be due to loss of hearing sensitivity at 16 kHz rather than a tinnitus percept at this frequency (**Figure 2**). Although not statistically significant, ebselen co-treatment trended towards the prevention of the tinnitus-like behaviors (**Figure 6H**).

As discussed above, hyperacusis was found to be more prevalent than tinnitus following tobramycin treatment which is consistent with what has been reported after amikacin treatment (Longenecker et al., 2020). Clinically, the incidence rates of these maladies are correlated, but not 1:1 (Baguley and Hoare, 2018; Cederroth et al., 2020). A major confound is that clinical studies are nearly entirely self-reported and based on patient reported outcomes over the last week or month. Large clinical studies have found a significant positive correlation between tinnitus and hyperacusis (Cederroth et al., 2020; Raj-Koziak et al., 2021). Another study found that hyperacusis percept shows a positive correlation for the persistence of tinnitus (Refat et al., 2021). It is likely that the neural code and anatomy for these maladies have unique but overlapping pathways, which could explain the results from these AG studies (Eggermont, 2021). A recent report demonstrated that hyperacusis was developed in rats to a non-damaging noise exposure of 70 dB SPL (Thomas et al., 2019). This study also showed that hearing sensitivity as assessed by ABR and light and fluorescence cochlear histology are grossly intact after AG treatment, suggesting that hyperacusis can be developed in the absence of significant cochlear cell loss (Thomas et al., 2019; Longenecker et al., 2020). A critical point to make when comparing amikacin and tobramycin studies is that there might be a link between behavior and electrophysiological measures of AG-induced auditory dysfunction. Amikacin treated mice demonstrated significant increases in ABR amplitude wave III/wave I ratios along with higher incidence and magnitude of hyperacusis-like behavior (Longenecker et al., 2020). Here we report lower incidence and magnitude rates of hyperacusis-like behavior which correlated to less significant increases in ABR ratios (**Figure 4** and **Supplementary Figure 1**). Future studies should evaluate if this correlation between behavior and brain physiology reveals an underlying mechanism of tinnitus and/or hyperacusis (**Figure 7**). However, an important validation of this animal work was seen in CF-patients with lifetime histories of AG use (Westman et al., 2021). The Westman et al. (2021), study demonstrated that AG use was correlated with enhanced acoustic reflex growth functions compared to those with less or no AG exposure. The authors speculate that this finding more likely explains a central mechanism of auditory dysfunction, like hyperacusis or tinnitus, rather than cochlear related dysfunctions.

Towards a Mechanistic Understanding of AG-Induced Tinnitus and Hyperacusis

In reviewing data from this tobramycin study, and the prior amikacin study (Longenecker et al., 2020), with the recent human study (Westman et al., 2021), it seems that hyperacusis and tinnitus might be common side-effects of AG treatment. The mechanism(s) to explain these AG-induced symptoms need to be investigated and could be explained in three unique, or more likely, overlapping pathways: peripheral dysfunction (cellular or molecular), central plasticity resulting from peripheral dysfunction, or direct central disfunction (**Figure 7**).

It is thought that all types of cells in the cochlea can be affected by aminoglycosides (Jiang et al., 2017a,b). Hair cells are known to be vulnerable to AGs and many other drugs (**Figure 7(1)**, but at clinically relevant doses, it is unlikely that AGs lead to significant hair cell damage in animals or humans (**Figure 3**; Ogier et al., 2020). Even if hair cell death were observed, the resulting auditory dysfunction would not be fluctuating or diminishing over time (**Figures 2**, **4**, **6**; Longenecker et al., 2020), as hair cell loss is permanent. Alternatively, cochlear supporting cells, actively phagocytize dying hair cells, and expand into the deficit, and maintain epithelial/ionic integrity (**Figure 7(2)**; Bird et al., 2010; Monzack et al., 2015) as well as release anti-inflammatory proteins (May et al., 2013). These cells need to be studied in more detail to ascertain if they are important in mediating or modulating AG-induced auditory dysfunction. Evidence supporting the hypothesis that SGNs and/or their synapses undergo temporary degradation or remodeling following AG exposure has been observed (**Figure 7(3)**; Liu et al., 2015; Hong et al., 2018). This hypothesis is further supported by data showing decreases in ABR wave I amplitudes following AG treatment, especially at high frequencies (**Supplementary Figures 2**, **3**). As mentioned above, when considering the wave III/wave I ratio, a temporary increase was observed (**Supplementary Figure 1**; Longenecker et al., 2020), because

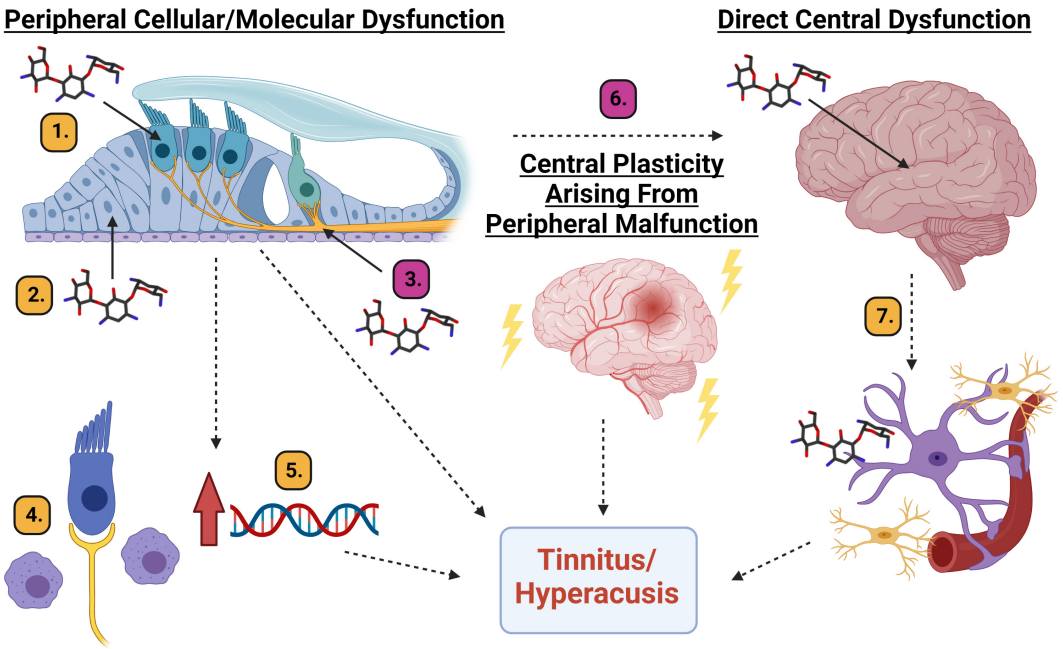

FIGURE 7 | Diagram of potential mechanistic explanations for AG-induced tinnitus and hyperacusis. Peripheral cellular or molecular dysfunction: (1). Hair cell cellular dysfunction. (2). Supporting cell dysfunction. (3). Spiral ganglion neuron/synapse dysfunction. (4). Inflammation induced macrophage activation. (5). Upregulation of genes responsible for inflammation. Central plasticity arising from peripheral malfunction. (6). Changes in the neural code related to maladaptive plastic changes to the auditory system. Direct central dysfunction. (7). Aminoglycoside crossing the blood brain barrier leading to inflammation and cellular/molecular responses from microglia and astrocytes which can result in changes to neural firing patterns. Magenta # mechanisms are partially supported by data from this manuscript and Longenecker et al., 2020. Yellow # mechanisms require further scientific exploration. Created with BioRender.com.

wave III amplitudes increased slightly while wave I decreased. Another likely mechanism for tinnitus and hyperacusis might increase inflammation in the cochlea (Jiang et al., 2017b). It has been shown that AGs cause inflammation in the cochlea and induce macrophage recruitment/activation which may modulate cochleotoxicity (**Figure 7(4)**; Sato et al., 2010; Wood and Zuo, 2017; Hirose and Li, 2019). Lastly, it has been shown that AGs can trigger altered gene expression in several pathways including JNK, NF-κB, stress response, apoptosis, cell cycle control, and DNA repair pathways, or modulate ion channels responsible for signal transduction (**Figure 7(5)**; Tao and Segil, 2015; Jiang et al., 2017b). Transient cochlear inflammation leading to macrophage recruitment and changes in gene expression changes may elicit the upstream dysfunctions marked by the behavioral symptoms of tinnitus and hyperacusis.

Central maladaptive plastic changes in response to peripheral insult has become central dogma in the field of tinnitus (**Figure 7(6)**; Roberts et al., 2010; Langguth et al., 2013; Auerbach et al., 2014; Henton and Tzounopoulos, 2021). Data from animals and humans have found many unique but likely overlapping mechanisms to explain the neural plastic changes related to tinnitus which include: increases in spontaneous (non-sound evoked) firing rate neural activity (Longenecker and Galazyuk, 2011; Berger et al., 2014; Galazyuk et al., 2019); increased incidence of neurons burst firing (Ma et al., 2006; Bauer et al., 2008), increased or decreased neural synchrony (Eggermont and Tass, 2015; Marks et al., 2018), thalamocortical dysrhythmia (De Ridder et al., 2015), altered balance between excitatory and inhibitory neurotransmission (Middleton et al., 2011; Llano et al., 2012; Ma et al., 2020; Zhang et al., 2021), cortical reorganization (Engineer et al., 2011; Jeschke et al., 2021), and neural inflammation (Fuentes-Santamaría et al., 2017; Wang et al., 2019; Deng et al., 2020). The mechanisms of hyperacusis are much less studied but are thought to have similar etiologies as tinnitus (Auerbach et al., 2014). A recent study found that hyperacusis-like behavior correlated to enhanced sound-driven firing rates and reduced first spike-latencies of auditory brainstem neurons (Martel and Shore, 2020). These findings corroborate the mechanistic explanation of hyperacusis observed in models of tobramycin, amikacin, and salicylate, that neural gain increases in the auditory neuroaxis (Supplemental **Figure 1**; Longenecker et al., 2020; Salvi et al., 2021). Central plasticity following any changes to the cochlea are likely, and thus represent a candidate mechanism for explaining the behavioral evidence of tinnitus and hyperacusis seen here (**Figures 4-6**).

To what extent do AGs cross the blood brain barrier and cause direct neural dysfunction (**Figure 7(7)**? Some evidence suggests it is indeed occurring in animals and humans. Recent reviews have described that aminoglycosides such as tobramycin and amikacin are neurotoxic (Grill and Maganti, 2011; Rezaei et al., 2018). Some of the proposed mechanisms for this neurotoxicity include: excitotoxic activation of NMDA receptors within the cochlea, oxidative stress, calcium channels modulation, and localized inflammatory response. Auditory brainstem neurons in

a chicken model were shown to decrease in size and then recover after 10 days of gentamicin treatment (Lippe, 1991). A similar set of studies in guinea pigs found that neurotropin-3 could protect spiral ganglion neurons from AG-induced degeneration (Ernfors et al., 1996; Duan et al., 2000). In mice, AG-induced ABR ratio amplitude increases were observed with tobramycin and amikacin (**Figure 4**, **5**, **6**; Longenecker et al., 2020) which suggests a clear trend towards increased neural activity in the auditory brainstem (Auerbach et al., 2014; Roberts and Salvi, 2019). Recent work has shown that brain inflammation can lead to tinnitus-like behavior in animals (Fuentes-Santamaría et al., 2017; Wang et al., 2019; Deng et al., 2020). If so, then ebselen would be a prime candidate for mitigating potential AG-induced inflammation (Kalinec et al., 2017; Jiang et al., 2017b; Wood and Zuo, 2017), as it has been implicated as a powerful anti-inflammatory and neuroprotective therapeutic (Wang et al., 2020). AG-penetration of the blood brain barrier in humans is understudied, however it has been suggested that AGs might be particularly neurotoxic in patients with compromised blood brain barriers (Segal et al., 1999), a condition which has been observed in CF patients (Vaughn et al., 1996).

Future Studies to Evaluate AG-Cochleotoxicity and Otoprotective Strategies

Recent evidence indicates that a single course of IV tobramycin can lead to hearing loss in CF patients (Garinis et al., 2020; Harruff et al., 2020) and that this loss of hearing sensitivity results in poorer speech discrimination (Harruff et al., 2020). More clinical studies need to document and confirm these results. Physiological examinations such as the ABR or middle-ear muscle reflex should also investigate if ABR wave III/wave I amplitude ratios are altered in patients taking AGs as they have been in noise/age related hearing loss investigations (Bharadwaj et al., 2019; Guest et al., 2019; Refat et al., 2021). Preclinical work should investigate the neurotoxic effects of AGs using clinically translatable dosing schedules (Longenecker et al., 2020), to parallel what has been reported in AG treated patients (Segal et al., 1999; Daud et al., 2014; Harruff et al., 2020; Sabur et al., 2021). As discussed above, the CBA/Ca mouse would make a good model for researching this question because of its good hearing sensitivity throughout its lifespan. Furthermore, mice with blood brain barrier vulnerabilities should be tested against CBA/Ca mice to investigate if AGs can cause a higher incidence of hyperacusis and tinnitus. These sorts of studies would benefit from neurological recordings from auditory nuclei as well as brain histology to investigate the direct effects of AGs on neural anatomy and physiology. Additionally, AG strain differences should be examined to see if all strains of common AGs like tobramycin, amikacin, and gentamycin result in differential cochleotoxic effects (O'Sullivan et al., 2020). This could lead to safer AG treatments and prevent many of the permanent side-effects. Future studies should continue to evaluate therapeutic interventions for AG cochleotoxicity. To improve translatability, future experiments should test if ebselen or other anti-inflammatory drugs can provide additional relief from cochleotoxic side-effects with extended dosing beyond the 14 day-AG treatment (Hammill and Campbell, 2018). If so, such pharmaceuticals could prevent or even treat the chronic ototoxic side-effects of AG treatment, especially in CF.

DATA AVAILABILITY STATEMENT

The raw data supporting the conclusions of this article will be made available by the authors, without undue reservation.

ETHICS STATEMENT

The animal study was reviewed and approved by Institutional Animal Care and Use Committee at Sound Pharmaceuticals, Inc.

AUTHOR CONTRIBUTIONS

RL, RG, and JK designed research. RL, RG, and JH performed research. RL and RG analyzed data. RL and JK wrote the manuscript. All authors contributed to the article and approved the submitted version.

FUNDING

All experiments were funded by Sound Pharmaceuticals, Inc.

SUPPLEMENTARY MATERIAL

The Supplementary Material for this article can be found online at: https://www.frontiersin.org/articles/10.3389/fnmol.2021.715952/full#supplementary-material

REFERENCES

Abd-Elhakim, Y. M., Abdel-Motal, S. M., Malhat, S. M., Mostafa, H. I., Moselhy, A. A. A., Beheiry, R. R., et al. (2021). Curcumin mitigates neurotoxic and neurobehavioral changes of gentamicin and sodium salicylate in rats by adjusting oxidative stress and apoptosis. *Life Sci.* 265:118824. doi: 10.1016/j.lfs.2020.118824

American Speech-Language-Hearing Association (1994). Guidelines for the audiologic management of individuals receiving cochleotoxic drug therapy. *ASHA* 36(Suppl. 12), 11–19. doi: 10.1044/policy.GL1994-00003

Apaydin, E., Dağli, E., Bayrak, S., Kankiliç, E. S., Şahin, H., and Acar, A. (2021). Protective effect of creatine on amikacin-induced ototoxicity. *Braz. J. Otorhinolaryngol.* S1 808-8694, 30155–30155. doi: 10.1016/j.bjorl.2020.09.002

Auerbach, B. D., Rodrigues, P. V., and Salvi, R. J. (2014). Central gain control in tinnitus and hyperacusis. *Front. Neurol.* 5:206. doi: 10.3389/fneur.2014.00206

Avci, D., Erkan, M., Sönmez, M. F., Kökoğlu, K., Güneş, M. S., Gündoğdu, R., et al. (2016). A prospective experimental study on the protective effect on resveratrol against amikacin-induced ototoxicity in rats. *J. Int. Adv. Otol.* 12, 290–297. doi: 10.5152/iao.2016.2617

Baguley, D. M., and Andersson, G. (2007). *Hyperacusis: Mechanisms, Diagnosis, and Therapies*. San Diego, CA: Plural Publishing Inc.

Baguley, D. M., and Hoare, D. J. (2018). Hyperacusis: major research questions. HNO 66, 358–363. doi: 10.1007/s00106-017-0464-3

Bauer, C. A., Turner, J. G., Caspary, D. M., Myers, K. S., and Brozoski, T. J. (2008). Tinnitus and inferior colliculus activity in chinchillas related to three distinct patterns of cochlea trauma. *J. Neurosci. Res.* 86, 2564–2578. doi: 10.1002/jnr.221699

Berger, J. I., Coomber, B., Wells, T. T., Wallace, M. N., and Palmer, A. R. (2014). Changes in the response properties of inferior colliculus neurons relating to tinnitus. *Front. Neurol.* 5:203. doi: 10.3389/fneur.2014.00203

Bharadwaj, H. M., Mai, A. R., Simpson, J. M., Choi, I., Heinz, M. G., and Shinn-Cunningham, B. G. (2019). Non-invasive assays of cochlear synaptopathy – candidates and considerations. *Neuroscience* 407, 53–66. doi: 10.1016/j.neuroscience.2019.02.031

Bird, J. E., Daudet, N., Warchol, M. E., and Gale, J. E. (2010). Supporting cells eliminate dying sensory hair cells to maintain epithelial integrity in the avian inner ear. *J. Neurosci.* 30, 12545–12556. doi: 10.1523/JNEUROSCI.3042-10.2010

Bullock, A. E., Slobe, B. S., Vázquez, V., and Collins, A. C. (1997). Inbred mouse strains differ in the regulation of startle and prepulse inhibition of the startle response. *Behav. Neurosci.* 111, 1353–1360. doi: 10.1037//0735-7044.111.6.1353

Cederroth, C. R., Lugo, A., Edvall, N. K., Lazar, A., Lopez-Escamez, J. A., Bulla, J., et al. (2020). Association between hyperacusis and tinnitus. *J. Clin. Med.* 9:2412. doi: 10.3390/jcm9082412

Coomber, B., Berger, J. I., Kowalkowski, V. L., Shackleton, T. M., Palmer, A. R., and Wallace, M. N. (2014). Neural changes accompanying tinnitus following unilateral acoustic trauma in the guinea pig. *Eur. J. Neurosci.* 40, 2427–2441. doi: 10.1111/ejn.12580

Daud, M. K., Mohamadl, H., Haron, A., and Rahman, N. A. (2014). Ototoxicity screening of patients treated with streptomycin using distortion product otoacoustic emissions. *B-ENT* 10, 53–58.

Davis, M. (1984). "The mammalian startle response," in *Neural Mechanisms of Startle Behavior*, ed. R. C. Eaton (New York, NY: Springer Science & Plenum Press), 287–351.

Davis, R. R., Newlander, J. K., Ling, X. B., Cortopassi, G. A., Krieg, E. F., and Erway, L. C. (2001). Genetic basis for susceptibility to noise-induced hearing loss in mice. *Hear. Res.* 155, 82–90. doi: 10.1016/s0378-5955(01)00250-7

De Ridder, D., Vanneste, S., Langguth, B., and Llinas, R. (2015). Thalamocortical dysrhythmia: a theoretical update in tinnitus. *Front. Neurol.* 6:124. doi: 10.3389/fneur.2015.00124

Deng, D., Wang, W., and Bao, S. (2020). Diffusible tumor necrosis factor-alpha (TNF-α) promotes noise-induced parvalbumin-positive (PV+) neuron loss and auditory processing impairments. *Front. Neurosci.* 14:573047. doi: 10.3389/fnins.2020.573047

Dogan, M., Polat, H., Yasar, M., Bayram, A., Karatas, D., Hira, I., et al. (2017). Protective role of misoprostol in prevention of gentamicin ototoxicity. *Int. J. Pediatr. Otorhinolaryngol.* 96, 140–144. doi: 10.1016/j.ijporl.2017.03.023

Duan, M., Agerman, K., Enfors, P., and Canlon, B. (2000). Complementary roles of neurotrophin 3 and a N-methyl-D-aspartate antagonist in the protection of noise and aminoglycoside-induced ototoxicity. *Proc. Natl. Acad. Sci. U.S.A.* 97, 7597–7602. doi: 10.1073/pnas.97.13.7597

Eggermont, J. J. (2021). Separate auditory pathways for the induction and maintenance of tinnitus and hyperacusis. *Prog. Brain Res.* 260, 101–127. doi: 10.1016/bs.pbr.2020.01.006

Eggermont, J. J., and Tass, P. A. (2015). Maladaptive neural synchrony in tinnitus: origin and restoration. *Front. Neurol.* 6:29. doi: 10.3389/fneur.2015.00029

El-Anwar, M. W., Abdelmonem, S., Nada, E., Galhoom, D., and Abdelsameea, A. A. (2018). Protective effect of pentoxifylline on amikacin-induced ototoxicity. *Ear Nose Throat J.* 97, E8–E12. doi: 10.1177/014556131809700802

Elson, E. C., Meier, E., and Oermann, C. M. (2020). The implementation of an aminoglycoside induced ototoxicity algorithm for people with cystic fibrosis. *J. Cyst. Fibros.* 20, 284–287. doi: 10.1016/j.jcf.2020.08.002

Engineer, N. D., Riley, J. R., Seale, J. D., Vrana, W. A., Shetake, J. A., Sudanagunta, S. P., et al. (2011). Reversing pathological neural activity using targeted plasticity. *Nature* 470, 101–104. doi: 10.1038/nature09656

Ernfors, P., Duan, M. L., Elshamy, W. M., and Canlon, B. (1996). Protection of auditory neurons from aminoglycoside toxicity by neurtrophin-3. *Nat. Med.* 2, 463–467. doi: 10.1038/nm0496-463

Flume, P. A., Mogayzel, P. J. Jr., Robinson, K. A., Goss, C. H., Rosenblatt, R. L., Kuhn, R. J., et al. (2009). Cystic fibrosis pulmonary guidelines: treatment of pulmonary exacerbations. *Am. J. Respir. Crit. Care Med.* 180, 802–808. doi: 10.1164/rccm.200812-1845PP

Fox, D. J., Cooper, M. D., Speil, C. A., Roberts, M. H., Yanik, S. C., Meech, R. P., et al. (2016). D-Methionine reduces tobramycin-induced ototoxicity without antimicrobial interference in animal models. *J. Cyst. Fibros.* 15, 518–530. doi: 10.1016/j.jcf.2015.06.005

Fuentes-Santamaría, V., Alvarado, J. C., Melgar-Rojas, P., Gabaldón-Ull, M. C., Miller, J. M., and Juiz, J. M. (2017). The role of glia in the peripheral and central auditory system following noise overexposure: contribution to TNF-α and IL-1β to the pathogenesis of hearing loss. *Front. Neuroanat.* 11:9. doi: 10.3389/fnana.2017.00009

Galazyuk, A. V., Longenecker, R. J., Voytenko, S. V., Kristaponyte, I., and Nelson, G. I. (2019). Residual inhibition: from the putative mechanisms to potential tinnitus treatment. *Hear. Res.* 375, 1–13. doi: 10.1016/j.heares.2019/01.022

Garinis, A., Gleser, M., Johns, A., Larsen, E., and Vachhani, J. (2020). Prospective cohort study of ototoxicity in persons with cystic fibrosis following a single course of intravenous tobramycin. *J. Cyst. Fibros.* 20, 278–283. doi: 10.1016/j.jcf.2020.07.001

Garinis, A. C., Cross, C. P., Srikanth, P., Carroll, K., Feeney, M. P., Keefe, D. H., et al. (2017). The cumulative effects of intravenous antibiotic treatments on hearing in patients with cystic fibrosis. *J. Cyst. Fibros.* 16, 401–409. doi: 10.1016/j.jcf.2017.01.006

Gold, J. R., and Bajo, V. M. (2014). Insult-induced adaptive plasticity of the auditory system. *Front. Neurosci.* 9:110. doi: 10.3389/fnins.2014.00110

Gómez-Nieto, R., Hormigo, S., and López, D. E. (2020). Perpulse inhibition of the auditory startle reflex assessment as hallmark of brainstem sensorimotor gating mechanisms. *Brain Sci.* 10:639. doi: 10.3390/brainsci10090639

Grill, M. F., and Maganti, R. K. (2011). Neurotoxic effects associated with antibiotic use: management considerations. *Br. J. Clin. Phamacol.* 73, 381–393. doi: 10.1111/j.1365-2125.2011.03991.x

Grimsley, C. A., Longenecker, R. J., Rosen, M. J., Young, J. W., Grimsley, J. M., and Galazyuk, A. V. (2015). An improved approach to separating startle data from noise. *J. Neurosci. Methods* 253, 206–217. doi: 10.1016/j.jneumeth.2015.07.001

Gu, R., Longenecker, R. J., Homan, J., and Kil, J. (2020). Ebselen attenuates tobramycin-induced ototoxicity in mice. *J. Cyst. Fibros.* 20, 271–277. doi: 10.1016/j/jcf.2020.02.014

Guest, H., Munro, K. J., Prendergast, G., and Plack, C. J. (2019). Reliability and interrelations of seven proxy measures of cochlear synaptopathy. *Hear. Res.* 375, 34–43. doi: 10.1016/j.heares.2019.01.018

Hammill, T. L., and Campbell, K. C. (2018). Protection for medication-induced hearing loss: the state of the science. *Int. J. Audiol.* 57, 87–95. doi: 10.1080/14992027.2018.1455114

Harruff, E. E., Kil, J., Ortiz, M. G. T., Dorgan, D., Jain, R., Poth, E. A., et al. (2020). Ototoxicity in cystic fibrosis patients receiving intravenous tobramycin for acute pulmonary exacerbation: ototoxicity following tobramycin treatment. *J. Cyst. Fibros.* 20, 288–294. doi: 10.1016/j.jcf.2020.11.020

Henton, A., and Tzounopoulos, T. (2021). What's the buzz? The neuroscience and the treatment of tinnitus. *Physiol. Rev.* 101, 1609–1632. doi: 10.1152/physrev.00029.2020

Hirose, K., and Li, S. Z. (2019). The role of monocytes and macrophages in the dynamic permeability of the blood-perilymph barrier. *Hear. Res.* 374, 49–57. doi: 10.1016/j.heares.2019.01.006

Hong, H., Dowdy, D. W., Dooley, K. E., Francis, H. W., Budhathoki, C., Han, H. R., et al. (2020). Risk of hearing loss among multidrug-resistant tuberculosis patients according to cumulative aminoglycoside dose. *Int. J. Tuberc. Lung Dis.* 24, 65–72. doi: 10.5588/ijtld.19.0062

Hong, J., Chen, Y., Zhang, Y., Li, J., Ren, L., Yang, L., et al. (2018). N-methyl-D-Aspartate receptors involvement in the gentamicin-induced hearing loss and pathological changes of ribbon synapse in the mouse cochlear inner hair cells. *Neural Plast* 2018:3989201. doi: 10.1155/2018/3989201

Huth, M. E., Ricci, A. J., and Cheng, A. G. (2011). Mechanisms of aminoglycoside ototoxicity and targets of hair cell protection. *Int. J. Otolaryngol.* 2011:937861. doi: 10.1155/2011/937861

Jeschke, M., Happel, M. F. K., Tziridis, K., Krauss, P., Schilling, A., Schulze, H., et al. (2021). Acute and long-term circuit-level effects in the auditory cortex after sound trauma. *Front. Neurosci.* 14:598406. doi: 10.3389/fnins.2020.598406

Jiang, M., Karasawa, T., and Steyger, P. S. (2017a). Aminoglycoside-induced cochleotoxicity: a review. *Front. Cell. Neurosci.* 11:308. doi: 10.3389/fncel.2017.00308

Jiang, M., Taghizadeh, F., and Steyger, P. S. (2017b). Potential mechanisms underlying inflammation-enhanced aminoglycoside-induced cochleotoxicity. *Front. Cell. Neurosci.* 11:362. doi: 10.3389/fncel.2017.00362

Kalinec, G. M., Lomberk, G., Urrutia, R. A., and Kalinec, F. (2017). Resolution of cochlear inflammation: novel target for preventing or ameliorating drug-, noise-, and age-related hearing loss. *Front. Cell. Neurosci.* 11:192. doi: 10.3389/fncel.2017.00192

Kil, J., Harruff, E. E., and Longenecker, R. J. (2021). Development of ebselen for the treatment of sensorineural hearing loss and tinnitus. *Hear. Res.* 108209. doi: 10.1016/j.heares.2021.108209 [Epub ahead of print].

Langguth, B., Kreuzer, P. M., Kleinjung, T., and De Ridder, D. (2013). Tinnitus: causes and clinical management. *Lancet Neurol.* 12, 920–930. doi: 10.1016/S1474-4422(13)70160-1

Lippe, W. R. (1991). Reduction and recovery of neuronal size in the cochlear nucleus of the chicken following aminoglycoside intoxication. *Hear. Res.* 51, 193–202. doi: 10.1016/0378-5955(91)90036-9

Liu, H., Li, G., Lu, J., Gao, Y. G., Song, L., Li, G. L., et al. (2019). Cellular differences in the cochlea of CBA and B6 mice may underlie their difference in susceptibility to hearing loss. *Front. Cell. Neurosci.* 13:60. doi: 10.3389/fncel.2019.00060

Liu, K., Chen, D., Guo, W., Yu, N., Wang, X., Ji, F., et al. (2015). Spontaneous and partial repair of ribbon synapse in cochlear inner hair cells after ototoxic withdrawal. *Mol. Neurobiol.* 52, 1680–1689. doi: 10.1007/s12035-014-8951-y

Llano, D. A., Turner, J., and Caspary, D. M. (2012). Diminished cortical inhibition in an aging mouse model of chronic tinnitus. *J. Neurosci.* 32, 16141–16148. doi: 10.1523/JNEUROSCI.2499-12.2012

Longenecker, R. J., and Galazyuk, A. V. (2011). Development of tinnitus in CBA/CaJ mice following sound exposure. *J. Assoc. Res. Otolaryngol.* 12, 647–658. doi: 10.1007/s10162-011-0276-1

Longenecker, R. J., and Galazyuk, A. V. (2012). Methodological optimization of tinnitus assessment using prepulse inhibition of the acoustic startle reflex. *Brain Res.* 1485, 54–62. doi: 10.1016/j.brainres.2012.02.067

Longenecker, R. J., and Galazyuk, A. V. (2016). Variable effects of acoustic trauma on behavioral and neural correlates of tinnitus in individual animals. *Front. Behav. Neurosci.* 10:207. doi: 10.3389/fnbeh.2016.00207

Longenecker, R. J., Gu, R., Homan, J., and Kil, J. (2020). A novel mouse model of aminoglycoside-induced hyperacusis and tinnitus. *Front. Neurosci.* 14:5611185. doi: 10.3389/fnins.2020.561185

Longenecker, R. J., Kristaponyte, I., Nelson, G. L., Young, J. W., and Galazyuk, A. V. (2018). Addressing variability in the acoustic startle reflex for accurate gap detection assessment. *Hear. Res.* 363, 119–135. doi: 10.1016/j.heares.2018.03.013

Ma, L., Ono, M., Qin, L., and Kato, N. (2020). Acoustic trauma induced the alteration of the activity balance of excitatory and inhibitory neurons in the inferior colliculus of mice. *Hear. Res.* 391:107957. doi: 10.1016/j.heares.2020.107957

Ma, W. L. D., Hidaka, H., and May, B. J. (2006). Spontaneous activity in the inferior colliculus of CBA/J mice after manipulations that induce tinnitus. *Hear. Res.* 212, 9–21. doi: 10.1016/j.heares.2005.10.003

Marks, K. L., Martel, D. T., Wu, C., Basura, G. J., Roberts, L. E., Schvartz-Leyzac, K. C., et al. (2018). Auditory-somatosensory bimodal stimulation desynchronizes brain circuitry to reduce tinnitus in guinea pigs and humans. *Sci. Transl. Med.* 10:eaal3175. doi: 10.1126/scitranslmed.aal3175

Martel, D. T., and Shore, S. E. (2020). Ventral cochlear nucleus bushy cells encode hyperacusis in guinea pigs. *Sci. Rep.* 10:20594. doi: 10.1038/s41598-020-77754-z

Martini, A. C., Gomez-Arboledas, A., Forner, S., Rodriguez-Ortiz, C. J., McQuade, A., Danhash, E., et al. (2019). Amyloid-beta impairs TOM1-mediated IL-1R1 signaling. *Proc. Natl. Acad. Sci. U.S.A.* 116, 21198–21206. doi: 10.1073/pnas.1914088116

May, L. A., Kramarenko, I. I., Brandon, C. S., Voelkel-Johnson, C., Roy, S., Truong, K., et al. (2013). Inner ear supporting cells protect hair cells by secreting HSP70. *J. Clin. Invest.* 123, 3577–3587. doi: 10.1172/JCI68480

Middleton, J. W., Kiritani, T., Pedersen, C., Turner, J. G., Shepherd, G. M. G., and Tzounopoulos, T. (2011). Mice with behavioral evidence of tinnitus exhibit dorsal cochlear nucleus hyperactivity because of decreased GABAergic inhibition. *Proc. Natl. Acad. Sci. U.S.A.* 108, 7601–7606. doi: 10.1073/pnas.1100223108

Monzack, E. L., May, L. A., Roy, S., Gale, J. E., and Cunningham, L. L. (2015). Live imaging the phagocytic activity of inner ear supporting cells in response to hair cell death. *Cell Death Differ.* 22, 1995–2005. doi: 10.1038/cdd.2015.48

Ogier, J. M., Lockhart, P. J., and Burt, R. A. (2020). Intravenously delivered aminoglycoside antibiotics, tobramycin and amikacin, are not ototoxic in mice. *Hear. Res.* 386:107870. doi: 10.1016/j.heares.2019.107870

O'Sullivan, M. E., Song, Y., Greenhouse, R., Lin, R., Perez, A., Atkinson, P. J., et al. (2020). Dissociating antibacterial from ototoxic effects of gentamicin C-subtypes. *Proc. Natl. Acad. Sci. U.S.A.* 117, 32423–32432. doi: 10.1073/pnas.2013065117

Peguero, B., and Tempel, B. L. (2015). A chromosome 17 locus engenders frequency-specific non-progressive hearing loss that contributes to age-related hearing loss in mice. *JARO* 16, 459–471. doi: 10.1007/s10162-015-0519-7

Pienkowski, M., Tyler, R. S., Roncancio, E. R., Jun, H. J., Brozoski, T., Dauman, N., et al. (2014). A review of hyperacusis and future directions: part II. Measurement, mechanisms, and treatment. *Am. J. Audiol.* 23, 420–436. doi: 10.1044/2014_AJA-13-0037

Pilz, P. K. D., Arnold, S. W., Rischawy, A. T., and Plappert, C. F. (2014). Longterm-habituation of the startle response in mice is stimulus modality, but not context specific. *Front. Integr. Neurosci.* 7:103. doi: 10.3389/fnint.2013.00103

Raj-Koziak, D., Gos, E., Kutyba, J., Skarzynski, H., and Sharzynski, P. H. (2021). Decreased sound tolerance in tinnitus patients. *Life* 11:87. doi: 10.3390/life11020087

Refat, F., Wertz, J., Hinrichs, P., Klose, U., Samy, H., Abdelkader, R. M., et al. (2021). Co-occurrence of hyperacusis accelerates with tinnitus burden over time and requires medical care. *Front. Neurol.* 12:627522. doi: 10.3389/fneur.2021.627522

Rezaei, N. J., Bazzazi, A. M., and Alavi, S. A. N. (2018). Neurotoxicity of the antibiotics: a comprehensive study. *Neurol. India* 66, 1732–1740. doi: 10.4103/0028-3886.246258

Roberts, L. E., Eggermont, J. J., Caspary, D. M., Shore, S. E., Melcher, J. R., and Kaltenbach, J. A. (2010). Ringing ears: the neuroscience of tinnitus. *J. Neurosci.* 30, 14972–14979. doi: 10.1523/JNEUROSCI.4028-10.2010

Roberts, L. E., and Salvi, R. (2019). Overview: hearing loss, tinnitus, hyperacusis, and the role of central gain. *Neurosci* 407, 1–7. doi: 10.1016/j.neuroscience.2019.03.021

Sabur, N. F., Brar, M. S., Wu, L., and Brode, S. K. (2021). Low-dose amikacin in the treatment of multidrug-resistant tuberculosis (MDR-TB). *BMC Infect. Dis.* 21:254. doi: 10.1186/s12879-021-05947-6

Salvi, R., Radziwon, K., Manohar, S., Auerbach, B., Ding, D., Liu, X., et al. (2021). Review: neural mechanisms of tinnitus and hyperacusis in acute drug-induced ototoxicity. *Am. J. Audiol.* 1–15. doi: 10.1044/2020_AJA-20-00023 [Epub ahead of print].

Sato, E., Shick, H. E., Ransohoff, R. M., and Hirose, K. (2010). Expression of fractalkine receptor CX3CR1 on cochlear macrophages influences survival of hair cells following ototoxic injury. *JARO* 11, 223–234. doi: 10.1007/s10162-009-0198-3

Segal, J. A., Harris, B. D., Kustova, Y., Basile, A., and Skolnick, P. (1999). Aminoglycoside neurotoxicity involves NMDA receptor activation. *Brain Res.* 815, 270–277. doi: 10.1016/s0006-8993(98)01123-8

Sharpley, A. L., Williams, C., Holder, A. A., Godlewska, B. R., Singh, N., Shanyinde, M., et al. (2020). A phase 2a randomized, double-blind, placebo-controlled, parallel-group, add-on clinical trial of ebselen (SPI-1005) as a novel treatment for mania or hypomania. *Psychopharmacology (Berl.)* 237, 3773–3782. doi: 10.1007/s00213-020-05654-1

Shore, S. E., and Wu, C. (2019). Mechanisms of noise-induced tinnitus: insights from cellular studies. *Neuron* 103, 8–20. doi: 10.1016/j.neuron.2019.05.008

Smith, S., Rowbotham, N. J., and Regan, K. H. (2018). Inhaled anti-pseudomonal antibiotics for long-term therapy in cystic fibrosis. *Cochrane Database of Syst. Rev.* 3:CD001021. doi: 10.1002/14651858.CD001021.pub3

Staecker, H. (2021). Re-evaluating aminoglycoside ototoxicity. *J. Cyst. Fibros.* 20:5. doi: 10.1016/j.jcf.2021.01.003

Tao, L., and Segil, N. (2015). Early transcriptional response to aminoglycoside antibiotic suggests alternate pathways leading to apoptosis in sensory hair cells

in the mouse inner ear. *Front. Cell. Neurosci.* 9:190. doi: 10.3389/fncel.2015.00190

Thomas, M. E., Guercio, G. D., Drudik, K. M., and de Villers-Sidani, E. (2019). Evidence of hyperacusis in adult rats following non-traumatic sound exposure. *Front. Syst. Neurosci.* 13:55. doi: 10.3389/fnsys.2019.00055

Turner, J., Larsen, D., Hughes, L., Moechars, D., and Shore, S. (2012). Time course of tinnitus development following noise exposure. *J. Neurosci. Res.* 90, 1480–1488. doi: 10.1002/jnr.22827

Vaughn, B. V., Ali, I. I., Olivier, K. N., Lackner, R. P., Robertson, K. R., Messenheimer, J. A., et al. (1996). Seizures in lung transplant recipients. *Epilepsia* 37, 1175–1179. doi: 10.1111/j.1528-1157.1996.tb00549.x

Wang, J., Wang, P., Dong, C., Zhao, Y., Zhou, J., Yuan, C., et al. (2020). Mechanisms of ebselen as a therapeutic and its pharmacology applications. *Future Med. Chem.* 12, 2141–2160. doi: 10.4155/fmc-2019-0218

Wang, W., Zhang, L. S., Zinsmaier, A. K., Patterson, G., Leptich, E. J., Shoemaker, S. L., et al. (2019). Neuroinflammation mediates noise-induced synaptic imbalance and tinnitus in rodent models. *PLoS Biol.* 17:e3000307. doi: 10.1371/journal.pbio.3000307

Westman, M. R., Putterman, D. B., Garinis, A. C., Hunter, A. C., and Freeney, M. P. (2021). Wideband acoustic reflex growth in adults with cystic fibrosis. *Am. J. Audiol.* 1–9. doi: 10.1044/2020_AJA-20-00117 [Epub ahead of print].

Wood, M. B., and Zuo, J. (2017). The contribution of immune infiltrates to ototoxicity and cochlear hair cell loss. *Front. Cell. Neurosci.* 11:106. doi: 10.3389/fncel.2017.00106

Zhang, L., Wu, C., Martel, D. T., West, M., Sutton, M. A., and Shore, S. E. (2021). Noise exposure alters glutamatergic and GABAergic synaptic connectivity in the hippocampus and its relevance to tinnitus. *Neural Plast.* 2021:8833087. doi: 10.1155/2021/8833087

Zheng, Q. Y., Johnson, K. R., and Erway, L. C. (1999). Assessment of hearing in 80 inbred strains of mice by ABR threshold analysis. *Hear. Res.* 130, 94–107. doi: 10.1016/s0378-5955(99)00003-9

Conflict of Interest: The authors disclose that they are employed by Sound Pharmaceuticals and have stock ownership in the Company.

The authors declare that this study received funding from Sound Pharmaceuticals, Inc. The funder had the following involvement with the study: provided full financial support for this study. The funder was not involved in the study design, data collection and analysis, or decision to publish. All authors declare no other competing interests.

Publisher's Note: All claims expressed in this article are solely those of the authors and do not necessarily represent those of their affiliated organizations, or those of the publisher, the editors and the reviewers. Any product that may be evaluated in this article, or claim that may be made by its manufacturer, is not guaranteed or endorsed by the publisher.

frontiers in Molecular Neuroscience

ORIGINAL RESEARCH
published: 05 October 2021
doi: 10.3389/fnmol.2021.729625

LGR5-Positive Supporting Cells Survive Ototoxic Trauma in the Adult Mouse Cochlea

Natalia Smith-Cortinez[1,2†], Rana Yadak[1,2†], Ferry G. J. Hendriksen[1], Eefje Sanders[1], Dyan Ramekers[1,2], Robert J. Stokroos[1,2], Huib Versnel[1,2] and Louise V. Straatman[1,2]*

[1] Department of Otorhinolaryngology and Head & Neck Surgery, University Medical Center Utrecht, Utrecht, Netherlands,
[2] UMC Utrecht Brain Center, University Medical Center Utrecht, Utrecht University, Utrecht, Netherlands

Sensorineural hearing loss is mainly caused by irreversible damage to sensory hair cells (HCs). A subgroup of supporting cells (SCs) in the cochlea express leucine-rich repeat-containing G-protein coupled receptor 5 (LGR5), a marker for tissue-resident stem cells. LGR5+ SCs could be used as an endogenous source of stem cells for regeneration of HCs to treat hearing loss. Here, we report long-term presence of LGR5+ SCs in the mature adult cochlea and survival of LGR5+ SCs after severe ototoxic trauma characterized by partial loss of inner HCs and complete loss of outer HCs. Surviving LGR5+ SCs (confirmed by GFP expression) were located in the third row of Deiters' cells. We observed a change in the intracellular localization of GFP, from the nucleus in normal-hearing to cytoplasm and membrane in deafened mice. These data suggests that the adult mammalian cochlea possesses properties essential for regeneration even after severe ototoxic trauma.

Keywords: inner ear regeneration, deafness, LGR5+ supporting cells, ototoxicity, adult mammalian cochlea

OPEN ACCESS

Edited by:
Leonard Rybak,
Southern Illinois University Carbondale, United States

Reviewed by:
Helge Rask-Andersen,
Uppsala University, Sweden
Nesrine Benkafadar,
Stanford University, United States

***Correspondence:**
Louise V. Straatman
L.V.Straatman@umcutrecht.nl

†These authors share first authorship

Specialty section:
This article was submitted to Molecular Signalling and Pathways, a section of the journal Frontiers in Molecular Neuroscience

Received: *23 June 2021*
Accepted: *07 September 2021*
Published: *05 October 2021*

Citation:
Smith-Cortinez N, Yadak R, Hendriksen FGJ, Sanders E, Ramekers D, Stokroos RJ, Versnel H and Straatman LV (2021) LGR5-Positive Supporting Cells Survive Ototoxic Trauma in the Adult Mouse Cochlea. Front. Mol. Neurosci. 14:729625. doi: 10.3389/fnmol.2021.729625

INTRODUCTION

Hearing loss affects almost 500 million people worldwide, including 34 million children (World Health Organization, 2021), and it has been estimated that 900 million people could have disabling hearing loss by 2050 (Wilson et al., 2017; Chadha et al., 2018). Diverse etiologies, including aging, trauma, noise exposure, ototoxic drugs or genetic diseases, cause irreversible damage to sensory hair cells (HCs) in the cochlea (Edge and Chen, 2008; Mittal et al., 2017). While hearing aids and cochlear implants often result in recovery of hearing in hearing-impaired patients, a key problem is limited quality of the auditory percept (Caldwell et al., 2017; Lesica, 2018; Peters et al., 2018). Regeneration of cochlear HCs from endogenous cochlear stem cells could be a novel approach to improve hearing without the need of an electronic device.

In non-mammalian vertebrates, HC loss triggers spontaneous regeneration through re-entry of supporting cells (SCs) into cell cycle and transdifferentiation into new HCs (Dooling et al., 1997). In mammals, it has been described that a subset of SCs from the mouse and human cochlea have stem cell characteristics, and possess the potential to differentiate into new HCs *in vitro* and *in vivo* (Warchol et al., 1993; Li et al., 2003; White et al., 2006; McLean et al., 2017; Shu et al., 2019). The differentiation of SCs into HCs is mainly controlled by the Notch and Wnt signaling pathways which promote cell proliferation and differentiation (Chai et al., 2011, 2012; Mizutari et al., 2013; Li et al., 2015; Żak et al., 2015). The leucine-rich repeat-containing G-protein coupled receptor 5 (LGR5) is a membrane receptor in the Wnt pathway, which has been described as a stem-cell marker in different organs including the cochlea. It is expressed in a subgroup of SCs which give rise

to HCs during murine embryonic development (Groves, 2010; Shi et al., 2012, 2013; Bramhall et al., 2014; Żak et al., 2016). Potentially these LGR5 positive (LGR5+) SCs can be utilized as endogenous stem cells for HC regeneration to treat hearing loss including deafness (severe hearing loss).

The differentiation into sensory HCs has been achieved by different experimental approaches using 3D-grown inner ear organoids derived from human pluripotent stem cells (Koehler et al., 2013), mouse embryonic stem cells (Koehler and Hashino, 2014) and human fetal cochlear progenitors (Roccio et al., 2018). Moreover, the differentiation of LGR5+ SCs into sensory HCs has also been observed by culturing 3D-grown cochlear organoids from the neonatal mouse cochlea after manipulation of the Wnt and/or Notch signaling pathways (Chai et al., 2012; Shi et al., 2012; McLean et al., 2017; Roccio and Edge, 2019). Preliminary results of one study demonstrated that myosin VIIA positive hair cell-like cells can even be regenerated from human adult inner ear epithelium *in vitro* (McLean et al., 2017).

Interestingly, neonatal LGR5+ SCs have been shown to survive and retain regeneration potential after an ototoxic trauma with neomycin *in vitro* (Zhang et al., 2017). Moreover, after selective ablation of HCs, LGR5+ SCs act as region-specific HC progenitors and are capable of both mitotic and non-mitotic HC regeneration in the neonatal mouse cochlea (Wang et al., 2015). Although it is known that LGR5+ SCs are still present in the organ of Corti in the adult mouse (Chai et al., 2011; Shi et al., 2012) their long-term presence in the mature mouse (after p60) has not been elucidated. Moreover, and critical toward therapeutic applications, it is unknown whether the LGR5+ SCs survive an ototoxic trauma in the adult cochlea. Therefore, we examined LGR5 expression in the organ of Corti 1 week after ototoxic medication in adult $Lgr5^{GFP}$ mice.

Here, we report for the first time the survival of LGR5+ SCs in the deafened adult cochlea, using a mouse model of ototoxicity previously established in our lab (Jansen et al., 2013) in adult $Lgr5^{GFP}$ transgenic mice. LGR5+ SCs might therefore be target cells for therapeutic treatment to regenerate HCs even in adulthood.

RESULTS

Auditory Brainstem Responses and Cochlear Anatomical Organization Are Similar in Normal-Hearing $Lgr5^{GFP}$ and Wild Type Adult Mice (p30 and p100)

To determine the hearing performance of the $Lgr5^{GFP}$ transgenic adult mice relative to WT mice, we recorded click-evoked auditory brainstem responses (ABRs) in both groups. The p30 WT and $Lgr5^{GFP}$ mice had similar ABR waveforms and their ABR thresholds were similar (difference smaller than 5 dB, data not shown). Immunofluorescence microscopy of whole-mount dissections of the cochlea of WT (p30) and $Lgr5^{GFP}$ mice (p30 and p100) showed the typical image of one row of inner hair cells (IHCs) and three rows of outer hair cells (OHCs) in the apex, middle and base of the cochlea, expressed as MYO7A+ cells (in red, **Figure 1**). Moreover, we could clearly observe LGR5+ SCs in the apex, middle and base of the cochlea of all $Lgr5^{GFP}$ adult mice, even until p100 (in green, **Figure 1**). The LGR5+ SCs were located in the third row of Deiters' cells (DC3s) as well as, to a lesser extent, in the inner pillar cells (IPCs) in the cochlea of p30 and p100 $Lgr5^{GFP}$ mice (**Figure 1**).

Ototoxic Trauma Causes Severe Hearing Loss, Extensive Loss of Outer Hair Cells but Survival of LGR5+ SCs

Animals had normal thresholds before deafening (approximately 45 dB peak equivalent sound pressure level, peSPL), as observed in click-evoked ABRs (**Figure 2A**). One week after ototoxic trauma, mice showed little or no click-evoked ABR (**Figure 2A**), so the ABR thresholds were near the upper limitation of the recordings (>90 dB peSPL), confirming successful deafening after 7 days. Two animals with significant residual hearing (threshold shifts < 25 dB) were excluded from the analyses. Immunofluorescence microscopy of cochlear whole-mount dissections showed that the ototoxic medication destroyed all OHCs in the apex, middle and base (**Figures 2B,C**) and the expression of MYO7A (in red, **Figure 2B**) indicated an average survival of 60–80% of IHCs (**Figures 2B,C**). Interestingly, LGR5 (GFP) was still expressed in DC3s in the apex, middle and base of cochleas from deafened mice (in green, **Figures 2B,C**). However, IPCs seemed to have lost the LGR5 (GFP) expression (**Figure 2B**). Notably, some of the deafened cochleas showed two rows of LGR5+ SCs and these were located significantly closer to IHCs than in cochleas from normal-hearing mice [$p < 0.001$, $F(1, 9) = 27$; **Figure 2D**]. Furthermore, we observed no changes in the number of LGR5+ SCs located in DC3s after deafening [$p = 0.17$, $F(1, 9) = 2.2$; **Figure 2C**, right panel].

Analysis of MYO7A and LGR5 (GFP) expression in cryosections showed that in control cochleas (up to p100) LGR5 (GFP) was present in DC3s and IPCs, and after deafening LGR5 (GFP) was present only in DC3s (**Figure 3**). Furthermore, MYO7A expression was observed mainly in IHCs in cochleas from deafened mice and in IHC and OHC in cochleas from normal-hearing mice (**Figure 3**).

GFP Changes Its Subcellular Localization After Deafening

In the immunofluorescence data, we observed that GFP expression was mainly localized in the nuclei and cytoplasm of SCs in cochleas from normal-hearing mice and in the cytoplasm and plasma membrane (PM) of SCs in cochleas from deafened mice. To quantify the subcellular localization of GFP, we calculated Pearson's correlation coefficient (PCC) in z-stacks taken for GFP (green) and DAPI (blue) in apex, middle and base of normal and deafened cochleas. We observed that GFP is present in the nuclei and to a lesser extent in the cytoplasm of SCs in control cochleas (**Figure 4A**, top panels) and mainly in the cytoplasm and PM of SCs in the deafened cochlea (**Figure 4A**, bottom panels). After plotting the green intensities vs. blue intensities of images in **Figure 4A** we can observe that in the normal conditions there is a gradient of

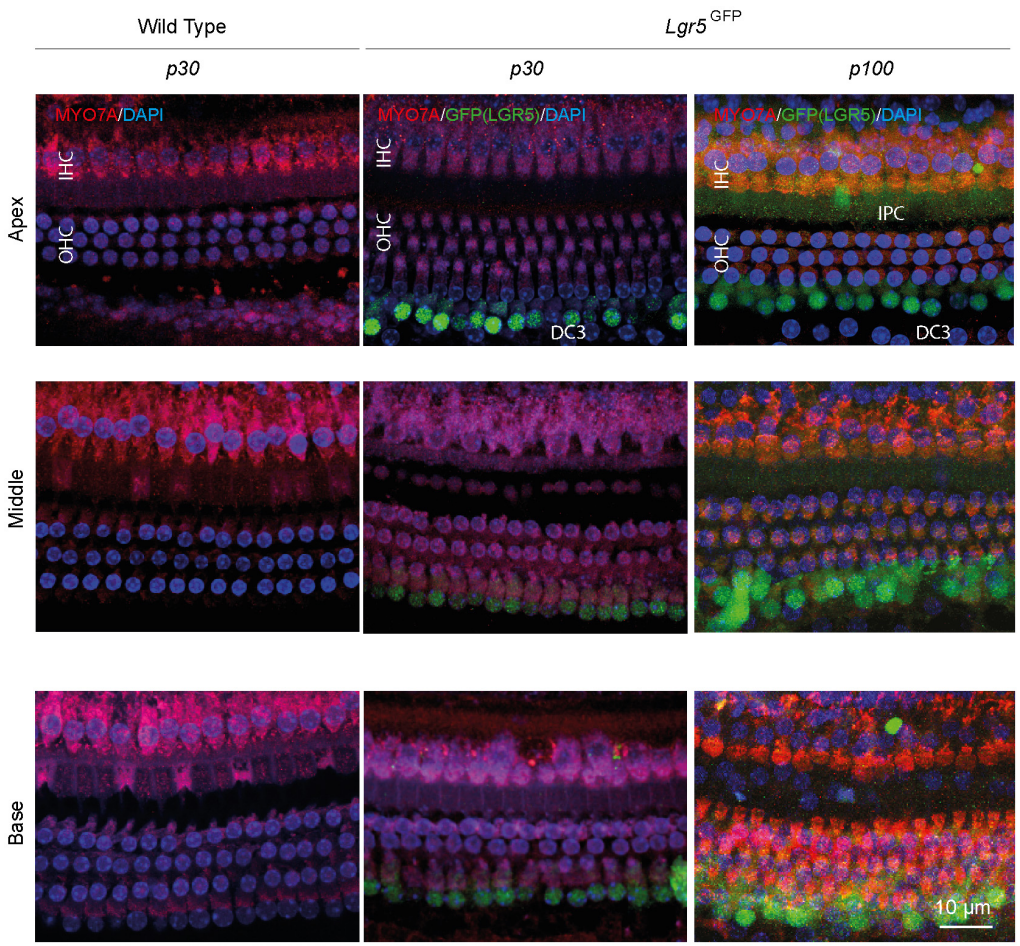

FIGURE 1 | Anatomy of the organ of Corti in normal-hearing wild type (WT) and Lgr5^{GFP} adult mice. Representative images of immunofluorescence microscopy of apex, middle and base in whole mount dissections of the cochlea of WT and Lgr5^{GFP} adult (p30 and p100) mice stained with myosin VII A (MYO7A) in red, GFP (LGR5) in green and DAPI in blue. GFP (LGR5) was detected particularly in the 3rd row of Deiters' cells (DC3s) and, to a lesser extent, in the inner pillar cells (IPCs). No changes in GFP (LGR5) expression were found between p30 and p100 mice. Bar = 10 µm. $n_{WT} = 3$; $n_{Lgr5GFP(p30)} = 7$; $n_{Lgr5GFP(p100)} = 3$ (representative images of 1 cochlea per group).

pixels that co-localize in both channels (square 1, **Figure 4B**) whereas in deafened conditions there are pixels that either express DAPI or GFP but not both (square 2, **Figure 4B**). According to PCC, which is independent from fluorophore intensity, the co-localization was significantly lower in deafened mice (characterized by a low PCC in the apex, middle and base) than in normal-hearing mice (characterized by a high PCC in the apex, middle and base) [$F(1, 9) = 39$, $p < 0.001$; **Figure 4C**]. These results suggest that the subcellular localization of GFP is mainly nuclear in SCs of the normal-hearing mice and non-nuclear after deafening.

DISCUSSION

In this study the presence of LGR5+ SCs in cochleas of adult normal-hearing and deafened mice was evaluated *in vivo*. In normal-hearing adult Lgr5^{GFP} transgenic mice, with a hearing threshold similar to wild type (WT) littermates, LGR5+ SCs were found in the DC3s and, to a lesser extent, in the IPCs. One week after deafening, using a single dose of ototoxic co-medication of kanamycin and furosemide, there was survival of LGR5+ SCs in adult Lgr5^{GFP} transgenic mice, even though there was extensive loss of OHCs and substantial loss of IHCs. Interestingly, a change in subcellular localization of GFP in SCs was observed, which was expressed in the nuclei of SCs in normal cochleas and in the cytoplasm of SCs in deafened cochleas.

Potential Endogenous Cochlear Stem Cells During Adulthood

Since the generation of the Lgr5^{GFP} transgenic mice (Barker et al., 2007) the LGR5 expression has been described in many tissues with known or previously unknown regeneration potential. In the neonatal mouse cochlea some SCs that express LGR5 have progenitor potential and can regenerate into new HCs *in vitro* and *in vivo* (Chai et al., 2012; Li et al., 2015;

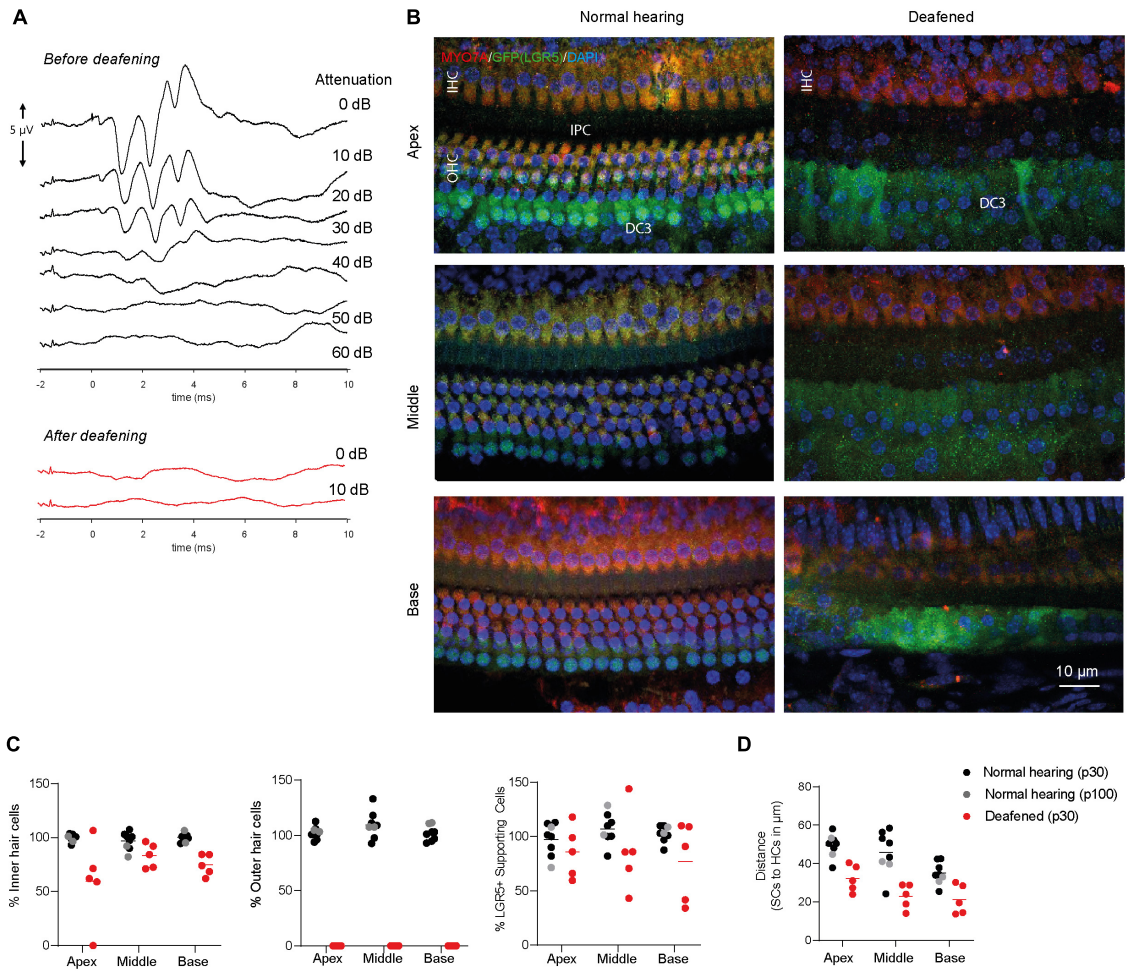

FIGURE 2 | LGR5+ supporting cells are detected in the deafened Lgr5^{GFP} adult mice. **(A)** Representative auditory brain stem responses (ABRs) of one Lgr5^{GFP} mouse before (in black) and 1 week after (in red) deafening. **(B)** Representative images of immunofluorescence microscopy of apex, middle and base in whole-mount dissections of the cochlea of Lgr5^{GFP} normal-hearing and deafened mice stained with myosin VIIA (MYO7A) in red, GFP (LGR5) in green and DAPI in blue. MYO7A stainings showed that the outer hair cells (OHCs) were completely abolished after deafening, with partial preservation of inner hair cells (IHCs). Compared to the normal cochlea, the GFP (LGR5) expression after deafening was still present in the third row of Deiters' cells (DC3s) and showed a cytoplasmic sublocalization and a more diffuse staining. **(C)** Cell counts, in percentage, for apex, middle and base of the cochlea of normal-hearing (p30 in black and p100 in gray) and deafened (p30) Lgr5^{GFP} mice. **(D)** Distance in µm from GFP + SCs to MYO7A+ IHCs. Bar = 10 µm. $n_{normal\ hearing(p30)}$ = 6; $n_{normal\ hearing(p100)}$ = 2 $n_{deafened(p30)}$ = 5, mean.

Ni et al., 2016; Chen et al., 2017). However, cochlear LGR5 expression has not been thoroughly described for adult mice, which is important since the majority of hearing-disabled people are adults (Cunningham and Tucci, 2017), so studying the role of LGR5+ SCs in adulthood is clinically very relevant. It has been shown that LGR5 expression gradually decreases until the second postnatal week and that it remains detectable only in the DC3s in the adult (p30) cochlea (Chai et al., 2011). Chai et al. (2011) also described that LGR5 expression is only detected in IPCs until p12. In contrast, another study showed that LGR5 is expressed in the adult (p30 and p60) mouse cochlea in the DC3s as well as in the IPCs (Shi et al., 2012). Our data further confirm these latter findings since we observed LGR5 expression even at p100 in DC3s and IPCs. As Shi et al., we performed immunofluorescence stainings using anti-GFP antibodies to increase the detection of LGR5, whereas Chai et al. (2011) did not use anti-GFP antibodies in their immunofluorescence, which potentially resulted in absence of a detectable LGR5 signal in the IPCs in mice older than p12. Moreover, in the present study no deterioration was found of LGR5 expression between p30 and p100. To our knowledge, this is the first study showing LGR5 expression in both DC3s and IPCs until p100 in Lgr5^{GFP} transgenic mice. This indicates that LGR5 expression in the cochlear SCs does not deteriorate during adulthood and suggests long-term availability of target cells for regenerative therapy for the adult cochlea.

LGR5+ Cell Survival and Regenerative Capacities After Severe Ototoxic Trauma

Interestingly, in neonatal mouse cochlear tissue, it has been shown that after application of neomycin *in vitro* to induce HC

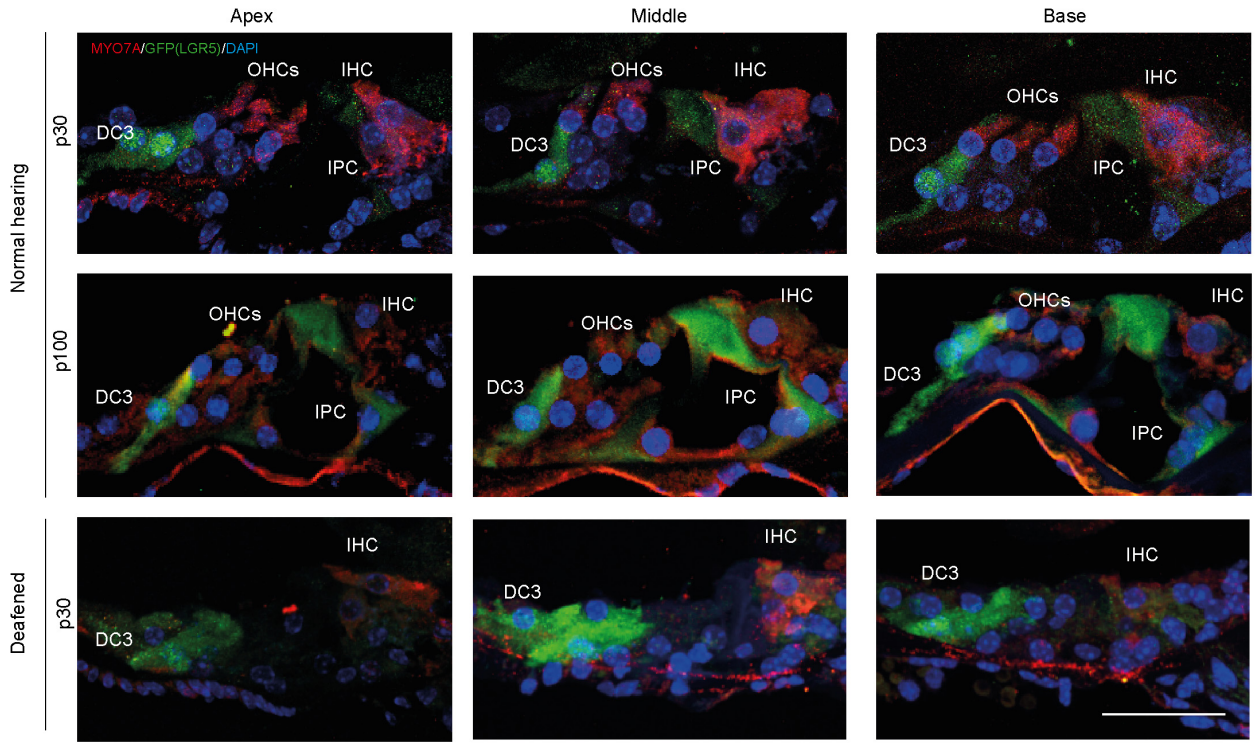

FIGURE 3 | After deafening inner pillar cells (IPCs) lose LGR5 expression. Representative images of immunofluorescence microscopy of cryosections of the cochlea of normal-hearing (p30 and p100) and deafened $Lgr5^{GFP}$ mice stained with myosin VII A (MYO7A) in red, GFP (LGR5) in green and DAPI in blue. IPCs of normal-hearing animals showed LGR5 expression, which disappeared after deafening. Bar = 10 μm. $n_{normal\ hearing(p30)} = 6$; $n_{normal\ hearing(p100)} = 1$ $n_{deafened(p30)} = 5$ (representative images of 1 cochlea per group).

loss, LGR5+ progenitors showed increased ability to proliferate and regenerate HCs 4 days after the ototoxic trauma (Zhang et al., 2017). For the adult mouse cochlea, this is the first study showing survival of LGR5+ SCs after deafening, which were located in the DC3s after deafening. This strongly suggests that the deafened mammalian cochlea retains regenerative potential, and hence therapeutic opportunities targeting the LGR5+ SCs could arise. A pioneering clinical trial has already shown that modulating the Wnt and Notch signaling pathway with a recently commercialized drug (FX322) in patients with sensorineural hearing loss improves speech recognition (both in quiet and in noise) 90 days after treatment (McLean et al., 2021). This report, including only patients with noise-induced or idiopathic sudden SNHL, supports the hypothesis that Wnt-responsive SCs with regeneration potential are present in human, even after deafness. The fact that we also found surviving LGR5+ progenitors after ototoxic trauma opens an opportunity for this treatment of ototoxically induced hearing loss as well.

The survival of SCs 1 week after an ototoxic event, even when resulting in extensive HC loss, is in accordance with previous studies and indicates that these are potentially less susceptible to ototoxic trauma. This is probably a result of less uptake of aminoglycoside (like kanamycin) in SCs, compared to HCs (Aran et al., 1995; Richardson et al., 1997, 1999; Young and Raphael, 2007; Taylor et al., 2012). Also in long-term experiments with mice deafened with 1 dose of kanamycin and bumetanide, survival of SCs 6 months after ototoxic trauma was shown, even when there was complete loss of IHCs and OHCs; however, it was not determined if the surviving SCs had progenitor potential (Taylor et al., 2012). Some other studies supported the hypothesis that there are SCs with regenerative capacities after ototoxic trauma: In adult guinea pigs treated with neomycin, the loss of HCs was accompanied by increasing number of dividing SCs 4 days after treatment, suggesting SCs were proliferating (Young and Raphael, 2007). Furthermore, in deafened adult guinea pigs, ototoxic trauma was accompanied by loss of IHCs and OHCs and survival of SCs. In these animals Atoh1 gene therapy improved regeneration and differentiation of new HCs 4 days (Izumikawa et al., 2005), 30 and 60 days (Kawamoto et al., 2003) after gene therapy.

In our study, we assessed expression of LGR5 1 week after deafening which represents an intermediate step between an acute and a chronic model. Further experiments need to be performed to assess the long-term effects of deafening on LGR5 expression and hence translate these findings into the patient's situation, which are usually chronically injured and establish the best therapeutic window for the treatment. However, based on previous studies showing long term (up to 1 year)

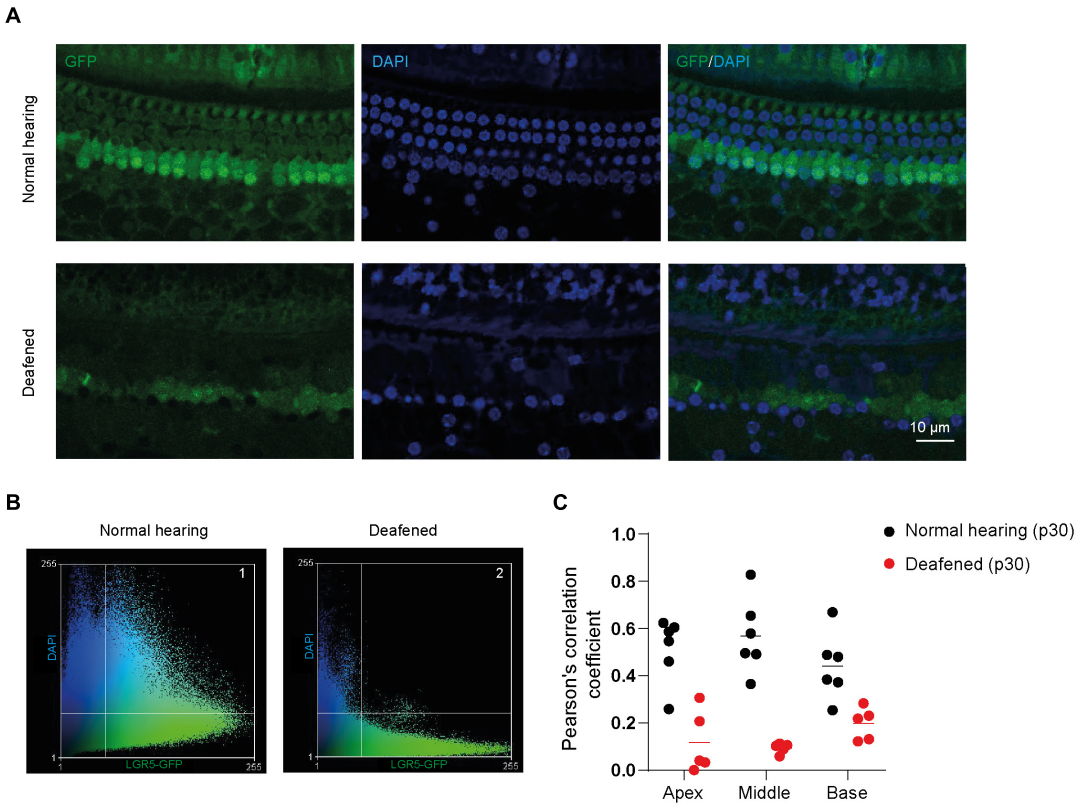

FIGURE 4 | GFP expression is located in different subcellular compartments in the cochlea of normal-hearing and deafened mice. **(A)** Representative images of immunofluorescence microscopy of whole-mount dissections of the cochlea of normal-hearing and deafened $Lgr5^{GFP}$ mice stained with GFP in green, DAPI in blue and merged images. **(B)** Scatter plot of green intensity vs. blue intensity of images in panel (A). Square 1 represents the pixels that are expressed in both channels in normal hearing and square 2 represents the pixels that are expressed in both channels in deafened. **(C)** Pearson's correlation coefficient (PCC) calculated for the apex, middle and base of the cochlea of normal-hearing and deafened $Lgr5^{GFP}$ mice. Bar = 10 µm. $n_{normal\ hearing(p30)} = 6$; $n_{deafened(p30)} = 5$.

survival of SOX2 + SCs in the mouse cochlea, even after injection of high concentrations of kanamycin and furosemide (Oesterle et al., 2008), long term survival of LGR5+ SCs is expected.

Change in Subcellular Localization of GFP After Deafening: From Nucleus to Cytoplasm

In the present study a change in the intracellular localization of GFP was found in the SCs after deafening. It must be taken into account that $Lgr5^{GFP}$ mice allow for visualization of LGR5+ cells due to a genetic modification that produces EGFP controlled by the promoter of LGR5 (Barker et al., 2007), however, GFP is not fused to LGR5. In the normal cochlea, the GFP expression was mainly localized in the nucleus of SCs. Interestingly, a nuclear localization of GFP is also visible in data of other studies using the $Lgr5^{GFP}$ animal model: in the normal cochlea of $Lgr5^{GFP}$ mice (p0-p19) GFP staining was localized in the nuclei of DC3s (Chai et al., 2011; Shi et al., 2012), and it colocalized with Prox1 (Chai et al., 2011), a transcription factor that is expressed in the nuclei of DCs and pillar cells (PCs) (Bermingham-McDonogh et al., 2006) and with SOX2 (Shi et al., 2012), a transcription factor that controls inner ear development and is expressed in the nuclei of some SCs (Steevens et al., 2019). The observations above further confirm the hypothesis that in both the neonatal and mature organ of Corti in normal-hearing mice, GFP localizes in the nuclei of SCs. After deafening there was a shift of GFP expression to the cytoplasm. The accumulation of GFP or EGFP in the cell nucleus has been previously reported in other models (Seibel et al., 2007) and it is known to occur due to the low molecular weight of the protein which, with only 27 kDa, is able to passively diffuse to the nuclei (Macara, 2001). Nuclear translocation of proteins is a mechanism that occurs in physiological conditions to control gene expression. Many proteins that move to the nuclei have a conserved nuclear localization sequence to signal the translocation through nuclear pore complexes or receptor-mediated import pathways. However, no nuclear localization sequences have been found for GFP or EGFP (Seibel et al., 2007). The change in intracellular localization from nuclei to cytoplasm after deafening could suggest that the nuclear membrane is becoming more permeable, thus promoting leakage of EGFP to the cytoplasm. It could also be due to changes in the concentration of EGFP molecules, which could suggest more EGFP production after deafening.

CONCLUSION

In conclusion, this study showed the presence of LGR5+ SCs in the cochlea of adult mice up to p100, which indicates potential endogenous cochlear stem cells with proliferative and regenerative capacities in adulthood. *In vivo* survival of these progenitor cells, after a severe ototoxic event, indicates the availability of target cells for future therapeutic approaches for ototoxic-induced deafness by manipulation of the Wnt- and Notch-signaling pathways. Furthermore, a change in the subcellular localization of GFP after deafening was reported. This report gives further insight into the regeneration potential of the adult deafened cochlea and sets the basis of future therapy to improve hair cell regeneration in hearing-impaired patients.

MATERIALS AND METHODS

Animals

We used 4 C57BL/6 WT mice and 18 heterozygous LGR5-EGFP-CreERT2 (Jackson Laboratory, Stock 008875) mice ($Lgr5^{GFP}$). Nineteen mice were used at postnatal day 30 (p30) and three $Lgr5^{GFP}$ mice at p100. Mice were housed in open cages with food and water *ad libitum* and standard laboratory conditions. All surgical and experimental procedures were approved by the Dutch Central Authority for Scientific Procedures on Animals (CCD:1150020186105).

Deafening Procedure

Mice were deafened as described previously (Jansen et al., 2013). Non-treated mice were used as normal-hearing controls and consisted of 8 $Lgr5^{GFP}$ and 4 WT p30 mice. The deafened group consisted of 7 $Lgr5^{GFP}$ p30 mice. Normal hearing was confirmed by recordings of ABRs, as described below. Then, 700 mg/kg kanamycin sulfate was injected subcutaneously (stock solution 100 mg/ml in saline). Within 5 min after kanamycin administration, 100 mg/kg furosemide was infused into the tail vein (stock solution 100 mg/ml). Mice were weighed before the deafening procedure and daily after the deafening, since substantial loss of weight can indicate kanamycin-induced kidney failure.

Auditory Brainstem Responses

ABRs were recorded under general anesthesia using three subcutaneously positioned needle electrodes. The active electrode was placed behind the right pinna, the reference electrode was placed anteriorly on the skull, and the ground electrode was placed in the hind limb. Stimulus generation and data acquisition were controlled by custom-written software involving a personal computer and a Multi-I/O processor (RZ6; Tucker-Davis Technologies, Alachua, FL, United States). Acoustic stimuli consisted of trains of 20-μs clicks with an interstimulus interval of 33 ms. Sounds were presented in an open-field configuration with an electrostatic speaker (TDT ES1) positioned at 3 cm from the pinna. Sound levels were varied from approximately 90 dB peSPL down to below threshold in 10 dB steps. Calibration was performed with Bruel and Kjaer equipment (2203 sound level meter; 1-inch condenser microphone 4132).

Genotyping

$Lgr5^{GFP}$ transgenic mice were genotyped by isolating DNA from ear tissue. Genomic DNA isolation was performed with DirectPCR lysis reagent (Viagen, Biotech, Los Angeles, CA, United States) according to the manufacturer's instructions. The primers for PCR amplification were: GFP, forward: CACTGCATTCTAGTTGTGG; and reverse: CGGTGCCCGCAGCGAG. Amplicons were separated by electrophoresis in a 3% agarose gel.

Cryosectioning and Whole Mount Sample Preparation

Mouse cochleas were harvested after termination by decapitation. Tissues were prepared as described previously (Żak et al., 2016). Briefly, tissues were fixed in 2% paraformaldehyde (Sigma–Aldrich) in phosphate-buffered saline (PBS, pH 7.4) and stored in 2% PFA in PBS at 4°C. Cochleas were decalcified in 270 mM (=10%) EDTA-2Na (Sigma–Aldrich: ED2SS) in dH_2O at room temperature under constant agitation for 7 days. Cryoprotection of tissues was performed using solutions of increasing concentrations of sucrose (Merck: 1.07653.1000), up to 30%, in PBS (pH 7.4). After subsequent infiltration in a mixture (1:1) of 30% sucrose/OCT compound (Sakura Finetek Europe B.V., Alphen aan den Rijn, The Netherlands) and pure OCT compound, tissues were embedded in OCT and stored at −80°C. Cryosections of 12 μm were cut using a Leica CM3050 cryostat and mounted on microscope slides. For whole-mount samples, tissues were fixed and decalcified as described above. After decalcification, the otic capsule was opened, the lateral wall, Reissner's membrane, tectorial membrane and modiolus were removed and the basilar membrane containing the organ of Corti was dissected into individual half-turns.

Immunofluorescence Microscopy

Immunofluorescence staining was performed on cryosections and whole-mount dissections. The tissues and slides were washed with blocking solution (2% donkey serum and 0.1% triton X-100 in PBS). Specimens were incubated with primary antibodies, anti-myosin VIIA (MYO7A, 1/300, rabbit, Proteus Biosciences, 25-6790) and anti-GFP (1/200, goat, Abcam, ab5450) overnight at 4°C. Later, slides and tissues were washed with blocking solution and incubated with secondary antibodies donkey-anti Rabbit-Alexa 594 (1/500, Invitrogen, A-21207), donkey-anti Goat-Alexa 488 (1/200, Abcam, AB150129), and DAPI solution (1/500, Abcam, AB228549) for 90 min at room temperature. Lastly, specimens were washed in PBS and mounted in Vectashield Antifade Mounting Medium (Vector laboratories, H-1000). Slides were imaged using a Zeiss LSM700 Scanning Confocal Microscope. Apical, middle, and basal regions were calculated by measuring the total length of each cochlear duct

in the whole-mount dissections and calculating 25% (apex), 50% (middle), and 75% (basal) distance from the apical end. Three-dimensional image reconstruction of Z-stacks and PCC analyses of DAPI and GFP signals were performed using ImageJ software.

Cell Counting

Cells were counted by three independent raters using whole-mount dissection immunofluorescence staining images. The total number of IHCs and OHCs were counted by analyzing MYO7A+ cells. SCs were counted by assessing LGR5+ cells located in the DC3s. Cells were counted in each of three cochlear segments (apical, middle and basal). Density (cells per 100 μm) was then calculated for each segment and numbers were normalized vs. normal-hearing littermates and shown in percentages.

Statistical Analysis

Significance of differences in cochlear tissues between the deafened and normal-hearing mice was tested by repeated measures ANOVA with ototoxic treatment as between-group factor and cochlear location (basal, middle, apical) as within-animal factor. These analyses were performed in SPSS statistics version 27 for windows (IBM Corp., Armonk, NY, United States). Results were considered statistically different when the p-value <0.05.

DATA AVAILABILITY STATEMENT

The raw data supporting the conclusions of this article will be made available by the authors, without undue reservation.

ETHICS STATEMENT

The animal study was reviewed and approved by the Utrecht Animal Welfare Body of Utrecht University and UMC Utrecht.

AUTHOR CONTRIBUTIONS

NS-C, RY, and LS: conceptualization. RY, FH, and HV: methodology. NS-C, RY, FH, ES, DR, and LS: investigation. NS-C and HV: formal analysis. HV, RS, and LS: resources, project administration, and funding. NS-C, HV, and LS: writing—original draft. HV and LS: writing—revision and editing and project supervision. All authors contributed to the article and approved the submitted version.

FUNDING

This research was funded by the Heinsius-Houbolt Foundation, Netherlands.

ACKNOWLEDGMENTS

We thank Corlinda ten Brink from the Cell Microscopy Core, Department of Cell Biology, Center for Molecular Medicine, UMC Utrecht for support in the confocal microscopy. We thank Jacco van Rheenen from the Netherlands Cancer Institute for providing p100 transgenic mice.

REFERENCES

Aran, J. M., Chappert, C., Dulon, D., Erre, J. P., and Aurousseau, C. (1995). Uptake of amikacin by hair cells of the guinea pig cochlea and vestibule and ototoxicity: comparison with gentamicin. *Hear. Res.* 82, 179–183. doi: 10.1016/0378-5955(94)00175-P

Barker, N., Van Es, J. H., Kuipers, J., Kujala, P., Van Den Born, M., Cozijnsen, et al. (2007). Identification of stem cells in small intestine and colon by marker gene Lgr5. *Nature* 449, 1003–1007. doi: 10.1038/nature06196

Bermingham-McDonogh, O., Oesterle, E. C., Stone, J. S., Hume, C. R., Huynh, H. M., and Hayashi, T. (2006). Expression of Prox1 during mouse cochlear development. *J. Comp. Neurol.* 496, 172–186. doi: 10.1002/cne.20944

Bramhall, N. F., Shi, F., Arnold, K., Hochedlinger, K., and Edge, A. S. B. (2014). Lgr5-positive supporting cells generate new hair cells in the postnatal cochlea. *Stem Cell Rep.* 2, 311–322. doi: 10.1016/j.stemcr.2014.01.008

Caldwell, M. T., Jiam, N. T., and Limb, C. J. (2017). Assessment and improvement of sound quality in cochlear implant users. *Laryngoscope Investigative Otolaryngol. Laryngoscope Investig Otolaryngol.* 2, 119–124. doi: 10.1002/lio2.71

Chadha, S., Cieza, A., and Krug, E. (2018). Global hearing health: future directions. *Bull. World Health Organ.* 96:146. doi: 10.2471/BLT.18.209767

Chai, R., Kuo, B., Wang, T., Liaw, E. J., Xia, A., Jan, T. A., et al. (2012). Wnt signaling induces proliferation of sensory precursors in the postnatal mouse cochlea. *Proc. Natl. Acad. Sci. U S A.* 109, 8167–8172. doi: 10.1073/pnas.1202774109

Chai, R., Xia, A., Wang, T., Jan, T. A., Hayashi, T., Bermingham-McDonogh, O., et al. (2011). Dynamic expression of Lgr5, a Wnt target gene, in the developing and mature mouse cochlea. *J. Assoc. Res. Otolaryngol.* 12, 455–469. doi: 10.1007/s10162-011-0267-2

Chen, Y., Lu, X., Guo, L., Ni, W., Zhang, Y., Zhao, L., et al. (2017). Hedgehog signaling promotes the proliferation and subsequent hair cell formation of progenitor cells in the neonatal mouse cochlea. *Front. Mol. Neurosci.* 10:426. doi: 10.3389/fnmol.2017.00426

Cunningham, L. L., and Tucci, D. L. (2017). Hearing loss in adults. *N. Engl. J. Med.* 377, 2465–2473. doi: 10.1056/NEJMra1616601

Dooling, R. J., Ryals, B. M., and Manabe, K. (1997). Recovery of hearing and vocal behavior after hair-cell regeneration. *Proc. Natl. Acad. Sci. U S A.* 94, 14206–14210. doi: 10.1073/pnas.94.25.14206

Edge, A. S., and Chen, Z. Y. (2008). Hair cell regeneration. *Curr. Opin. Neurobiol.* 18, 377–382. doi: 10.1016/j.conb.2008.10.001

Groves, A. K. (2010). The challenge of hair cell regeneration. *Exp. Biol. Med. (Maywood)* 235, 434–446. doi: 10.1258/ebm.2009.009281

Izumikawa, M., Minoda, R., Kawamoto, K., Abrashkin, K. A., Swiderski, D. L., Dolan, D. F., et al. (2005). Auditory hair cell replacement and hearing improvement by Atoh1 gene therapy in deaf mammals. *Nat. Med.* 11, 271–276. doi: 10.1038/nm1193

Jansen, T. T. G., Bremer, H. G., Topsakal, V., Hendriksen, F. G. J., Klis, S. F. L., and Grolman, W. (2013). Deafness induction in mice. *Otol. Neurotol.* 34, 1496–1502. doi: 10.1097/MAO.0b013e318291c610

Kawamoto, K., Ishimoto, S. I., Minoda, R., Brough, D. E., and Raphael, Y. (2003). Math1 gene transfer generates new cochlear hair cells in mature guinea pigs in vivo. *J. Neurosci.* 23, 4395–4400. doi: 10.1523/jneurosci.23-11-04395.2003

Koehler, K. R., and Hashino, E. (2014). 3D mouse embryonic stem cell culture for generating inner ear organoids. *Nat. Protoc.* 9, 1229–1244. doi: 10.1038/nprot.2014.100

Koehler, K. R., Mikosz, A. M., Molosh, A. I., Patel, D., and Hashino, E. (2013). Generation of inner ear sensory epithelia from pluripotent stem cells in 3D culture. *Nature* 500, 217–221. doi: 10.1038/nature12298

Lesica, N. A. (2018). Why do hearing aids fail to restore normal auditory perception? *Trends Neurosci.* 41, 174–185. doi: 10.1016/j.tins.2018.01.008

Li, H., Liu, H., and Heller, S. (2003). Pluripotent stem cells from the adult mouse inner ear. *Nat. Med.* 9, 1293–1299. doi: 10.1038/nm925

Li, W., Wu, J., Yang, J., Sun, S., Chai, R., Chen, Z. Y., et al. (2015). Notch inhibition induces mitotically generated hair cells in mammalian cochleae via activating the Wnt pathway. *Proc. Natl. Acad. Sci. U S A.* 112, 166–171. doi: 10.1073/pnas.1415901112

Macara, I.G. (2001). Transport into and out of the nucleus. *Microbiol. Mol. Biol. Rev.* 65, 570–594. doi: 10.1128/mmbr.65.4.570-594

McLean, W. J., Hinton, A. S., Herby, J. T. J., Salt, A. N., Hartsock, J. J., Wilson, S., et al. (2021). Improved speech intelligibility in subjects with stable sensorineural hearing loss following intratympanic dosing of FX-322 in a phase 1b study. *Otol. Neurotol.* 42, e849–e857.

McLean, W. J., Yin, X., Lu, L., Lenz, D. R., McLean, D., Langer, R., et al. (2017). Clonal expansion of Lgr5-Positive cells from mammalian cochlea and high-purity generation of sensory hair cells. *Cell Rep.* 18, 1917–1929. doi: 10.1016/j.celrep.2017.01.066

Mittal, R., Nguyen, D., Patel, A. P., Debs, L. H., Mittal, J., Yan, D., et al. (2017). Recent advancements in the regeneration of auditory hair cells and hearing restoration. *Front. Mol. Neurosci.* 10:236. doi: 10.3389/fnmol.2017.00236

Mizutari, K., Fujioka, M., Hosoya, M., Bramhall, N., Okano, H. J., Okano, H., et al. (2013). Notch inhibition induces cochlear hair cell regeneration and recovery of hearing after acoustic trauma. *Neuron* 77, 58–69. doi: 10.1016/j.neuron.2012.10.032

Ni, W., Zeng, S., Li, W., Chen, Y., Zhang, S., Tang, M., et al. (2016). Wnt activation followed by Notch inhibition promotes mitotic hair cell regeneration in the postnatal mouse cochlea. *Oncotarget* 7, 66754–66768.

Oesterle, E. C., Campbell, S., Taylor, R. R., Forge, A., and Hume, C. R. (2008). Sox2 and Jagged1 expression in normal and drug-damaged adult mouse inner ear. *JARO - J. Assoc. Res. Otolaryngol.* 9, 65–89. doi: 10.1007/s10162-007-0106-7

Peters, J. P. M., Wendrich, A. W., Van Eijl, R. H. M., Rhebergen, K. S., Versnel, H., and Grolman, W. (2018). The sound of a cochlear implant investigated in patients with single-sided deafness and a cochlear implant. *Otol. Neurotol.* 39, 707–714. doi: 10.1097/MAO.0000000000001821

Richardson, G. P., Forge, A., Kros, C. J., Fleming, J., Brown, S. D. M., and Steel, K. P. (1997). Myosin VIIA is required for aminoglycoside accumulation in cochlear hair cells. *J. Neurosci.* 17, 9506–9519. doi: 10.1523/jneurosci.17-24-09506.1997

Richardson, G. P., Forge, A., Kros, C. J., Marcotti, W., Becker, D., Williams, D. S., et al. (1999). A missense mutation in myosin VIIA prevents aminoglycoside accumulation in early postnatal cochlear hair cells. *Ann. N. Y. Acad. Sci.* 884, 110–11024.

Roccio, M., and Edge, A. S. B. (2019). Inner ear organoids: new tools to understand neurosensory cell development, degeneration and regeneration. *Development* 146:dev177188. doi: 10.1242/dev.177188

Roccio, M., Perny, M., Ealy, M., Widmer, H. R., Heller, S., and Senn, P. (2018). Molecular characterization and prospective isolation of human fetal cochlear hair cell progenitors. *Nat. Commun.* 9:4027. doi: 10.1038/s41467-018-06334-7

Seibel, N. M., Eljouni, J., Nalaskowski, M. M., and Hampe, W. (2007). Nuclear localization of enhanced green fluorescent protein homomultimers. *Anal. Biochem*. 368, 95–99.

Shi, F., Hu, L., and Edge, A. S. B. (2013). Generation of hair cells in neonatal mice by β-catenin overexpression in Lgr5-positive cochlear progenitors. *Proc. Natl. Acad. Sci. U S A.* 110, 13851–13856. doi: 10.1073/pnas.1219952110

Shi, F., Kempfle, J. S., and Edge, A. S. B. (2012). Wnt-responsive Lgr5-expressing stem cells are hair cell progenitors in the cochlea. *J. Neurosci.* 32, 9639–9684. doi: 10.1523/JNEUROSCI.1064-12.2012

Shu, Y., Li, W., Huang, M., Quan, Y. Z., Scheffer, D., Tian, C., et al. (2019). Renewed proliferation in adult mouse cochlea and regeneration of hair cells. *Nat. Commun.* 10:5530. doi: 10.1038/s41467-019-13157-7

Steevens, A. R., Glatzer, J. C., Kellogg, C. C., Low, W. C., Santi, P. A., and Kiernan, A. E. (2019). SOX2 is required for inner ear growth and cochlear nonsensory formation before sensory development. *Development* 146:dev170522. doi: 10.1242/dev.170522

Taylor, R. R., Jagger, D. J., and Forge, A. (2012). Defining the cellular environment in the organ of corti following extensive hair cell loss: a basis for future sensory cell replacement in the cochlea. *PLoS One* 7:e30577. doi: 10.1371/journal.pone.0030577

Wang, T., Chai, R., Kim, G. S., Pham, N., Jansson, L., Nguyen, et al. (2015). Lgr5+ cells regenerate hair cells via proliferation and direct transdifferentiation in damaged neonatal mouse utricle. *Nat. Commun.* 6:6613. doi: 10.1038/ncomms7613

Warchol, M. E., Lambert, P. R., Goldstein, B. J., Forge, A., and Corwin, J. T. (1993). Regenerative proliferation in inner ear sensory epithelia from adult guinea pigs and humans. *Science* 259, 1619–1622. doi: 10.1126/science.8456285

White, P. M., Doetzlhofer, A., Lee, Y. S., Groves, A. K., and Segil, N. (2006). Mammalian cochlear supporting cells can divide and trans-differentiate into hair cells. *Nature* 441, 984–987. doi: 10.1038/nature04849

World Health Organization (2021). *Deafness and Hearing Loss.* Available online at: https://www.who.int/news-room/fact-sheets/detail/deafness-and-hearing-loss (accessed April 1, 2021).

Wilson, B. S., Tucci, D. L., Merson, M. H., and O'Donoghue, G. M. (2017). Global hearing health care: new findings and perspectives. *Lancet* 390, 2503–2515. doi: 10.1016/S0140-6736(17)31073-5

Young, H. K., and Raphael, Y. (2007). Cell division and maintenance of epithelial integrity in the deafened auditory epithelium. *Cell Cycle* 6, 612–619. doi: 10.4161/cc.6.5.3929

Żak, M., Klis, S. F. L., and Grolman, W. (2015). The Wnt and Notch signalling pathways in the developing cochlea: formation of hair cells and induction of regenerative potential. *Int. J. Dev. Neurosci.* 47(Pt B), 247–258. doi: 10.1016/j.ijdevneu.2015.09.008

Żak, M., Van Oort, T., Hendriksen, F. G., Garcia, M. I., Vassart, G., and Grolman, W. (2016). LGR4 and LGR5 regulate hair cell differentiation in the sensory epithelium of the developing mouse cochlea. *Front. Cell. Neurosci.* 10:186. doi: 10.3389/fncel.2016.00186

Zhang, S., Zhang, Y., Yu, P., Hu, Y., Zhou, H., Guo, L., et al. (2017). Characterization of Lgr5+ progenitor cell transcriptomes after neomycin injury in the neonatal mouse cochlea. *Front. Mol. Neurosci.* 10:213. doi: 10.3389/fnmol.2017.00213

Conflict of Interest: The authors declare that the research was conducted in the absence of any commercial or financial relationships that could be construed as a potential conflict of interest.

Publisher's Note: All claims expressed in this article are solely those of the authors and do not necessarily represent those of their affiliated organizations, or those of the publisher, the editors and the reviewers. Any product that may be evaluated in this article, or claim that may be made by its manufacturer, is not guaranteed or endorsed by the publisher.

frontiers in Molecular Neuroscience

ORIGINAL RESEARCH
published: 10 February 2022
doi: 10.3389/fnmol.2022.835448

The Mechanotransduction Channel and Organic Cation Transporter Are Critical for Cisplatin Ototoxicity in Murine Hair Cells

*Jinan Li, Chang Liu, Samuel Kaefer, Mariam Youssef and Bo Zhao**

Department of Otolaryngology-Head and Neck Surgery, Indiana University School of Medicine, Indianapolis, IN, United States

Cisplatin is one of the most widely used chemotherapeutic drugs across the world. However, the serious ototoxic effects, leading to permanent hair cell death and hearing loss, significantly limit the utility of cisplatin. In zebrafish, the functional mechanotransduction channel is required for cisplatin ototoxicity. However, it is still unclear the extent to which the mechanotransduction channel is involved in cisplatin uptake and ototoxicity in mammalian hair cells. Herein, we show that genetically disrupting mechanotransduction in mouse partially protects hair cells from cisplatin-induced hair cell death. Using a fluorescent-dye conjugated cisplatin, we monitored cisplatin uptake in cochlear explants and found that functional mechanotransduction is required for the uptake of cisplatin in murine hair cells. In addition, cimetidine, an inhibitor of the organic cation transporter, also partially protects hair cells from cisplatin ototoxicity. Notably, the otoprotective effects of cimetidine do not require mechanotransduction. These findings suggest that both the mechanotransduction channel and the organic cation transporter are critical for cisplatin ototoxicity in murine hair cells.

Keywords: cisplatin, ototoxicity, mechanotransduction, TMIE, organic cation transporter

OPEN ACCESS

Edited by:
Leonard Rybak, Southern Illinois University Carbondale, United States

Reviewed by:
Agnieszka J. Szczepek, Charité Universitätsmedizin Berlin, Germany
Sofia Waissbluth, Pontificia Universidad Católica de Chile, Chile
Giuliano Ciarimboli, University of Münster, Germany

****Correspondence:***
Bo Zhao
zhaozb@iu.edu

Specialty section:
This article was submitted to Molecular Signalling and Pathways, a section of the journal Frontiers in Molecular Neuroscience

Received: *14 December 2021*
Accepted: *10 January 2022*
Published: *10 February 2022*

Citation:
Li J, Liu C, Kaefer S, Youssef M and Zhao B (2022) The Mechanotransduction Channel and Organic Cation Transporter Are Critical for Cisplatin Ototoxicity in Murine Hair Cells. Front. Mol. Neurosci. 15:835448. doi: 10.3389/fnmol.2022.835448

INTRODUCTION

Hair cells, the sensory receptors of auditory system, are susceptible to numerous insults such as noise, ototoxic drugs, trauma and aging. Cisplatin is a chemotherapeutic drug widely used to treat various types of cancers, including testicular, ovarian, bladder, head and neck, lung, and cervical cancers. However, patients treated with cisplatin frequently suffer from nausea, vomiting, fatigue, serious kidney problems, tinnitus and hearing loss. The strong ototoxicity of cisplatin, which leads to the permanent hair cell death and irreversible hearing loss in 22–77% of patients, significantly limits its usage in clinics (Knight et al., 2005; Kushner et al., 2006; Coradini et al., 2007; Sheth et al., 2017; Kros and Steyger, 2019; Meijer et al., 2021).

Over the years, the understanding of the ototoxic mechanisms of cisplatin has increased (Sheth et al., 2017; Hazlitt et al., 2018; Kros and Steyger, 2019; Rybak et al., 2019; Prayuenyong et al., 2021). Systemically administrated cisplatin traffics across the blood–labyrinth barrier, enters hair cells predominantly from their apical surface, and remains in the cochlea for months to years (Chu et al., 2016; Breglio et al., 2017). After entry into hair cells, cisplatin induces an accumulation of platinated DNA and reactive oxygen species (ROS), activation of BRAF/MEK/ERK cellular

pathway, and ultimately leads to hair cell damage and permanent hearing loss (Sheth et al., 2017; Kros and Steyger, 2019; Ingersoll et al., 2020; Ramkumar et al., 2021). However, the entry routes of cisplatin into hair cells are still not very clear. In cancer cells, copper transport 1 (CTR1) and organic cation transporter 2 (OCT2) have been revealed to mediate cisplatin uptake (Harrach and Ciarimboli, 2015). In HEI-OC1 cells, an auditory cell line derived from the mouse organ of Corti, as well as in neonatal rat cochlear explants, CTR1 and OCT2 mediate cisplatin-induced ototoxicity, suggesting that the influx of cisplatin into hair cells occurs *via* the above two proteins (Ciarimboli et al., 2010; More et al., 2010; Ding et al., 2011). Notably, mice lacking organic cation transporters are insusceptible to cisplatin ototoxicity (Ciarimboli et al., 2010). However, inhibiting CTR1 or OCT2 does not completely protect hair cells from cisplatin-induced hair cell death (Ding et al., 2011), indicating that there are some other proteins involved in cisplatin uptake and ototoxicity. Interestingly, in the lateral line hair cells of zebrafish, functional mechanotransduction but not CTR1 or OCT2 is required for cisplatin-induced hair cell death (Thomas et al., 2013). Several other studies have also indicated a potential role of the mechanotransduction channel in cisplatin ototoxicity (Waissbluth and Daniel, 2013). ORC-13661, a high-affinity permeant blocker of the mechanotransduction channel, protects murine hair cells from cisplatin ototoxicity (Kitcher et al., 2019). In addition, in chicken hair cells, high doses of cisplatin are able to block mechanotransduction currents (Kimitsuki et al., 1993). However, direct evidence of an essential role of mechanotransduction in cisplatin uptake and ototoxicity in murine hair cells is still missing.

The mechanotransduction machinery of hair cells is localized within the stereocilia that protrude from the apical surface of hair cells. The mechanotransduction machinery in hair cells is formed by several distinctive proteins, including transmembrane channel-like 1 and 2 (TMC1/2), LHFPL tetraspan subfamily member 5 protein (LHFPL5; previously named TMHS), transmembrane inner ear protein (TMIE), calcium and integrin-binding family member 2 (CIB2), and tip link proteins (Protocadherin-15 and Cadherin-23) (Siemens et al., 2004; Sollner et al., 2004; Kazmierczak et al., 2007; Kawashima et al., 2011; Xiong et al., 2012; Zhao et al., 2014; Giese et al., 2017; Pan et al., 2018; Pacentine and Nicolson, 2019; Cunningham et al., 2020). Previous studies have found that TMIE is an essential subunit of the mechanotransduction channel defining its pore and gating properties (Zhao et al., 2014; Cunningham et al., 2020). Notably, murine hair cells that lack TMIE have no mechanotransduction currents (Zhao et al., 2014; Cunningham et al., 2020).

In this study, we compared the murine hair cell death caused by cisplatin in wild-type and TMIE-deficient cochlear explants. Furthermore, using commercially available Texas Red-conjugated cisplatin (TR–cisplatin), we investigated the cisplatin uptake in wild-type and TMIE-deficient hair cells. Since OCT2 has been reported to mediate the toxicity of cisplatin in cancer cells and murine hair cells (Harrach and Ciarimboli, 2015), we studied the otoprotective effects of cimetidine on wild-type and TMIE-deficient hair cells. Our results suggest that both the mechanotransduction channel and OCT2 are critical for cisplatin ototoxicity in murine hair cells.

MATERIALS AND METHODS

Animal Models and Animal Care

Tmie$^{-/-}$ mice (MGI: 5784557) have been described previously (Zhao et al., 2014). More than three mice per group, including both male and female mice, were used. All of the animal experiments were carried out in accordance with the National Institutes of Health Guide and were approved by the Institutional Animal Care and Use Committee of Indiana University School of Medicine (IACUC; Protocol #19075).

Cochlear Explants Culture and TR-Cisplatin Uptake Assay

Cochlear explants were dissected from P3 mice and cultured in DMEM/F12 medium (Cat.# 21041025, Life Technologies Corporation) overnight at 37°C in a 5% CO2 humidified atmosphere. Then, the samples were incubated in DMEM/F12 medium containing various concentrations of cisplatin (Cat.# 232120, Millipore Sigma, dissolved in DMEM/F12) for 2 days at 37°C. Cimetidine (Cat.# AAJ6282506, Fisher Scientific) was also dissolved in DMEM/F12 and added to the cochlear explants prior to adding of cisplatin. To monitor the cisplatin uptake in hair cells, the cochlear explants were incubated in DMEM/F12 medium containing 2 μg/mL of TR–cisplatin (Ursa BioScience) for various amounts of time. Stacked images were then captured using a deconvolution microscope (Leica) with a 63 × objective (HCX APO L63X/0.90 Water). The images were then deconvoluted using the blind deconvolution method.

Immunostaining

Immunostaining was performed as described previously (Liu et al., 2018). In brief, the cochlear explants were fixed in 4% PFA for 20 min at room temperature and then washed three times for 5 min each in HBSS. The tectorial membrane was then removed and the samples were blocked in blocking buffer (5% bovine serum albumin and 0.5% Triton X-100 in HBSS solution) for 20 min at room temperature. Then, the samples were incubated with primary antibodies diluted in antibody dilution buffer (1% BSA and 0.1% Triton X-100 in HBSS solution) overnight at 4°C. After being washed with HBSS, the samples were incubated with secondary antibodies for 2 h at room temperature. Then, the samples were mounted in ProLong® Antifade Reagents (Cat.# P36971, Life technologies Corporation). Stacked images were then captured using a deconvolution microscope (Leica) with a 20 × objective (HC PL FLUOTAR 20x/0.55) or a 100 × objective (HCX PL APO 100x/1.40-0.70 OIL). Antibodies used in this study were anti-β2 spectrin (1:200, Cat.# sc-136074, Santa Cruz) and Alexa Fluor 488 goat anti-mouse (1:2,000, Cat.# A11017, Life technologies Corporation).

Data Analysis

At least three different animals, including both genders, were used for each experiment. The precise numbers, sample size,

repetitions, and statistical tests are indicated in the figures and figure legends. The Kolmogorov–Smirnov test was used to determine the normality of data distribution. Then two-way ANOVA followed by Bonferroni *post hoc* test or two-tailed unpaired Student's *t*-test was used to determine statistical significance ($^{*}p < 0.05$, $^{**}p < 0.01$, and $^{***}p < 0.001$).

RESULTS

Cisplatin Dose-Dependently Kills Wild-Type Murine Hair Cells

To investigate the extent to which functional mechanotransduction affects cisplatin ototoxicity, we first determined the concentration at which cisplatin effectively kills wild-type hair cells. Mouse cochlear explants dissected from postnatal day 3 (P3) wild-type C57/BL6J mice were cultured overnight and then exposed to cisplatin at a range of concentrations from 0 to 50 μM for 2 days. Then, the samples were fixed and labeled with an antibody against β2-spectrin, a protein highly expressed in cochlear hair cells (Holley and Ashmore, 1990; Scheffer et al., 2015; Liu et al., 2019). Without cisplatin exposure, we observed a highly organized cochlear epithelium with three rows of outer hair cells (OHCs) on the external side of the tunnel of Corti and one row of inner hair cells (IHCs) on the internal side (**Figure 1A**). Cisplatin caused a reliable dose-dependent loss of hair cells (**Figures 1A,B**). The loss of hair cells, mainly OHCs, was observed in the cochlear explants exposed to cisplatin at a concentration as low as 5 μM. Furthermore, we found that 20 μM of cisplatin led to an ∼80% reduction of hair cells in the middle region of the cochlea. Cisplatin at a 30 μM or higher concentration killed almost all of the hair cells from the apical to basal regions of the cochlea (**Figures 1A,B**). Consistent with previous findings (Anniko and Sobin, 1986; Cardinaal et al., 2000; Rainey et al., 2016), the OHCs were more sensitive to cisplatin ototoxicity compared to the IHCs (**Figure 1A**). In addition, the hair cells in the basal region were also more susceptible to cisplatin ototoxicity compared to the hair cells in the apical region (**Figures 1A,B**). Due to the tonotopic susceptibility of the hair cells to cisplatin toxicity, in the following studies, we imaged and analyzed the hair cells in the middle region of the cochlear explants.

Abolishing Mechanotransduction Partially Protects Hair Cells From Cisplatin Ototoxicity

We next sought to determine whether murine hair cells lacking mechanotransduction are more resistant to cisplatin ototoxicity. The cochlear explants were dissected from P3 *Tmie* homozygous ($Tmie^{-/-}$) mice, which have no mechanotransduction current in their hair cells (Zhao et al., 2014). The samples were then exposed to various concentrations of cisplatin for 2 days. Similar to that in the wild-type hair cells, 20 μM of cisplatin killed ∼80% of the hair cells in the *Tmie* heterozygous ($Tmie^{\pm}$) cochlear explants. Interestingly, we did not observe any significant hair cell loss in the $Tmie^{-/-}$ mice after exposure to 20 μM of cisplatin (**Figures 2A,B**). Notably, there was significant $Tmie^{-/-}$ hair cell death after exposure to 30 μM of cisplatin, but much less compared to that of the $Tmie^{\pm}$ mice (**Figures 2A,B**). At concentrations of 50 μM or higher, cisplatin killed almost all of the hair cells in both the $Tmie^{\pm}$ and $Tmie^{-/-}$ (**Figures 2A,B**), suggesting that abolishing mechanotransduction partially protects hair cells from cisplatin ototoxicity.

Abolishing Mechanotransduction Blocks Cisplatin Uptake

Impaired mechanotransduction partially protects hair cells from cisplatin ototoxicity, suggesting that functional mechanotransduction might be critical for cisplatin uptake into murine hair cells. Fluorophore–cisplatin conjugates have been widely used to study the cellular uptake of cisplatin (Thomas et al., 2013; Chu et al., 2016). Thus, wild-type and $Tmie^{-/-}$ hair cells were incubated with Texas Red-conjugated cisplatin (TR–cisplatin). Fifteen minutes after the exposure to TR–cisplatin, a robust fluorescent signal was detected in the cell body of the wild-type hair cells, but not in the $Tmie^{-/-}$ hair cells (**Figure 3A**). Two hours after the exposure to TR–cisplatin, we still did not detect a fluorescent signal in the cell body of the $Tmie^{-/-}$ hair cells (**Figure 3B**), suggesting an essential role of mechanotransduction in cisplatin uptake. A very weak fluorescent signal at the stereociliary region was observed in the $Tmie^{-/-}$ hair cells, as well as in the wild-type hair cells (**Figures 3A,B**).

Otoprotective Effects of Cimetidine Do Not Require Mechanotransduction

Although OCT2 is not involved in cisplatin uptake and ototoxicity in zebrafish hair cells (Thomas et al., 2013), it might play a significant role in murine hair cells, as suggested by several studies (Ding et al., 2011). To investigate the extent to which OCT2 is involved in protecting hair cells from cisplatin ototoxicity, wild-type and $Tmie^{-/-}$ hair cells were exposed to different concentrations of cisplatin with/without 1 mM cimetidine for 2 days. Cimetidine prevented hair cell death in the wild-type cochlear explants exposed to low concentrations of cisplatin (**Figures 4A,B**). Notably, higher concentrations of cisplatin still efficiently killed wild-type hair cells even in the presence of cimetidine (**Figures 4A,B**). Then, we asked whether the protection effects of cimetidine rely on mechanotransduction. Thus, $Tmie^{-/-}$ hair cells were exposed to 50, 70, 100, and 120 μM of cisplatin with/without 1 mM cimetidine for 2 days. Remarkably, cimetidine also protected the $Tmie^{-/-}$ hair cells from cisplatin ototoxicity (**Figures 5A,B**), suggesting that the otoprotective effects of cimetidine occur *via* other mechanisms instead of affecting mechanotransduction.

DISCUSSION

Sensorineural hearing loss occurs in 22–77% of patients treated with cisplatin (Knight et al., 2005; Kushner et al., 2006; Coradini et al., 2007; Sheth et al., 2017; Kros and Steyger, 2019). Patients suffering hearing loss nowadays benefit from

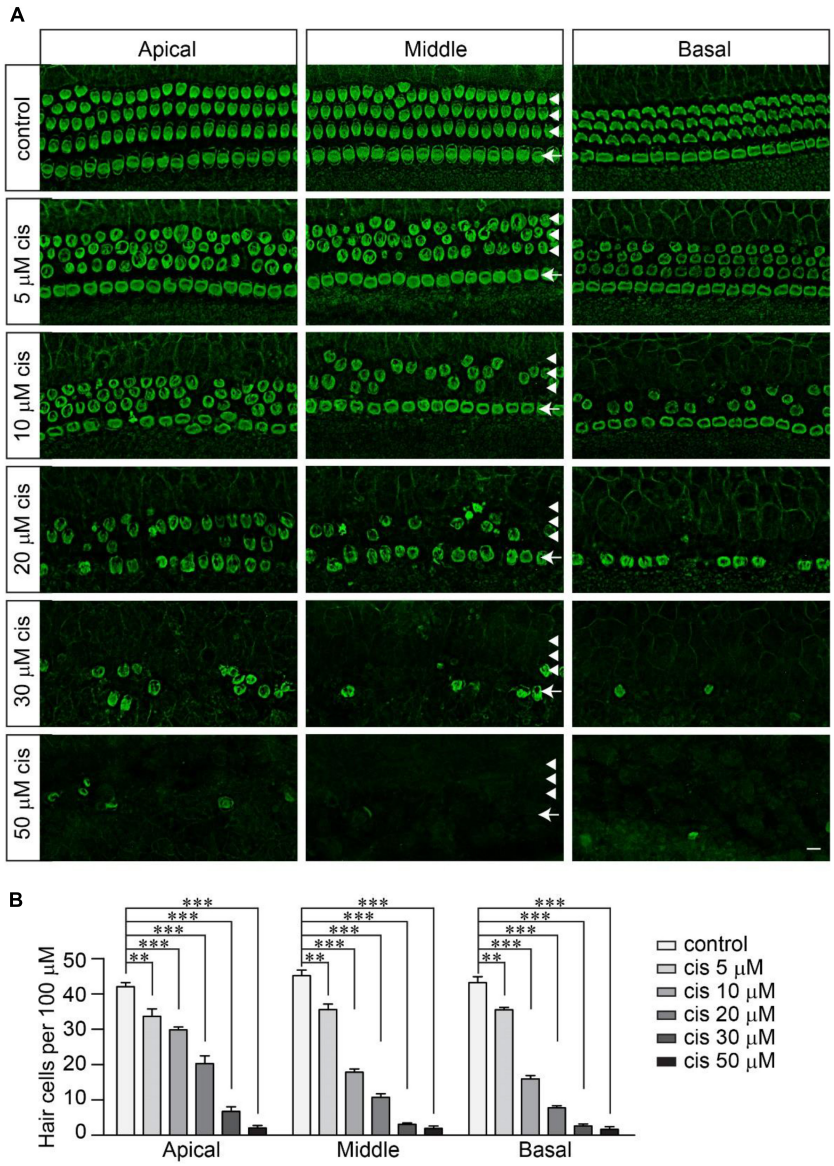

FIGURE 1 | Cisplatin dose-dependently kills wild-type murine hair cells. **(A)** Cochlear explants were dissected from P3 wild-type C57/BL6J mice and cultured overnight in DMEM/F12 culture medium. Then, the cochlear explants were exposed to cisplatin at different concentrations for 2 days. The samples were fixed and labeled with an antibody against β2-spectrin, a hair cell marker. Note, OHCs (arrowheads) were more susceptible to cisplatin than IHCs (arrows). Scale bar: 10 μm. **(B)** Numbers of hair cells per 100 μm (3 mice per group). Data are represented as the mean ± standard error (SE). Two-way ANOVA followed by Bonferroni *post hoc* test was performed (**$p < 0.01$ and ***$p < 0.001$).

the use of hearing aids and cochlear implants (Brant et al., 2021). With the upgrade in hearing aids and the improvement in cochlear implant surgery to reduce the discomfort of patients (Freni et al., 2020), outcomes will continue to improve in the future. To restore natural hearing, it will be of interest to study the molecular mechanisms underlying cisplatin ototoxicity. The uptake of cisplatin in murine hair cells is not clear. Taking advantage of *Tmie* mutant mouse, we found that genetic abolishing mechanotransduction in hair cells prevents cisplatin uptake and partially prevents cisplatin-induced hair cell death, suggesting an essential role of the functional mechanotransduction channel in cisplatin uptake and toxicity in murine hair cells. In addition, we also found that cimetidine, an OCT2 inhibitor, protects murine hair cells from cisplatin ototoxicity *via* a mechanism that does not require mechanotransduction in hair cells.

Our results show that functional mechanotransduction is critical for cisplatin uptake in murine hair cells, similar to that in the zebrafish hair cells (Thomas et al., 2013). Cisplatin at high concentrations blocks mechanotransduction current (Kimitsuki et al., 1993). The uptake kinetics of TR–cisplatin and cisplatin in hair cells might be slightly different due

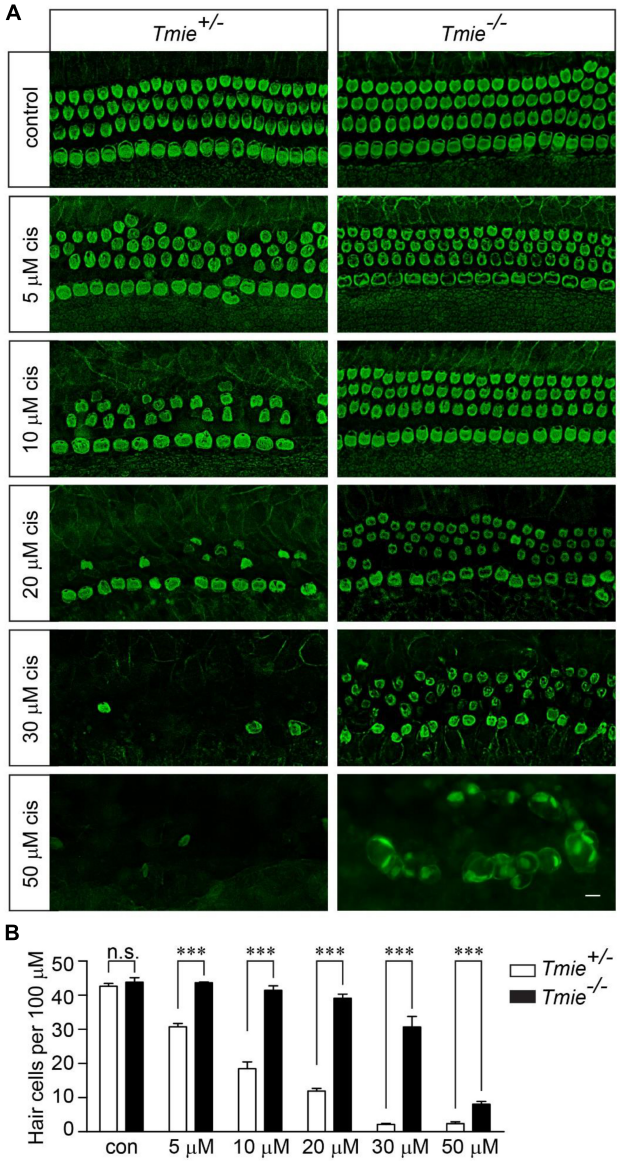

FIGURE 2 | *Tmie* mutant hair cells are more resistant to cisplatin ototoxicity. **(A)** Cochlear explants were dissected from P3 $Tmie^{\pm}$ and $Tmie^{-/-}$ mice and then exposed to cisplatin at different concentrations for 2 days. The samples were fixed and labeled with an antibody against β2-spectrin. The majority of the $Tmie^{-/-}$ hair cells were dead with a few swollen hair cells in the explants, after the exposure to 50 μM of cisplatin for 2 days. Note, the $Tmie^{-/-}$ hair cells are more resistant to cisplatin ototoxicity. Scale bar: 10 μm. **(B)** Numbers of hair cells per 100 μm in the middle region of the cochlea (5 mice per group, control; 3 mice per group, 5 μM cisplatin; 7 mice per group, 10 μM cisplatin; 4 mice per group, 20 μM cisplatin; 4 mice per group, 30 μM cisplatin; 3 mice per group, 50 μM cisplatin). Data are represented as the mean ± SE. n.s., not significant; ***$p < 0.001$ by Student's *t*-test.

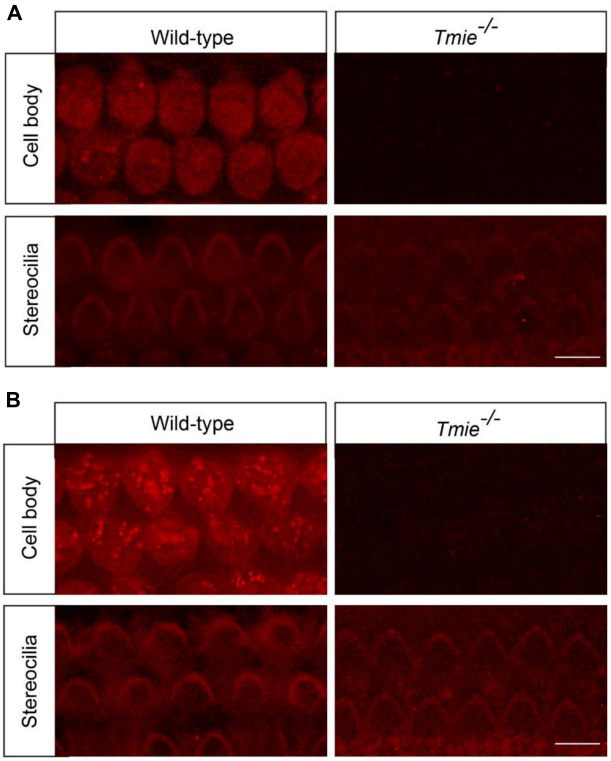

FIGURE 3 | Cisplatin uptake relies on functional mechanotransduction. Cochlear explants dissected from P3 wild-type and $Tmie^{-/-}$ mice were incubated with Texas Red-conjugated cisplatin (TR–cisplatin) for 15 min **(A)** or 2 h **(B)**. Note, a robust TR–cisplatin signal was detected in the cell body of the wild-type OHCs. A weak cisplatin signal was detected in the stereocilia in the wild-type and $Tmie^{-/-}$ hair cells. Scale bars: 10 μm.

to their different sizes. In our studies, we did not observe a significant TR–cisplatin signal in the cell body of hair cells lacking mechanotransduction, even after a long-term incubation with TR-cisplatin (**Figure 3**). Consistently, abolishing mechanotransduction protects hair cells from cisplatin ototoxicity (**Figure 2**). These results strongly implicate the mechanotransduction channel as being a major entry route of cisplatin into murine hair cells. However, we could not exclude the possibility that cisplatin enters hair cells *via* another channel that is regulated by mechanotransduction (Thomas et al., 2013). It will be important to reconstitute the mechanotransduction machinery in a heterologous system (Zhao and Muller, 2015) and then investigate whether the mechanotransduction channel is responsible for cisplatin uptake. A very weak fluorescent signal at the stereociliary region was observed in the $Tmie^{-/-}$ hair cells, as well as in wild-type hair cells (**Figures 3A,B**). Consistently, in zebrafish hair cells with impaired mechanotransduction, a weak cisplatin signal was also detected in the stereociliary region (Thomas et al., 2013). It is possible that some cisplatin entered hair cells *via* another route and was then retained in the stereociliary region. Another possibility is that cisplatin did not cross the cell membrane, but instead bound to the extracellular region of some stereociliary proteins. Unfortunately, the stereocilia are very tiny structures, which makes it extremely difficult to determine the detailed subcellular localization of cisplatin in stereocilia using fluorescent microscopy.

In our studies, we found that cimetidine, an inhibitor of the organic cation transporter, protected $Tmie^{-/-}$ hair cells

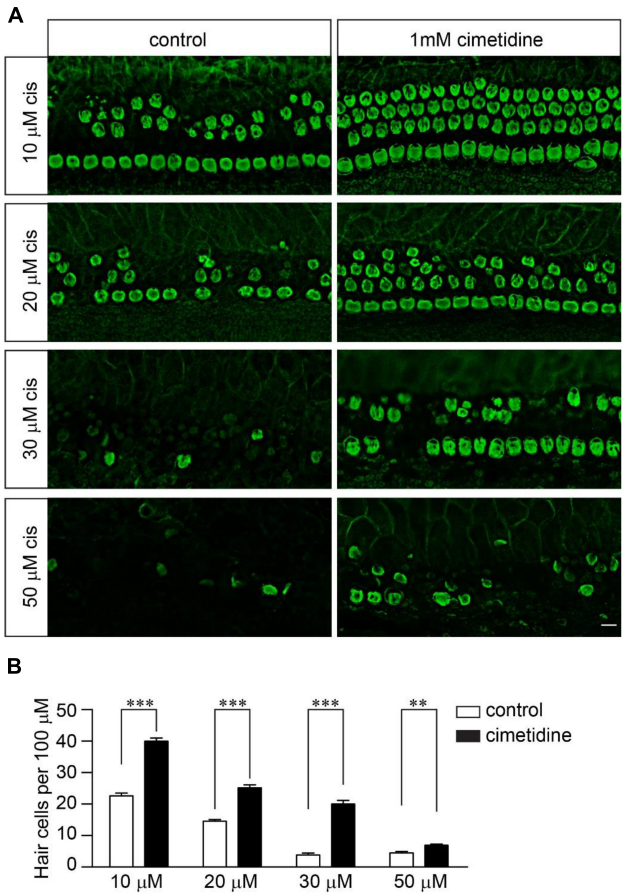

FIGURE 4 | Cimetidine protects wild-type hair cells from cisplatin ototoxicity. **(A)** Cochlear explants were dissected from P3 wild-type mice and then exposed to different concentrations of cisplatin with/without 1 mM cimetidine for 2 days. The samples were then fixed and labeled with an antibody against β2-spectrin. Note, 1 mM cimetidine partially protected hair cells from cisplatin ototoxicity. Scale bar: 10 μm. **(B)** Numbers of hair cells per 100 μm in the middle region of the cochlea (5 mice per group, 10 μM cisplatin; 6 mice per group, 20 μM cisplatin; 3 mice per group, 30 μM cisplatin; 3 mice per group, 50 μM cisplatin). Data are represented as the mean ± SE. $^{**}p < 0.01$ and $^{***}p < 0.001$ by Student's *t*-test.

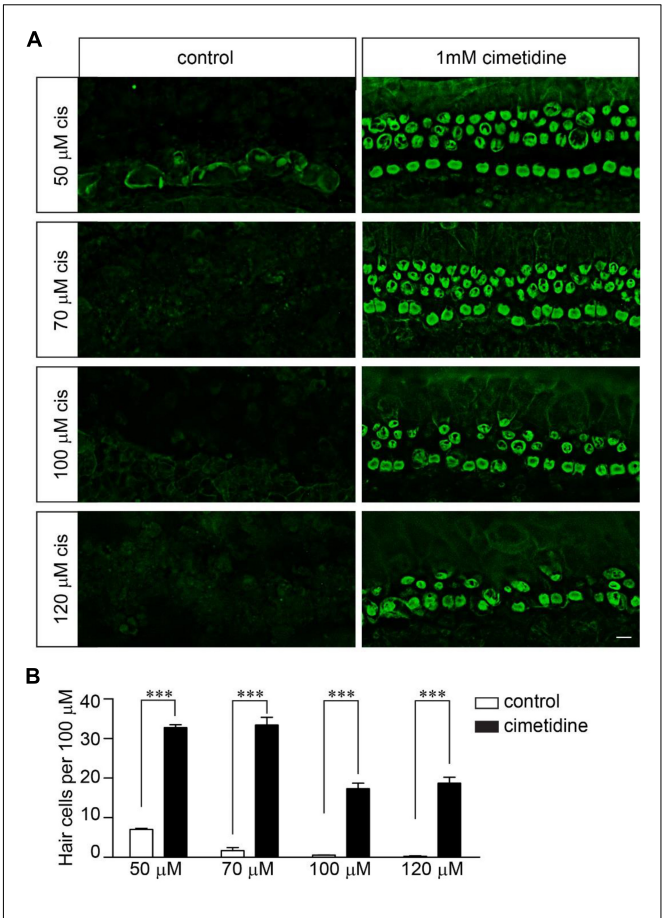

FIGURE 5 | Cimetidine protects *Tmie*$^{-/-}$ hair cells from cisplatin ototoxicity. **(A)** Cochlear explants were dissected from P3 *Tmie*$^{-/-}$ mice and then exposed to cisplatin at the indicated doses with/without 1 mM cimetidine for 2 days. The samples were fixed and labeled with an antibody against β2-spectrin. Note, cimetidine protected the *Tmie* mutant hair cells from cisplatin ototoxicity. Scale bar: 10 μm. **(B)** Numbers of hair cells per 100 μm in the middle region of cochlea (5 mice per group, 50 μM cisplatin; 4 mice per group, 70 μM cisplatin; 3 mice per group, 100 μM cisplatin; 3 mice per group, 120 μM cisplatin). Data are represented as the mean ± SE. $^{***}p < 0.001$ by Student's *t*-test.

from cisplatin ototoxicity, suggesting that the otoprotective effects of cimetidine occur *via* other mechanisms instead of affecting mechanotransduction. Interestingly, previous studies found that OCT2 is highly expressed in both IHCs and OHCs in murine inner ear and mice lacking OCT1/2 are insusceptible to cisplatin ototoxicity (Ciarimboli et al., 2010). These results suggest an essential role of OCT2 in cisplatin ototoxicity. Other studies found that cimetidine could also inhibit histamine H2 receptor, which is expressed in the inner ear (Takumida et al., 2016). Thus, it is possible that histamine receptors might also be involved in cisplatin ototoxicity and characterization of mice lacking histamine receptor(s) would be informative. In our studies, we found that blocking both mechanotransduction and OCT2 did not provide complete protection against cisplatin (**Figure 5**), implicating the possibility of additional entry routes of cisplatin into murine hair cells. Thus, it will be of interest to investigate the extent to which other candidates such as TRP channels (Sheth et al., 2017; Jiang et al., 2019) are involved in cisplatin uptake and ototoxicity in murine hair cells.

Mechanotransduction channel is essential for auditory perception. Mutations of TMIE lead to permanent hearing loss in humans and mice (Mitchem et al., 2002; Naz et al., 2002; Zhao et al., 2014). Disrupting mechanotransduction protects hair cells from cisplatin-induced hair cell death (**Figure 2**). Notably, some compounds, such as d-Tubocurarine and Berbamine, could reversibly block the mechanotransduction channel, suggesting that transiently blocking the mechanotransduction channel in hair cells is a potential therapeutic method to prevent cisplatin ototoxicity (Kirkwood et al., 2017).

Besides hair cells, spiral ganglion neurons that innervate hair cells and stria vascularis cells that generate the endocochlear potential are another two major targets of cisplatin in the inner ear (Van Ruijven et al., 2004, 2005; Taukulis et al., 2021). Before entering hair cells, systemically administered cisplatin enters the stria vascularis through the blood-labyrinth barrier (Chu et al., 2016; Breglio et al., 2017; Prayuenyong et al., 2021). Revealed by LacZ staining, the expression level of *Tmie* is low in mouse stria vascularis or spiral ganglion neurons (Zhao et al., 2014). Interestingly, specific OCT2 expression was detected in the stria vascularis cells and spiral ganglion neurons (Ciarimboli et al., 2010; Hellberg et al., 2015), suggesting that OCT2 is a potential target for protecting stria vascularis cells and spiral ganglion neurons against cisplatin ototoxicity.

In summary, we found that both mechanotransduction and the organic cation transporter are critical for cisplatin ototoxicity in murine hair cells. Extensively illustrating the entry routes and ototoxic mechanisms of cisplatin in murine hair cells may lead to the development of novel therapeutic approaches to prevent cisplatin-induced hearing loss.

DATA AVAILABILITY STATEMENT

The original contributions presented in the study are included in the article/supplementary material, further inquiries can be directed to the corresponding author.

ETHICS STATEMENT

The animal study was reviewed and approved by Institutional Animal Care and Use Committee of Indiana University School of Medicine.

AUTHOR CONTRIBUTIONS

JL, CL, SK, and BZ: methodology and investigation. MY and JL: counting survived cells. JL, CL, and BZ: writing manuscript. BZ: conceptualization and supervision. All authors contributed to the article and approved the submitted version.

FUNDING

This work was supported by the National Institute on Deafness and Other Communication Disorders (NIDCD) grant DC017147 (BZ); the Discovery Research Grant from Royal National Institute for Deaf People (BZ); and the Indiana University School of Medicine startup funding (BZ).

ACKNOWLEDGMENTS

Tmie mutant mice were generated in Ulrich Müller's lab, and we would like to thank Müller for his support.

REFERENCES

Anniko, M., and Sobin, A. (1986). Cisplatin: evaluation of its ototoxic potential. *Am. J. Otolaryngol.* 7, 276–293. doi: 10.1016/s0196-0709(86)80050-3

Brant, J. A., Adewole, D. O., Vitale, F., and Cullen, D. K. (2021). Bioengineering applications for hearing restoration: emerging biologically inspired and biointegrated designs. *Curr. Opin. Biotechnol.* 72, 131–138. doi: 10.1016/j.copbio.2021.11.002

Breglio, A. M., Rusheen, A. E., Shide, E. D., Fernandez, K. A., Spielbauer, K. K., Mclachlin, K. M., et al. (2017). Cisplatin is retained in the cochlea indefinitely following chemotherapy. *Nat. Commun.* 8:1654. doi: 10.1038/s41467-017-01837-1

Cardinaal, R. M., De Groot, J. C., Huizing, E. H., Veldman, J. E., and Smoorenburg, G. F. (2000). Cisplatin-induced ototoxicity: morphological evidence of spontaneous outer hair cell recovery in albino guinea pigs? *Hear Res.* 144, 147–156. doi: 10.1016/s0378-5955(00)00060-5

Chu, Y. H., Sibrian-Vazquez, M., Escobedo, J. O., Phillips, A. R., Dickey, D. T., Wang, Q., et al. (2016). Systemic Delivery and Biodistribution of Cisplatin in Vivo. *Mol. Pharm.* 13, 2677–2682. doi: 10.1021/acs.molpharmaceut.6b00240

Ciarimboli, G., Deuster, D., Knief, A., Sperling, M., Holtkamp, M., Edemir, B., et al. (2010). Organic cation transporter 2 mediates cisplatin-induced oto- and nephrotoxicity and is a target for protective interventions. *Am. J. Pathol.* 176, 1169–1180. doi: 10.2353/ajpath.2010.090610

Coradini, P. P., Cigana, L., Selistre, S. G., Rosito, L. S., and Brunetto, A. L. (2007). Ototoxicity from cisplatin therapy in childhood cancer. *J. Pediatr. Hematol. Oncol.* 29, 355–360. doi: 10.1097/MPH.0b013e318059c220

Cunningham, C. L., Qiu, X., Wu, Z., Zhao, B., Peng, G., Kim, Y. H., et al. (2020). TMIE Defines Pore and Gating Properties of the Mechanotransduction Channel of Mammalian Cochlear Hair Cells. *Neuron* 107:e128. doi: 10.1016/j.neuron.2020.03.033

Ding, D., He, J., Allman, B. L., Yu, D., Jiang, H., Seigel, G. M., et al. (2011). Cisplatin ototoxicity in rat cochlear organotypic cultures. *Hear Res.* 282, 196–203. doi: 10.1016/j.heares.2011.08.002

Freni, F., Gazia, F., Slavutsky, V., Scherdel, E. P., Nicenboim, L., Posada, R., et al. (2020). Cochlear Implant Surgery: endomeatal Approach versus Posterior Tympanotomy. *Int. J. Environ. Res. Public. Health* 17:4187. doi: 10.3390/ijerph17124187

Giese, A. P. J., Tang, Y. Q., Sinha, G. P., Bowl, M. R., Goldring, A. C., Parker, A., et al. (2017). CIB2 interacts with TMC1 and TMC2 and is essential for mechanotransduction in auditory hair cells. *Nat. Commun.* 8:43. doi: 10.1038/s41467-017-00061-1

Harrach, S., and Ciarimboli, G. (2015). Role of transporters in the distribution of platinum-based drugs. *Front. Pharmacol.* 6:85. doi: 10.3389/fphar.2015.00085

Hazlitt, R. A., Min, J., and Zuo, J. (2018). Progress in the Development of Preventative Drugs for Cisplatin-Induced Hearing Loss. *J. Med. Chem.* 61, 5512–5524. doi: 10.1021/acs.jmedchem.7b01653

Hellberg, V., Gahm, C., Liu, W., Ehrsson, H., Rask-Andersen, H., and Laurell, G. (2015). Immunohistochemical localization of OCT2 in the cochlea of various species. *Laryngoscope* 125, E320–E325.

Holley, M. C., and Ashmore, J. F. (1990). Spectrin, actin and the structure of the cortical lattice in mammalian cochlear outer hair cells. *J. Cell. Sci.* 96, 283–291. doi: 10.1242/jcs.96.2.283

Ingersoll, M. A., Malloy, E. A., Caster, L. E., Holland, E. M., Xu, Z., Zallocchi, M., et al. (2020). BRAF inhibition protects against hearing loss in mice. *Sci. Adv.* 6:eabd0561. doi: 10.1126/sciadv.abd0561

Jiang, M., Li, H., Johnson, A., Karasawa, T., Zhang, Y., Meier, W. B., et al. (2019). Inflammation up-regulates cochlear expression of TRPV1 to potentiate drug-induced hearing loss. *Sci. Adv.* 5:eaaw1836. doi: 10.1126/sciadv.aaw1836

Kawashima, Y., Geleoc, G. S., Kurima, K., Labay, V., Lelli, A., Asai, Y., et al. (2011). Mechanotransduction in mouse inner ear hair cells requires transmembrane channel-like genes. *J. Clin. Invest.* 121, 4796–4809. doi: 10.1172/JCI60405

Kazmierczak, P., Sakaguchi, H., Tokita, J., Wilson-Kubalek, E. M., Milligan, R. A., Muller, U., et al. (2007). Cadherin 23 and protocadherin 15 interact to form tip-link filaments in sensory hair cells. *Nature* 449, 87–91. doi: 10.1038/nature06091

Kimitsuki, T., Nakagawa, T., Hisashi, K., Komune, S., and Komiyama, S. (1993). Cisplatin blocks mechano-electric transducer current in chick cochlear hair cells. *Hear Res.* 71, 64–68. doi: 10.1016/0378-5955(93)90021-r

Kirkwood, N. K., O'reilly, M., Derudas, M., Kenyon, E. J., Huckvale, R., Van Netten, S. M., et al. (2017). d-Tubocurarine and Berbamine: alkaloids That Are Permeant Blockers of the Hair Cell's Mechano-Electrical Transducer Channel and Protect from Aminoglycoside Toxicity. *Front. Cell. Neurosci.* 11:262. doi: 10.3389/fncel.2017.00262

Kitcher, S. R., Kirkwood, N. K., Camci, E. D., Wu, P., Gibson, R. M., Redila, V. A., et al. (2019). ORC-13661 protects sensory hair cells from aminoglycoside and cisplatin ototoxicity. *JCI Insight* 4:e126764. doi: 10.1172/jci.insight.126764

Knight, K. R., Kraemer, D. F., and Neuwelt, E. A. (2005). Ototoxicity in children receiving platinum chemotherapy: underestimating a commonly occurring toxicity that may influence academic and social development. *J. Clin. Oncol.* 23, 8588–8596. doi: 10.1200/JCO.2004.00.5355

Kros, C. J., and Steyger, P. S. (2019). Aminoglycoside- and Cisplatin-Induced Ototoxicity: mechanisms and Otoprotective Strategies. *Cold Spring Harb. Perspect Med.* 9:a033548. doi: 10.1101/cshperspect.a033548

Kushner, B. H., Budnick, A., Kramer, K., Modak, S., and Cheung, N. K. (2006). Ototoxicity from high-dose use of platinum compounds in patients with neuroblastoma. *Cancer* 107, 417–422. doi: 10.1002/cncr.22004

Liu, C., Luo, N., Tung, C. Y., Perrin, B. J., and Zhao, B. (2018). GRXCR2 Regulates Taperin Localization Critical for Stereocilia Morphology and Hearing. *Cell. Rep.* 25, 1268.e–1280.e. doi: 10.1016/j.celrep.2018.09.063

Liu, Y., Qi, J., Chen, X., Tang, M., Chu, C., Zhu, W., et al. (2019). Critical role of spectrin in hearing development and deafness. *Sci. Adv.* 5:eaav7803. doi: 10.1126/sciadv.aav7803

Meijer, A. J. M., Li, K. H., Brooks, B., Clemens, E., Ross, C. J., Rassekh, S. R., et al. (2021). The cumulative incidence of cisplatin-induced hearing loss in young children is higher and develops at an early stage during therapy compared with older children based on 2052 audiological assessments. *Cancer* 128, 169–179. doi: 10.1002/cncr.33848

Mitchem, K. L., Hibbard, E., Beyer, L. A., Bosom, K., Dootz, G. A., Dolan, D. F., et al. (2002). Mutation of the novel gene Tmie results in sensory cell defects in the inner ear of spinner, a mouse model of human hearing loss DFNB6. *Hum. Mol. Genet.* 11, 1887–1898. doi: 10.1093/hmg/11.16.1887

More, S. S., Akil, O., Ianculescu, A. G., Geier, E. G., Lustig, L. R., and Giacomini, K. M. (2010). Role of the copper transporter, CTR1, in platinum-induced ototoxicity. *J. Neurosci.* 30, 9500–9509. doi: 10.1523/JNEUROSCI.1544-10.2010

Naz, S., Giguere, C. M., Kohrman, D. C., Mitchem, K. L., Riazuddin, S., Morell, R. J., et al. (2002). Mutations in a novel gene, TMIE, are associated with hearing loss linked to the DFNB6 locus. *Am. J. Hum. Genet.* 71, 632–636. doi: 10.1086/342193

Pacentine, I. V., and Nicolson, T. (2019). Subunits of the mechano-electrical transduction channel, Tmc1/2b, require Tmie to localize in zebrafish sensory hair cells. *PLoS Genet* 15:e1007635. doi: 10.1371/journal.pgen.1007635

Pan, B., Akyuz, N., Liu, X. P., Asai, Y., Nist-Lund, C., Kurima, K., et al. (2018). TMC1 Forms the Pore of Mechanosensory Transduction Channels in Vertebrate Inner Ear Hair Cells. *Neuron* 99, 736–753.e6. doi: 10.1016/j.neuron.2018.07.033

Prayuenyong, P., Baguley, D. M., Kros, C. J., and Steyger, P. S. (2021). Preferential Cochleotoxicity of Cisplatin. *Front. Neurosci.* 15:695268. doi: 10.3389/fnins.2021.695268

Rainey, R. N., Ng, S. Y., Llamas, J., Van Der Horst, G. T., and Segil, N. (2016). Mutations in Cockayne Syndrome-Associated Genes (Csa and Csb) Predispose to Cisplatin-Induced Hearing Loss in Mice. *J. Neurosci.* 36, 4758–4770. doi: 10.1523/JNEUROSCI.3890-15.2016

Ramkumar, V., Mukherjea, D., Dhukhwa, A., and Rybak, L. P. (2021). Oxidative Stress and Inflammation Caused by Cisplatin Ototoxicity. *Antioxidants* 10:1919. doi: 10.3390/antiox10121919

Rybak, L. P., Mukherjea, D., and Ramkumar, V. (2019). Mechanisms of Cisplatin-Induced Ototoxicity and Prevention. *Semin. Hear* 40, 197–204. doi: 10.1055/s-0039-1684048

Scheffer, D. I., Shen, J., Corey, D. P., and Chen, Z. Y. (2015). Gene Expression by Mouse Inner Ear Hair Cells during Development. *J. Neurosci.* 35, 6366–6380. doi: 10.1523/JNEUROSCI.5126-14.2015

Sheth, S., Mukherjea, D., Rybak, L. P., and Ramkumar, V. (2017). Mechanisms of Cisplatin-Induced Ototoxicity and Otoprotection. *Front. Cell. Neurosci.* 11:338. doi: 10.3389/fncel.2017.00338

Siemens, J., Lillo, C., Dumont, R. A., Reynolds, A., Williams, D. S., Gillespie, P. G., et al. (2004). Cadherin 23 is a component of the tip link in hair-cell stereocilia. *Nature* 428, 950–955. doi: 10.1038/nature02483

Sollner, C., Rauch, G. J., Siemens, J., Geisler, R., Schuster, S. C., Muller, U., et al. (2004). Mutations in cadherin 23 affect tip links in zebrafish sensory hair cells. *Nature* 428, 955–959. doi: 10.1038/nature02484

Takumida, M., Takumida, H., and Anniko, M. (2016). Localization of histamine (H1, H2, H3 and H4) receptors in mouse inner ear. *Acta Otolaryngol.* 136, 537–544. doi: 10.3109/00016489.2015.1136433

Taukulis, I. A., Olszewski, R. T., Korrapati, S., Fernandez, K. A., Boger, E. T., Fitzgerald, T. S., et al. (2021). Single-Cell RNA-Seq of Cisplatin-Treated Adult Stria Vascularis Identifies Cell Type-Specific Regulatory Networks and Novel Therapeutic Gene Targets. *Front. Mol. Neurosci.* 14:718241. doi: 10.3389/fnmol.2021.718241

Thomas, A. J., Hailey, D. W., Stawicki, T. M., Wu, P., Coffin, A. B., Rubel, E. W., et al. (2013). Functional mechanotransduction is required for cisplatin-induced hair cell death in the zebrafish lateral line. *J. Neurosci.* 33, 4405–4414. doi: 10.1523/JNEUROSCI.3940-12.2013

Van Ruijven, M. W., De Groot, J. C., Klis, S. F., and Smoorenburg, G. F. (2005). The cochlear targets of cisplatin: an electrophysiological and morphological time-sequence study. *Hear Res.* 205, 241–248. doi: 10.1016/j.heares.2005.03.023

Van Ruijven, M. W., De Groot, J. C., and Smoorenburg, G. F. (2004). Time sequence of degeneration pattern in the guinea pig cochlea during cisplatin administration. *Hear Res.* 197, 44–54. doi: 10.1016/j.heares.2004.07.014

Waissbluth, S., and Daniel, S. J. (2013). Cisplatin-induced ototoxicity: transporters playing a role in cisplatin toxicity. *Hear Res.* 299, 37–45. doi: 10.1016/j.heares.2013.02.002

Xiong, W., Grillet, N., Elledge, H. M., Wagner, T. F., Zhao, B., Johnson, K. R., et al. (2012). TMHS is an integral component of the mechanotransduction machinery of cochlear hair cells. *Cell* 151, 1283–1295. doi: 10.1016/j.cell.2012.10.041

Zhao, B., and Muller, U. (2015). The elusive mechanotransduction machinery of hair cells. *Curr. Opin. Neurobiol.* 34, 172–179. doi: 10.1016/j.conb.2015.08.006

Zhao, B., Wu, Z., Grillet, N., Yan, L., Xiong, W., Harkins-Perry, S., et al. (2014). TMIE is an essential component of the mechanotransduction machinery of cochlear hair cells. *Neuron* 84, 954–967. doi: 10.1016/j.neuron.2014.10.041

Conflict of Interest: The authors declare that the research was conducted in the absence of any commercial or financial relationships that could be construed as a potential conflict of interest.

Publisher's Note: All claims expressed in this article are solely those of the authors and do not necessarily represent those of their affiliated organizations, or those of the publisher, the editors and the reviewers. Any product that may be evaluated in this article, or claim that may be made by its manufacturer, is not guaranteed or endorsed by the publisher.

frontiers in Molecular Neuroscience

ORIGINAL RESEARCH
published: 18 March 2022
doi: 10.3389/fnmol.2022.844568

Kif15 Is Required in the Development of Auditory System Using Zebrafish as a Model

Shimei Zheng[1†], Dongmei Tang[2,3†], Xin Wang[4†], Chang Liu[2,3], Na Zuo[1], Renchun Yan[1], Cheng Wu[1], Jun Ma[1], Chuanxi Wang[1], Hongfei Xu[5], Yingzi He[2,3], Dong Liu[4]* and Shaofeng Liu[1]**

[1] Department of Otolaryngology-Head and Neck Surgery, Yijishan Hospital of Wannan Medical College, Wuhu, China, [2] State Key Laboratory of Medical Neurobiology and MOE Frontiers Center for Brain Science, ENT Institute and Department of Otorhinolaryngology, Eye & ENT Hospital, Fudan University, Shanghai, China, [3] NHC Key Laboratory of Hearing Medicine, Fudan University, Shanghai, China, [4] Nantong Laboratory of Development and Diseases, School of Life Sciences, Co-innovation Center of Neuroregeneration, Key Laboratory of Neuroregeneration of Jiangsu and MOE, Nantong University, Nantong, China, [5] Department of Forensic Medicine, Soochow University, Suzhou, China

OPEN ACCESS

Edited by:
Vikrant Borse,
Washington University in St. Louis, United States

Reviewed by:
Tamara Stawicki,
Lafayette College, United States
Marc Ekker,
University of Ottawa, Canada

***Correspondence:**
Yingzi He
yingzihe09611@126.com
Dong Liu
liudongtom@gmail.com;
tom@ntu.edu.cn
Shaofeng Liu
liusf_cn@163.com

[†] These authors have contributed equally to this work

Specialty section:
This article was submitted to Molecular Signaling and Pathways, a section of the journal Frontiers in Molecular Neuroscience

Received: 28 December 2021
Accepted: 21 February 2022
Published: 18 March 2022

Citation:
Zheng S, Tang D, Wang X, Liu C, Zuo N, Yan R, Wu C, Ma J, Wang C, Xu H, He Y, Liu D and Liu S (2022) Kif15 Is Required in the Development of Auditory System Using Zebrafish as a Model. Front. Mol. Neurosci. 15:844568. doi: 10.3389/fnmol.2022.844568

Kif15, a kinesin family member, is powerful in the formation of bipolar spindles. There is emerging evidence indicating that Kif15 plays vital roles in influencing the growth of axons and interference with the progression of the tumor. However, the function of Kif15 in the auditory organs remains unknown. The Western blotting test was used to examine the effect of Kif15 downregulation by specific morpholino targeting Kif15 (Kif15-MO). The development of the inner ear and posterior lateral line (PLL) system in zebrafish was under continuous observation from spawns to 96 h postfertilization (hpf) to investigate the potential role of Kif15 in the auditory and vestibular system. We uncovered that Kif15 inhibition induced otic organ deformities in zebrafish, including malformed semicircular canals, abnormal number and location of otoliths, and reduced number of hair cells (HCs) both in utricle and saccule. Furthermore, a remarkable reduction in the number of PLL neuromasts was also explored in Kif15-MO morphants compared to the normal larvae. We also detected notably reduced activity in locomotion after Kif15 was knocked down. Additionally, we performed rescue experiments with co-injection of Kif15 mRNA and found that the Kif15 splicing MO-induced deformities in otic vesicle and PLL of zebrafish were successfully rescued, and the severely reduced locomotor activity caused by Kif15-MO was partially rescued compared to the control-MO (Con-MO) embryos. Our findings uncover that Kif15 is essential in the early development of auditory and vestibular organs using zebrafish as models.

Keywords: Kif15, morpholino knockdown, auditory organs, development, zebrafish

INTRODUCTION

Kif15 (also called Kinesin-12), a pivotal member of the kinesin family, is essential for the production of bipolar spindles (Sturgill and Ohi, 2013). Recent studies have revealed that some kinesin family members are exploited for the invention of antimitotic drugs especially used in cancer therapy (Milic et al., 2018). Among those, Eg5 (Kif11 or Kinesin-5) and Kif15 are

most highlighted. Eg5 is fundamental for spindle assembly while Kif15 is non-essential in the establishment of spindle bipolarity when Eg5 is in full activity. However, Kif15 becomes essential in the maintenance of spindle bipolarity when Eg5 is partially inhibited (Tanenbaum et al., 2009). Kif15 is also demonstrated involved in developing neurons, influencing axonal growth, navigation, and branching. For example, using morpholino (MO) injection strategy or CRISPR/Cas9-based knockout technology, the axons grow faster and longer when the Kif15 level is reduced compared to the Kif15 wild type (Liu et al., 2010; Dong et al., 2019). More and more studies show that Kif15 plays a pretty important role in the occurrence and development of some cancers (Gao et al., 2020a,b; Kitagawa et al., 2020; Ma et al., 2020). Moreover, previous studies have demonstrated that Kif15 also plays a pretty important role in mitosis, meiosis, spermiogenesis, cell growth, and differentiation (Ma et al., 2017; Malaby et al., 2019; Yu et al., 2019). Increasingly, the functions of Kif15 in distinct models have gained more attention. As reported by Mei Liu's laboratory, Kif15 is detected from two-cell stage, mainly concentrated in the central nervous system from 14 to 30 hpf and also distributed in organs such as brain, eyes, ears, fin, and olfactory bulbs in zebrafish (Xu et al., 2014). However, the role of Kif15 in ears has not been explored.

In recent years, zebrafish has become a popular experimental model in the study of auditory system development and inner ear hair cell (HC) regeneration for advantages in the transparent body, short growth period, large oviposition, direct observation, and easier regulation (Blanco-Sánchez et al., 2017; He et al., 2017; Tang et al., 2019, 2021). The mechanosensory organs of zebrafish are composed of the otic vesicle, anterior lateral line in the cephalic region, and posterior lateral line (PLL; Kimmel et al., 1995). Different from the mammals, zebrafish is devoid of the cochlea, and the main components of zebrafish otic vesicle are three pairs of semicircular canals, two pairs of sensory patches named utricle and saccule (Kimmel et al., 1995; Whitfield et al., 2002; Geng et al., 2013). Otoliths composed of calcium carbonate crystalline are overlain on the two maculae; thus, utricle and saccule are called otolith organs (Whitfield et al., 2002; Lundberg et al., 2015; Kalka et al., 2019). The PLL neuromasts (NMs) consist of HCs in the center and supporting cells and mantle cells in the periphery; these HCs share similar structure and function with those in the mammalian inner ear (Whitfield et al., 2002; Nicolson, 2017).

In this study, we first investigated the function of Kif15 in the development of zebrafish otic vesicle and PLL using splicing- and translation-blocking MO targeting Kif15. Our findings uncover the pivotal role of Kinesin superfamily member Kif15 in the development of hearing organs for the purpose of hearing research.

MATERIALS AND METHODS

Zebrafish Maintenance and Operation

The embryos of zebrafish were obtained from *Tg(cldnb:lynGFP)*$^{zf\,106}$ line, *Tg(brn3c:mGFP)*^{s356t} line, and AB wild type. Spawns were maintained in embryo medium at 28.5°C according to the standard recipe. Hours/days postfertilization (hpf/dpf) was used to take a record of marking embryos' different developmental stages. Embryos lived in E3 water which add 0.03‰ 1-phenyl-2-thiourea (PTU; Sigma–Aldrich, St Louis, MO, United States) at the stage of 14 hpf, in the result of avoiding pigment formation. The Institutional Animal Care and Use Committee of Fudan University approved all the animal experiments.

Morpholino Injections

Two endogenous blocking strategies were used for inhibiting the expression of Kif15 (Kif15-MO), and the precise sequences were shown as follows:

Splicing-blocking: 5′-ATGTATTAAAAACCTCACCTGGCTG-3′;
Translation-blocking: 5′-CATGATTCATTACTATATTTCCTCT-3′.

A total final concentration of 0.3 mM was injected into the yolk sacs of zebrafish embryos at the one- to two-cell stage for Kif15 knockdown. As a control, the parallel embryos were injected with the standard control-MO (Con-MO), sequenced in 5′-CCTCTTACCTCAGTTACAATTTATA-3′ to avoid errors due to injections.

Imaging

The live zebrafish were anesthetized in 0.02% MS-222 (ethyl 3-aminobenzoate methanesulfonate; Sigma–Aldrich, Inc., Saint Louis, MO, United States) for 3 min and then placed on the glass slide with E3 water under the corresponding microscope. The images were taken with a stereomicroscope or an inverted fluorescence microscope.

Zebrafish Locomotion Assay

After treatment, larvae were moved into wells of a 48-well plate (1 fish/well) to monitor their swimming behavior. Zebrafish behavior was monitored by a digital video tracking system (DVTS, Noldus Information Technology, United States). Each larva was allowed to habituate to the test environment of the system for 30 min before the start of the data acquisition. Notably, 10 acoustic/vibrational stimuli (Danio Vision intensity setting 6) with a 20-s interstimulus interval were set and applied. The total swimming distance of the larvae that responded to this stimulus was recorded. Swimming behavior studies were repeated at least three times.

Western Blotting Analysis

Zebrafish embryos at 48 hpf after removal of yolk sac were immersed in precooled radioimmunoprecipitation assay (RIPA) lysis buffer plus cocktail and phenylmethanesulfonyl fluoride (PMSF) for schizolysis. To know the exact concentrations of the extracted proteins, we chose a BCA Protein Kit (Beyotime Institute Biotechnology, China) with the supernatant of the RIPA lysate after dissolving the samples. After electrophoresis on SDS–PAGE, the separated proteins were transferred onto poly(vinylidene fluoride) (PVDF) membranes (Immobilon-P;

Millipore, Bedford, United States). Before incubation with the primary antibodies, the membranes were blocked with 5% skim milk for 2 h at room temperature. Anti-Kif15 (1:400 dilution, Proteintech, Shanghai, China) and anti-glyceraldehyde 3-phosphate dehydrogenase (anti-GAPDH; 1: 2000) were incubated with the membranes for a whole night at 4°C. Corresponding proteins were combined with Goat Anti-Mouse/Anti-Rabbit immunoglobulin G [IgG; (H + L)] HRP (1:2000 dilution, Abways Technology, Shanghai, China) after being incubated for 2 h. Using an ECL Kit (Millipore, United States), such protein bands could be colored and detected by an Azure C280 imager. The membranes need to be washed thoroughly with Tris-buffered saline with Tween 20 (TBST) before each incubation step. All experiments were strictly from three repeats. GAPDH served as the internal reference.

Statistical Analysis

GraphPad Prism (version, 8.0) supports whole statistical analyses. Comparisons between every two groups were demonstrated with a *t*-test (two-tailed), while multiple comparisons were illustrated using one-way ANOVA. Statistics were all displayed as mean ± standard error of the mean (SEM), with p-value < 0.05 identified as statistical significance.

RESULTS

Knockdown of Kif15 Inhibits the Normal Formation of Vestibular Apparatus

The role of Kif15 during inner ear development was investigated by the knockdown of Kif15 through the injection of Kif15 splicing MO to the zebrafish embryos at one- or two-cell stages. We used the Western blotting analysis to test the efficacy of Kif15 downregulation, and we detected a substantial transcript reduction of Kif15 in the zebrafish larvae after Kif15-MO injection compared to the controls injected with Con-MO (**Figures 1A,B**). We chose 48, 72, and 96 hpf in chronology to observe the morphology changes in the inner

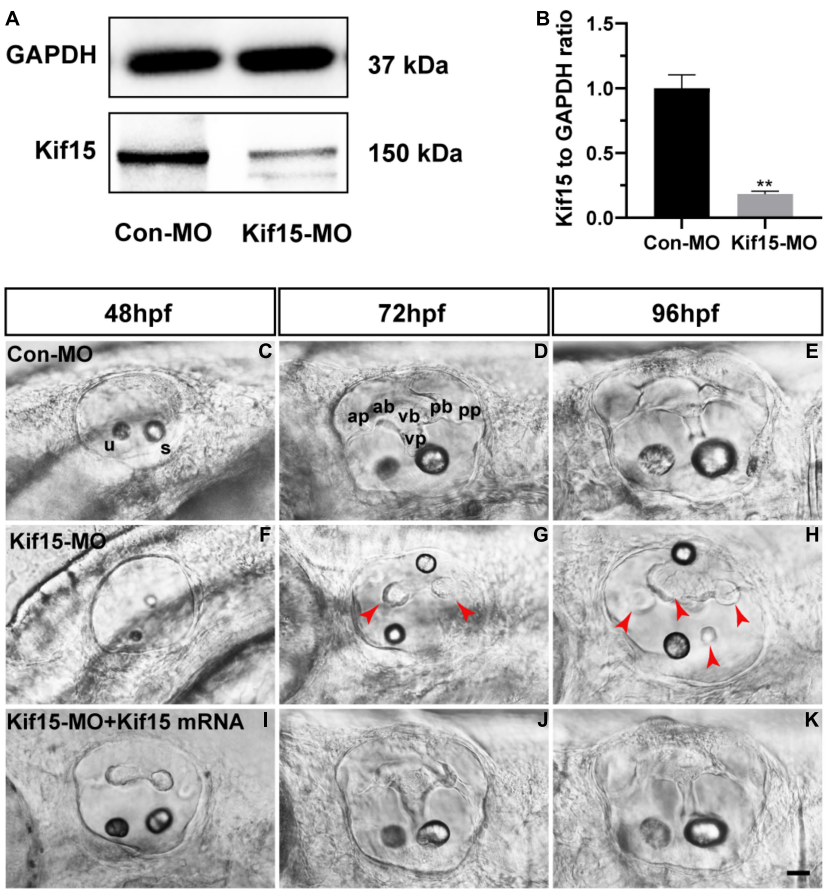

FIGURE 1 | Knockdown of Kif15 with splicing-blocking method inhibits the normal formation of vestibular. **(A,B)** The protein level of Kif15 is severely decreased in Kif15-morpholino (MO)-injected embryos both in the band intensity **(A)** and in the semiquantitative analysis **(B)**, in comparison with control embryos. Data are recorded as mean ± SEM. $^{**}p < 0.01$. **(C–H)** Kif15-MO suppresses the normal development of semicircular canals. The abnormal manifestations are observed at 48 hpf **(C,F)**, 72 hpf **(D,G)**, and 96 hpf **(E,H)**, respectively. ap, anterior protrusion; ab, anterior bulge; vb, ventral bulge; vp, ventral protrusion; pb, posterior bulge; pp, posterior protrusion; u, utricle; and s, saccule. Red arrowheads show the abnormal fusion of anterior and posterior protrusions. **(I–K)** Co-injection using Kif15-MO and Kif15 mRNA successfully rescues the phenotypes of semicircular canals and otoliths at 48 hpf **(I)**, 72 hpf **(J)**, and 96 hpf **(K)**, respectively. Scale bar is 20 μm.

ear of zebrafish after Kif15-MO injection (**Figures 1C–H**). At 72 and 96 hpf, the essential structures of three pairs of semicircular canals (i.e., anterior, posterior, and lateral) were clearly discernible as labeled in **Figure 1D**, including anterior (a-), posterior (p-), and ventral (v-) protrusions and bulges. However, the normal structures of semicircular canals disappeared and were replaced by short and fused protuberances in Kif15-MO morphants (**Figures 1F–H**). To verify the role of Kif15 on zebrafish semicircular canal development, we performed a rescue experiment by the co-injection of Kif15 mRNA together with Kif15 splicing MO, and we found a successful rescue in the phenotype of otic vesicle (**Figures 1I–K**). Our observation implied that the inhibition of Kif15 by specific MO completely ruined the normal development of semicircular canals in the inner ear of zebrafish.

Kif15 Inhibition Induces Malformed Otolith Organs in Zebrafish

The morphology of otoliths in control and Kif15-MO-injected embryos was detected with a white optical microscope in the bright field at 48 hpf (**Figures 2A–E**). Kif15 splicing MO-injected embryos exhibited various abnormalities containing increased number of otoliths (35.5%), decreased number of otoliths (4.3%), and two abnormal otoliths (15.4%) (**Figures 2B–E,G**). Among them, the two abnormal otolith deformities involved situations such as the abnormal size of two otoliths (**Figure 2C**), the abnormal arranged position of two otoliths (**Figure 2D**), and the combined disordered form. The proportion of normal otolith phenotype in the Kif15-MO group is only 44.9% in contrast to 87.5% in controls (**Figure 2G**). On the contrary, there is almost no abnormality in the number of otoliths in the Con-MO injection group (**Figure 2G**). We also detected successful rescue in the phenotype of otoliths after co-injecting Kif15 mRNA and Kif15 splicing MO compared to that in Kif15-MO morphants (**Figures 2F,G**).

Both Utricular and Saccular HCs Decreased Severely After Kif15 Knockdown

Using *Tg(brn3c:mGFP)*^{s356t} line, the HCs that insert into the otoliths were identifiable and labeled by green fluorescence, named utricular (anterior to left) and saccular (posterior to right) HCs, respectively (**Figures 3A,D,G**). After Kif15 knockdown with splicing MO, two smaller sizes of otoliths were examined, and the numbers of both utricular and saccular HCs in otic vesicles were reduced significantly compared to the controls (**Figures 3B,E,H**). However, the decreased number of HCs in both utricle and saccule after Kif15 knocking down could be completely rescued by co-injection with Kif15 mRNA (**Figures 3C,F,I**). The quantitative analysis further showed that the number of utricular HCs in Kif15 morphants was significantly decreased at 48 hpf compared to that in Con-MO-injected larvae, while a remarkably increased number of utricular HCs were found in Kif15-MO + Kif15 mRNA group (**Figure 3J**). Similarly,

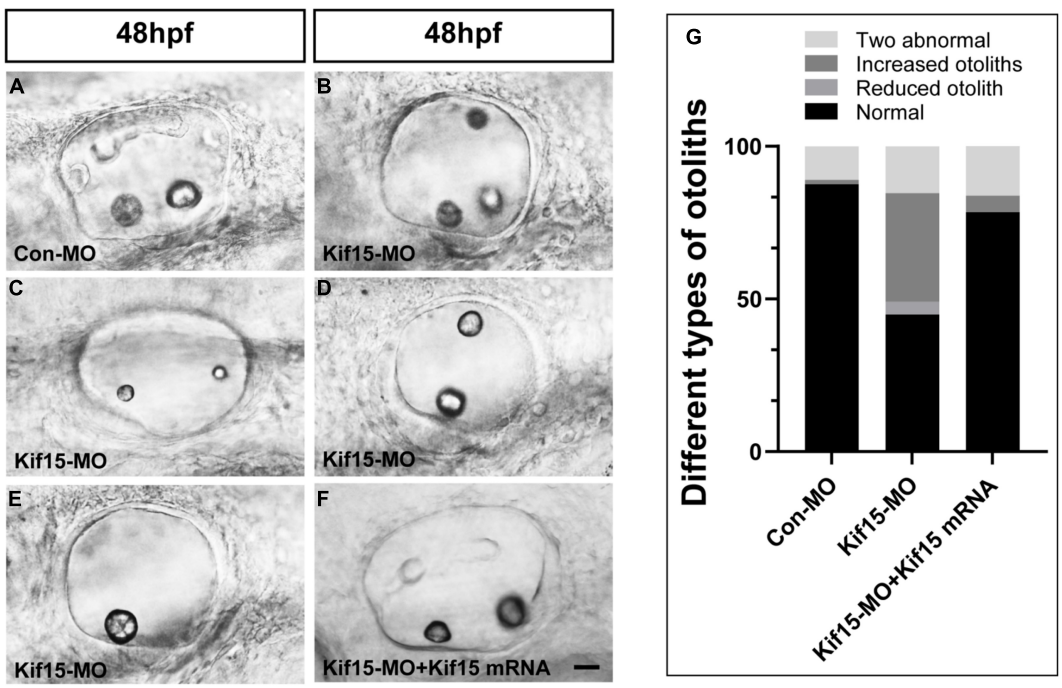

FIGURE 2 | Knockdown of Kif15 disturbs the normal development of otolith organs. **(A–E)** Kif15 inhibition causes abnormal phenotypes of otoliths, including multiplication **(B)** and reduction **(E)** in number, and two abnormal otoliths **(C,D)** at 48 hpf. **(F)** Co-injection Kif15 mRNA with Kif15-MO successfully rescues the phenotypes of otolith organs at 48 hpf. **(G)** Different types of abnormal otoliths and the corresponding proportion analysis in Kif15-MO-injected embryos (n = 234), untreated controls (n = 136), and Kif15-MO + Kif15 mRNA group (n = 111). Scale bar is 20 μm.

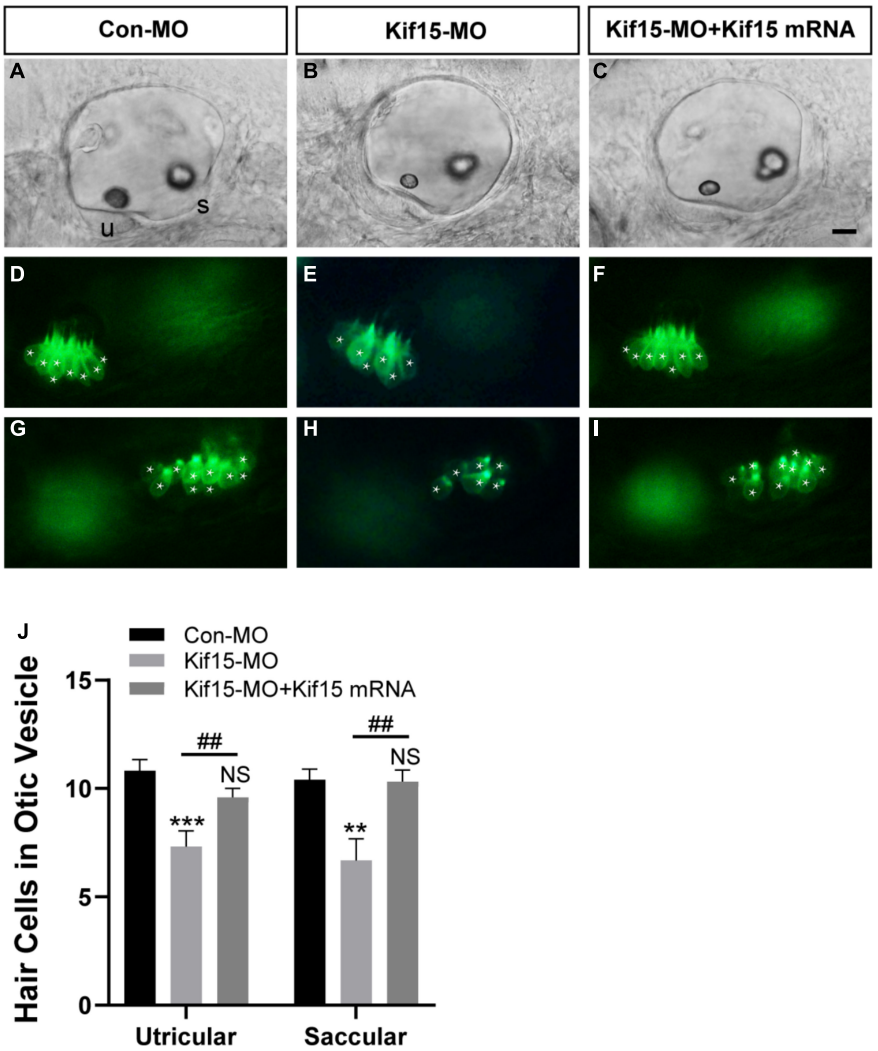

FIGURE 3 | Kif15 inhibition results in decreased hair cells (HCs) in the inner ear. **(A–C)** The gross morphology of otic vesicle in different groups at 48 hpf using the white light field microscope. u, utricle; s, saccule. Scale bar is 20 μm. **(D–F)** Representative images of utricular HCs in different groups at 48 hpf. **(G–I)** Representative images of saccular HCs in different groups at 48 hpf. White star labels the HC. **(J)** Quantification of the number of HCs in utricle and saccule in control-MO (Con-MO) group (n = 22), Kif15-deficient morphants (n = 22), and Kif15-MO + Kif15 mRNA group. Data are recorded as mean ± SEM. $^{**}p < 0.01$, $^{***}p < 0.001$ vs. Con-MO group; $^{\#\#}p < 0.01$ vs. Kif15-MO group; NS, no significance.

HCs in saccule also severely reduced in Kif15-MO-injected morphants but markedly increased in Kif15-MO + Kif15 mRNA co-injected embryos (**Figure 3J**).

Kif15-MO Leads to Decreased Number of Neuromasts in Posterior Lateral Line System of Zebrafish

Then, the function of Kif15 during the development of the PLL system was investigated. The transgenic zebrafish *Tg(cldnb:lynGFP)*^{zf106} was used to visualize NMs in green fluorescence (Haas and Gilmour, 2006). The NMs manifested in severely reduced number and disordered arrangement along the trunk of zebrafish after Kif15-MO injection at 48 hpf, a time point when PLL primordium finishes migration (**Figures 4A–C**). Co-injecting Kif15 mRNA and splicing MO notably increased the number of NMs in comparison with that in Kif15-MO morphants (**Figure 4D**). The quantitative analysis showed that the number of PLL NMs in Kif15 morphants was significantly decreased compared to that displayed in Con-MO-injected larvae at 48 hpf (**Figure 4E**). The number of PLL NMs in the Kif15-MO + Kif15 mRNA group was remarkably larger than that in Kif15-MO morphants but a little smaller than that in Con-MO embryos, indicating a successful but not complete rescue in the number of NMs by Kif15 mRNA (**Figure 4E**). The diagrammatic sketch demonstrating changes in the number and arrangement of NMs along the trunk and tail of zebrafish was presented after injection with Kif15-MO (**Figure 4F**). The result provided substantial evidence that Kif15 is critical to zebrafish in auditory system development.

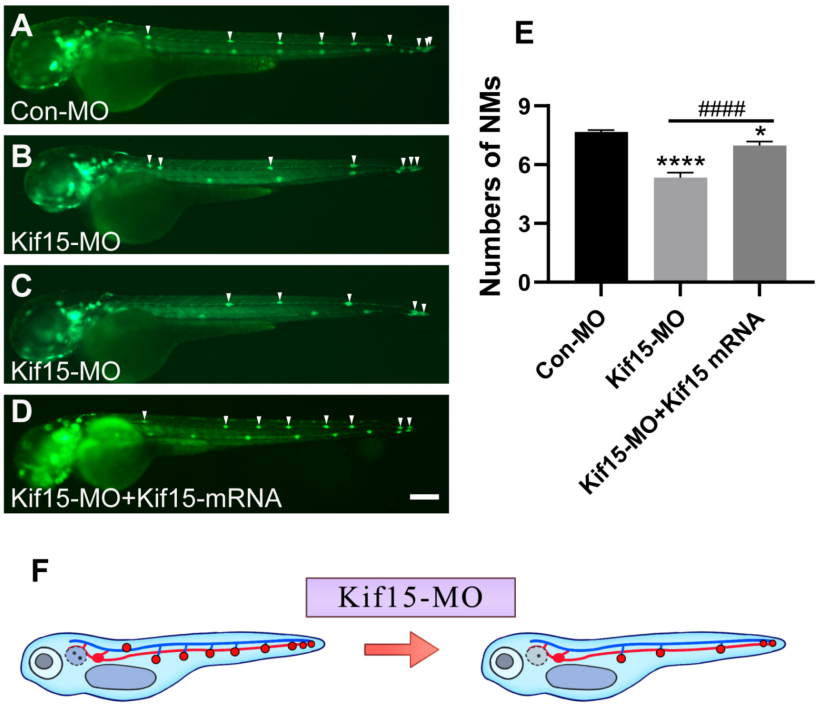

FIGURE 4 | Kif15 knocking down leads to abnormal posterior lateral line (PLL) development, which is represented by a decrease in the number of neuromasts (NMs). **(A–D)** Kif15 inhibition induces the reduction of NMs in zebrafish PLL, while co-injection of Kif15 mRNA with Kif15-MO successfully rescues the decreased number of NMs compared to the Con-MO-treated controls. The PLL NMs are indicated by white arrowheads. Scale bar is 200 μm. **(E)** Statistical analysis in quantification of PLL NMs in Con-MO-injected controls, Kif15-MO-injected embryos, and Kif15-MO + Kif15 mRNA group (n = 50 in the three groups). Data are recorded as mean ± SEM. $^{*}p < 0.05$, $^{****}p < 0.0001$ vs. Con-MO group; $^{\#\#\#\#}p < 0.0001$ vs. Kif15-MO group. **(F)** Simple and intuitive schematic diagram of changes in PLL development after Kif15 knockdown by MO.

Kif15 Transcript Knockdown Disrupts the Normal Locomotor Activity of Zebrafish

According to the brief review of the literature in the background that sensory organs of zebrafish including otoliths, semicircular canals, and PLL NMs can detect sound and water movement stimuli and move in directionality, we wondered if the locomotor behavior of zebrafish was disturbed in Kif15-MO embryos. The locomotion assay was conducted to detect the locomotor behavior of zebrafish after Kif15 inhibition with splicing MO since behavioral change is a comprehensive indicator to show the impact of environmental factors on the organisms. The locomotor traces were recorded during the light-dark photoperiod stimulation with a 20-s interstimulus interval, and we detected a severe reduction in locomotor traces compared to that in the controls (**Figure 5A**). However, a significant increase in locomotor traces was found after performing the rescue experiment with co-injected Kif15 mRNA compared to that in Kif15-MO morphants (**Figure 5A**). Data analysis on the distance moved from the original point in different groups showed that the Kif15-MO injection caused a significant reduction in the distance of locomotion in comparison with the parallel controls. There was also a significant difference in distance of movement between Kif15-MO + Kif15 mRNA and Con-MO groups, indicating a partial rescue effect of Kif15 mRNA in the locomotor behavior (**Figure 5B**). The results were indicative that behavioral dysfunction also existed in addition to morphological deformity after Kif15 inhibition.

DISCUSSION

Kif15 has been previously reported to be widely involved in the progression of several malignancies, such as hepatocellular carcinoma (HCC), and gastric, breast, colorectal, and prostate cancer by regulating cell cycle, migration, and invasion (Li et al., 2020; Zeng et al., 2020; Qureshi et al., 2021). The previous study detected high expression of Kinesin-12 (Kif15) in the otic vesicle of zebrafish (Xu et al., 2014), indicating a potential role of Kif15 in the embryonic development of the inner ear. However, to our knowledge, there are no reports considering the effect of Kif15 on the auditory system. In this study, we first explored the role of Kif15 in the developing hearing organ of zebrafish using the knocking down strategy by Kif15-MO injection.

An MO knockdown approach is a popular tool in studying the function of objective genes (Moulton and Yan, 2008; Stainier et al., 2017); however, the known off-target effect by MOs limits the application of MO to some extent (Gerety and Wilkinson, 2011). In this study, we chose splicing-blocking MO for Kif15 knockdown, and the efficacy of Kif15 inhibition in transcript level was examined by the Western blotting experiment

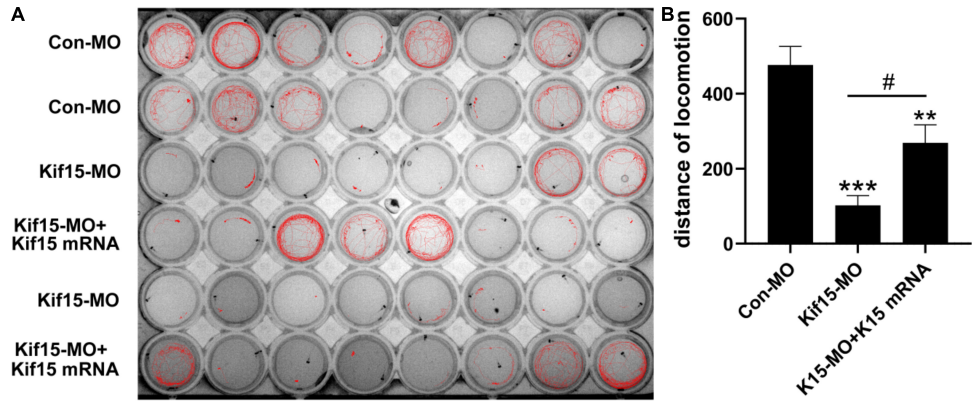

FIGURE 5 | The activity and behavior of zebrafish are abnormal after knocking down Kif15. **(A)** The locomotion assay of zebrafish in Con-MO (n = 32), Kif15-MO (n = 31), and Kif15-MO + Kif15 mRNA (n = 30) injected larvae in traced locomotion curve. **(B)** The moved distance from the original point is analyzed and compared among different groups. The unit of the Y-axis is mm. Data are recorded as mean ± SEM. **p < 0.01, ***p < 0.001 vs. Con-MO group; $^{\#}p$ < 0.05 vs. Kif15-MO group.

with anti-Kif15 antibody. We found that the formations of otolith organs, semicircular canals, and PLL NMs were all remarkably deformed in the structure after the inhibition of Kif15. Besides, the further rescue experiments with Kif15 mRNA demonstrated successful rescue of the phenotypical deformities caused by Kif15-MO. To confirm our findings by Kif15 splicing MO, we performed an experiment using the translation-blocking MO strategy for Kif15. As shown in **Supplementary Figure 1**, the expression of Kif15 was significantly decreased in Kif15 translation MO morphants compared to the Con-MO group (**Supplementary Figures 1A,B**). Additionally, malformed otoliths and semicircular canals, together with the reduced number of PLL NMs, were also found in Kif15 translation MO morphants (**Supplementary Figures 1C,D**), which were consistent with the findings in Kif15 splicing MO morphants. Therefore, our findings uncovered that Kif15 is essential in the maintenance of the normal structures and functions of auditory organs of zebrafish, and Kif15-MO with splicing- and translation-blocking strategy was potent for the regulation of Kif15.

As previously reported, the knockdown of Kif15 inhibits cell proliferation, promotes cell apoptosis, and causes cell cycle arrest in glioma cells (Wang et al., 2020). Another study reveals that the inhibition of Kif15 in human HCC xenograft models delays the invasive and proliferative ability of tumors *via* increasing intracellular reactive oxygen species (ROS) levels (Li et al., 2020). In this study, Kif15-MO induced remarkable inhibition of the HC differentiation in both utricle and saccule. Since the proliferative behavior is active in the early development of zebrafish inner ear and lateral line system, we speculated that the reduced number of NMs in PLL and decreased HCs in otic vesicle might be related to the suppression of cell proliferation or increased apoptosis by Kif15 knockdown. Moreover, we detected abnormal locomotion in the Kif15-MO morphants, and the reduced locomotor distance could be partially rescued by co-injection with Kif15 mRNA, indicating a potential role of Kif15 in zebrafish mechanosensory organ function. However, Kif15 is also known to influence neuronal development so it is possible that these defects are simply locomotor defects unrelated to the response to the vibrational stimulus (Xu et al., 2014; Dong et al., 2019). Therefore, in future study, we will use alternative approaches such as prepulse assay to test if abnormal locomotion by Kif15 knockdown is due to ear defects. Altogether, we explored that Kif15 plays an important role during the development of the auditory and vestibular system of zebrafish.

DATA AVAILABILITY STATEMENT

The original contributions presented in the study are included in the article/**Supplementary Material**, further inquiries can be directed to the corresponding author/s.

ETHICS STATEMENT

The animal study was reviewed and approved by The Institutional Animal Care and Use Committee of Fudan University approved all the animal experiments.

AUTHOR CONTRIBUTIONS

YH, DL, and SL: conceptualization, methodology, writing—review and editing, and project administration. SZ, DT, CL, XW, NZ, RY, CWu, HX, JM, and CWa: methodology and formal analysis. SZ, DT, and XW: validation, investigation, and formal analysis. All authors read and approved the final manuscript.

FUNDING

This study was supported by grants from the National Natural Science Foundation of China (Nos. 82071045, 81870728, and 81800912) and the Shanghai Rising-Star Program (19QA1401800).

SUPPLEMENTARY MATERIAL

The Supplementary Material for this article can be found online at: https://www.frontiersin.org/articles/10.3389/fnmol.2022.844568/full#supplementary-material

Supplementary Figure 1 | Knockdown of Kif15 with the translation-blocking method inhibits the normal development of zebrafish. **(A,B)** The protein level of Kif15 is severely decreased in Kif15-MO (translation-blocking)-injected embryos both in the band intensity **(A)** and in the semiquantitative analysis **(B)**, compared to the control embryos. Data are recorded as mean ± SEM. $^{***}p < 0.001$. **(C)** Kif15-MO (translation-blocking) disturbs the normal development of otic vesicles. The abnormal manifestations in both otolith organs and semicircular canals are observed at 48, 72, and 96 hpf, respectively. Scale bar is 20 μm. **(D)** A reduced number of NMs in zebrafish PLL is detected in Kif15 morphants (translation-blocking). Scale bar is 200 μm, $n = 10$.

REFERENCES

Blanco-Sánchez, B., Clément, A., Phillips, J. B., and Westerfield, M. (2017). Zebrafish models of human eye and inner ear diseases. *Methods Cell. Biol.* 138, 415–467. doi: 10.1016/bs.mcb.2016.10.006

Dong, Z., Wu, S., Zhu, C., Wang, X., Li, Y., Chen, X., et al. (2019). Clustered Regularly Interspaced Short Palindromic Repeats (CRISPR)/Cas9-mediated kif15 mutations accelerate axonal outgrowth during neuronal development and regeneration in zebrafish. *Traffic* 20, 71–81. doi: 10.1111/tra.12621

Gao, L., Zhang, W., Zhang, J., Liu, J., Sun, F., Liu, H., et al. (2020a). KIF15-mediated stabilization of AR and AR-V7 contributes to enzalutamide resistance in prostate cancer. *Cancer Res*. 81, 1026-1039

Gao, X., Zhu, L., Lu, X., Wang, Y., Li, R., and Jiang, G. (2020b). KIF15 contributes to cell proliferation and migration in breast cancer. *Hum Cell* 33, 1218–1228. doi: 10.1007/s13577-020-00392-0

Geng, F. S., Abbas, L., Baxendale, S., Holdsworth, C. J., Swanson, A. G., Slanchev, K., et al. (2013). Semicircular canal morphogenesis in the zebrafish inner ear requires the function of gpr126 (lauscher), an adhesion class G protein-coupled receptor gene. *Development* 140, 4362–4374. doi: 10.1242/dev.098061

Gerety, S. S., and Wilkinson, D. G. (2011). Morpholino artifacts provide pitfalls and reveal a novel role for pro-apoptotic genes in hindbrain boundary development. *Dev. Biol.* 350, 279–289. doi: 10.1016/j.ydbio.2010.11.030

Haas, P., and Gilmour, D. (2006). Chemokine signaling mediates self-organizing tissue migration in the zebrafish lateral line. *Dev. Cell.* 10, 673–680. doi: 10.1016/j.devcel.2006.02.019

He, Y., Bao, B., and Li, H. (2017). Using zebrafish as a model to study the role of epigenetics in hearing loss. *Expert Opin. Drug Discov.* 12, 967–975. doi: 10.1080/17460441.2017.1340270

Kalka, M., Markiewicz, N., Ptak, M., Sone, E. D., Ożyhar, A., Dobryszycki, P., et al. (2019). *In vivo* and *in vitro* analysis of starmaker activity in zebrafish otolith biomineralization. *FASEB J.* 33, 6877–6886. doi: 10.1096/fj.201802268R

Kimmel, C. B., Ballard, W. W., Kimmel, S. R., Ullmann, B., and Schilling, T. F. (1995). Stages of embryonic development of the zebrafish. *Dev. Dyn.* 203, 253–310. doi: 10.1002/aja.1002030302

Kitagawa, A., Masuda, T., Takahashi, J., Tobo, T., Noda, M., Kuroda, Y., et al. (2020). KIF15 Expression in Tumor-associated Monocytes Is a Prognostic Biomarker in Hepatocellular Carcinoma. *Cancer Genomics Proteomics* 17, 141–149. doi: 10.21873/cgp.20174

Li, Q., Qiu, J., Yang, H., Sun, G., Hu, Y., Zhu, D., et al. (2020). Kinesin family member 15 promotes cancer stem cell phenotype and malignancy via reactive oxygen species imbalance in hepatocellular carcinoma. *Cancer Lett.* 482, 112–125. doi: 10.1016/j.canlet.2019.11.008

Liu, M., Nadar, V. C., Kozielski, F., Kozlowska, M., Yu, W., and Baas, P. W. (2010). Kinesin-12, a mitotic microtubule-associated motor protein, impacts axonal growth, navigation, and branching. *J. Neurosci.* 30, 14896–14906. doi: 10.1523/JNEUROSCI.3739-10.2010

Lundberg, Y. W., Xu, Y., Thiessen, K. D., and Kramer, K. L. (2015). Mechanisms of otoconia and otolith development. *Dev. Dyn.* 244, 239–253.

Ma, D. D., Wang, D. H., and Yang, W. X. (2017). Kinesins in spermatogenesis. *Biol. Reprod.* 96, 267–276. doi: 10.1095/biolreprod.116.144113

Ma, Y., Zhan, S., Lu, H., Wang, R., Xu, Y., Zhang, G., et al. (2020). B7-H3 regulates KIF15-activated ERK1/2 pathway and contributes to radioresistance in colorectal cancer. *Cell Death Dis.* 11, 824. doi: 10.1038/s41419-020-03041-4

Malaby, H. L. H., Dumas, M. E., Ohi, R., and Stumpff, J. (2019). Kinesin-binding protein ensures accurate chromosome segregation by buffering KIF18A and KIF15. *J. Cell Biol.* 218, 1218–1234. doi: 10.1083/jcb.201806195

Milic, B., Chakraborty, A., Han, K., Bassik, M. C., and Block, S. M. (2018). KIF15 nanomechanics and kinesin inhibitors, with implications for cancer chemotherapeutics. *Proc. Natl. Acad. Sci.U.S.A.* 115, E4613–E4622. doi: 10.1073/pnas.1801242115

Moulton, J. D., and Yan, Y.-L. (2008). Using Morpholinos to control gene expression. *Curr. Proto. Mol. Biol.* 26, 2681–2626. doi: 10.1002/0471142727.mb2608s83

Nicolson, T. (2017). The genetics of hair-cell function in zebrafish. *J. Neurogenet.* 31, 102–112. doi: 10.1080/01677063.2017.1342246

Qureshi, Z., Ahmad, M., Yang, W. X., and Tan, F. Q. (2021). Kinesin 12 (KIF15) contributes to the development and tumorigenicity of prostate cancer. *Biochem. Biophys. Res. Commun.* 576, 7–14. doi: 10.1016/j.bbrc.2021.08.072

Stainier, D. Y. R., Raz, E., Lawson, N. D., Ekker, S. C., Burdine, R. D., Eisen, J. S., et al. (2017). Guidelines for morpholino use in zebrafish. *PLoS. Genet.* 13:e1007000. doi: 10.1371/journal.pgen.1007000

Sturgill, E. G., and Ohi, R. (2013). Kinesin-12 differentially affects spindle assembly depending on its microtubule substrate. *Curr. Biol.* 23, 1280–1290. doi: 10.1016/j.cub.2013.05.043

Tanenbaum, M. E., Macùrek, L., Janssen, A., Geers, E. F., Alvarez-Fernández, M., and Medema, R. H. (2009). Kif15 cooperates with eg5 to promote bipolar spindle assembly. *Curr. Biol.* 19, 1703–1711. doi: 10.1016/j.cub.2009.08.027

Tang, D., He, Y., Li, W., and Li, H. (2019). Wnt/β-catenin interacts with the FGF pathway to promote proliferation and regenerative cell proliferation in the zebrafish lateral line neuromast. *Exp. Mol. Med.* 51, 1–16. doi: 10.1038/s12276-019-0247-x

Tang, D., Lu, Y., Zuo, N., Yan, R., Wu, C., Wu, L., et al. (2021). The H3K27 demethylase controls the lateral line embryogenesis of zebrafish. *Cell Biol. Toxicol.*[Online ahead of print].doi: 10.1007/s10565-021-09669-y

Wang, Q., Han, B., Huang, W., Qi, C., and Liu, F. (2020). Identification of KIF15 as a potential therapeutic target and prognostic factor for glioma. *Oncol. Rep.* 43, 1035–1044. doi: 10.3892/or.2020.7510

Whitfield, T. T., Riley, B. B., Chiang, M. Y., and Phillips, B. (2002). Development of the zebrafish inner ear. *Dev. Dyn.* 223, 427–458. doi: 10.1002/dvdy.10073

Xu, M., Liu, D., Dong, Z., Wang, X., Wang, X., Liu, Y., et al. (2014). Kinesin-12 influences axonal growth during zebrafish neural development. *Cytoskeleton* 71, 555–563. doi: 10.1002/cm.21193

Yu, X., He, X., Heindl, L. M., Song, X., Fan, J., and Jia, R. (2019). KIF15 plays a role in promoting the tumorigenicity of melanoma. *Exp. Eye Res.* 185:107598. doi: 10.1016/j.exer.2019.02.014

Zeng, H., Li, T., Zhai, D., Bi, J., Kuang, X., Lu, S., et al. (2020). ZNF367-induced transcriptional activation of KIF15 accelerates the progression of breast cancer. *Int. J. Biol. Sci.* 16, 2084–2093. doi: 10.7150/ijbs.44204

Conflict of Interest: The authors declare that the research was conducted in the absence of any commercial or financial relationships that could be construed as a potential conflict of interest.

Publisher's Note: All claims expressed in this article are solely those of the authors and do not necessarily represent those of their affiliated organizations, or those of the publisher, the editors and the reviewers. Any product that may be evaluated in this article, or claim that may be made by its manufacturer, is not guaranteed or endorsed by the publisher.

frontiers in Molecular Neuroscience

ORIGINAL RESEARCH
published: 22 March 2022
doi: 10.3389/fnmol.2022.842132

The Acute Effects of Furosemide on Na-K-Cl Cotransporter-1, Fetuin-A and Pigment Epithelium-Derived Factor in the Guinea Pig Cochlea

Jesper Edvardsson Rasmussen, Patrik Lundström, Per Olof Eriksson, Helge Rask-Andersen, Wei Liu† and Göran Laurell†*

Otorhinolaryngology and Head and Neck Surgery, Department of Surgical Sciences, Uppsala University, Uppsala, Sweden

OPEN ACCESS

Edited by:
Pranav Mathur, Otonomy Inc., United States

Reviewed by:
Jeremy Duncan, Western Michigan University, United States
Agnieszka J. Szczepek, Charité Universitätsmedizin Berlin, Germany
Phillip Uribe, Otonomy Inc., United States

***Correspondence:**
Jesper Edvardsson Rasmussen
jesper.rasmussen@surgsci.uu.se

† These authors share senior authorship

Specialty section:
This article was submitted to Molecular Signalling and Pathways, a section of the journal Frontiers in Molecular Neuroscience

Received: *23 December 2021*
Accepted: *22 February 2022*
Published: *22 March 2022*

Citation:
Edvardsson Rasmussen J, Lundström P, Eriksson PO, Rask-Andersen H, Liu W and Laurell G (2022) The Acute Effects of Furosemide on Na-K-Cl Cotransporter-1, Fetuin-A and Pigment Epithelium-Derived Factor in the Guinea Pig Cochlea. Front. Mol. Neurosci. 15:842132. doi: 10.3389/fnmol.2022.842132

Background: Furosemide is a loop diuretic used to treat edema; however, it also targets the Na-K-Cl cotransporter-1 (NKCC1) in the inner ear. In very high doses, furosemide abolishes the endocochlear potential (EP). The aim of the study was to gain a deeper understanding of the temporal course of the acute effects of furosemide in the inner ear, including the protein localization of Fetuin-A and PEDF in guinea pig cochleae.

Material and Method: Adult guinea pigs were given an intravenous injection of furosemide in a dose of 100 mg per kg of body weight. The cochleae were studied using immunohistochemistry in controls and at four intervals: 3 min, 30 min, 60 min and 120 min. Also, cochleae of untreated guinea pigs were tested for Fetuin-A and PEDF mRNA using RNAscope® technology.

Results: At 3 min, NKCC1 staining was abolished in the type II fibrocytes in the spiral ligament, followed by a recovery period of up to 120 min. In the stria vascularis, the lowest staining intensity of NKCC1 presented after 30 min. The spiral ganglion showed a stable staining intensity for the full 120 min. Fetuin-A protein and mRNA were detected in the spiral ganglion type I neurons, inner and outer hair cells, pillar cells, Deiters cells and the stria vascularis. Furosemide induced an increased staining intensity of Fetuin-A at 120 min. PEDF protein and mRNA were found in the spiral ganglia type I neurons, the stria vascularis, and in type I and type II fibrocytes of the spiral ligament. PEDF protein staining intensity was high in the pillar cells in the organ of Corti. Furosemide induced an increased staining intensity of PEDF in type I neurons and pillar cells after 120 min.

Conclusion: The results indicate rapid furosemide-induced changes of NKCC1 in the type II fibrocytes. This could be part of the mechanism that causes reduction of the EP within minutes after high dose furosemide injection. Fetuin-A and PEDF are present in many cells of the cochlea and probably increase after furosemide exposure, possibly as an otoprotective response.

Keywords: furosemide (frusemide), NKCC1 = Na^+-K^+-$2Cl^-$ cotransporter, type II fibrocyte, fetuin-A, PEDF, stria vascularis, organ of corti (OoC), spiral ganglion neurons

INTRODUCTION

Furosemide is a loopdiuretic widely used in the treatment of edema in patients with congestive heart failure, liver failure, or kidney disease. It has an ototoxic effect if used in high doses (Schwartz et al., 1970; Santos and Nadol, 2017; Robertson et al., 2019). Loopdiuretics cause diuresis and lower blood pressure by inhibiting Na^+-K^+-$2Cl^-$ cotransporters 1 and 2 (NKCC1, NKCC2) in the loop of Henle in the kidney, thus increasing the loss of Na^+, K^+, and water in the urine. NKCC1 is expressed in many tissues in the body and is also present in the inner ear (Crouch et al., 1997), while NKCC2 is kidney-specific (Delpire and Gagnon, 2018). In the inner ear, furosemide is reported to inhibit NKCC1 in the stria vascularis (Shindo et al., 1992).

Due to the greatly increased risk of synergistic damage to the cochlea, furosemide is not suitable for use with other ototoxic drugs such as aminoglycosides and cisplatin (Laurell and Engström, 1989; Alam et al., 1998; Hirose and Sato, 2011; Li et al., 2011). Furosemide reduces the endocochlear DC potential (EP) generated in the stria vascularis (Kusakari et al., 1978; Asakuma and Snow, 1980; Sewell, 1984). EP is the driving force that allows K^+ to swiftly enter the hair cells in response to sound stimulus (Tasaki and Spyropoulos, 1959) initiating the first step of otoacoustic neurotransmission. The prolonged treatment of experimental animals with furosemide induces edema and intercellular vacuoles in the marginal cells of the stria vascularis and eventually hair cell loss in the organ of Corti (Forge, 1976; Pike and Bosher, 1980; Forge and Brown, 1982; Rarey and Ross, 1982; Naito and Watanabe, 1997). Postmortem studies have reported similar changes in the human cochlea (Arnold et al., 1981; Santos and Nadol, 2017). EP decreases in experimental animals within a few min of a high dose of furosemide, and recovers almost completely after 120 min (Kusakari et al., 1978; Asakuma and Snow, 1980; Sewell, 1984). The morphological changes in the stria vascularis induced by furosemide are observed much later. The exact mechanism behind the initial rapid EP loss is not known. Vasoconstriction and anoxia have been proposed as mechanisms involved in the initial loss of EP in experiments using another loop diuretic (Ding et al., 2002, 2016).

Fetuin-A, also known as alpha-2-HS-glycoprotein (*AHSG*), is a protein belonging to the cystatin super family synthesized in the liver and adipose tissue. Its best-known functions are the regulation of bone mineralization and protection against extra osseous calcium phosphate deposits by binding calcium phosphates (Jahnen-Dechent et al., 1997). Fetuin-A also plays a part in the anti-acute phase response (Lebreton et al., 1979; Wang and Sama, 2012), plaque formation in arteriosclerosis (Westenfeld et al., 2009; Trepanowski et al., 2015) and insulin resistance (Trepanowski et al., 2015).

Pigment epithelium-derived factor (PEDF), also known as Serpin-F1 (*SERPINF1*), is a neuroprotective, neurotrophic, and anti-angiogenetic protein first identified in the retinal pigment epithelia (Tombran-Tink et al., 1991). It is also reported to have regulating functions in osteogenesis, to promote stem cell renewal and inhibit tumor angiogenesis (Brook et al., 2020). PEDF has been identified in the stria vascularis, spiral ganglion, neurons, and basilar membrane in the rat inner ear (Gleich and Piña, 2008).

We previously reported that Fetuin-A and PEDF are part of the human perilymph (Edvardsson Rasmussen et al., 2018) and the endolymphatic sac endolymph proteome (Ölander et al., 2021). It is not known whether Fetuin-A is expressed in any cells of the inner ear or if it only appears extracellularly in the perilymph and endolymph.

The aim of the study was to gain a deeper understanding of the temporal course of the acute effects of furosemide in the inner ear, including the protein localization of Fetuin-A and PEDF in guinea pig cochleae.

MATERIAL AND METHODS

Experimental Design

Using a guinea pig animal model, protein localization and staining intensity in the cochlea was studied after an intravenous (IV) injection of 100 mg/kg body weight of furosemide. This dose is previously known to abolish the EP (Kusakari et al., 1978). The following intervals were used: 3 min, 30 min, 60 min and 120 min. Three guinea pigs were used for each interval and as controls. The guinea pigs were anesthetized, intravenously injected with furosemide and then decapitated at the desired point in time. The cochleae were quickly dissected from the temporal bone and fixated. The cochleae were cryosectioned, stained using the immunofluorescence technique and photographed with a confocal microscope. Sections from three guinea pigs without furosemide exposure were also examined using RNAscope® technology. Image analysis densitometry was performed in ImageJ to semi-quantify the protein staining intensity.

Animals

Adult (age 6–9 weeks) albino guinea pigs of both sexes (body weight 262–310 g) were used in the experiment, 15 guinea pigs for immunohistochemistry and three for RNAscope examination. The animals were housed in an enriched environment with 12/12-h day and night cycle and a temperature of 21°C and 60% humidity. They had free access to food and water. All animal procedures were performed in accordance with local ethical guidelines at Uppsala University and national legislation and regulation concerning the care and use of laboratory animals.

Furosemide Administration

The animals were deeply anesthetized using ketamine (40 mg/kg, intramuscularly; Pfizer AB, Sweden) and xylazine (10 mg/kg, intramuscularly; Bayer, Denmark). Ophthalmic ointment was applied to the eyes to prevent corneal ulceration. The animals were given a local anesthetic by subcutaneous injection of bupivacaine hydrochloride (2.5 mg/ml) before exposure of the internal jugular vein, which was used for the IV injection. In total 12 guinea pigs were injected with 100 mg/kg of furosemide IV and were sacrificed by decapitation at four different intervals. Three control animals received the same anesthesia but were not given the furosemide injection.

Sample Preparation

After decapitation, the temporal bone was removed and the bulla opened to expose the cochlea. Small fenestrations were performed in the apex and the round window (RW) within minutes and the cochlea was gently flushed with a 4% formaldehyde solution stabilized with phosphate buffer. The cochlea was immersed in 4% formaldehyde for 24 h and then in 0.5% formaldehyde until decalcification in 0.1 M Na-ethylenediaminetetraacetic acid (EDTA). After decalcification the cochlea was rinsed and placed in a 15% sucrose solution for 24 h followed by a gradual infiltration of 15% sucrose and Tissue-Tek Optimal Cutting Temperature (OCT) Cryomount (Histolab, Sweden) for 4 days. Finalized by infusion of pure OCT overnight, after which the cochlea was embedded in OCT. The cochlea was cryosectioned with a microtome into 8 μm thick sections throughout the cochlea and mounted on Super Frost Plus slides (Menzel-Gläser, Braunschweig, Germany), and stored in a freezer at −70°C prior to immunohistochemistry (IHC) preparation.

Immunohistochemistry

Cochlear sections were stained according to the following protocol. Sections were rinsed three times in a glass slide staining jar with 0.01 M Phosphate Buffer Saline (PBS) with pH7.4 (Medicago) for 5 min (3 × 5 min). They were then incubated in 0.4% triton X-100 diluted in PBS at room temperature (RT) for 30 min and rinsed in PBS (3 × 5 min). The sections were incubated with primary antibodies diluted in 2% bovine serum albumin (BSA) in a humidified atmosphere at 4°C for 20 h. A negative control section was at the same time incubated with 2% BSA without primary antibody (Burry, 2011). Surplus primary antibody solution was carefully removed, and the slides were rinsed with PBS (3 × 5 min). All the sections, including negative control, were incubated with secondary antibody conjugated to Alexa Fluor 405, 488, 555, and 670 (Thermo Fisher Scientific, Sweden) for 2 h under RT. Slides were rinsed with PBS (3 × 5 min). Counterstaining was performed with the nuclear dye DAPI (4',6-diamidino-2-phenylindole dihydrochloride) for 5–7 min at RT, after which slides were rinsed with PBS (3 × 5 min). Mounting was done with ProLong® Gold or ProLong® Glass Antifading Mountant and cover slipped with the specified cover glass (0.17 ± 0.005 mm) for optically matching confocal and super-resolution (SIM) microscopes. At least one representative section from each animal was selected for analysis of immunohistochemistry after all the confocal images were assessed. Images from basal or mid turn were selected since the protein localization and intensity were uniform in between the turns. Antibodies used for immunohistochemistry are listed in **Table 1**.

RNAscope Protocol

RNA *in situ* hybridization (ISH) trials were performed using RNAscope®. The frozen fixed (4% paraformaldehyde) cochlear tissue sections were prepared according to the manufacturer's instructions with the RNAscope® Reagent Kit (Bio-Techne, Minneapolis, USA) (kit version 2). Sections were briefly pretreated with H_2O_2 (10 min, RT) and protease III (30 min, 40°C). After protease III incubation, the sections were subjected to RNAscope hybridization assay. The paired double-Z oligonucleotide probes were designed and produced by Bio-Techne based on the targets' gene ID. To start the hybridization, the RNA probe fluid was added to the slide with sections. Incubation continued in a HybEZ™ Oven (Bio-Techne) for 2 h at 40°C. After hybridization incubation, the slides were washed using 1× RNAscope® Wash Buffer. Sections were then incubated with RNAscope® Multiplex FL v2 Amp 1, Amp 2, and Amp 3 (for 30, 30, and 15 min respectively) sequentially at 40°C to amplify the signal. For signal development, RNAscope® Multiplex FL v2 hP-C1, HRP-C2 and HRP-C3 were added to the sections sequentially (incubation time 15 min each). For detecting signals, TSA-diluted Opal™ 520, 570, and 690 fluorophores were added to sections after HRP-C1, C2, and C3, incubating the sections for 30 min at 40°C for each HRP-fluorophore pare. Each of the three fluorophore incubations was followed by washing with 1× RNAscope® Wash Buffer. Multiplex FL v2 hP blocker, specific for each channel, was added and incubated in the oven at 40°C for 15 min. Finally, the sections were counterstained with DAPI and the slides cover slipped with ProLong® Glass Antifade Mountant (Thermo Fisher Scientific). RNAscope ISH produces puncta of signal that represent a single mRNA transcript (Grabinski et al., 2015).

A DapB probe was used for negative control. DapB is only present in a very rare strain of soil bacteria and should not produce any signal in the tissue, hence it's utility as a negative control. Our RNAscope negative control result was consistent with the RNAscope technical protocol. The probes used for RNAscope are listed in **Table 2**.

Imaging and Photography

Confocal laser scanning microscopy was performed using a Nikon TE2000 inverted fluorescence microscope equipped with a three-channel laser emission system with three emission spectra filters (maxima 358, 461, and 555 nm). Confocal images were acquired using a Nikon EZ-C1 (ver. 3.80) software, with all

TABLE 1 | Immunohistochemistry antibodies.

Antibody	Type	Species reactivity	Dilution	Host	Catalogue number	Producer
Fetuin-A	P	GP	1:100	Rabbit	ABIN2778140	Antibodies-online.com
PEDF	P	H, M	1:50	Rabbit	NBP2–19767	Novus biological
NKCC1	P	H, M, R	1:100	Rabbit	Ab59791	Abcam
Parvalbumin	M	H, M, R, P	1:200	Mouse	MAB1572	Merck
Tubulin β3	M	H, M, R, P etc.	1:200	Mouse	MAB1637	Merck

List of antibodies used for imunohistochemistry. Type: Polyclonal (P); monoclonal (M). Species reactivty: guinea pig (GP); human (H); mouse (M); rat (R); porcine (P).

TABLE 2 | RNAscope probes.

Protein	Species	Gene	Gene ID	Probe	Producer
PEDF	Guinea pig	*SerpinF1*	100216362	874151	BioTechne
Fetuin-A	Guinea pig	*AHSG*	100135479	897851-C2	BioTechne

List of probes used for RNAscope©.

acquisition settings kept equal within each figure, except for the blue (DAPI) channel which was optimized for illustration of the morphology. The Nikon EZ-C1 was also used for reconstructions of z-stacks to 3D-images. The confocal images were saved as tag image file format red-green-blue (TIFF-RGB) with a resolution of 512 × 512 pixels and transferred to Fiji ImageJ 1.53C (Schindelin et al., 2012). Fiji ImageJ was used to perform densitometry. The image was split into channels for red, green, and blue immunostaining. The channel of interest was isolated and converted into a grayscale image in which each pixel was assigned a value between 0 and 65,535 depending on the intensity of immunofluorescence, where 0 is black and 65,535 is white. The grayscale image was used for intensity measurement. A region of interest was manually drawn to exclude areas of the sample that were not subject to examination. The threshold for minimum intensity required of a pixel to be included was set according to "Li" to remove background pixels (Li and Lee, 1993; Li and Tam, 1998). Fiji ImageJ measured the histogram of the remaining pixels and their intensity value. The mean intensity value of the remaining pixels was calculated. All immunohistochemistry images selected for analysis in controls and at 120 min were included in densitometry analysis. Densitometry values were calculated for one representative confocal image from each animal in the controls and 120 min group, and presented as mean values with error bars for standard deviation. Counting and rating of the nuclei staining of Fetuin-A was done in one representative confocal image from each animal in the five groups. The staining of the nuclei of the marginal cells of the stria vascularis and the type I neurons of the spiral ganglia were rated as no, weak or strong intensity. Mean and standard deviation was calculated.

RESULTS

Longitudinal Pattern of Immunostaining

Patterns of immunohistochemistry were studied at the four intervals and compared to control. Densitometry was calculated for 0 and 120 min for Fetuin-A and PEDF immunohistochemistry and Fetuin-A nuclei staining was rated and counted. The presence of Fetuin-A mRNA and PEDF mRNA in guinea pigs not exposed to furosemide were analyzed using RNAscope. The protein localization and signal intensity as well as mRNA detection were uniform in the different turns of the cochlea when the sections were studied visually. The results are presented below for the different compartments of the cochlea.

The Lateral Cochlear Wall

NKCC1 is known to be localized to the baso-lateral wall of the marginal cells in the stria vascularis (Crouch et al., 1997) and the type II fibrocytes of the spiral ligament (Spicer and Schulte, 1991). The control animals showed strong NKCC1 staining intensity in the marginal cells of the stria vascularis and type II fibrocytes in the spiral prominence region. Confocal microscopy revealed a drastic reduction of NKCC1 staining intensity in the type II fibrocytes at 3 min compared to the control. A progressive increase of NKCC1 staining intensity followed at the subsequent intervals in the type II fibrocytes until 120 min when NKCC1 staining intensity had nearly recovered to control levels (**Figure 1**).

The marginal cells of the stria vascularis had stronger NKCC1 staining intensity in the controls and at all intervals following furosemide injection compared to the type II fibrocytes. The staining intensity of NKCC1in the stria vascularis was decreased at 3 min, but was prominently lower at 30 min. Thereafter the staining intensity of NKCC1 gradually recovered in the stria vascularis (**Figure 2**).

Fetuin-A protein was detected with a low and consistent staining intensity in the stria vascularis, spiral ligament and bone surrounding the cochlear structures in the controls. The stria vascularis had the strongest staining intensity of the different compartments in the lateral wall, and some of the marginal cells' nuclei showed Fetuin-A staining (**Figure 3**). The percentage of marginal cell nuclei with strong Fetuin-A staining increased between 30 min and 120 min after furosemide injection. In the control group had 35% of the marginal cells' nuclei a strong staining intensity, which was in the 120 min group increased to 63%. However, the mean staining intensity of stria vascularis did not change (**Figure 4**).

PEDF protein was detected in the stria vascularis, spiral prominence epithelia and type I and type II fibrocytes, while the type III, IV, and V fibrocytes were negative. The stria vascularis was positive for PEDF in all cell layers. PEDF staining intensity was similar in the spiral prominence and in the stria vascularis (**Figure 5**). There were no visual differences in PEDF protein localization or staining intensity in the lateral wall after furosemide exposure compared to the controls (**Figure 6**).

The Spiral Ganglion

NKCC1 was detected in the cell membrane of the spiral ganglion neurons in all controls and furosemide exposed animals, with no difference during the studied period of 120 min.

Fetuin-A protein was seen in the cytoplasm and nuclei of the spiral ganglion type I neurons (**Figure 7**). The mean percent of type I neuron cell nuclei with strong Fetuin-A staining was 26% in the controls. This was increased to 49% at 60 min, and 53% at 120 min (**Figure 4**). The mean intensity of the total staining in the spiral ganglion measured with densitometry in controls and at 120 min was presented in **Figure 6**.

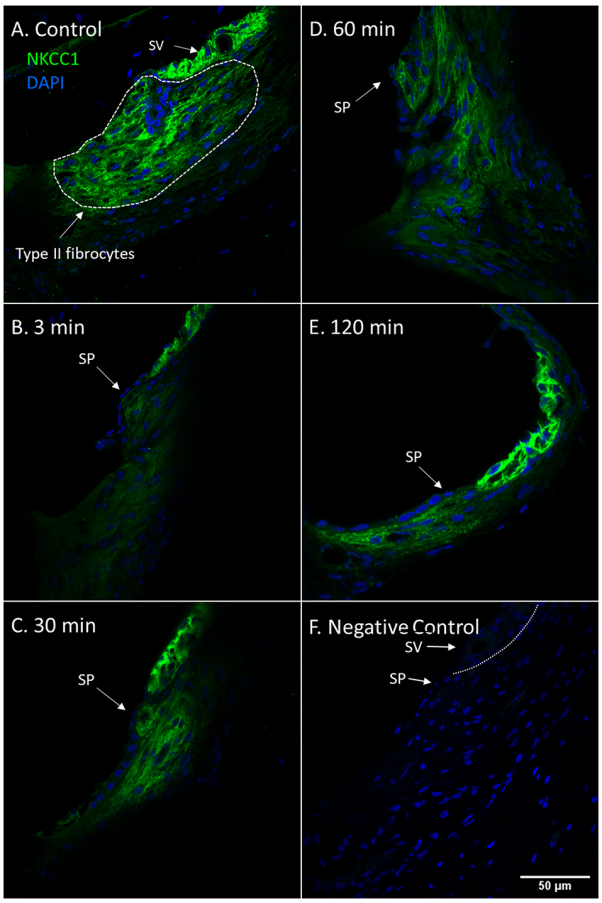

FIGURE 1 | NKCC1 in type II fibrocytes following furosemide injection. **(A–F)** Staining intensity of NKCC1 in the type II fibrocyte following administration of furosemide with DAPI staining of cell nuclei. Focus was set on the type II fibrocytes. Spiral prominence (SP); Stria vascularis (SV). **(A)** Normal NKCC1 staining in type II fibrocytes in a control guinea pig. **(B)** At 3 min after injection there was almost no staining of NKCC1 in the type II fibrocytes. **(C)** At 30 min the staining intensity of NKCC1 in the type II fibrocytes had returned to a low level. **(D)** At 60 min staining intensity was still decreased compared to control. **(E)** After 120 min the signal intensity had returned to near initial levels. **(F)** Negative control section with DAPI.

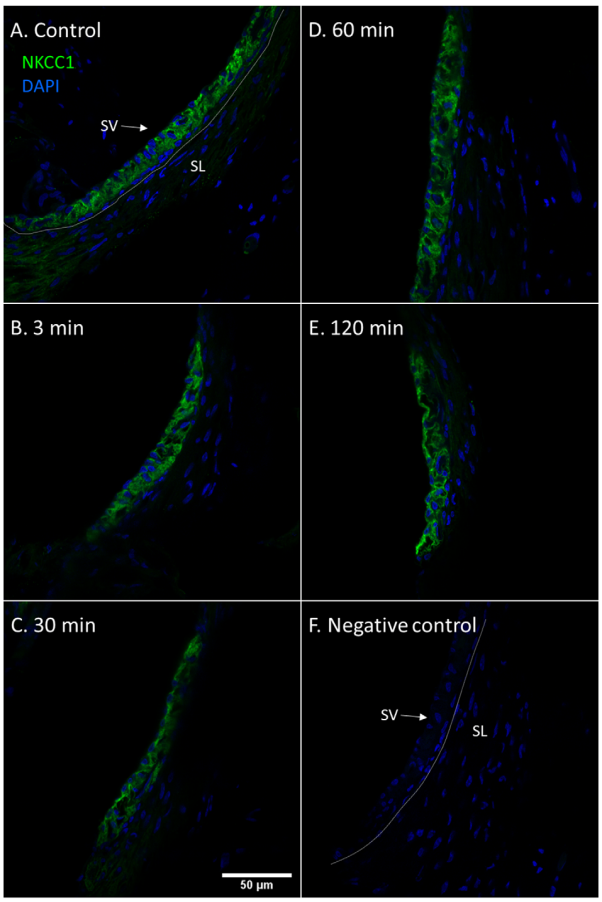

FIGURE 2 | NKCC1 in the stria vascularis following furosemide injection. **(A–F)** Staining intensity of NKCC1 in the marginal cells of the stria vascularis following furosemide injection with DAPI staining of nuclei. Focus was set on the stria vascularis. Spiral ligament (SL); Stria vascularis (SV). **(A)** Normal NKCC1 staining in the stria vascularis in a control animal. **(B)** Intensity had decreased after 3 min. **(C)** The lowest intensity was seen at 30 min. **(D)** It then recovers partially at 60 min. **(E)** Further recovery at 120 min. **(F)** Negative control with DAPI.

PEDF protein was detected in the cytoplasm of the type I neurons in the spiral ganglion in the control and at all intervals after furosemide administration (**Figure 8**). The signal was stable over time and densitometry indicates a minor increase in the type I neurons at 120 min (**Figure 6**).

The Organ of Corti

Fetuin-A protein was detected with a strong staining intensity in the pillar cells of the control animals. The inner and outer hair cells (IHCs and OHCs) and Deiters cells had a low staining in the control and was judged negative. However, after furosemide exposure, the signal intensity increased markedly in the pillar cells, and after 120 min also in IHCs, OHCs, and Deiters cells (**Figure 9**). Densitometry measurement showed an increased mean value of the signal intensity in the organ of Corti at 120 min (**Figure 4**).

Immunohistochemistry detected PEDF protein in the pillar cells and Deiters cells in the controls. After 120 min PEDF protein were also detected in the IHCs, OHCs, and Deiter cells in the organ of Corti. The staining intensity increased most in the pillar cells. No immunostaining was observed in the basilar membrane in the guinea pig's organ of Corti (**Figure 10**). Densitometry showed that the mean staining intensity of PEDF in organ of Corti had increased by 120 min and the highest staining intensity in the organ of Corti was observed in the pillar cells (**Figure 6**).

RNAscope

The RNAscope technique was used in untreated guinea pigs with consistent results compared to the protein localization detected with immunohistochemistry in all cochlear compartments, except for PEDF in the organ of Corti.

In the cochlear lateral wall, Fetuin-A mRNA transcripts were detected in the whole stria vascularis and spiral ligament. In the

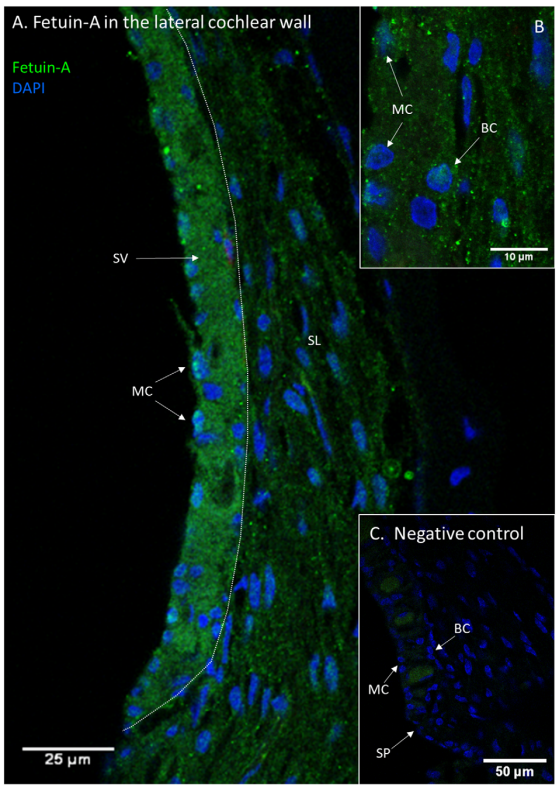

FIGURE 3 | Fetuin-A in the lateral cochlear wall. Protein localization of Fetuin-A in the lateral cochlear wall of a control guinea pig. Spiral ligament (SL); Stria vascularis (SV); Spiral prominence (SP); Marginal cell (MC); Basal cell (BC). **(A)** Fetuin-A protein in the spiral ligament, spiral prominence, and stria vascularis. **(B)** Inset of higher magnification of stria vascularis. Marginal cells (MC) and also basal cells (BC) have Fetuin-A protein. **(C)** Negative control of lateral wall with stria vascularis, spiral prominence and spiral ligament. Vessels have a weak unspecific staining.

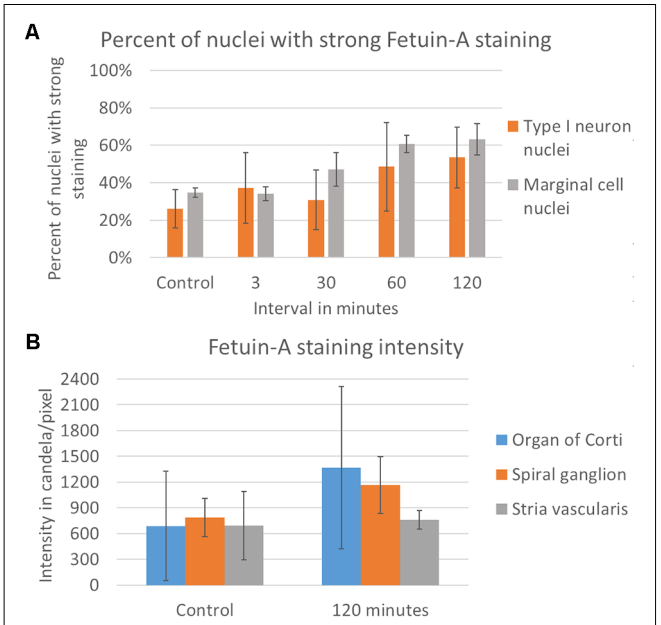

FIGURE 4 | Rating of Fetuin-A nuclei staining and densitometry. **(A)** Rating of Fetuin-A staining intensity in type I neuron nuclei (orange) and marginal cell nuclei (gray). Result presented as the mean value of each group, with error bars showing standard deviation. **(B)** Densitometry of Fetuin-A staining intensity. Result presented as mean value of the control and 120 min group, with error bars showing standard deviation. Intensity increased in the organ of Corti (blue) and the spiral ganglion (orange), with no change in the stria vascularis (gray).

spiral ganglion, Fetuin-A transcripts were detected in the type I neurons. In the organ of Corti Fetuin-A mRNA transcripts were detected in the IHCs, OHCs, pillar cells, and Deiters cells as well as Hensen's cells and Boetcher's cells in accordance with the findings in the furosemide groups (**Figure 11**).

PEDF mRNA transcripts were found in the basal cells of the stria vascularis and in type I and type II fibrocytes. In the lateral wall, transcripts were most abundant in type II fibrocytes. In the spiral ganglion, type I neurons had abundant transcripts. No PEDF mRNA was found in the organ of Corti in the control guinea pig, despite positive protein immunohistochemistry (**Figure 12**).

DISCUSSION

Furosemide-Induced Changes to NKCC1 Staining

This explorative study has identified a new important target and possible mechanisms of furosemide ototoxicity. Many previous experimental studies have shown that a high dose of furosemide, either alone or in combination with other ototoxic drugs, causes a rapid reduction in the endocochlear potential (EP) (Kusakari et al., 1978; Asakuma and Snow, 1980; Sewell, 1984). In the guinea pig cochleae, we observed that furosemide targets NKCC1 in type II fibrocytes in the spiral ligament almost immediately after an IV administration. The spiral ligament fibrocytes are classified into types I to V (Spicer and Schulte, 1991). The classification is based on the expression of specific ion pumps or channels and the location in the spiral ligament. The function of the spiral ligament fibrocytes is believed to be active recirculation of K^+ from the hair cells and perilymph back to the stria vascularis (Spicer and Schulte, 1996). Disruption of the spiral ligament is known to decrease the EP and increase the threshold of the auditory brainstem response (ABR) in experimental animals (Kikuchi et al., 2000; Marcus et al., 2002; Takiguchi et al., 2013; Yoshida et al., 2015; Kitao et al., 2016). The major transporting mechanisms of K^+ are thought to be through gap junctions and connexin channels, inward rectifying potassium channel Kir4.1 and the ion pumps NKCC1 and Na-K-ATPase (Spicer and Schulte, 1991, 1996; Weber et al., 2001; Liu et al., 2017). The type II fibrocytes are recognized by expression of Na-K-ATPase and NKCC1 (Spicer and Schulte, 1991; Crouch et al., 1997) and they are located in the spiral prominence area and outer sulcus inferior to stria vascularis. Observations in a mouse model after acute cochlear energy trauma revealed that hearing recovery was linked to re-expression of Na-K-ATPase and connexin26 (Kitao et al., 2016). Furthermore, reductions in NKCC1 and NK-K-ATPase in type II fibrocytes in addition to

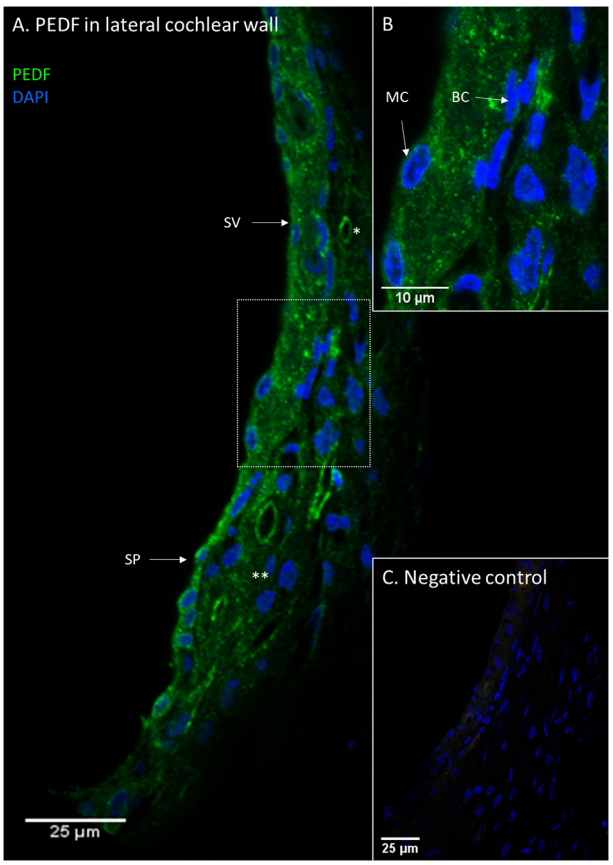

FIGURE 5 | PEDF in the lateral cochlear wall. PEDF protein localization in the lateral cochlear wall. Stria vascularis (SV); Spiral prominence (SP); Marginal cell (MC); Basal cell (BC); type I fibrocytes (*); type II fibrocytes (**). **(A)** PEDF was localized to the spiral ligament, the stria vascularis and the spiral prominence. In the spiral ligament were type I and II fibrocytes PEDF positive. **(B)** Inset of higher magnification of marked area in **(A)**. The distribution of PEDF in sub-cellular level of stria vascularis and spiral ligament. **(C)** Negative control of the immunohistochemistry.

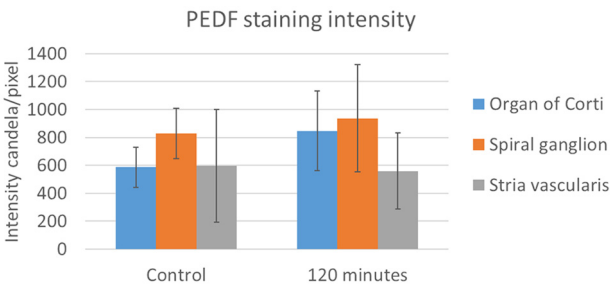

FIGURE 6 | PEDF in the stria vascularis following furosemide injection. Densitometry of PEDFstaining intensity. Result presented as mean values of the control and 120 min group, with error bars showing standard deviation. The organ of Corti (blue) showed a large increase and in the spiral ganglion (orange) a marginal increase, while the stria vascularis (gray) had no change.

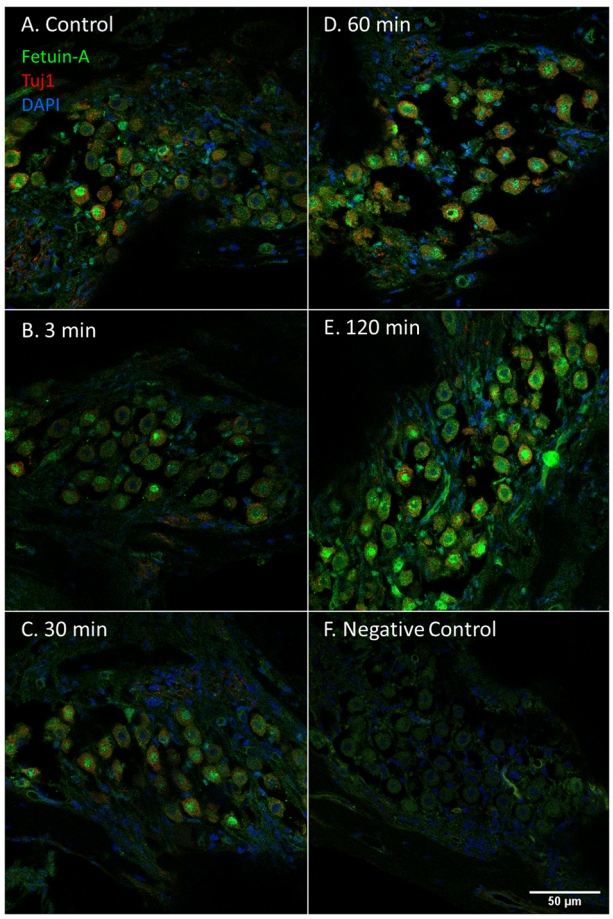

FIGURE 7 | Fetuin-A in the spiral ganglion following furosemide injection. **(A–F)** Fetuin-A protein staining of guinea pig spiral ganglion following IV furosemide injection. **(A)** Fetuin-A protein was localized to the type I neurons cytoplasm and nuclei in the control. **(B–E)** The staining intensity after furosemide at different intervals. **(F)** Negative control.

age-related hearing loss have been reported in Sprague-Dawley rats (Takiguchi et al., 2013). Another experiment, in which the perilymph compartment was perfused with the loop diuretic bumetanide, showed a decrease in EP at the same time as an increase in the intrastrial space, K^+, indicating a blockade of NKCC1 in the lateral wall and marginal cells (Yoshida et al., 2015). This is in line with the present finding of immediate reduction in NKCC1 staining in type II fibrocytes, and this loss of function may be the first target of the loop diuretic effect on EP.

Previous research has shown that NKCC1 is located in the basolateral surface of marginal cells in the stria vascularis (Shindo et al., 1992; Crouch et al., 1997) and in type II fibrocyte (Spicer and Schulte, 1991). While NKCC1 staining intensity reached the lowest point in type II fibrocytes at 3 min after furosemide administration, the stria vascularis was most inhibited at 30 min after furosemide administration. This time difference might be explained by the vascular structure of the lateral wall of the cochlea. The concept of a barrier system between the blood compartment and inner ear structures is widely accepted. In analyzing the barrier systems between the blood compartment and inner ear structures, it is anatomically and functionally

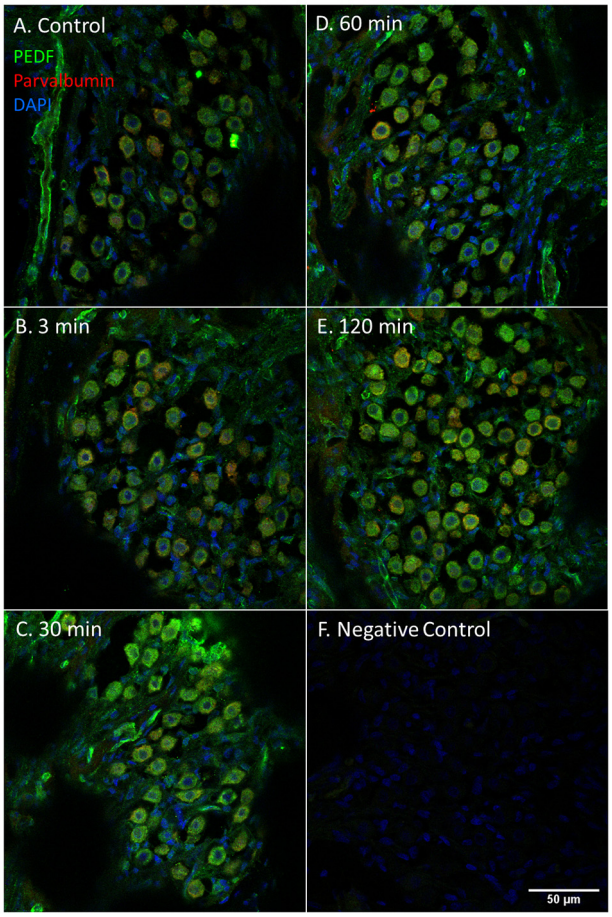

FIGURE 8 | PEDF in the spiral ganglion following furosemide injection. **(A–F)** PEDF protein staining of guinea pig spiral ganglion following IV furosemide injection. **(A)** In the control was PEDF localized in the cytoplasm of the spiral ganglion type I neurons. **(B–E)** The staining intensity after furosemide at the different intervals. **(F)** Negative control.

relevant to separate the blood-labyrinth barrier into the blood-perilymph barrier and the intrastrial fluid-blood barrier (Juhn and Rybak, 1981; Cohen-Salmon et al., 2007). The intrastrial fluid-barrier in the stria vascularis is formed by endothelial cells connected to each other by tight junctions and surrounded by a basal membrane. The next layer is formed by pericytes and perivascular resident macrophage-like melanocytes (PVM/M) around the capillaries (Juhn and Rybak, 1981; Cohen-Salmon et al., 2007; Liu et al., 2016; Shi, 2016). This barrier protects the stria vascularis and the endolymphatic compartment from exogenous substances in the circulatory system. The other parts of the spiral ligament, including the type II fibrocytes, are protected by the more permeable blood-perilymph barrier. This barrier consists of endothelial cells connected to each other by tight junctions but with a few fenestrations (Jahnke, 1980). It is known that the blood-perilymph barrier is more permeable than the intrastrial fluid-blood barrier (Sterkers et al., 1987; Juhn et al., 2001; Counter et al., 2017). Experiments on the permeability of the blood-perilymph barrier in the chinchilla

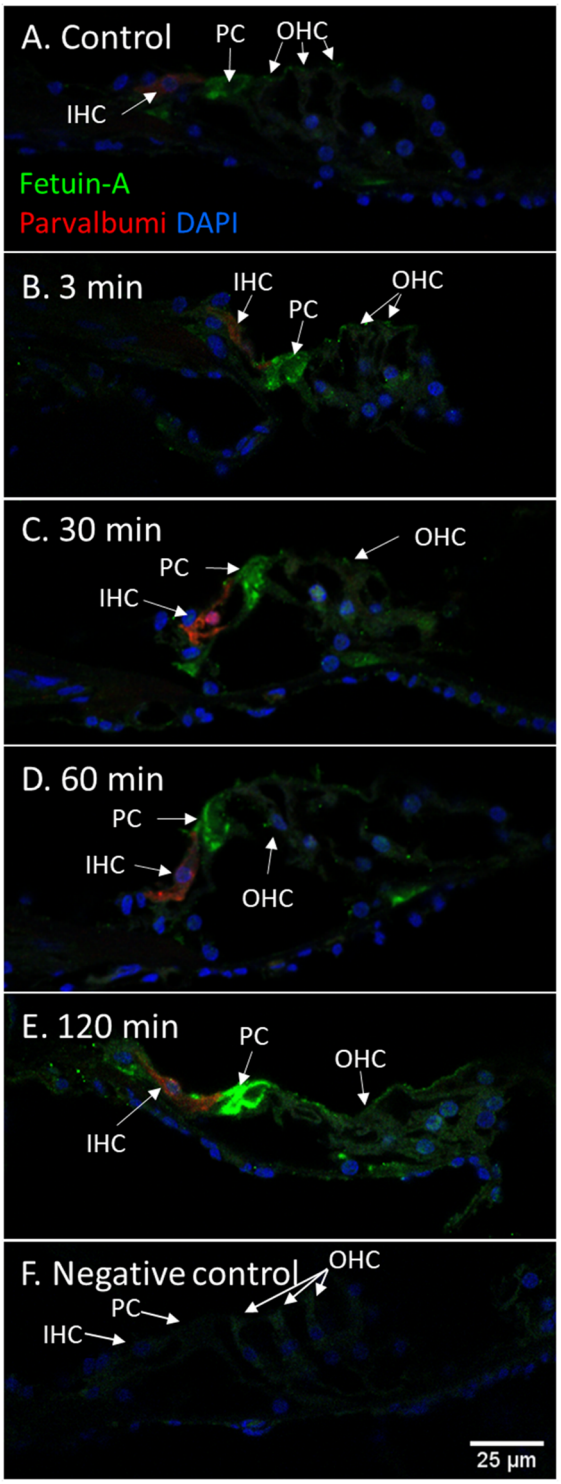

FIGURE 9 | Fetuin-A in the organ of Corti following furosemide injection. **(A–F)** Fetuin-A protein localization and staining intensity in the guinea pig's organ of Corti following IV furosemide injection. Parvalbumin stains the IHC red. **(A)** In the control was Fetuin-A detected in the pillar cells. **(B–E)** Staining intensity in the guinea pig's organ of Corti following IV furosemide injection. Fetuin-A staining was greatly increased in the pillar cells, and the IHCs, OHCs, and Deiters were positive after 120 min. **(F)** Negative control of organ of Corti.

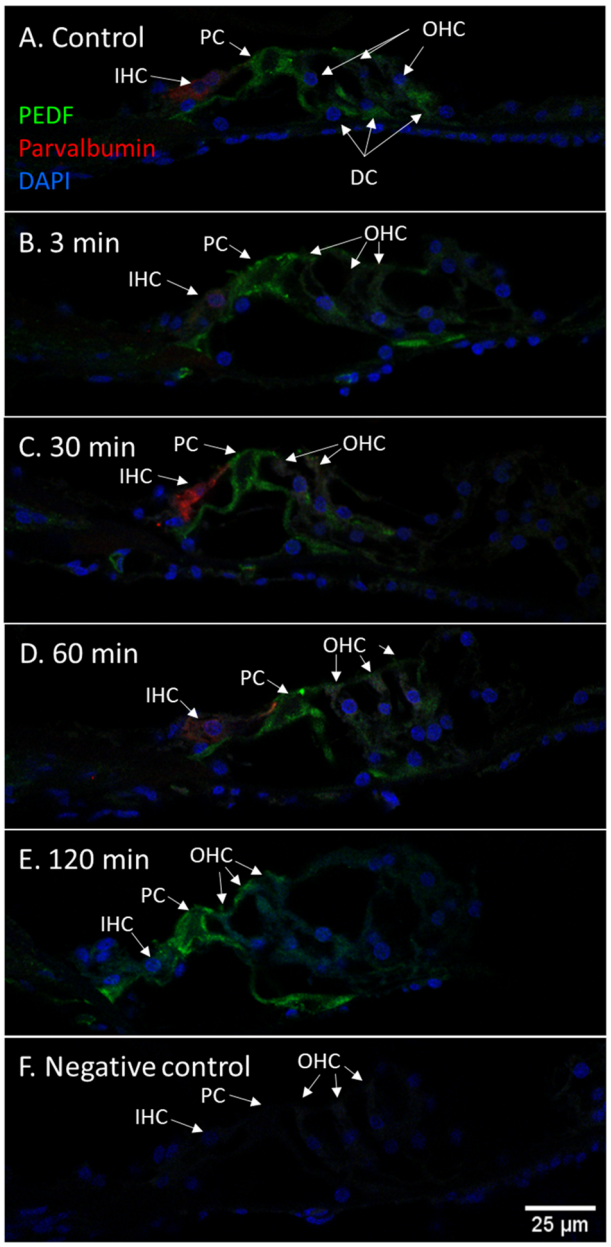

FIGURE 10 | PEDF in guinea pig organ of Corti following furosemide injection. **(A–F)** PEDF protein localization and staining intensity in the guinea pig's organ of Corti following IV furosemide injection. Parvalbumin stains the IHC red. **(A)** PEDF was in the control detected in pillar cells and Deiters cells. **(B–E)** Staining intensity in the guinea pig's organ of Corti following IV furosemide injection. **(E)** At 120 min staining increased in the pillar cells and the IHCs and OHCs stained for PEDF protein. **(F)** Negative control of organ of Corti.

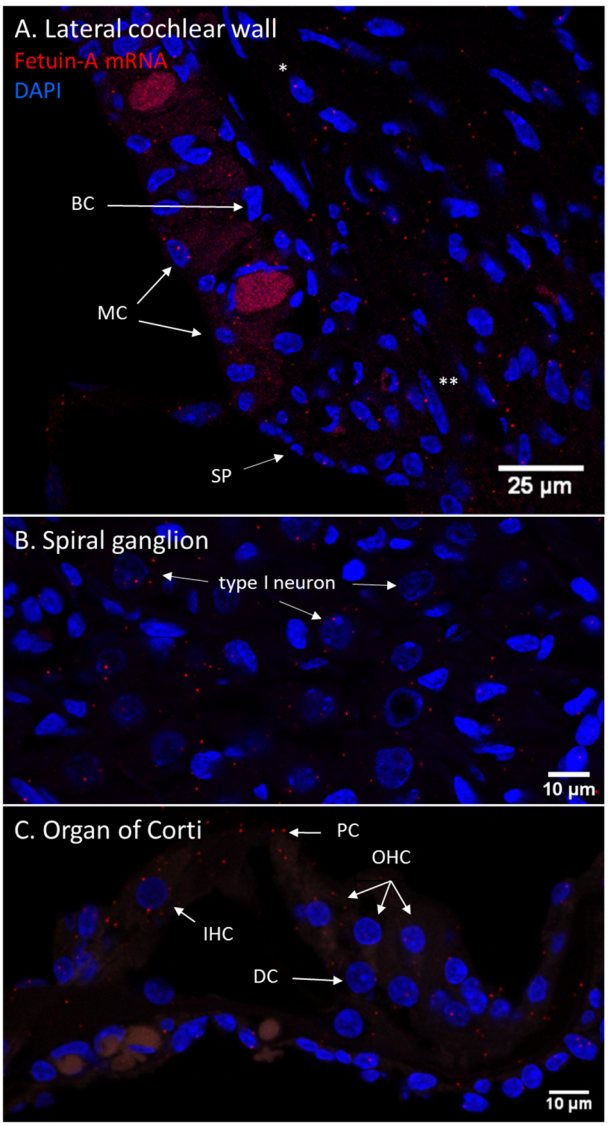

FIGURE 11 | Fetuin-A m-RNA in the guinea pig cochlea. **(A–C)** RNAscope of Fetuin-A mRNA in the control guinea pig cochlea. Red dots indicate mRNA transcripts. DAPI staining of nuclei. Spiral prominence (SP); Marginal cell (MC); Basal cell (BC); type I fibrocytes (*); type II fibrocytes (**). **(A)** Fetuin-A mRNA was detected in all cell layers of stria vascularis, spiral ligament, and prominence. **(B)** The spiral ganglion type I neurons had Fetuin-A mRNA transcripts, but in small numbers. **(C)** In the guinea pig organ of Corti was Fetuin-A mRNA transcripts detected in the IHCs, OHCs, Deiters cells (DC), and pillar cells (PC). PEDF mRNA in the guinea pig cochlea.

demonstrate that EP loss after furosemide administration is correlated to the concentration of the drug in perilymph (Juhn and Rybak, 1981). More recent findings in an MRI study showed a much slower opening of the intrastrial fluid-barrier after the administration of a high dose of furosemide (Videhult Pierre et al., 2020) than the expected loss of EP. We, therefore, consider the observation of a more rapid loss of NKCC1 in type II fibrocytes than in marginal cells, to be consistent with previous experiments on inner ear barriers and the differences in the permeability of the barriers might be a mechanism behind the more rapid effect on the type II fibrocytes of furosemide.

The changes seen in NKCC1 staining intensity of the type II fibrocytes were very rapid and might therefore not be related to change in the gene expression (Ding et al., 2014). Regulation of NKCC1 activity has been studied in

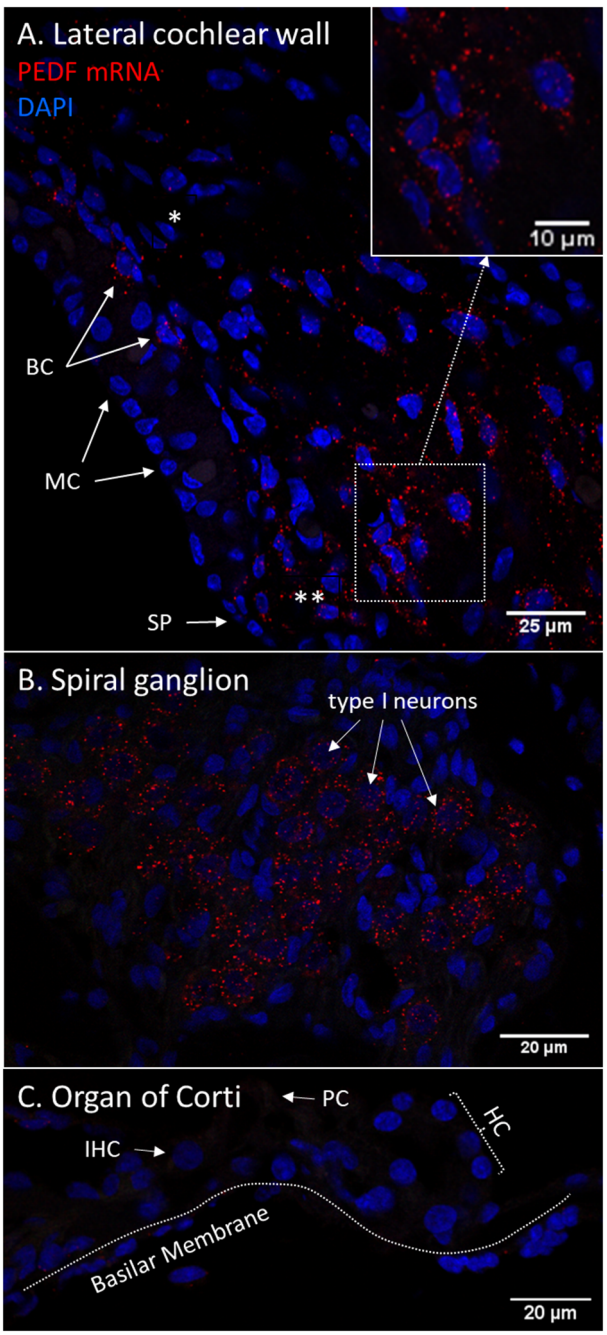

FIGURE 12 | (A–C) RNAscope of PEDF mRNA in the normal guinea pig cochlea. Red dots indicate mRNA transcripts. DAPI staining of nuclei. Spiral prominence (SP); Marginal cell (MC); Basal cell (BC); Hensen's cells (HC); type I fibrocytes (*); type II fibrocytes (**). **(A)** PEDF mRNA transcripts were found in the stria vascularis, spiral ligament, and spiral prominence. The type II fibrocytes had the most abundant transcripts. Transcripts were detected in type I fibrocytes in the basal layer of the stria vascularis. **(B)** The spiral ganglion type I neurons demonstrate high numbers of PEDF mRNA transcripts. **(C)** No PEDF mRNA were found in the organ of Corti.

brain tissue and posttranslational mechanisms are reported to contribute to homeostatic regulation (Watanabe and Fukuda, 2020). Examples of posttranslational mechanisms contributing to the regulation of NKCC1 are glycosylation and phosphorylation. Glycosylation of the N-terminal increases membrane trafficking (Singh et al., 2015) and ion transportation (Ye et al., 2012) of NKCC1. Phosphorylation of NKCC1 by Serine/threonine-protein kinase WNK3 activates NKCC1 ion transportation and de-phosphorylationby protein phosphatase 1 inhibits ion transportation (Kahle et al., 2005). If these mechanisms can also be influenced by a high dose of furosemide has not been reported earlier. Studies on the structural molecular interaction of furosemide and NKCC1 are few. Furosemide has been reported to bind transiently to the Cl^- transporting site of NKCC1 (Somasekharan et al., 2012). If the binding of furosemide to the NKCC1 protein interferes with the binding of the immunohistochemistry antibody against NKCC1 or if posttranslational modifications of NKCC1 could explain the loss of signal intensity has yet to be elucidated.

Longitudinal Fetuin-A Response

The vulnerability of the cochlea to insults induced by various ototoxic drugs has been known for decades. The combination of an aminoglycoside antibiotic and furosemide has been shown to induce an inflammatory response in the cochlea (García-Alcántara et al., 2018; Kaur et al., 2018). Whether an immune response in the cochlea can be activated by a single high dose of furosemide as used in the present study remains open to question. There has been no previous mapping of Fetuin-A in either human cochlear structures or in experimental research. In the cochleae of our control guinea pigs, Fetuin-A was present in the neurons of the spiral ganglion, pillar cells of the organ of Corti and marginal cells of the stria vascularis. Following furosemide administration, a clear temporal staining pattern for Fetuin-A was observed in the cochlea, with an increase of the protein staining intensity in all the Fetuin-A-positive cells after 60–120 min. After 120 min Fetuin-A protein was also detected in IHCs, OHCs, and Deiters cells. To further explore the Fetuin-A expression, we analyzed control guinea pig cochleae for Fetuin-A mRNA using the RNAscope method. The presence of Fetuin-A mRNA in the cells of the cochleae where Fetuin-A protein was detected, verified the results obtained by immunohistochemistry, and indicates that the Fetuin-A gene was expressed. Presence of Fetuin mRNA suggest that the observation of a time-dependent increase of Fetuin-A staining intensity in these cochlear structures may be a manifestation of local cellular activation due to furosemide ototoxicity, in contrast to an increased uptake from the systemic circulation.

Fetuin-A is a multifunctional protein known to be primarily secreted from the liver and reported to be mainly involved in anti-inflammatory mechanisms (Lebreton et al., 1979; Wang and Sama, 2012). In the early phase of an acute inflammation, Fetuin-A concentration in plasma is lowered by pro-inflammatory cytokines and increased by the late inflammation response (Wang and Sama, 2012). Fetuin-A does, however, protect against peripheral artery disease in patients with chronic kidney disease (Westenfeld et al., 2009; Jirak et al., 2019). On the other hand, Fetuin-A is shown to increase insulin resistance and arteriosclerosis in patients

with metabolic syndrome (Trepanowski et al., 2015). Fetuin-A function can, therefore, be considered to be dualistic. In our earlier assessment of perilymph proteome in patients with vestibular schwannoma, Fetuin-A was found to be positively correlated with preserved hearing (Edvardsson Rasmussen et al., 2018). We therefore interpret the finding of increased Fetuin-A after injection with furosemide as a possible otoprotective function after acute insults to the cochlea.

Longitudinal PEDF Response

PEDF protein was detected with immunohistochemistry in the lateral cochlear wall, spiral ganglion and organ of Corti in control guinea pigs. The protein was most evident in type II fibrocytes, the basal and marginal cells of the stria vascularis, the type I neurons of the spiral ganglion and in the pillar cells in the organ of Corti. After 120 min of IV furosemide administration, PEDF had increased in the type I neurons and in the pillar cells. IHCs, OHCs, and Deiters cells were also PEDF-positive after 120 min. PEDF was not detected in the basilar membrane in guinea pigs, which has been reported in rats (Gleich and Piña, 2008). PEDF gene expression was further analyzed using RNAscope in the cochleae of normal guinea pigs and we found mRNA transcripts in spiral ganglion type 1 neurons, type I and type II fibrocytes, marginal cells, and basal cells of the stria vascularis. The finding of mRNA transcripts was a first validation of the detected protein localization and indicate that PEDF gene expression was active in these cells. We could not confirm PEDF mRNA in the organ of Corti, although the immunohistochemistry protein localization was consistent in the experiment. Based on these results, we speculate that PEDF could be produced by cells in the lateral cochlear wall and can reach the organ of Corti from the endolymph. An alternative possible explanation could be that PEDF was transported by axonal transportation from the type I neurons to the organ of Corti. However, it cannot fully be ruled out that PEDF gene transcription could be very low in the organ of Corti in the normal situation and could be increased from cellular stress induced by furosemide.

PEDF has been reported in the perivascular melanocyte-like macrophages (PVM/M) (Zhang et al., 2012), part of the second layer in the intrastrial fluid-blood barrier. Further, the PEDF signaling pathway was reported to be important for the formation of tight junctions between endothelial cells to maintain the integrity of the intrastrial fluid-blood barrier after acoustic trauma (Zhang et al., 2013). The timing of the increase of PEDF staining intensity in our experiment was similar to that observed after acoustic trauma by Zhang et al. (2013). Stimulation of PEDF production was reported to increase the survival of PVM/M in cell culture and stimulate the formation of tight junctions (Zhang et al., 2021). It could therefore be part of a counter mechanism to the increased permeability of the intrastrial fluid-blood barrier caused by furosemide (Videhult Pierre et al., 2020).

Increased staining intensity of PEDF protein were observed in the organ of Corti in the pillar cells, IHCs, OHCs, and Deiters cells after 120 min. PEDF is known to promote the survival of photoreceptors and retinal ganglion cells (Barnstable and Tombran-Tink, 2004; Polato and Becerra, 2016; Zwanzig et al., 2021) and the suppression of pro-inflammatory cytokines (Ma et al., 2021). We, therefore, speculate that increased PEDF in the organ of Corti also promotes cell survival after the cochlear insult induced by furosemide.

We detected PEDF in the cytoplasm of the spiral gangliontype I neurons, and an increase in PEDF over time reaching a maximum at 60–120 min. The PEDF increase was similar to the known neuroprotective response in retinal ganglion cells (Unterlauft et al., 2012) and probably a mechanism to protect type I neurons from undergoing apoptosis.

The finding of increased Fetuin-A and PEDF in the cochlea after furosemide exposure and the information of their anti-inflammatory and protective functions suggest a possible causal effect behind the observed correlation of high Fetuin-A in perilymph and preserved hearing in vestibular schwannoma patients (Edvardsson Rasmussen et al., 2018). Given the reported links between PEDF-gene mutations and hereditary otosclerosis (Ziff et al., 2016), it is relevant to further explore PEDF in the inner ear.

It may be argued that it is difficult to draw conclusions from a longitudinal study using immunohistochemistry, as it is not possible to follow immunohistochemically changes in the inner ear over time in the same experimental animal. We, therefore, created a timeline comparing different individuals with carefully minimized experimental differences. This immunohistochemistry study was designed to gain more knowledge of time-dependent changes induced by furosemide in the cochlea. However, the number of animals used in the study did not allow for statistical analysis of the signal intensity changes. One further limitation of the study was that no *in vivo* measurements of ABRs or EP were taken.

CONCLUSION

NKCC1 staining was found to be greatly reduced in type II fibrocytes of the spiral ligament 3 min after the administration of a high dose of furosemide. The NKCC1 signal followed the temporal course previously reported for EP recovery. This suggests that one underlying mechanism of EP decrease following furosemide administration could be the disruption of K^+ recirculation *via* the type II fibrocytes into the syncytium of the stria vascularis.

PEDF and Fetuin-A protein were both present in the stria vascularis, spiral ganglion and organ of Corti in controls. The cells with high staining of both proteins were marginal cells of the stria vascularis, type I neurons and pillar cells. The presence of Fetuin-A mRNA and PEDF mRNA shows a local gene expression in the cochlea. There was a temporal pattern with increase in both Fetuin-A and PEDF 120 min after furosemide administration, indicating that these proteins may play a role in the cellular response to cochlear insults.

DATA AVAILABILITY STATEMENT

The raw data supporting the conclusions of this article will be made available by the authors, without undue reservation.

ETHICS STATEMENT

The animal study was reviewed and approved by Ethics Committee on Animal Experiments in Uppsala, Sweden (ref. no. 5.8.18-13236/2018).

AUTHOR CONTRIBUTIONS

GL, PE, and JE conceived the study design and primary hypothesis. WL and JE performed the immunohistochemical staining and microscopy. WL also performed the RNAscope and microscopy. PL was responsible for the densitometry analysis. HR-A and JE interpreted the morphological results. All authors discussed the results and thereafter JE wrote the manuscript. All authors contributed to the article and approved the submitted version.

FUNDING

This work was supported by Uppsala University Hospital ALF Grant [AS 1905702], the Swedish Research Council [2017-03801], the Acta Otolaryngologica Foundation, the Tysta Skolan Foundation, the Swedish Association of Hard of Hearing People, and generous private funds from Arne Sundström, Sweden.

ACKNOWLEDGMENTS

We would like to specially thank Anette Fransson PhD for excellent technical work in the laboratory.

REFERENCES

Alam, S. A., Ikeda, K., Kawase, T., Kikuchi, T., Katori, Y., Watanabe, K., et al. (1998). Acute effects of combined administration of kanamycin and furosemide on the stria vascularis studied by distortion product otoacoustic emission and transmission electron microscopy. *Tohoku J. Exp. Med.* 186, 79–86. doi: 10.1620/tjem.186.79

Arnold, W., Nadol, J. B., and Weidauer, H. (1981). Ultrastructural histopathology in a case of human ototoxicity due to loop diuretics. *Acta Otolaryngol.* 91, 399–414. doi: 10.3109/00016488109138521

Asakuma, S., and Snow, J. B. (1980). Effects of furosemide and ethacrynic acid on the endocochlear direct current potential in normal and kanamycin sulfate-treated guinea pigs. *Otolaryngol. Head Neck Surg.* 88, 188–193.

Barnstable, C. J., and Tombran-Tink, J. (2004). Neuroprotective and antiangiogenic actions of PEDF in the eye: molecular targets and therapeutic potential. *Prog. Retin. Eye Res.* 23, 561–577. doi: 10.1016/j.preteyeres.2004.05.002

Brook, N., Brook, E., Dharmarajan, A., Chan, A., and Dass, C. R. (2020). Pigment epithelium-derived factor regulation of neuronal and stem cell fate. *Exp. Cell Res.* 389:111891. doi: 10.1016/j.yexcr.2020.111891

Burry, R. W. (2011). Controls for immunocytochemistry. *J. Histochem. Cytochem.* 59, 6–12. doi: 10.1369/jhc.2010.956920

Cohen-Salmon, M., Regnault, B., Cayet, N., Caille, D., Demuth, K., Hardelin, J.-P., et al. (2007). Connexin30 deficiency causes instrastrial fluid-blood barrier disruption within the cochlear stria vascularis. *Proc. Natl. Acad. Sci. U S A* 104, 6229–6234. doi: 10.1073/pnas.0605108104

Counter, S. A., Nikkhou-Aski, S., Damberg, P., Berglin, C. E., and Laurell, G. (2017). Ultra-high-field (9.4 T) MRI analysis of contrast agent transport across the blood-perilymph barrier and intrastrial fluid-blood barrier in the mouse inner ear. *Otol. Neurotol.* 38, 1052–1059. doi: 10.1097/MAO.0000000000001458

Crouch, J. J., Sakaguchi, N., Lytle, C., and Schulte, B. A. (1997). Immunohistochemical localization of the Na-K-Cl co-transporter (NKCC1) in the gerbil inner ear. *J. Histochem. Cytochem.* 45, 773–778. doi: 10.1177/002215549704500601

Delpire, E., and Gagnon, K. B. (2018). Na^+-K^+-$2Cl^-$ cotransporter (NKCC) physiological function in nonpolarized cells and transporting epithelia. *Compr. Physiol.* 8, 871–901. doi: 10.1002/cphy.c170018

Ding, B., Frisina, R. D., Zhu, X., Sakai, Y., Sokolowski, B., and Walton, J. P. (2014). Direct control of Na^+-K^+-$2Cl^-$-cotransport protein (NKCC1) expression with aldosterone. *Am. J. Physiol. Cell Physiol.* 306, C66–C75. doi: 10.1152/ajpcell.00096.2013

Ding, D., Liu, H., Qi, W., Jiang, H., Li, Y., Wu, X., et al. (2016). Ototoxic effects and mechanisms of loop diuretics. *J. Otol.* 11, 145–156. doi: 10.1016/j.joto.2016.10.001

Ding, D., McFadden, S. L., Woo, J. M., and Salvi, R. J. (2002). Ethacrynic acid rapidly and selectively abolishes blood flow in vessels supplying the lateral wall of the cochlea. *Hear. Res.* 173, 1–9. doi: 10.1016/s0378-5955(02)00585-3

Edvardsson Rasmussen, J., Laurell, G., Rask-Andersen, H., Bergquist, J., and Eriksson, P. O. (2018). The proteome of perilymph in patients with vestibular schwannoma. A possibility to identify biomarkers for tumor associated hearing loss. *PLoS One* 13:e0198442. doi: 10.1371/journal.pone.0198442

Forge, A. (1976). Observations on the stria vascularis of the guinea pig cochlea and the changes resulting from the administration of the diuretic furosemide. *Clin. Otolaryngol. Allied Sci.* 1, 211–219. doi: 10.1111/j.1365-2273.1976.tb00879.x

Forge, A., and Brown, A. M. (1982). Ultrastructural and electrophysiological studies of acute ototoxic effects of furosemide. *Br. J. Audiol.* 16, 109–116. doi: 10.3109/03005368209081455

García-Alcántara, F., Murillo-Cuesta, S., Pulido, S., Bermúdez-Muñoz, J. M., Martínez-Vega, R., Milo, M., et al. (2018). The expression of oxidative stress response genes is modulated by a combination of resveratrol and N-acetylcysteine to ameliorate ototoxicity in the rat cochlea. *Hear. Res.* 358, 10–21. doi: 10.1016/j.heares.2017.12.004

Gleich, O., and Piña, A. L. (2008). Protein expression of pigment-epithelium-derived factor in rat cochlea. *Cell Tissue Res.* 332, 565–571. doi: 10.1007/s00441-008-0608-6

Grabinski, T. M., Kneynsberg, A., Manfredsson, F. P., and Kanaan, N. M. (2015). A method for combining rnascope *in situ* hybridization with immunohistochemistry in thick free-floating brain sections and primary neuronal cultures. *PLoS One* 10:e0120120. doi: 10.1371/journal.pone.0120120

Hirose, K., and Sato, E. (2011). Comparative analysis of combination kanamycin-furosemide versus kanamycin alone in the mouse cochlea. *Hear. Res.* 272, 108–116. doi: 10.1016/j.heares.2010.10.011

Jahnen-Dechent, W., Schinke, T., Trindl, A., Müller-Esterl, W., Sablitzky, F., Kaiser, S., et al. (1997). Cloning and targeted deletion of the mouse fetuin gene*. *J. Biol. Chem.* 272, 31496–31503. doi: 10.1074/jbc.272.50.31496

Jahnke, K. (1980). The blood-perilymph barrier. *Arch. Otorhinolaryngol.* 228, 29–34. doi: 10.1007/BF00455891

Jirak, P., Stechemesser, L., Moré, E., Franzen, M., Topf, A., Mirna, M., et al. (2019). Clinical implications of fetuin-A. *Adv. Clin. Chem.* 89, 79–130. doi: 10.1016/bs.acc.2018.12.003

Juhn, S. K., Hunter, B. A., and Odland, R. M. (2001). Blood-labyrinth barrier and fluid dynamics of the inner ear. *Int. Tinnitus J.* 7, 72–83.

Juhn, S. K., and Rybak, L. P. (1981). Labyrinthine barriers and cochlear homeostasis. *Acta Otolaryngol.* 91, 529–534. doi: 10.3109/00016488109138538

Kahle, K. T., Rinehart, J., de los Heros, P., Louvi, A., Meade, P., Vazquez, N., et al. (2005). WNK3 modulates transport of Cl- in and out of cells: implications for control of cell volume and neuronal excitability. *Proc. Nat. Acad. Sci. U S A* 102, 16783–16788. doi: 10.1073/pnas.0508307102

Kaur, T., Ohlemiller, K. K., and Warchol, M. E. (2018). Genetic disruption of fractalkine signaling leads to enhanced loss of cochlear afferents following

ototoxic or acoustic injury. *J. Comp. Neurol.* 526, 824–835. doi: 10.1002/cne.24369

Kikuchi, T., Adams, J. C., Miyabe, Y., So, E., and Kobayashi, T. (2000). Potassium ion recycling pathway *via* gap junction systems in the mammalian cochlea and its interruption in hereditary nonsyndromic deafness. *Med. Electron Microsc.* 33, 51–56. doi: 10.1007/s007950070001

Kitao, K., Mizutari, K., Nakagawa, S., Matsunaga, T., Fukuda, S., and Fujii, M. (2016). Recovery of endocochlear potential after severe damage to lateral wall fibrocytes following acute cochlear energy failure. *Neuroreport* 27, 1159–1166. doi: 10.1097/WNR.0000000000000673

Kusakari, J., Ise, I., Comegys, T. H., Thalmann, I., and Thalmann, R. (1978). Effect of ethacrynic acid, furosemide and ouabain upon the endolymphatic potential and upon high energy phosphates of the stria vascularis. *Laryngoscope* 88, 12–37. doi: 10.1002/lary.1978.88.1.12

Laurell, G., and Engström, B. (1989). The combined effect of cisplatin and furosemide on hearing function in guinea pigs. *Hear. Res.* 38, 19–26. doi: 10.1016/0378-5955(89)90124-x

Lebreton, J. P., Joisel, F., Raoult, J. P., Lannuzel, B., Rogez, J. P., and Humbert, G. (1979). Serum concentration of human alpha 2 HS glycoprotein during the inflammatory process: evidence that alpha 2 HS glycoprotein is a negative acute-phase reactant. *J. Clin. Invest.* 64, 1118–1129. doi: 10.1172/JCI109551

Li, Y., Ding, D., Jiang, H., Fu, Y., and Salvi, R. (2011). Co-administration of cisplatin and furosemide causes rapid and massive loss of cochlear hair cells in mice. *Neurotox. Res.* 20:307. doi: 10.1007/s12640-011-9244-0

Li, C. H., and Lee, C. K. (1993). Minimum cross entropy thresholding. *Pattern Recognit.* 26, 617–625. doi: 10.1016/0031-3203(93)90115-D

Li, C. H., and Tam, P. K. S. (1998). An iterative algorithm for minimum cross entropy thresholding. *Pattern Recognit. Lett.* 19, 771–776. doi: 10.1016/S0167-8655(98)00057-9

Liu, W., Edin, F., Blom, H., Magnusson, P., Schrott-Fischer, A., Glueckert, R., et al. (2016). Super-resolution structured illumination fluorescence microscopy of the lateral wall of the cochlea: the connexin26/30 proteins are separately expressed in man. *Cell Tissue Res.* 365, 13–27. doi: 10.1007/s00441-016-2359-0

Liu, W., Schrott-Fischer, A., Glueckert, R., Benav, H., and Rask-Andersen, H. (2017). The human "cochlear battery" – claudin-11 barrier and ion transport proteins in the lateral wall of the cochlea. *Front. Mol. Neurosci.* 10:239. doi: 10.3389/fnmol.2017.00239

Ma, B., Zhou, Y., Liu, R., Zhang, K., Yang, T., Hu, C., et al. (2021). Pigment epithelium-derived factor (PEDF) plays anti-inflammatory roles in the pathogenesis of dry eye disease. *Ocul. Surf.* 20, 70–85. doi: 10.1016/j.jtos.2020.12.007

Marcus, D. C., Wu, T., Wangemann, P., and Kofuji, P. (2002). KCNJ10 (Kir4.1) potassium channel knockout abolishes endocochlear potential. *Am. J. Physiol. Cell Physiol.* 282, C403–C407. doi: 10.1152/ajpcell.00312.2001

Naito, H., and Watanabe, K. (1997). Alteration in capillary permeability of horseradish peroxidase in the stria vascularis and movement of leaked horseradish peroxidase after administration of furosemide. *ORL J. Otorhinolaryngol. Relat. Spec.* 59, 248–257. doi: 10.1159/000276948

Ölander, C., Edvardsson Rasmussen, J., Eriksson, P. O., Laurell, G., Rask-Andersen, H., and Bergquist, J. (2021). The proteome of the human endolymphatic sac endolymph. *Sci Rep.* 11:11850. doi: 10.1038/s41598-021-89597-3

Pike, D. A., and Bosher, S. K. (1980). The time course of the strial changes produced by intravenous furosemide. *Hear. Res.* 3, 79–89. doi: 10.1016/0378-5955(80)90009-x

Polato, F., and Becerra, S. P. (2016). Pigment epithelium-derived factor, a protective factor for photoreceptors *in vivo*. *Adv. Exp. Med. Biol.* 854, 699–706. doi: 10.1007/978-3-319-17121-0_93

Rarey, K. E., and Ross, M. D. (1982). A survey of the effects of loop diuretics on the zonulae occludentes of the perilymph-endolymph barrier by freeze fracture. *Acta Otolaryngol.* 94, 307–316. doi: 10.3109/00016488209128918

Robertson, C. M. T., Bork, K. T., Tawfik, G., Bond, G. Y., Hendson, L., Dinu, I. A., et al. (2019). Avoiding furosemide ototoxicity associated with single-ventricle repair in young infants*. *Pediatr. Crit. Care Med.* 20:350. doi: 10.1097/PCC.0000000000001807

Santos, F., and Nadol, J. B. (2017). Temporal bone histopathology of furosemide ototoxicity. *Laryngoscope Investig. Otolaryngol.* 2, 204–207. doi: 10.1002/lio2.108

Schindelin, J., Arganda-Carreras, I., Frise, E., Kaynig, V., Longair, M., Pietzsch, T., et al. (2012). Fiji: an open-source platform for biological-image analysis. *Nat. Methods* 9, 676–682. doi: 10.1038/nmeth.2019

Schwartz, G. H., David, D. S., Riggio, R. R., Stenzel, K. H., and Rubin, A. L. (1970). Ototoxicity induced by furosemide. *N Engl. J. Med.* 282, 1413–1414. doi: 10.1056/NEJM197006182822506

Sewell, W. F. (1984). The effects of furosemide on the endocochlear potential and auditory-nerve fiber tuning curves in cats. *Hear. Res.* 14, 305–314. doi: 10.1016/0378-5955(84)90057-1

Shi, X. (2016). Pathophysiology of the cochlear intrastrial fluid-blood barrier (review). *Hear. Res.* 338, 52–63. doi: 10.1016/j.heares.2016.01.010

Shindo, M., Miyamoto, M., Abe, N., Shida, S., Murakami, Y., and Imai, Y. (1992). Dependence of endocochlear potential on basolateral Na+ and Cl- concentration: a study using vascular and perilymph perfusion. *Jpn. J. Physiol.* 42, 617–630. doi: 10.2170/jjphysiol.42.617

Singh, R., Almutairi, M. M., Pacheco-Andrade, R., Almiahuob, M. Y. M., and Di Fulvio, M. (2015). Impact of hybrid and complex N-Glycans on cell surface targeting of the endogenous chloride cotransporter Slc12a2. *Int. J. Cell Biol.* 2015, 1–20. doi: 10.1155/2015/505294

Somasekharan, S., Tanis, J., and Forbush, B. (2012). Loop diuretic and ion-binding residues revealed by scanning mutagenesis of transmembrane helix 3 (TM3) of Na-K-Cl cotransporter (NKCC1). *J. Biol. Chem.* 287, 17308–17317. doi: 10.1074/jbc.M112.356014

Spicer, S. S., and Schulte, B. A. (1991). Differentiation of inner ear fibrocytes according to their ion transport related activity. *Hear. Res.* 56, 53–64. doi: 10.1016/0378-5955(91)90153-z

Spicer, S. S., and Schulte, B. A. (1996). The fine structure of spiral ligament cells relates to ion return to the stria and varies with place-frequency. *Hear. Res.* 100, 80–100. doi: 10.1016/0378-5955(96)00106-2

Sterkers, O., Ferrary, E., Saumon, G., and Amiel, C. (1987). Na and nonelectrolyte entry into inner ear fluids of the rat. *Am. J. Physiol.* 253, F50–F58. doi: 10.1152/ajprenal.1987.253.1.F50

Takiguchi, Y., Sun, G., Ogawa, K., and Matsunaga, T. (2013). Long-lasting changes in the cochlear K^+ recycling structures after acute energy failure. *Neurosci. Res.* 77, 33–41. doi: 10.1016/j.neures.2013.06.003

Tasaki, I., and Spyropoulos, C. S. (1959). Stria vascularis as source of endocochlear potential. *J. Neurophysiol.* 22, 149–155. doi: 10.1152/jn.1959.22.2.149

Tombran-Tink, J., Chader, G. G., and Johnson, L. V. (1991). PEDF: a pigment epithelium-derived factor with potent neuronal differentiative activity. *Exp. Eye Res.* 53, 411–414. doi: 10.1016/0014-4835(91)90248-d

Trepanowski, J. F., Mey, J., and Varady, K. A. (2015). Fetuin-A: a novel link between obesity and related complications. *Int. J. Obes. (Lond)* 39, 734–741. doi: 10.1038/ijo.2014.203

Unterlauft, J. D., Eichler, W., Kuhne, K., Yang, X. M., Yafai, Y., Wiedemann, P., et al. (2012). pigment epithelium-derived factor released by Müller glial cells exerts neuroprotective effects on retinal ganglion cells. *Neurochem. Res.* 37, 1524–1533. doi: 10.1007/s11064-012-0747-8

Videhult Pierre, P., Edvardsson Rasmussen, J., Nikkhou Aski, S., Damberg, P., and Laurell, G. (2020). High-dose furosemide enhances the magnetic resonance signal of systemic gadolinium in the mammalian cochlea. *Otol. Neurotol.* 41, 545–553. doi: 10.1097/MAO.0000000000002571

Wang, H., and Sama, A. E. (2012). Anti-inflammatory role of Fetuin-A in Injury and Infection. *Curr. Mol. Med.* 12, 625–633. doi: 10.2174/156652412800620039

Watanabe, M., and Fukuda, A. (2020). "Post-translational modification of neuronal chloride transporters," in *Neuronal Chloride Transporters in Health and Disease*, ed Xin Tang (Academic Press Elsevier), 243–255. Available online at: https://linkinghub.elsevier.com/retrieve/pii/B978012815318500011X.

Weber, P. C., Cunningham III, C. D., and Schulte, B. A. (2001). Potassium recycling pathways in the human cochlea. *Laryngoscope* 111, 1156–1165. doi: 10.1097/00005537-200107000-00006

Westenfeld, R., Schäfer, C., Krüger, T., Haarmann, C., Schurgers, L. J., Reutelingsperger, C., et al. (2009). Fetuin-A protects against atherosclerotic

calcification in CKD. *J. Am. Soc. Nephrol.* 20, 1264–1274. doi: 10.1681/ASN.2008060572

Ye, Z.-Y., Li, D.-P., Byun, H. S., Li, L., and Pan, H.-L. (2012). NKCC1 upregulation disrupts chloride homeostasis in the hypothalamus and increases neuronal activity-sympathetic drive in hypertension. *J. Neurosci.* 32, 8560–8568. doi: 10.1523/JNEUROSCI.1346-12.2012

Yoshida, T., Nin, F., Ogata, G., Uetsuka, S., Kitahara, T., Inohara, H., et al. (2015). NKCCs in the fibrocytes of the spiral ligament are silent on the unidirectional K^+ transport that controls the electrochemical properties in the mammalian cochlea. *Pflugers Arch.* 467, 1577–1589. doi: 10.1007/s00424-014-1597-9

Zhang, W., Dai, M., Fridberger, A., Hassan, A., DeGagne, J., Neng, L., et al. (2012). Perivascular-resident macrophage-like melanocytes in the inner ear are essential for the integrity of the intrastrial fluid-blood barrier. *Proc. Nat. Acad. Sci. U S A* 109:10388. doi: 10.1073/pnas.1205210109

Zhang, F., Dai, M., Neng, L., Zhang, J. H., Zhi, Z., Fridberger, A., et al. (2013). Perivascular macrophage-like melanocyte responsiveness to acoustic trauma—a salient feature of strial barrier associated hearing loss. *FASEB J.* 27, 3730–3740. doi: 10.1096/fj.13-232892

Zhang, J., Fan, W., Neng, L., Chen, B., Zuo, B., and Lu, W. (2021). Long non-coding RNA Rian promotes the expression of tight junction proteins in endothelial cells by regulating perivascular-resident macrophage-like melanocytes and PEDF secretion. *Hum. Cell* 34, 1093–1102. doi: 10.1007/s13577-021-00521-3

Ziff, J. L., Crompton, M., Powell, H. R. F., Lavy, J. A., Aldren, C. P., Steel, K. P., et al. (2016). Mutations and altered expression of SERPINF1 in patients with familial otosclerosis. *Hum. Mol. Genet.* 25, 2393–2403. doi: 10.1093/hmg/ddw106

Zwanzig, A., Meng, J., Müller, H., Bürger, S., Schmidt, M., Pankonin, M., et al. (2021). Neuroprotective effects of glial mediators in interactions between retinal neurons and Müller cells. *Exp. Eye Res.* 209:108689. doi: 10.1016/j.exer.2021.108689

Conflict of Interest: The authors declare that the research was conducted in the absence of any commercial or financial relationships that could be construed as a potential conflict of interest.

frontiers | Frontiers in Molecular Neuroscience

ORIGINAL RESEARCH
published: 05 May 2022
doi: 10.3389/fnmol.2022.844668

Cingulin b Is Required for Zebrafish Lateral Line Development Through Regulation of Mitogen-Activated Protein Kinase and Cellular Senescence Signaling Pathways

Yitong Lu[1†], Dongmei Tang[2,3†], Zhiwei Zheng[2,3†], Xin Wang[4], Na Zuo[1], Renchun Yan[1], Cheng Wu[1], Jun Ma[1], Chuanxi Wang[1], Hongfei Xu[5], Yingzi He[2,3], Dong Liu[4*] and Shaofeng Liu[1*]*

[1] Department of Otolaryngology-Head and Neck Surgery, Yijishan Hospital of Wannan Medical College, Wuhu, China, [2] State Key Laboratory of Medical Neurobiology and MOE Frontiers Center for Brain Science, ENT Institute and Department of Otorhinolaryngology, Eye and ENT Hospital, Fudan University, Shanghai, China, [3] NHC Key Laboratory of Hearing Medicine, Fudan University, Shanghai, China, [4] Nantong Laboratory of Development and Diseases, School of Life Sciences, Co-innovation Center of Neuroregeneration, Key Laboratory of Neuroregeneration of Jiangsu and MOE, Nantong University, Nantong, China, [5] Department of Forensic Medicine, Soochow University, Suzhou, China

OPEN ACCESS

Edited by:
Pranav Mathur,
Otonomy Inc., United States

Reviewed by:
Allison B. Coffin,
Washington State University, United States
Zhiyong Shao,
Fudan University, China
Phillip Uribe,
Otonomy Inc., United States

***Correspondence:**
Yingzi He
yingzihe09611@126.com
Dong Liu
liudongtom@gmail.com;
tom@ntu.edu.cn
Shaofeng Liu
liusf_cn@163.com

[†] These authors have contributed equally to this work

Specialty section:
This article was submitted to Neuroplasticity and Development, a section of the journal Frontiers in Molecular Neuroscience

Received: 28 December 2021
Accepted: 11 March 2022
Published: 05 May 2022

Citation:
Lu Y, Tang D, Zheng Z, Wang X, Zuo N, Yan R, Wu C, Ma J, Wang C, Xu H, He Y, Liu D and Liu S (2022) Cingulin b Is Required for Zebrafish Lateral Line Development Through Regulation of Mitogen-Activated Protein Kinase and Cellular Senescence Signaling Pathways. Front. Mol. Neurosci. 15:844668. doi: 10.3389/fnmol.2022.844668

Cingulin, a cytoplasmic element of tight junctions (TJs), is involved in maintenance of the integrity of epithelial and endothelial cells. However, the role of cingulin in the development of auditory organs remains unclear. Zebrafish is popular as a model organism for hearing research. Using the whole mount *in situ* hybridization (WISH) experiment, we detected the expression of *cingulin b* in the posterior lateral line system (PLLs) of zebrafish. We traced the early development progress of zebrafish PLLs from 36 hpf to 72 hpf, and found that inhibition of *cingulin b* by target morpholinos resulted in severe developmental obstruction, including decreased number of neuromasts, reduced proliferative cells in the primordium, and repressed hair cell differentiation in the neuromasts. To examine the potential mechanism of *cingulin b* in the development of zebrafish PLL neuromasts, we performed RNA-seq analysis to compare the differently expressed genes (DEGs) between *cingulin b* knockdown samples and the controls. The KEGG enrichment analysis revealed that MAPK signaling pathway and cellular senescence were the key pathways with most DEGs in *cingulin b*-MO morphants compared to the Control-MO embryos. Furthermore, quantitative RT-PCR analysis confirmed the findings by RNA-seq that the transcript levels of cell cycle negative regulators such as *tp53* and *cdkn1a*, were remarkably upregulated after inhibition of *cingulin b*. Our results therefore indicated an important role of *cingulin b* in the development of auditory organs, and MAPK signaling pathway was inhibited while cellular senescence pathway was activated after downregulation of *cingulin b*. We bring forward new insights of cingulin by exploring its function in auditory system.

Keywords: *cingulin b*, zebrafish, development, MAPK signaling pathway, cellular senescence

Abbreviations: DEGs, differently expressed genes; HCs, hair cells; hpf, hours post-fertilization; JNK, Jun N-terminal kinase; MAPK, Mitogen-activated protein kinase; PLL, posterior lateral line; qRT-PCR, quantitative real-time PCR; TJ, tight junctions; WISH, whole mount *in situ* hybridization; GFP, green fluorescent protein.

INTRODUCTION

Tight junctions (TJs), mainly composed of claudins, occludin, ZO proteins, cingulin and paracingulin, are widely localized at the apicolateral borders of cells, and play important roles in maintaining the integrity, permeability and polarity of cells (González-Mariscal et al., 2014; Citi, 2019). Cingulin is localized in the cytoplasmic region of TJs, comprised of a head, a rod and a tail domain (Cordenonsi et al., 1999). Cingulin connects to actin and microtubule cytoskeleton in the head domain, and interacts with Rho family GTPases in the coiled-coil rod region (Cordenonsi et al., 1999; D'atri et al., 2002; Ohnishi et al., 2004; Van Itallie et al., 2009; Yano et al., 2013). Cingulin is mainly involved in regulating the paracellular and blood-brain barrier, for example, edema is more severe in the specific cingulin knock-out mouse model compared to the controls (Hawkins and Davis, 2005; Zhuravleva et al., 2020). In addition, cingulin is found expressed in the organ of Corti, and its distribution is rearranged after high-intensity noise exposure (Raphael and Altschuler, 1991). In a kanamycin damaged guinea pig model, cingulin together with adherens junctions such as E-cadherin and beta-catenin are found reorganized in two distinct planes, and they would preserve the integrity of tissues during scar formation and hair cell degeneration, indicating a barrier function of cingulin in the organ of Corti (Leonova and Raphael, 1997). Cingulin is also expressed in key regions of mouse cochlea, such as spiral ligament, stria vascularis, spiral limbus, and tectorial membrane (Batissoco et al., 2018). However, the role of cingulin in the development of auditory system is unknown.

Zebrafish have a high genetic similarity with the genome of human, and many critical genes required for the development of eyes, ear, brain, heart and other organs are highly conserved between zebrafish and humans, which makes zebrafish an excellent model for studying the human disease (Dooley and Zon, 2000; Howe et al., 2013; Kalueff et al., 2014). Besides, the characteristics of short reproductive cycle, strong reproductive ability, and transparent embryos increase the popularity of zebrafish as an animal model compared to mice (Mandrekar and Thakur, 2009; He et al., 2017). The mature neuromast of zebrafish PLL is consisted of the central hair cells (HCs) and the surrounding supporting cells (SCs), which share many structural and functional similarities with the inner ear cochlea of mammals (Nicolson, 2005), making zebrafish lateral line system a significant model for studying hair cell development, survival and regeneration (Driever et al., 1994; Pyati et al., 2007; Brignull et al., 2009).

In this study, we chose zebrafish as the animal model to explore the potential role of cingulin in the development of lateral line system of zebrafish. In zebrafish, *cingulin b* is orthologous to human cingulin. We firstly designed anti-sense morpholinos to downregulate the expression of *cingulin b*, and the efficacy of *cingulin b*-MO was confirmed by ISH staining and qPCR analysis of *cingulin b*. We observed reduced number of neuromasts, decreased cell proliferation, and repressed HC differentiation in the PLL system of zebrafish after knocking down *cingulin b* compared to the control group. The RNA-seq analysis revealed that MAPK signaling pathway and cellular senescence genes were involved in the development of zebrafish PLL after inhibition of *cingulin b*. Our findings uncover a potential role of cingulin in the development of zebrafish mechanosensory organs.

MATERIALS AND METHODS

Animal Operations

All zebrafish, including the wild type AB line and the transgenic *Tg (cldnb: lynGFP)* and *Tg (brn3c: mGFP)*^{s356t} lines were bred in 28.5°C constant temperature incubator in embryo medium according to the standard formula (Kimmel et al., 1995). The stage of embryonic development was marked as hours- or days- after fertilization (hpf or dpf) (Kimmel et al., 1995). In order to avoid pigmentation, the embryos should be further immersed in 1-phenyl-2-thiourea (PTU) (Sigma-Aldrich) in the culture medium from 10 hpf (Tang et al., 2019). The operations on zebrafish were discussed and permitted by the Animal Conservation and Utilization Committee of Fudan University in Shanghai.

Morpholino Injection and mRNA Rescue Test

Cingulin b-MO, sequenced in 5'-TCCTGTCCGCAGAGAGGG AACTCAT-3', was injected at a dose of 2 ng or 3 ng at one or two cell stage of embryos to reduce the expression of *cingulin b*. The other siblings were considered as controls by injection with a sequence of 5'-CCTCTTACCTCAGT TACAATTTATA-3', namely control-MO (Control-MO). For the messenger RNA (mRNA) rescue experiment, a mixture of *cingulin b*-MO and *cingulin b* mRNA (Forward primer: 5'-AT GAGTTCCCTCTCTGCGGA-3'; Reverse primer: 5'-TCAACAG CTGGTGGTCTGAA-3') was injected at the same stage with other groups.

Whole Mount *in situ* Hybridization in Zebrafish

WISH experiment was operated as previously disclosed (He et al., 2014; Thisse and Thisse, 2014). To examine the expression pattern of *cingulin b* in zebrafish, we collected embryos at various stages including 3.7, 14, and 48 hpf. To verify the efficacy of *cingulin b*-MO in the lateral line system of zebrafish, we collected embryos at 48 hpf. After a series of gradient solutions for dehydration, the collected embryos were stored in pure methanol (100% concentration) at −20°C. Before hybridization, the embryos would be gradient rehydrated first, and then digested with 20 μg/ml protease K. The probe was added and hybridized at 65°C constant temperature overnight. After thorough washes with the SSC-series at 65°C, the embryos were blocked in 2x BBR at room temperature for at least 1 h. Anti- digoxigenin (Dig)-AP Fab fragment (Roche) was added and incubated with specimens overnight at 4°C. Primers for synthesizing the objective genes were listed in **Supplementary Table 1**. Color reaction was implemented with BM purple AP substrate (Roche) in the dark at 37°C, and stopped with NTMT. The embryos after three times rinses were then re-fixed in 4% PFA and treated

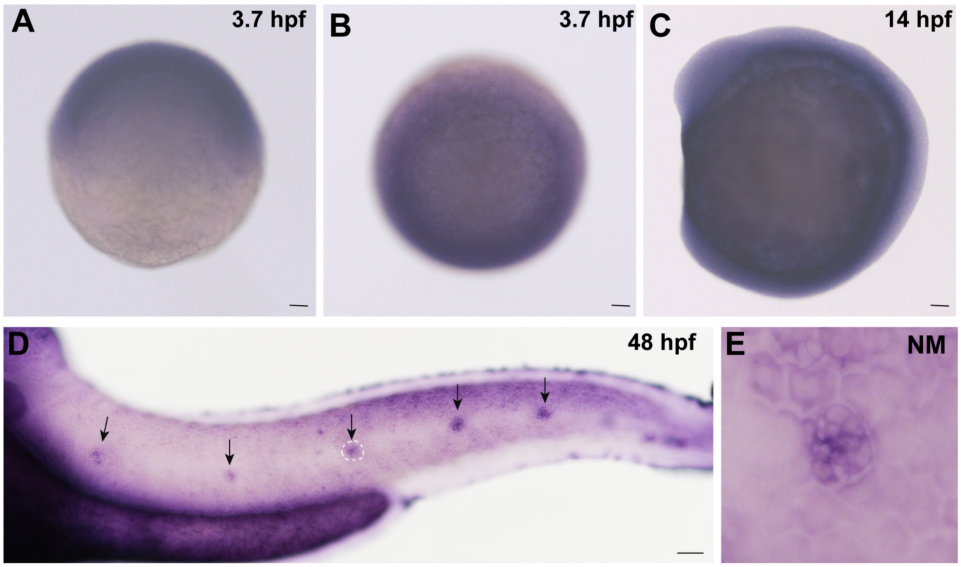

FIGURE 1 | Expression of *cingulin b* is detected during the early development of zebrafish. **(A,B)** *In situ* hybridization staining of *cingulin b* at 3.7 hpf (n = 13) from the lateral view **(A)** and the top view **(B)**. **(C)** *Cingulin b* is expressed in the whole somite at 14 hpf from the lateral view (n = 14). **(D–E)** The expression of *cingulin b* is focused on the neuromasts of the posterior lateral line system at 48 hpf (n = 11). Scale bars mark 50 μm in panel **(A–D)**. The black arrows in D indicate neuromasts, and the white dotted lines labeled neuromast in D is magnified in panel **(E)**.

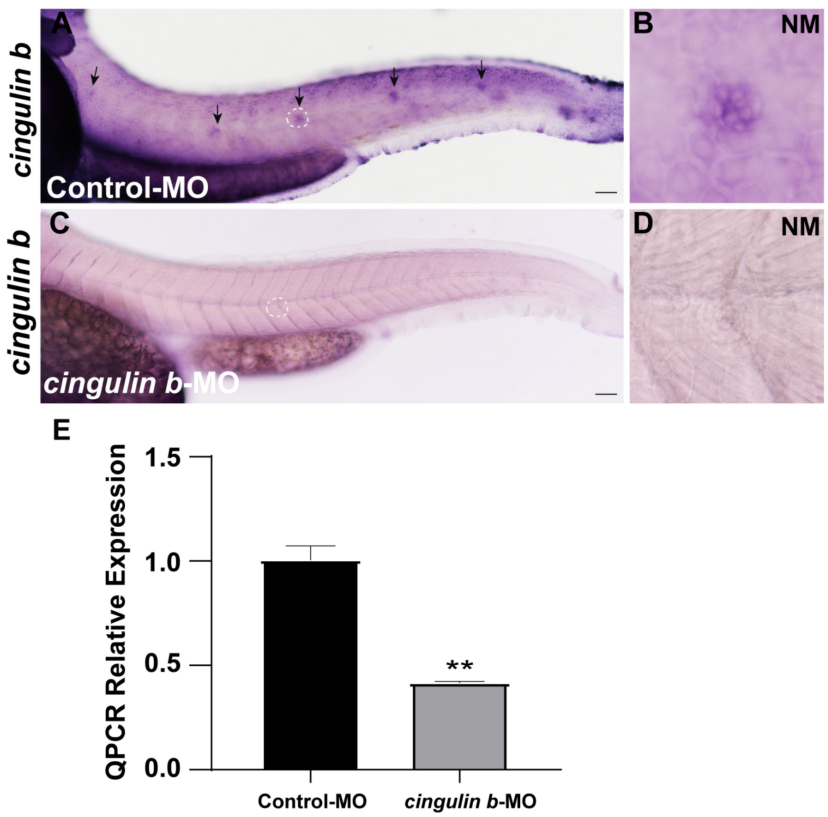

FIGURE 2 | The efficacy of *cingulin b*-MO. **(A–D)** The expression of *cingulin b* is significantly reduced in the *cingulin b*-MO morphants **(C)**, n = 8 compared to that in the Control-MO embryos **(A)** n = 5. **(E)** Quantitative analysis on the level of *cingulin b* between Control-MO and *cingulin b*-MO groups (n = 8 in each group). Data are shown in mean ± SEM, $^{**}p < 0.01$. Scale bars in panel **(A,C)** mark 50 μm. The black arrows in panel **(A)** indicate the neuromasts, and the white dotted lines labeled neuromasts in panel **(A,C)** are magnified in panel **(B,D)**, respectively.

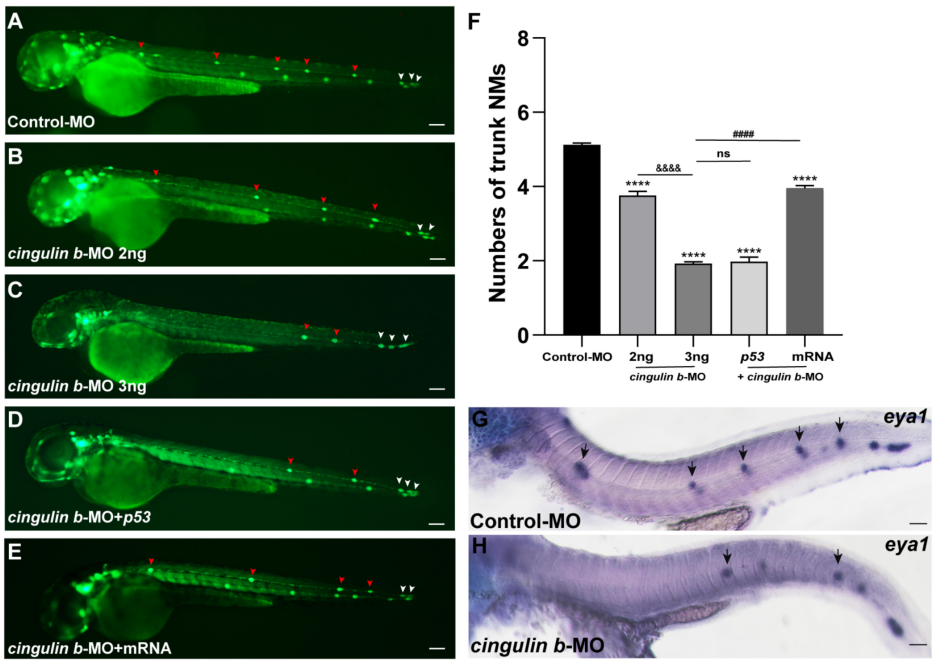

FIGURE 3 | Inhibition of *cingulin b* affects the normal deposition of neuromasts in zebrafish. **(A–E)** In transgenic *cldnb:lynGFP* embryos, the neuromasts of PLL are labeled with green fluorescence. At 48 hpf, the deposition of neuromasts in zebrafish is shown in the control group **(A)**, *cingulin b* knockdown group **(B,C)**, *cingulin b*-MO + *p53* group **(D)**, and *cingulin b*-MO + *cingulin b* mRNA group **(E)**, respectively. **(F)** The number of PLL neuromasts in controls (n = 235), *cingulin b* knockdown (2 ng or 3 ng) group (n = 86 and 264, respectively), *cingulin b*-MO (3 ng) + *p53* group (n = 81), and *cingulin b*-MO (3 ng) + mRNA embryos (n = 180) at 48 hpf. The number of neuromasts decreased dose-dependently after knockdown of *cingulin b* **(A–C,F)**. The decrease in the number of neuromasts is also confirmed when co-injecting with *cingulin b*-MO and *p53* **(C,D,F)**. Combined injection of *cingulin b*-MO and *cingulin b* mRNA can partially rescue the decrease in the number of neuromasts caused by *cingulin b*-MO **(E,F)**. Red arrowheads mark the neuromasts in the trunk, and white arrowheads mark the terminal neuromasts of the PLL system **(A–E)**. Scale bars represent 100 μm. Data are shown in mean ± SEM. *Stands by the comparison with the control group: $^{***}p < 0.0001$. $^{\#}$Stands by the comparison between *cingulin b*-MO group and *cingulin b*-MO + *cingulin b* mRNA group: $^{\#\#\#\#}p < 0.0001$. $^{\&}$Stands by the comparison between 2 ng *cingulin b*-MO group and 3 ng *cingulin b*-MO group: $^{\&\&\&\&}p < 0.0001$. ns means no significance. **(G,H)** The number of *eya1* labeled neuromasts is markedly reduced after knocking down of *cingulin b* **(G)** n = 21 compared to the Control-MOs **(H)** n = 14. The black arrows in G and H indicate the neuromasts. Scale bars in panel **(G,H)** mark 50 μm.

with different gradients of glycerol/PBS. The final specimens were stored in 100% glycerol and photographed by fluorescence stereoscopic microscope. All images were prepared by Photoshop and Illustrator software (2018, Adobe).

BrdU Labeled Cell Proliferation Analysis and Immunohistochemical Staining

Bromodeoxyuridine (BrdU) co-incubation was conducted to label the proliferative cells. The dechorionated embryos at 34 hpf were incubated in 10 mM BrdU (Sigma-Aldrich) for 2 hours to show the cell proliferation in the PLL primordium, while the dechorionated larvae at 2 dpf were incubated in 10 mM BrdU (Sigma-Aldrich) for 24 hours to examine the proliferative cells in PLL neuromasts of zebrafish. The corresponding embryos or larvae were collected, anesthetized in 0.02%MS-222 (Sigma-Aldrich), and fixed in 4% PFA at 4°C overnight. After washing with PBT-2 for 3 times, the collected embryos were soaked in 2 N HCl at 37°C for 30 min. After incubation with the primary anti-BrdU monoclonal antibody (1:200 dilution; Santa Cruz Biotechnology) for 1 h at 37°C following 4°C overnight, the samples were washed for several times and then incubated with the secondary Cy3 polyclonal antibody (1:300 dilution; Jackson) for 1 h at 37°C. DAPI (1:800 dilution; Invitrogen) was added and incubated with the embryos or larvae for 20 min at room temperature to label the nuclei. The fluorescence-labeled embryos were imaged by Leica confocal fluorescence microscope (TCS SP8; Leica). The images obtained were further rotated, cut, and adjusted in the brightness by Photoshop (2018, Adobe) and then the images were aligned and added with fonts or labels by Illustrator software (2018, Adobe).

RNA-Sequencing Analysis

Before specimen collection, the zebrafish embryos at 48 hpf accepted depletion of chorion and the yolk sac. The total RNA was extracted with TRIzol reagent (Thermo Fisher Science) and reversely transcribed into cDNA using the first strand of transcriptional cDNA synthesis kit (Roche). An Illumina HiSeq X Ten platform was used for library sequencing. Raw reads were firstly filtered out the data in low-quality, and the remaining high quality raw data were used for downstream analyses. We used the Spliced Transcripts Alignment to a Reference (STAR) software as the reference genome library. Differential expression

analysis was conducted with the DESeq (2012) R package, and *p*-value <0.05 indicated significant difference. R package was performed for KEGG pathway enrichment analysis of DEGs on the basis of hypergeometric distribution. KEGG pathway database were the reference for further functional and pathway enrichment analysis.

Quantitative Real-Time PCR

In order to fully quantity the mRNA level of target genes, a quantitative real-time PCR (qRT-PCR) system (LightCycler®480) was operated on 48 hpf larvae in the Control-MO group and the *cingulin b*-MO group, using the PrimeScript RT reagent Kit (RR047A, Takara Biomedical Technology) and the SYBR PreMix Ex Taq Kit (RR820A, Takara Biomedical Technology). $^{\Delta\Delta}$Ct method was chosen for results analysis. The primer sequences used in the study were described in **Supplementary Table 2**. Each qPCR assay was repeated in triplicate, and GAPDH was used as the internal reference genes.

Statistical Analysis

All statistics were performed with GraphPad Prism software (version, 8.0c). Comparison between two groups was conducted with double-tailed Student t test, while comparisons among multiple groups were carried out by One-way ANOVA. Statistics were recorded as mean ± SEM (standard error of mean), and the difference was considered to be of significant difference with *p*-value less than 0.05.

RESULTS

Expression of *Cingulin b* in Zebrafish

In order to detect whether *cingulin b* is expressed in zebrafish, we collected embryos at various stages and conducted WISH analysis for *cingulin b* staining. As shown in **Figure 1**, *cingulin b* was detected expressed in the oblong stage at 3.7 hpf (**Figures 1A,B**), the 10-somite stage at 14 hpf (**Figure 1C**), and the deposited PLL neuromasts at 48 hpf (**Figure 1D**), mainly in the central HC area (**Figure 1E**). To confirm the expression of *cingulin b* in the early development of zebrafish, we also conducted the sense control probe for *cingulin b* at 48 hpf, however, we didn't detect any expression of *cingulin b* in the lateral line system of zebrafish compared to that using antisense mRNA probe for *cingulin b* (**Supplementary Figure 1**).

Cingulin b Is Required for Normal Deposition of Neuromasts in Posterior Lateral Line System of Zebrafish

To explore the role of *cingulin b* in the development of zebrafish, we injected specific morpholino (MO) targeting *cingulin b* at

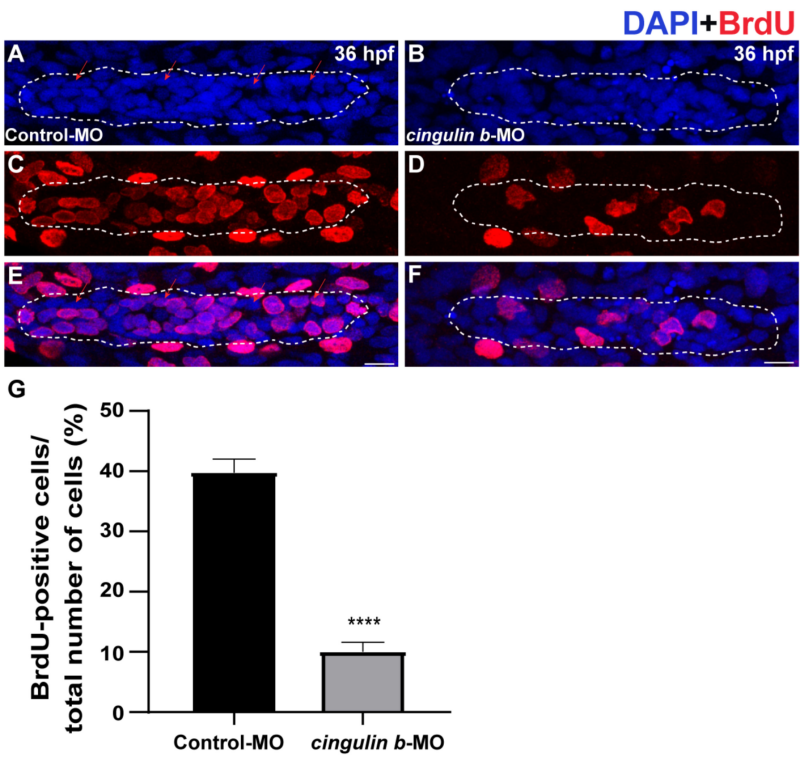

FIGURE 4 | The proliferative cells in the PLL primordium are severely decreased while downregulation of *cingulin b*. **(A–F)** Representative images of BrdU positive proliferating cells and DAPI labeled nuclei in the controls **(A,C,E)** and *cingulin b*-deficient embryos **(B,D,F)** at 36 hpf. Red arrows indicate the rosette-shaped cell clusters in the primordium **(A)**. Scale bars mark the 10 μm scale. **(G)** The quantitative analysis of BrdU index in control (n = 16) and *cingulin b*-MO embryos (n = 18). Data are shown in mean ± SEM. ****p < 0.0001.

one or two cell stage of embryos for knockdown of *cingulin b*. The control group was injected with Control-MO to eliminate the effect of injection operation. The efficacy of *cingulin b*-MO-injection was examined by *in situ* staining of *cingulin b* and qRT-PCR analysis, that we found significantly down-regulated expression of *cingulin b* in the PLL neuromasts in the *cingulin b*-MO morphants compared to the controls (**Figures 2A–D**), and the quantitative level of *cingulin b* was remarkably decreased after *cingulin b*-MO injection compared to the embryos injected with Control-MO (**Figure 2E**). We also examined the embryos as a whole in the Control-MO and *cingulin b*-MO groups, and we did not find any obvious malformation in the entire zebrafish after injection with *cingulin b*-MO (**Supplementary Figure 2**).

The *Tg (cldnb: lynGFP)* zebrafish were used in this study to directly observe the morphology of neuromasts (**Figure 3A**). We counted the number of neuromasts at 48 hpf, a time point when the PLL primordium stops migration and finishes deposition (Kimmel et al., 1995; Nechiporuk and Raible, 2008).

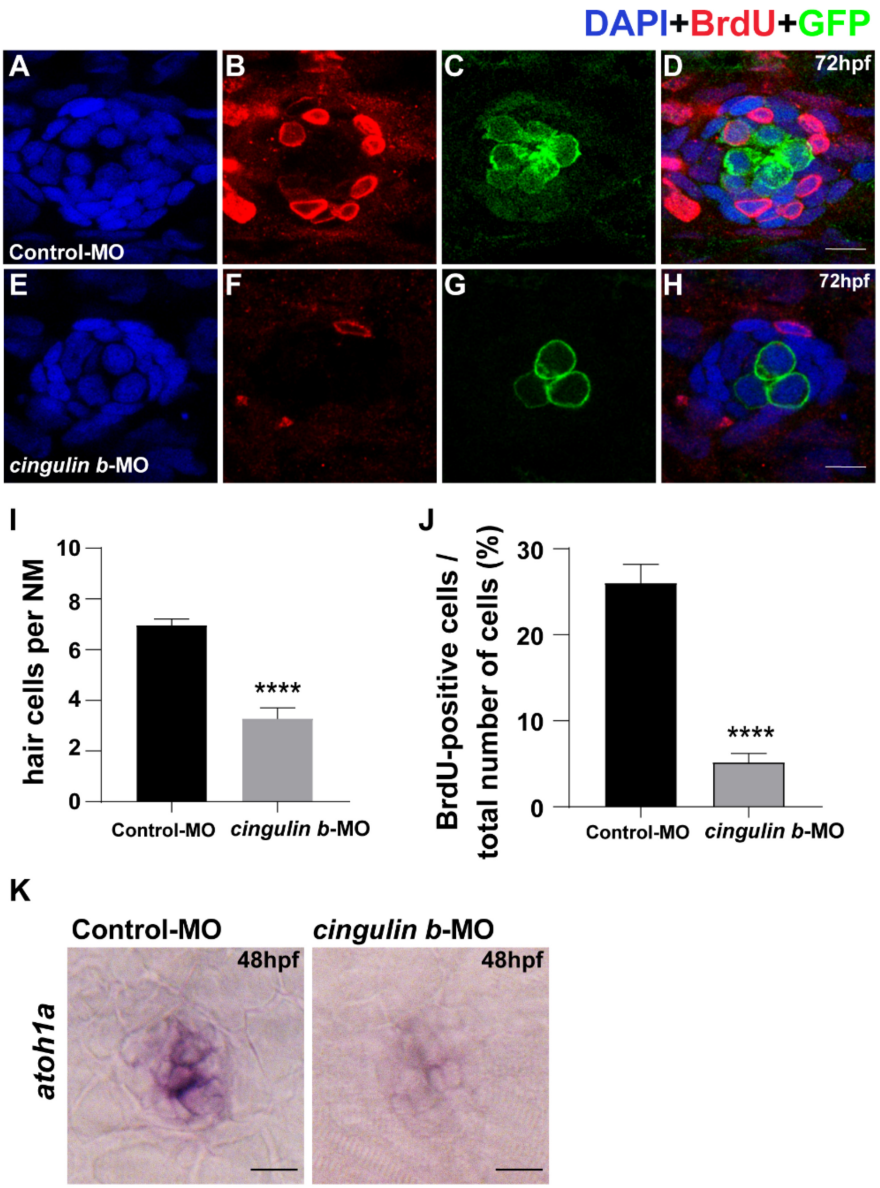

FIGURE 5 | Knockdown of *cingulin b* reduces the number of HCs and cell proliferation in the neuromasts of zebrafish at 72 hpf. **(A–H)** The immunochemical staining of PLL neuromasts in the Control-MO group (n = 19) and *cingulin b*-MO group (n = 15). DAPI (green) labels nuclei **(A,E)** and BrdU (red) labels proliferative cells in the neuromast **(B,F)**. In transgenic *Tg (brn3c: mGFP)*^{s356t} lines, the membrane of HCs in PLL neuromasts are labeled with green fluorescence (GFP) **(C,G)**. **(I)** The average number of hair cells per neuromast is significantly reduced after inhibition of *cingulin b*. **(J)** BrdU index in the neuromasts is also severely downregulated in the *cingulin b*-MO injected embryos compared to the controls. Scale bars mark 10 μm **(A–H)**. Data are shown in mean ± SEM, and $^{****}p < 0.0001$. **(K)** The differentiation of HCs indicated by *atoh1* ISH staining is inhibited after injection with *cingulin b*-MO. Scale bars in panel **(K)** mark 30 μm.

The average number of neuromasts in the trunk was notably decreased in the *cingulin b*-MO-injected morphants compared to that in the Control-MO-injected embryos (**Figures 3A–C,F**). The average number of neuromasts was even lower in 3 ng *cingulin b*-MO group than that in 2 ng *cingulin b*-MO group (**Figures 3B–C,F**), showing a dose-dependent manner, thus, we chose 3 ng dose for the following experiments. To avoid the non-specific effect of morpholino technology, we co-injected *p53* with *cingulin b*-MO, and surprisingly the average number of neuromasts in the trunk in *cingulin b*-MO + *p53* group was equivalent to that in *cingulin b*-MO-only group (**Figures 3C–D,F**). In addition, we also carried out rescue experiment, that combined injection with *cingulin b* mRNA and morpholino could partially restore the reduced number of neuromasts in the trunk (**Figures 3E,F**). The findings suggested that loss of *cingulin b* would affect the normal deposition of PLL neuromasts during the embryonic development of zebrafish. These findings were further validated by the expression of *eya1*, a marker for the neuromast in the lateral line of zebrafish (Kozlowski et al., 2005), that the number of neuromasts in the trunk was severely reduced in the *cingulin b*-MO morphants compared to that in the Control-MO embryos (**Figures 3G,H**). Taken together, our findings indicated that *cingulin b* was required in the lateral line system of zebrafish.

Knockdown of *Cingulin b* Inhibits Cell Proliferation and Hair Cell Differentiation in the Lateral Line System of Zebrafish

During the development of zebrafish lateral line, the collective cells migrate and form rosette-like structure in the trailing region (Aman and Piotrowski, 2008). The deposition of neuromasts occurs after assembly of the last rosette (Nechiporuk and Raible, 2008). Here, we found that cell proliferation in the primordium was destroyed during the embryonic development of zebrafish by BrdU staining after knocking down the gene expression of *cingulin b* (**Figures 4A–F**). BrdU index was defined as the number of BrdU-positive cells divided by the number of total cells labeled by DAPI in this article, which was used to evaluate cell proliferation ability. In 36 dpf, the BrdU index in the primordium of *cingulin b*-MO morphants decreased significantly, that the BrdU index was 10.04% ± 0.02 (n = 17) compared to 39.74% ± 0.02 in the Control-MO group (**Figure 4G**).

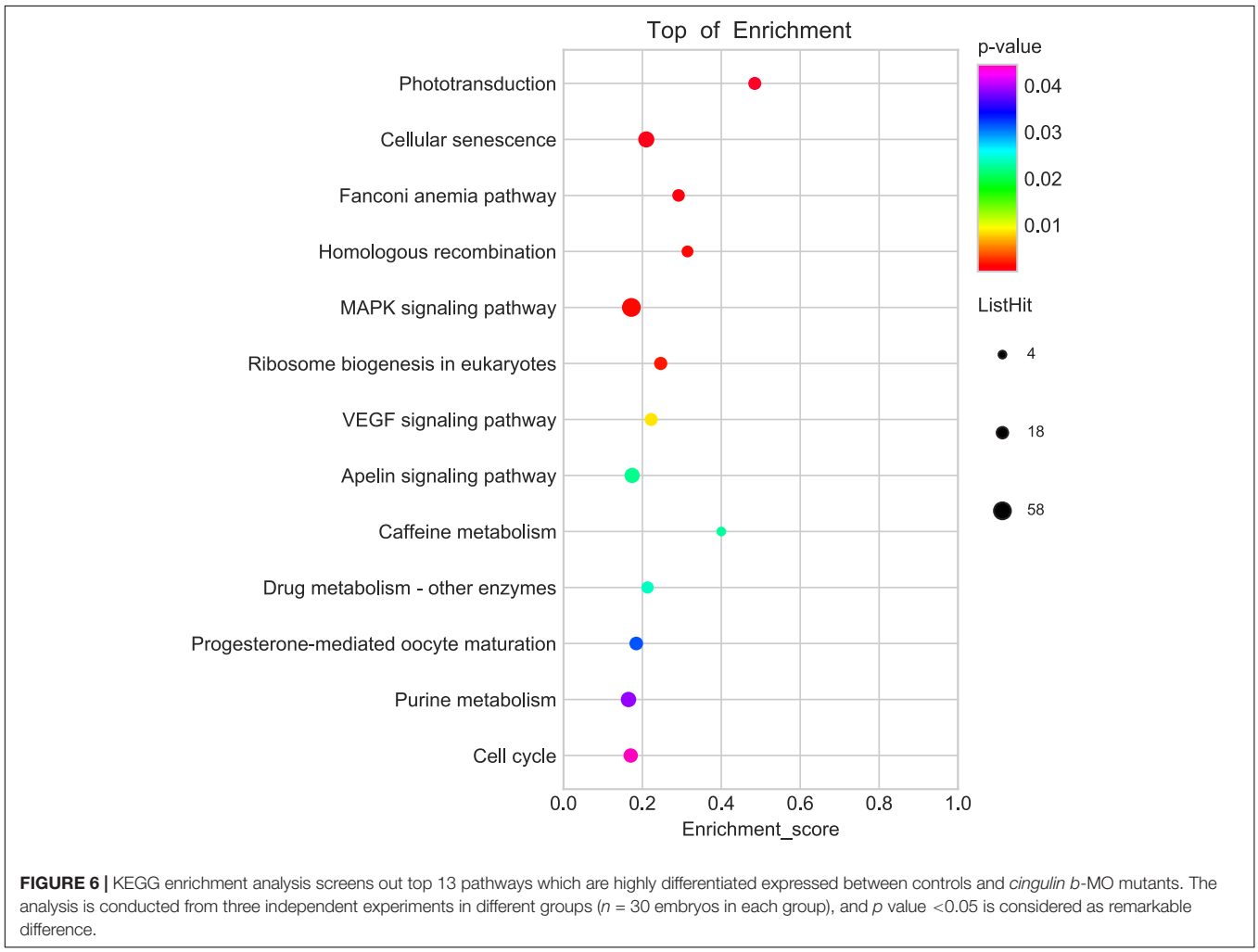

FIGURE 6 | KEGG enrichment analysis screens out top 13 pathways which are highly differentiated expressed between controls and *cingulin b*-MO mutants. The analysis is conducted from three independent experiments in different groups (n = 30 embryos in each group), and p value <0.05 is considered as remarkable difference.

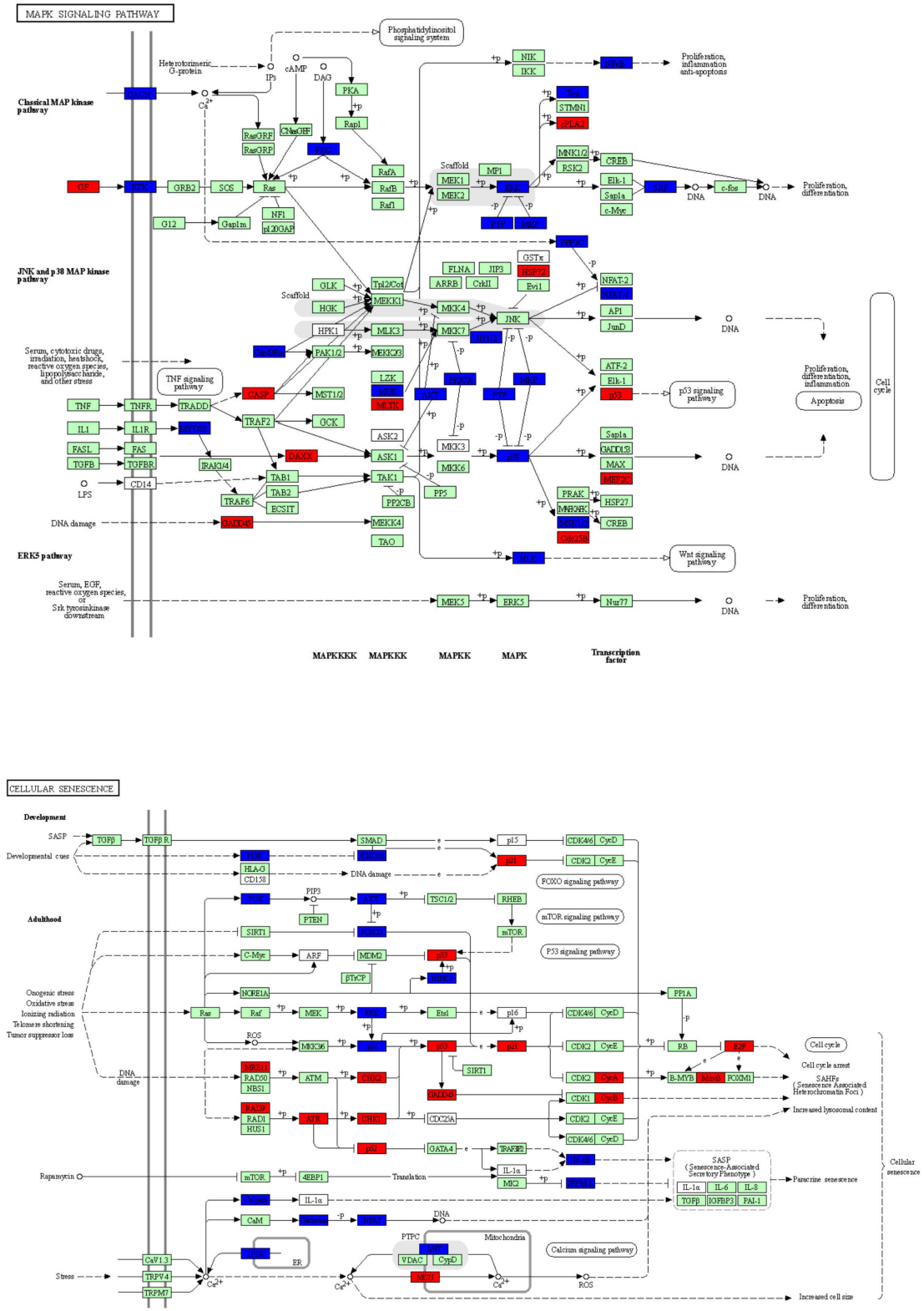

FIGURE 7 | The key KEGG pathways: MAPK signaling pathway and cellular senescence signaling pathway. The red nodes represent upregulated DEGs in *cingulin b*-MO mutants, the green marked node represents downregulated DEGs in *cingulin b*-MO mutants, and the blue marked node represents overlapping targets between Control-MO and *cingulin b*-MO embryos. The analysis is conducted from three independent experiments in different groups, and each group has 30 embryos.

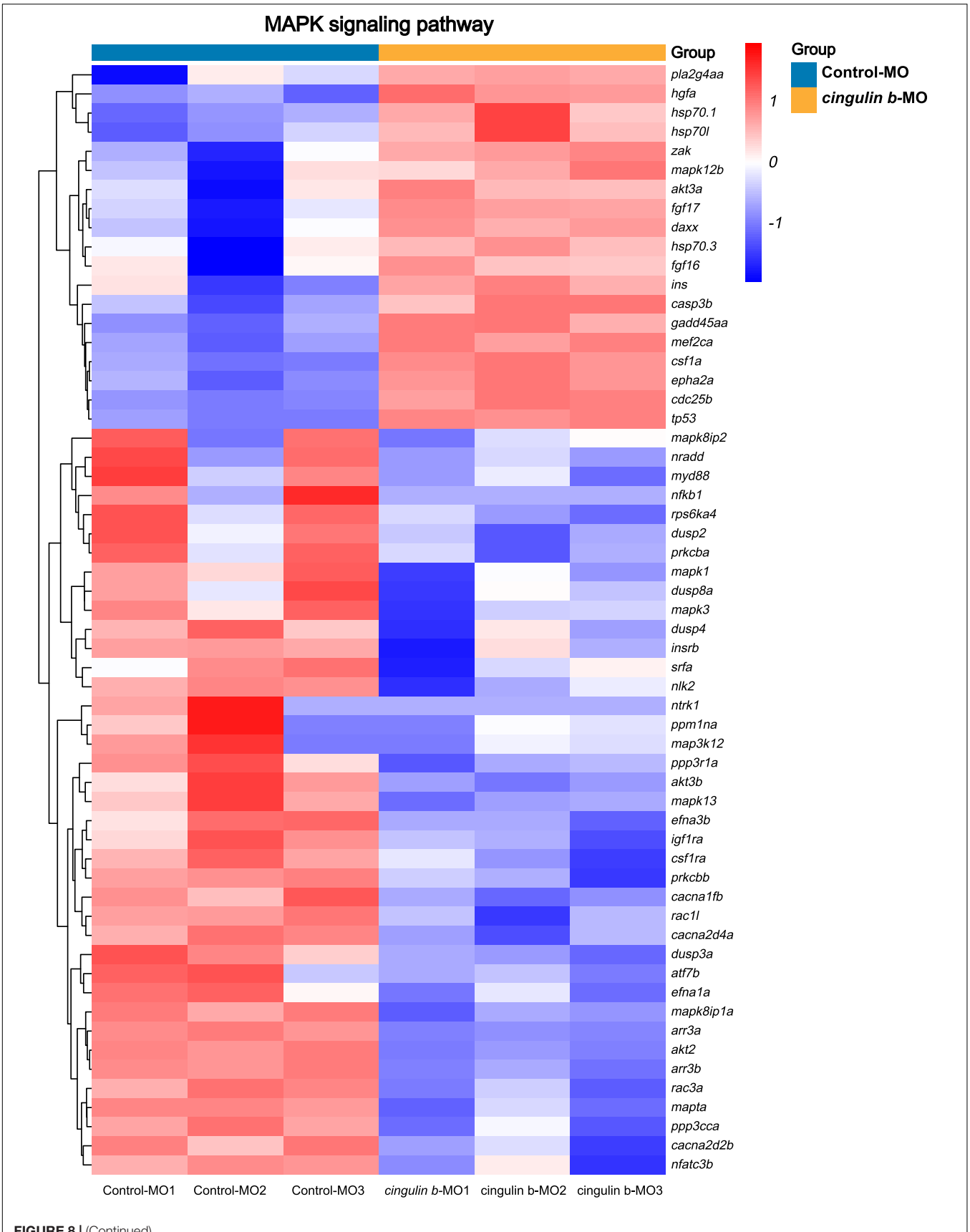

FIGURE 8 | (Continued)

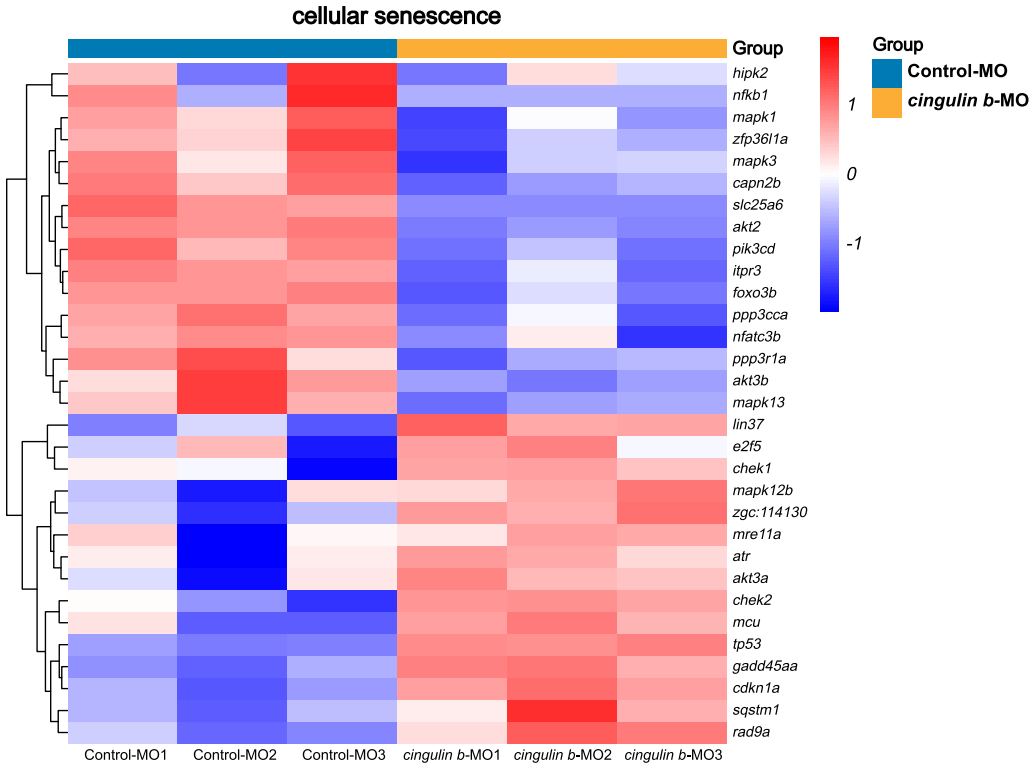

FIGURE 8 | Heatmap analysis of MAPK signaling pathway and cellular senescence signaling pathway in comparison between Control-MO embryos and *cingulin b*-MO morphants. The red indicates upregulated DEGs and the blue indicates downregulated DEGs. The analysis is conducted from three independent experiments in different groups, and each group has 30 embryos.

To investigate the sustained effect of *cingulin b* in zebrafish embryonic development, we stained the proliferative cells with BrdU (**Figures 5B,F**) and collected embryos at 3 dpf. The *Tg (brn3c: mGFP)*^{s356t} zebrafish were used here because of the HCs in neuromasts were labeled with GFP (**Figures 5C,G**). The total cells in neuromast were labeled with DAPI (**Figures 5A,E**). The merged images were shown in **Figures 5D,H**. The number of neuromast HCs in the trunk in *cingulin b*-MO experimental group decreased significantly compared to that of Control-MO group (**Figure 5I**). The BrdU index was also decreased severely in the *cingulin b*-MO group compared to that in the Control-MO group (**Figure 5J**). We also performed ISH staining of *atohla*, a maeker of HC, and found the expression of *atoh1a* was significantly decressed after knocking down of *cigulin b* compared to the control group (**Figure 5K**). Altogether, the data showed that knocking down *cingulin b* inhibited cell proliferation during primordia migration and neuromasts deposition in the early development process of zebrafish PLL system.

Mitogen-Activated Protein Kinase and Cellular Senescence Signaling Pathway Are Significantly Affected After Inhibition of *Cingulin b*

To explore the potential mechanism of *cingulin b* in regulating the development of zebrafish PLL system, we conducted RNA sequencing analysis to compare the difference between the control group and the *cingulin b*-MO mutants. KEGG analysis figured out the 13 top enriched pathways, of which MAPK signaling pathway and cellular senescence were the most two significant pathways evaluated by *p* value and gene counts (**Figure 6**). The key KEGG pathways, namely MAPK signaling pathway and cellular senescence pathway were listed in **Figure 7**. Also, the location of DEGs in *cingulin b*-MO siblings and overlapping genes of enriched pathways were revealed.

Heatmap analysis of DEGs of MAPK pathway and cellular senescence was screened in **Figure 8** for Control-MO group vs. *cingulin b*-MO experimental group, respectively. RT-PCR analysis for some genes from MAPK and cellular senescence signaling pathways was conducted to verify our findings in RNA-sequencing data. The primer sequences were as listed in **Supplementary Table 2**. As shown in **Figure 9**, a total 9 genes in MAPK signaling pathways, 4 genes in cellular senescence pathway, and 9 genes overlapped in the two signaling pathways were examined. The mRNA levels of *mapk1*, *mapk3*, *akt2*, *akt3b*, *atf7b*, *ppp3cca*, and *ppp3r1a* were significantly decreased after knockdown of *cingulin b*, while the expression levels of *tp53*, *mef2ca*, *mapk12b*, and *gadd45aa* were significantly increased in *cingulin b*-MO group. The results of qRT-PCR were in consistency with those found in KEGG analysis, indicating that MAPK signaling was inhibited

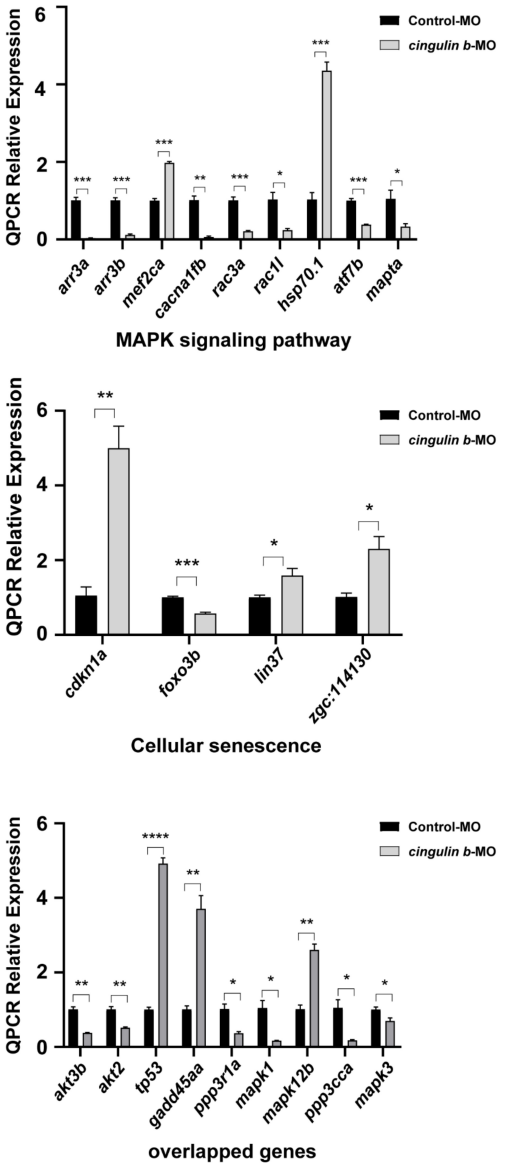

FIGURE 9 | The relative mRNA levels of the indicated genes from MAPK and cellular senescence signaling pathways were normalized to the GAPDH level as determined by qRT-PCR. The results are recorded as mean ± SEM from three independent experiments (n = 8 embryos in each group). $^{*}p < 0.05$, $^{**}p < 0.01$, $^{***}p < 0.001$, and $^{****}p < 0.0001$.

whereas cellular senescence was activated by repression of *cingulin b*.

DISCUSSION

Cingulin is found interacting with connexin-26, a GJB2 encoding gene pivotal in hearing (Kelsell et al., 1997; Najmabadi et al., 2002), through the protein-protein interaction analysis (Batissoco et al., 2018). Besides, cingulin and connexin-26 are also found co-immuno-precipitated in the mouse organ of Cotri and stria vascularis (Batissoco et al., 2018). However, the role of cingulin in the cochlear development has not been identified. Previous studies have demonstrated that the PLL system of zebrafish is a good animal model for the research of mechanosensory organ development for the reason that the HCs in PLL neuromasts share similar structure and function with the mammalian inner ear HCs (He et al., 2017; Tang et al., 2019; Tang et al., 2021). In this study, we detected obvious expression of *cingulin b* in the PLL neuromasts of zebrafish. However, the number of PLL neuromasts was significantly decreased after knockdown of *cingulin b* by antisense MO injection, and we also found severe repression of cell proliferation and hair cell differentiation in the PLL primordium and neuromasts. Additionally, the RNA sequence analysis revealed that MAPK signaling was downregulated while cellular senescence signaling was upregulated in the *cingulin b*-MO embryos compared to the Control-MO injection embryos. Furthermore, we also confirmed the findings by heatmap differential analysis through qRT-PCR experiment. Our findings demonstrated that *cingulin b* was required for the normal development of zebrafish posterior lateral line by regulating the MAPK and cellular senescence signaling pathways.

Mitogen-activated protein kinase (MAPK) has been reported to be related to the formation of primordium in the posterior lateral line system of zebrafish (Harding and Nechiporuk, 2012). MAPK signaling pathway has three subfamilies, namely classical ERK pathway, Jun N-terminal kinase (JNK) pathway, and p38 pathway (Zhang and Liu, 2002). Activation of *ERK1/2* enhances cell proliferation (Lavoie et al., 2020), induces the expression of Cyclin D1 (Chen et al., 2020), and regulates the G1/S progression of cell cycle (Jirmanova et al., 2002). JNK and p38 pathways are often activated by stresses from environment or toxic agents, and usually exert antagonistic effects on cell proliferation and cell survival (Wagner and Nebreda, 2009). As previously reported, *p38* is considered as a negative regulator of cell cycle procession through downregulating cyclins and upregulating inhibitors of cyclin-dependent kinase (CDKIs) (Thornton and Rincon, 2009). In our previous study, we find that JNK inhibitor SP600125 suppresses the development of zebrafish lateral line by induction of *p21* and *p53* (Cai et al., 2016), which links the JNK pathway with tumor suppressor *p53*. Another study also demonstrates that JNK is the negative modulation of *p53* (Das et al., 2007). In the present study, *mapk1* and *mapk3* were significantly downregulated while *tp53* and *gadd45aa* were remarkably upregulated after knockdown of *cingulin b* in comparison with the Control-MO-injected controls, which were in consistency with the previous reporters.

Cellular senescence is a permanent cell cycle arrest after different damages, such as aging, oncogenes, oxidative agents, chemotherapeutic drugs, or epigenetic modulators (Hernandez-Segura et al., 2018). Senescent cells have variable phenotypes but share some common hallmarks in the mechanism, of which CDKIs are widely involved in the progression of cellular senescence, and the main components driving cell cycle arrest in senescence are *cdkn1a* (*p21*), *cdkn2a* (*p16*), and *cdkn2b* (*p15*) (Hernandez-Segura et al., 2018). Cellular senescence is found relevant to the development and tissue regeneration of zebrafish (Da Silva-Alvarez et al., 2020a,b). In this study, we observed

strong elevation in the expression of *tp53*, *cdkn1a*, and *gadd45aa* in the morphants injected with *cingulin b*-MO compared to the control embryos, suggesting the activation of cellular senescence after inhibition of *cingulin b*.

CONCLUSION

We demonstrate that *cingulin b* is required in the development of zebrafish lateral line system, and MAPK signaling pathway and cellular senescence are regulated by morpholino knockdown of *cingulin b*. To our knowledge, it's the first time that the function of *cingulin b* is explored in the mechanosensory organs of zebrafish, but further studies are needed to detect direct evidence between auditory organ development and cingulin, the proteins of tight junctions.

DATA AVAILABILITY STATEMENT

The datasets presented in this study can be found in online repositories. The names of the repository/repositories and accession number(s) can be found below: https://www.ncbi.nlm.nih.gov/search/all/?term=PRJNA802059.

ETHICS STATEMENT

The animal study was reviewed and approved by the Animal Conservation and Utilization Committee of Fudan University in Shanghai.

AUTHOR CONTRIBUTIONS

YH, DL, and SL: conceptualization, methodology, writing—review and editing, and project administration. YL, DT, ZZ, XW, NZ, RY, CeW, HX, JM, and CuW: methodology and formal analysis. YL, DT, and ZZ: validation, investigation, and formal analysis. All authors read and approved the final manuscript.

FUNDING

This work was supported by grants from the National Natural Science Foundation of China (Nos. 82071045, 81870728, and 81800912) and Shanghai Rising-Star Program (19QA1401800).

SUPPLEMENTARY MATERIAL

The Supplementary Material for this article can be found online at: https://www.frontiersin.org/articles/10.3389/fnmol.2022.844668/full#supplementary-material

Supplementary Figure 1 | The representative S (sense control) and AS (antisense mRNA probe) images of *cingulin b* in the PLL of zebrafish at 48 hpf. Black arrowheads indicate neuromasts. Scale bars represent 50 μm, $n = 10$ in S group, and $n = 7$ in AS group.

Supplementary Figure 2 | The representative images of embryos as a whole as followed in the Control-MO and *cingulin b*-MO groups.

Supplementary Table 1 | Primers for the synthesis of objective genes in WISH experiment.

Supplementary Table 2 | Primers for Real-Time PCR experiment.

REFERENCES

Aman, A., and Piotrowski, T. (2008). Wnt/beta-catenin and Fgf signaling control collective cell migration by restricting chemokine receptor expression. *Dev. Cell* 15, 749–761. doi: 10.1016/j.devcel.2008.10.002

Batissoco, A. C., Salazar-Silva, R., Oiticica, J., Bento, R. F., Mingroni-Netto, R. C., and Haddad, L. A. (2018). A Cell Junctional Protein Network Associated with Connexin-26. *Int. J. Mol. Sci.* 2018:19. doi: 10.3390/ijms19092535

Brignull, H. R., Raible, D. W., and Stone, J. S. (2009). Feathers and fins: non-mammalian models for hair cell regeneration. *Brain Res.* 1277, 12–23. doi: 10.1016/j.brainres.2009.02.028

Cai, C., Lin, J., Sun, S., and He, Y. (2016). JNK Inhibition Inhibits Lateral Line Neuromast Hair Cell Development. *Front. Cell Neurosci.* 10:19. doi: 10.3389/fncel.2016.00019

Chen, C. A., Chang, J. M., Yang, Y. L., Chang, E. E., and Chen, H. C. (2020). Macrophage migration inhibitory factor regulates integrin-β1 and cyclin D1 expression *via* ERK pathway in podocytes. *Biomed. Pharmacother.* 124:109892. doi: 10.1016/j.biopha.2020.109892

Citi, S. (2019). The mechanobiology of tight junctions. *Biophys. Rev.* 11, 783–793. doi: 10.1007/s12551-019-00582-7

Cordenonsi, M., D'atri, F., Hammar, E., Parry, D. A., Kendrick-Jones, J., Shore, D., et al. (1999). Cingulin contains globular and coiled-coil domains and interacts with ZO-1, ZO-2, ZO-3, and myosin. *J. Cell Biol.* 147, 1569–1582. doi: 10.1083/jcb.147.7.1569

Da Silva-Alvarez, S., Guerra-Varela, J., Sobrido-Camean, D., Quelle, A., Barreiro-Iglesias, A., Sanchez, L., et al. (2020a). Cell senescence contributes to tissue regeneration in zebrafish. *Aging Cell* 19:e13052. doi: 10.1111/acel.13052

Da Silva-Alvarez, S., Guerra-Varela, J., Sobrido-Camean, D., Quelle, A., Barreiro-Iglesias, A., Sanchez, L., et al. (2020b). Developmentally-programmed cellular senescence is conserved and widespread in zebrafish. *Aging* 12, 17895–17901. doi: 10.18632/aging.103968

Das, M., Jiang, F., Sluss, H. K., Zhang, C., Shokat, K. M., Flavell, R. A., et al. (2007). Suppression of p53-dependent senescence by the JNK signal transduction pathway. *Proc. Natl. Acad. Sci. U S A* 104, 15759–15764. doi: 10.1073/pnas.0707782104

D'atri, F., Nadalutti, F., and Citi, S. (2002). Evidence for a functional interaction between cingulin and ZO-1 in cultured cells. *J. Biol. Chem.* 277, 27757–27764. doi: 10.1074/jbc.M203717200

Dooley, K., and Zon, L. I. (2000). Zebrafish: a model system for the study of human disease. *Curr. Opin. Genet. Dev.* 10, 252–256. doi: 10.1016/s0959-437x(00)00074-5

Driever, W., Stemple, D., Schier, A., and Solnica-Krezel, L. (1994). Zebrafish: genetic tools for studying vertebrate development. *Trends Genet.* 10, 152–159. doi: 10.1016/0168-9525(94)90091-4

González-Mariscal, L., Domínguez-Calderón, A., Raya-Sandino, A., Ortega-Olvera, J. M., Vargas-Sierra, O., and Martínez-Revollar, G. (2014). Tight junctions and the regulation of gene expression. *Semin. Cell Dev. Biol.* 36, 213–223.

Harding, M. J., and Nechiporuk, A. V. (2012). Fgfr-Ras-MAPK signaling is required for apical constriction *via* apical positioning of Rho-associated kinase during mechanosensory organ formation. *Development* 139, 3130–3135. doi: 10.1242/dev.082271

Hawkins, B. T., and Davis, T. P. (2005). The blood-brain barrier/neurovascular unit in health and disease. *Pharmacol. Rev.* 57, 173–185. doi: 10.1124/pr.57.2.4

He, Y., Bao, B., and Li, H. (2017). Using zebrafish as a model to study the role of epigenetics in hearing loss. *Expert Opin. Drug Discov.* 12, 967–975. doi: 10.1080/17460441.2017.1340270

He, Y., Wu, J., Mei, H., Yu, H., Sun, S., Shou, J., et al. (2014). Histone deacetylase activity is required for embryonic posterior lateral line development. *Cell Prolif* 47, 91–104. doi: 10.1111/cpr.12081

Hernandez-Segura, A., Nehme, J., and Demaria, M. (2018). Hallmarks of Cellular Senescence. *Trends Cell Biol.* 28, 436–453. doi: 10.1016/j.tcb.2018.02.001

Howe, K., Clark, M. D., Torroja, C. F., Torrance, J., Berthelot, C., Muffato, M., et al. (2013). The zebrafish reference genome sequence and its relationship to the human genome. *Nature* 496, 498–503. doi: 10.1038/nature12111

Jirmanova, L., Afanassieff, M., Gobert-Gosse, S., Markossian, S., and Savatier, P. (2002). Differential contributions of ERK and PI3-kinase to the regulation of cyclin D1 expression and to the control of the G1/S transition in mouse embryonic stem cells. *Oncogene* 21, 5515–5528. doi: 10.1038/sj.onc.1205728

Kalueff, A. V., Stewart, A. M., and Gerlai, R. (2014). Zebrafish as an emerging model for studying complex brain disorders. *Trends Pharmacol. Sci.* 35, 63–75. doi: 10.1016/j.tips.2013.12.002

Kelsell, D. P., Dunlop, J., Stevens, H. P., Lench, N. J., Liang, J. N., Parry, G., et al. (1997). Connexin 26 mutations in hereditary non-syndromic sensorineural deafness. *Nature* 387, 80–83. doi: 10.1038/387080a0

Kimmel, C. B., Ballard, W. W., Kimmel, S. R., Ullmann, B., and Schilling, T. F. (1995). Stages of embryonic development of the zebrafish. *Dev. Dyn.* 203, 253–310. doi: 10.1002/aja.1002030302

Kozlowski, D. J., Whitfield, T. T., Hukriede, N. A., Lam, W. K., and Weinberg, E. S. (2005). The zebrafish dog-eared mutation disrupts eya1, a gene required for cell survival and differentiation in the inner ear and lateral line. *Dev. Biol.* 277, 27–41. doi: 10.1016/j.ydbio.2004.08.033

Lavoie, H., Gagnon, J., and Therrien, M. (2020). ERK signalling: a master regulator of cell behaviour, life and fate. *Nat. Rev. Mol. Cell Biol.* 21, 607–632. doi: 10.1038/s41580-020-0255-7

Leonova, E. V., and Raphael, Y. (1997). Organization of cell junctions and cytoskeleton in the reticular lamina in normal and ototoxically damaged organ of Corti. *Hear Res.* 113, 14–28. doi: 10.1016/s0378-5955(97)00130-5

Mandrekar, N., and Thakur, N. L. (2009). Significance of the zebrafish model in the discovery of bioactive molecules from nature. *Biotechnol. Lett.* 31, 171–179. doi: 10.1007/s10529-008-9868-1

Najmabadi, H., Cucci, R. A., Sahebjam, S., Kouchakian, N., Farhadi, M., Kahrizi, K., et al. (2002). GJB2 mutations in Iranians with autosomal recessive non-syndromic sensorineural hearing loss. *Hum. Mutat.* 19:572. doi: 10.1002/humu.9033

Nechiporuk, A., and Raible, D. W. (2008). FGF-dependent mechanosensory organ patterning in zebrafish. *Science* 320, 1774–1777. doi: 10.1126/science.1156547

Nicolson, T. (2005). The genetics of hearing and balance in zebrafish. *Annu. Rev. Genet.* 39, 9–22. doi: 10.1146/annurev.genet.39.073003.105049

Ohnishi, H., Nakahara, T., Furuse, K., Sasaki, H., Tsukita, S., and Furuse, M. (2004). JACOP, a novel plaque protein localizing at the apical junctional complex with sequence similarity to cingulin. *J. Biol. Chem.* 279, 46014–46022. doi: 10.1074/jbc.M402616200

Pyati, U. J., Look, A. T., and Hammerschmidt, M. (2007). Zebrafish as a powerful vertebrate model system for *in vivo* studies of cell death. *Semin. Cancer Biol.* 17, 154–165. doi: 10.1016/j.semcancer.2006.11.007

Raphael, Y., and Altschuler, R. A. (1991). Reorganization of cytoskeletal and junctional proteins during cochlear hair cell degeneration. *Cell Motil. Cytoskeleton.* 18, 215–227. doi: 10.1002/cm.970180307

Tang, D., He, Y., Li, W., and Li, H. (2019). Wnt/β-catenin interacts with the FGF pathway to promote proliferation and regenerative cell proliferation in the zebrafish lateral line neuromast. *Exp. Mol. Med.* 51, 1–16. doi: 10.1038/s12276-019-0247-x

Tang, D., Lu, Y., Zuo, N., Yan, R., Wu, C., Wu, L., et al. (2021). The H3K27 demethylase controls the lateral line embryogenesis of zebrafish. *Cell Biol. Toxicol.* 2021:9669. doi: 10.1007/s10565-021-09669-y

Thisse, B., and Thisse, C. (2014). In situ hybridization on whole-mount zebrafish embryos and young larvae. *Methods Mol. Biol.* 1211, 53–67. doi: 10.1007/978-1-4939-1459-3_5

Thornton, T. M., and Rincon, M. (2009). Non-classical p38 map kinase functions: cell cycle checkpoints and survival. *Int. J. Biol. Sci.* 5, 44–51. doi: 10.7150/ijbs.5.44

Van Itallie, C. M., Fanning, A. S., Bridges, A., and Anderson, J. M. (2009). ZO-1 stabilizes the tight junction solute barrier through coupling to the perijunctional cytoskeleton. *Mol. Biol. Cell* 20, 3930–3940. doi: 10.1091/mbc.e09-04-0320

Wagner, E. F., and Nebreda, A. R. (2009). Signal integration by JNK and p38 MAPK pathways in cancer development. *Nat. Rev. Cancer* 9, 537–549. doi: 10.1038/nrc2694

Yano, T., Matsui, T., Tamura, A., Uji, M., and Tsukita, S. (2013). The association of microtubules with tight junctions is promoted by cingulin phosphorylation by AMPK. *J. Cell Biol.* 203, 605–614. doi: 10.1083/jcb.201304194

Zhang, W., and Liu, H. T. (2002). MAPK signal pathways in the regulation of cell proliferation in mammalian cells. *Cell Res.* 12, 9–18. doi: 10.1038/sj.cr.7290105

Zhuravleva, K., Goertz, O., Wölkart, G., Guillemot, L., Petzelbauer, P., Lehnhardt, M., et al. (2020). The tight junction protein cingulin regulates the vascular response to burn injury in a mouse model. *Microvasc. Res.* 132:104067. doi: 10.1016/j.mvr.2020.104067

Conflict of Interest: The authors declare that the research was conducted in the absence of any commercial or financial relationships that could be construed as a potential conflict of interest.

The reviewer ZS declared a shared affiliation with several of the authors DT and ZZ to the handling editor at the time of the review.

Publisher's Note: All claims expressed in this article are solely those of the authors and do not necessarily represent those of their affiliated organizations, or those of the publisher, the editors and the reviewers. Any product that may be evaluated in this article, or claim that may be made by its manufacturer, is not guaranteed or endorsed by the publisher.

frontiers | Frontiers in Molecular Neuroscience

ORIGINAL RESEARCH
published: 30 May 2022
doi: 10.3389/fnmol.2022.916458

Salubrinal Protects Against Cisplatin-Induced Cochlear Hair Cell Endoplasmic Reticulum Stress by Regulating Eukaryotic Translation Initiation Factor 2α Signalling

Wen Lu[1†], Kun Ni[1,2†], Zhuangzhuang Li[1†], Lili Xiao[1], Yini Li[1], Yumeng Jiang[1], Jincheng Zhang[3] and Haibo Shi[1]**

[1] Department of Otolaryngology-Head and Neck Surgery, Shanghai Jiao Tong University Affiliated Sixth People's Hospital, Shanghai, China, [2] Department of Otolaryngology-Head and Neck Surgery, Shanghai Children's Hospital, Shanghai Jiao Tong University, Shanghai, China, [3] Department of Critical Care Medicine, Zhongshan Hospital, Fudan University, Shanghai, China

OPEN ACCESS

Edited by:
Leonard Rybak,
Southern Illinois University Carbondale, United States

Reviewed by:
Federico Kalinec,
University of California, Los Angeles, United States
Bo Zhao,
Indiana University, United States

***Correspondence:**
Jincheng Zhang
pipijincheng@sohu.com
Haibo Shi
hbshi@sjtu.edu.cn

[†] These authors have contributed equally to this work

Specialty section:
This article was submitted to Molecular Signalling and Pathways, a section of the journal Frontiers in Molecular Neuroscience

Received: 09 April 2022
Accepted: 10 May 2022
Published: 30 May 2022

Citation:
Lu W, Ni K, Li Z, Xiao L, Li Y, Jiang Y, Zhang J and Shi H (2022) Salubrinal Protects Against Cisplatin-Induced Cochlear Hair Cell Endoplasmic Reticulum Stress by Regulating Eukaryotic Translation Initiation Factor 2α Signalling. Front. Mol. Neurosci. 15:916458. doi: 10.3389/fnmol.2022.916458

Objective: Cisplatin is a broad-spectrum anti-tumour drug commonly used in clinical practice. However, its ototoxicity greatly limits its clinical application, and no effective method is available to prevent this effect. Endoplasmic reticulum stress (ERS) is reportedly involved in cisplatin ototoxicity, but the exact mechanism remains unclear. Therefore, this study aimed to investigate the role of eukaryotic translation initiation factor 2α (eIF2α) signalling and its dephosphorylation inhibitor salubrinal in cisplatin ototoxicity.

Methods: We evaluated whether salubrinal could protect against cisplatin-induced damage in House Ear Institute-Organ of Corti 1 (HEI-OC1) cells and mouse cochlear explants. By knocking down eIF2α, we elucidated the vital role of eIF2α in cisplatin-induced damage in HEI-OC1 cells. Whole-mount immunofluorescent staining and confocal microscopy of mouse cochlear explants and HEI-OC1 cells were performed to analyse cisplatin-induced damage in cochlear hair cells and the auditory cell line.

Results: Data suggested salubrinal attenuated cisplatin-induced hair cell injury by inhibiting apoptosis. In addition, salubrinal significantly reduced ERS levels in hair cells *via* eIF2α signalling, while eIF2α knockdown inhibited the protective effect of salubrinal.

Significance: Salubrinal and eIF2α signalling play a role in protecting against cisplatin-induced ototoxicity, and pharmacological inhibition of eIF2α-mediated ERS is a potential treatment for cisplatin-induced damage in the cochlea and HEI-OC1 cells.

Keywords: cisplatin, endoplasmic reticulum stress, salubrinal, apoptosis, hearing loss, ototoxicity

INTRODUCTION

Drug-induced hearing loss is one of the most common types of sensorineural hearing loss (Cunningham and Tucci, 2017). Cisplatin is a broad-spectrum anti-tumour drug commonly used in clinical practice, but its extensive and severe adverse effects on normal tissues greatly limit its clinical application (Wilson et al., 2017). Ototoxicity and nephrotoxicity are the main side effects

of cisplatin (Gentilin et al., 2019). Diuretic hydration and other methods may prevent cisplatin nephrotoxic injury (Duan et al., 2020; Bégin et al., 2021). However, the FDA has not yet approved any drug that can effectively prevent cisplatin-induced hearing loss. According to the latest World Hearing Report, 23–50% of adults and up to 60% of children treated with cisplatin suffer from significant hearing loss (Chadha et al., 2021). Hearing loss has a negative effect on a person's quality of life and creates a heavy healthcare burden (Knight et al., 2005; Frisina et al., 2016; Brock et al., 2018). To date, no proven strategy has been established for preventing and treating cisplatin-induced hearing damage, mainly because the mechanism of cisplatin-induced cochlear damage is not fully understood. It is acknowledged that cochlear hair cell (HC) and spiral ganglion cell death is a main pathology contributing to cisplatin-induced hearing loss (Kros and Steyger, 2019). However, an in-depth mechanism of cisplatin damage to cochlea is not well understood, highlighting the importance of further investigation.

The endoplasmic reticulum is found in eukaryotic cells, and it is directly associated with cholesterol metabolism, membrane/secreted proteins, phospholipids, calcium ion signals, and aminoglycosides (Luongo et al., 2017). When the body is subjected to unfavourable stimulation, such as ischemia-reperfusion injury, the endoplasmic reticulum lumen environment is destroyed due to a disorder in Ca^{2+} metabolism (Luongo et al., 2017). As a result, the newly synthesised protein cannot fold normally, resulting in an excessive protein load, which eventually triggers endoplasmic reticulum stress (ERS) (Oyadomari and Mori, 2004; Delaunay-Moisan and Appenzeller-Herzog, 2015; Hetz et al., 2020). An increasing number of studies found that ERS was involved in drug-induced hearing loss and played an important role in the development of ototoxicity, but the precise molecular mechanism was still unclear (Jia et al., 2018; Wen et al., 2021).

Salubrinal (Sal) is a selective protein phosphatase I complex inhibitor, which dephosphorylates eIF2α (Boyce et al., 2005; Binet and Sapieha, 2015). EIF2α phosphorylation reduces the expression of reaction initiators, resulting in reduced synthesis of unfolded proteins and the preservation of the ability to synthesise proteins, which is beneficial for ERS reduction (Hetz, 2012). Therefore, Sal can reduce ERS overexpression and block the initiation of the apoptotic program by selectively inhibiting the dephosphorylation of the PERK-eIF2α phosphate complex (Boyce et al., 2005). Sal plays a cytoprotective role during ERS in various diseases (López-Hernández et al., 2015; Matsuoka and Komoike, 2015; Font-Belmonte et al., 2019). Our previous studies revealed (Zhang et al., 2015, 2020) that Sal treatment improved neurological dysfunction through the inhibition of ER stress after postresuscitation brain injury. This finding suggests that ERS inhibition with Sal could be a neuroprotective strategy. However, whether activating eIF2α phosphorylation with Sal in cochlear HCs could inhibit ERS and thus protect against cisplatin-induced hearing loss is unknown.

In this study, we aimed to investigate the role of eIF2α signalling in cisplatin-induced cochlear damage and establish an effective therapy against cisplatin induced-hearing loss. We hypothesised that Sal could attenuate cisplatin-induced auditory HC apoptosis by inhibiting ERS and this effect was dependent on the eIF2α phosphorylation.

MATERIALS AND METHODS

Animals

All animals were purchased from Shanghai Jie Si Jie Laboratory Animal Co., Ltd. (Shanghai, China). C57BL/6 mice were used in this study for the cochlear explant experiments. Total 28 mice aged P3 was used in our experiments. All experiments were conducted in accordance with the recommendations of the Constitution of the Animal Ethical and Welfare Committee. The study protocol was approved by the Animal Research Committee of the Shanghai Jiao Tong University Affiliated Sixth People's Hospital. Efforts were made to minimise animal pain and the number used as much as possible.

Materials

We used the following reagents and antibodies: Sal (HY-15486; MedChemExpress, Monmouth Junction, NJ, United States), cisplatin (P4394; Sigma-Aldrich, St. Louis, MO, United States), anti-BIP/GRP78 (5,174; Cell Signaling Technology, Danvers, MA, United States), anti-eIF2α (5,324; Cell Signaling Technology), anti-phospho-eIF2α-S51 (AP0692; ABclonal China, Wuhan, China), anti-cleaved caspase 3 (9,661; Cell Signaling Technology), anti-C/EBP homologous protein (CHOP) (2,895; Cell Signaling Technology), anti-cleaved PARP (9,544; Cell Signaling Technology), a rabbit anti-myosin-VIIa antibody (25–6,790; Proteus Bioscience, Ramona, CA, United States), DAPI (ab104139; Abcam, Cambridge, United Kingdom), anti-GAPDH (5,174; Cell Signalling Technology), anti-β-tubulin (2,128; Cell Signalling Technology), and Phalloidin-iFluor 488, 555 (ab176753, ab176756; Abcam), [anti-β-Actin(AC026; ABclonal China, Wuhan, China)].

Cell Culture and Drug Administration

House Ear Institute-Organ of Corti 1 (HEI-OC1) cells provided by Dr. Iris Heredia were cultured according to the guidelines (Kalinec et al., 2016). Before use, the cell line was verified by performing an immunohistochemical analysis of myosin-VIIa, a marker of cochlear hair cells. HEI-OC1 cells were cultured in six-well plates and proliferated under non-permissive conditions (10% CO_2, 33°C) in high-glucose Dulbecco's Modified Eagle's Medium (DMEM) containing 10% foetal bovine serum (Gibco; Thermo Fisher Scientific, Waltham, MA, United States) without antibiotics. When cells reached 80% confluence, subculture was performed using 0.25% trypsin/EDTA (Gibco). Cisplatin (P4394; Sigma-Aldrich) at a final concentration of 20 μM was added and incubated for 24 h to induce HEI-OC1 cell damage.

Cochlear Explants and Drug Administration

The cochlear tissues of C57BL/6J mice on postnatal day 3 (P3) were quickly dissected and cleaned in cold phosphate-buffered saline (PBS) (Sangon Biotech Co., Ltd., Shanghai, China). Next, the cochlea was cultured on glass coverslips coated with Cell-Tak in four-well plates (BD Biosciences, Franklin Lakes, NJ,

United States) with DMEM/F12 growth medium (11330-032; Gibco) containing B-27 supplement (17504-44; Gibco), N-2 supplement (17502-048; Gibco), and ampicillin (50 g/mL, A5354-10ML; Sangon Biotech Co., Ltd.) at 37°C in an incubator environment of 5% CO_2 and 95% O_2. After incubation for a day, we pretreated cochlear explants with or without Sal (10 μM) and then co-treated them with 20 μM cisplatin for 24 h. Cisplatin at a concentration of 20 μM was selected based on our previous study (Li et al., 2022). After removing the cisplatin-containing medium, the cochlear explants were recovered in normal medium for 36 h.

Measurement of Cell Viability

Cell viability analyses were performed using a cell counting kit-8 assay (CCK-8; HY-K0301; MedChemExpress). We trypsinised cells with 0.25% trypsin/EDTA, centrifuged them at 1,000 rpm for 3 min, and resuspended them in medium. Thereafter, HEI-OC1 cells were seeded at a density of 4,000 cells/well in 96-well plates. After 24 h of incubation, the medium was replaced with medium containing cisplatin (20 μM) and different doses of Sal. After 24 h of incubation, CCK8 solution was added per well and incubated with the cells at 37°C for 1 h. Finally, we used a microplate reader to determine the absorbance at 450 nm. The above experiment was repeated thrice.

Immunofluorescence

Immunofluorescence experiments were performed to determine the different apoptosis and ERS markers. After different treatments, the HEI-OC1 cells or cochlear explants were washed with PBS thrice for 15 min. Afterward, we fixed HEI-OC1 cells or cochlear explants with 4% paraformaldehyde (Sangon Biotech Co., Ltd.) for 1 h at 25°C and then washed them thrice with 0.01 M PBS (Sangon Biotech Co., Ltd.). After permeabilisation with 1% Triton X-100 (Solarbio Life Sciences, Beijing, China) for 30 min, non-specific sample binding sites were blocked with 5% bovine serum albumin in PBS (Sigma-Aldrich) at 25°C for 1 h and then incubated with primary antibodies at 4°C overnight (dilution: 1:200–1:500). Subsequently, the samples were washed thrice with PBS and incubated with secondary antibodies (A32723, A32731, A32727, and A32732; Thermo Fisher Scientific) at room temperature for 1 h. Thereafter, the auditory HCs were labelled with FITC-labelled phalloidin (P5282; Sigma-Aldrich), and cell nuclei were labelled with DAPI (Sigma-Aldrich). Finally, we washed the cells thrice with PBS, mounted them with DAPI, and imaged them using an LSM 710 confocal microscope (Zeiss, Oberkochen, Germany). The fluorescence intensity of CHOP was measured using Image J software (NIH, Bethesda, MD, United States).

Western Blotting

HEI-OC1 cells were lysed and prepared in RIPA buffer (Sangon Biotech Co., Ltd.) containing protease and phosphatase inhibitor cocktail (Sangon Biotech Co., Ltd.) on ice for 30 min. Thereafter, cell lysates were centrifuged at 12,000 rpm for 20 min, and the supernatants were collected for protein quantification. Protein concentrations were quantified using a BCA protein assay kit (Sangon Biotech). Equal amounts of proteins were loaded on 10% sodium dodecyl sulphate-polyacrylamide gel for separation *via* electrophoresis and then transferred onto nitrocellulose membranes, which were then blocked with 5% skim milk powder in Tris-buffered saline containing 0.1% Tween 20 (TBST) (Sangon Biotech) for 1 h at room temperature. Subsequently, the membranes were incubated with anti-BIP (5,174; Cell Signaling Technology), anti-eIF2α (5,324; Cell Signaling Technology), anti-phospho-eIF2α-S51 (AP0692; ABclonal), anti-cleaved caspase 3 (9,661; Cell Signaling Technology), anti-CHOP (2,895; Cell Signaling Technology), anti-cleaved PARP (9,544; Cell Signaling Technology), anti-GAPDH (5,174; Cell Signaling Technology), and anti-β-tubulin (2,128; Cell Signaling Technology). The antibodies used ranged from 1:500 to 1:1,000. After incubation with the primary antibodies overnight at 4°C, the membranes were washed thrice for 30 min with 1 × TBST and then incubated with the corresponding secondary antibodies (AS014 and AS003; ABclonal) at room temperature for 2 h. The cell membranes were examined using an Omni-ECL Femto Light Chemiluminescence Kit (SQ201; Epizyme, Cambridge, MA, United States) and imaged using a ChemiDocXRS imaging system (Bio-Rad Laboratories, Hercules, CA, United States). ImageJ software was used to measure band intensities. Each experiment was repeated more than thrice.

Small Interference RNA Transfection

We designed three eIF2α-specific mouse Small Interference RNA (siRNAs) (RiboBio, Guangzhou, China) to knock down eIF2α expression in HEI-OC1 cells. A siRNA encoding a nonsense sequence was designed as the negative control. HEI-OC1 cells were transfected with eIF2α-siRNA or negative-siRNA according to the manufacturer's instructions. HEI-OC1 cells were plated in six-well culture plates at a density of 3×10^5 and transfected with siRNA using Lipofectamine 3000 (L3000001; Invitrogen, Waltham, MA, United States) for 24 h. The transfection efficiency was measured using western blotting. The following siRNAs were used to knock down eIF2α expression: 5′-TCCAAGAGCTTGAAGATTT-3′, 5′-CCTTCTCCAAGAGCTTGAA-3′, and 5′-CTCCAAGAGCT TGAAGATT-3′.

Cell Counts

For HC quantification, cells labelled with myosin7a and showing normal nuclei were considered surviving HCs. To quantify HCs, we imaged the entire cochlea using a Zeiss microscope with a 40 × lens and used ImageJ software to quantify immunopositive cells. The average number of HCs per 130 μm in the apical, middle, and basal turns of the cochlea was calculated for each group. For quantification of apoptotic HCs, we selected only the middle portion of each explant.

Statistical Analysis

Data were analysed using GraphPad Prism statistical software (version 8, GraphPad Software, Inc., San Diego, CA, United States). Normally distributed measures are expressed as mean ± Standard Error of Mean (SEM). Independent sample *t*-tests were performed for comparisons between two groups.

One-way ANOVA was used for comparisons between multiple groups. *P*-values < 0.05 were considered statistically significant.

RESULTS

Sal Reduced the Cytotoxicity of Cisplatin-Induced House Ear Institute-Organ of Corti 1 Cells

Our previous study determined that cisplatin damaged HEI-OC1 cells appropriately at a concentration of 20 μm for 24 h (Li et al., 2022). HEI-OC1 cells were treated with different Sal concentrations (0–100 μM) for 24 h to determine its toxicity. The CCK-8 results showed that Sal did not decrease the viability of HEI-OC1 cells (**Figure 1A**). Therefore, HEI-OC1 cells were treated with or without Sal to determine whether Sal could protect against cisplatin-induced damage. The CCK-8 results showed that viability increased gradually with increasing doses of Sal (0–100 μM) (**Figure 1B**). Since the viability of 50 μM Sal-treated HEI-OC1 cells did not significantly differ from that of 100 μM Sal-treated cells following cisplatin exposure, 50 μM Sal was selected as the treatment condition for 24 h in the rest of this study. Moreover, dead cells on the top of the monolayer are more numerous in the cisplatin-treated group, while 50 μM Sal significantly alleviated this damage (**Figure 1C**). These findings suggest that Sal could effectively reverse cisplatin-induced ototoxicity at an appropriate dose.

Sal Alleviated Cisplatin-Induced Apoptosis in House Ear Institute-Organ of Corti 1 Cells

To determine the protective effect of Sal in HEI-OC1 cells, we measured the percentage of apoptotic cells in the control, Sal, cisplatin, and cisplatin + Sal groups. Immunofluorescence analysis of cleaved caspase 3 showed that the number of cisplatin-induced apoptotic cells was reduced after Sal treatment (**Figures 2A,B**). Consistent with the immunofluorescence results, western blotting showed that the expression of cleaved caspase 3 and cleaved-PARP was significantly reduced after Sal treatment (**Figures 2C–E**). These findings suggested that Sal attenuated cisplatin-induced apoptosis in HEI-OC1 cells.

Sal Decreased Cisplatin-Induced Apoptosis in Cochlear Hair Cells

To determine the effect of Sal in protecting cochlear HCs after cisplatin damage, we used cochlear organ explant cultures. The cochleae of C57BL/6 mice were dissected at P3, and the surrounding tissue and bone were removed using PBS. Cochlear

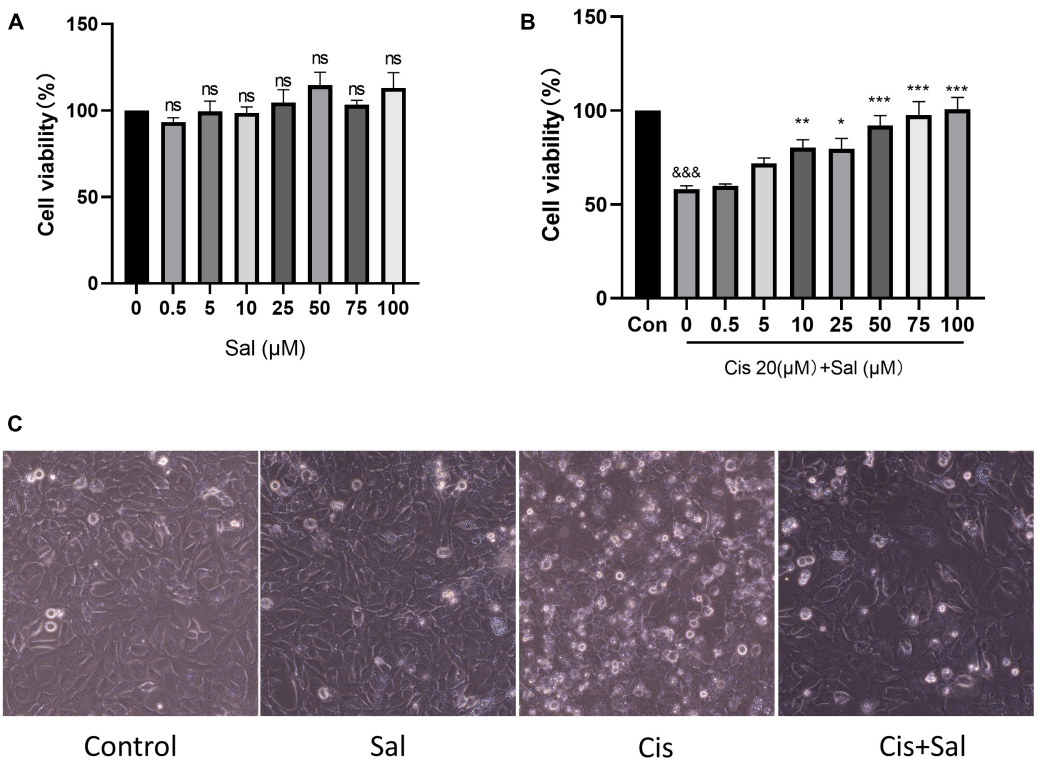

FIGURE 1 | Sal enhances the viability of HEI-OC1 cells after cisplatin damage. **(A)** HEI-OC1 cells were treated with different Sal concentrations for 24 h. **(B)** HEI-OC1 cells were pretreated with or without different Sal concentrations (0–100 μM) for 4 h, followed by 20 μM co-treatment for 24 h except for those in the control group. **(C)** Image of HEI-OC1 cells cultured with different Sal or cisplatin concentrations. Scale bars = 100 μm. Cell viability was measured using the CCK-8 assay. Values are presented as mean ± SEM from independent experiments. $^{*}P < 0.05$, $^{**}P < 0.01$, and $^{***}P < 0.001$ vs. the control group; $^{\&\&\&}P < 0.001$ vs. the cisplatin group. ns, no statistical difference; Sal, salubrinal; Cis, cisplatin; con, control.

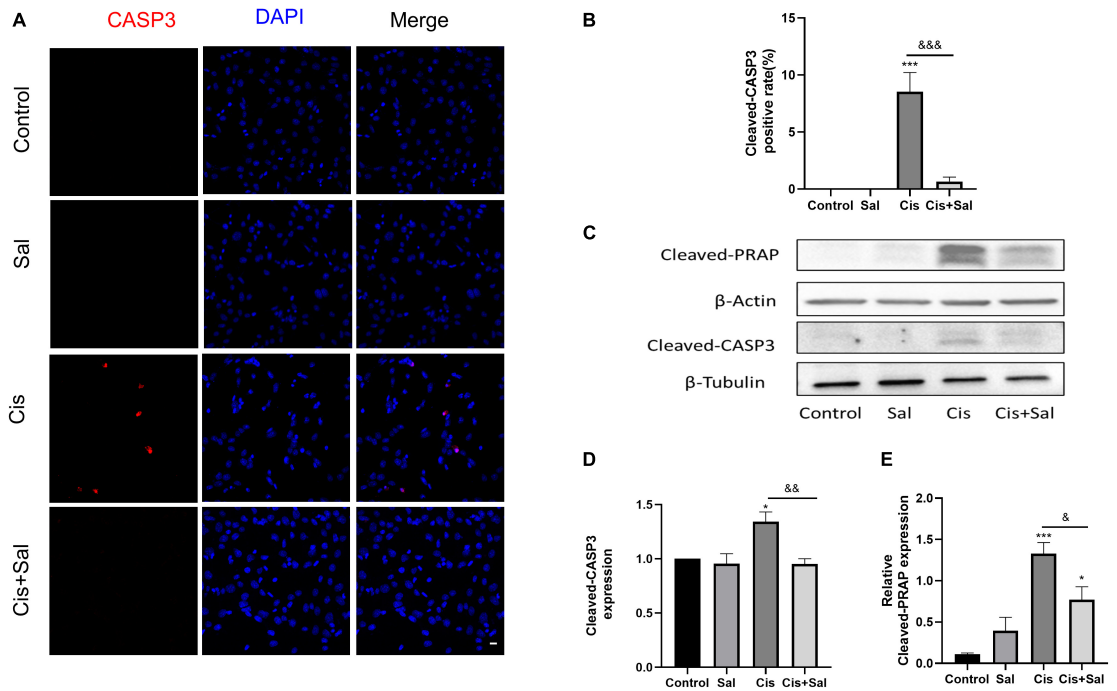

FIGURE 2 | Sal reduces cisplatin-induced apoptosis in HEI-OC1 cells. **(A)** Cleaved caspase 3 (red) and DAPI (blue) double staining showing apoptotic cells after the different treatments (n = 3). **(B)** Quantitative analysis of apoptotic cells in **(A)**. **(C)** Western blotting results showing cleaved PARP (n = 3) and cleaved caspase 3 (n = 3) in the different groups. **(D,E)** Quantitative analysis of the western blotting results in **(C)**. Values are presented as mean ± SEM from independent experiments. $^{*}P < 0.05$ and $^{***}P < 0.001$ vs. the control group; $^{\&}P < 0.05$, $^{\&\&}P < 0.01$, and $^{\&\&\&}P < 0.001$ vs. the cisplatin group. Sal, salubrinal; Cis, cisplatin. Scale bars = 20 μm.

explants were glued to glass cover slides coated with Cell-Tak (BD Biosciences) and divided into the following groups: control, Sal alone, cisplatin, and Sal + cisplatin (10 μM Sal pretreated for 4 h and 20 μM cisplatin co-treated for 24 h) (**Figure 3A**). To better characterise cochlear HCs, we performed immunofluorescence staining using antibodies against myosin-VIIa. Consistent with the results for HEI-OC1 cells, the number of HCs was significantly reduced in the cisplatin alone group, whereas Sal treatment significantly increased the number of HCs after cisplatin exposure (**Figures 3B–E**). Furthermore, no significant difference was found between the Sal alone and control groups, suggesting that Sal at 10 μM did not affect the survival of HCs. To further validate these results, immunofluorescence staining of cleaved caspase 3 was performed to analyse apoptotic HCs in different groups. Consistent with the number of HCs, the number of cleaved caspase 3-positive HCs was significantly increased in the cisplatin group, when10 μM Sal significantly reduced the cleaved caspase 3-positive HCs in the Sal + cisplatin group (**Figure 4**).

Sal Attenuated Cisplatin-Induced Endoplasmic Reticulum Stress in Hair Cells and House Ear Institute-Organ of Corti 1 Cells

To determine whether Sal protects against cisplatin-induced damage by inhibiting ERS, the expression of CHOP and GRP78/BIP ERS markers was measured in HEI-OC1 cells in the different groups (**Figure 5**). Immunofluorescence staining showed that cisplatin treatment induced nuclear CHOP accumulation compared with the untreated controls (**Figures 5A,B**), whereas Sal and cisplatin co-treatment reduced CHOP expression and increased BIP expression. To further verify that Sal alleviated HC damage, we used immunofluorescence staining of CHOP in the cochlear explants. Similar to the results in HEI-OC1 cells, cisplatin treatment significantly increased CHOP expression, whereas Sal and cisplatin co-treatment significantly decreased CHOP expression (**Figures 5C,D**). Consistent with the immunofluorescence staining results, western blotting results showed that CHOP expression increased in the cisplatin group but decreased in the Sal group (**Figures 5E–H**). These data suggest that cisplatin caused significant ERS in cochlear HCs, and Sal could effectively reverse this damage.

Sal Protected House Ear Institute-Organ of Corti 1 Cells Against Cisplatin-Induced Apoptosis by Eukaryotic Translation Initiation Factor 2α Regulation

Sal selectively attenuates the dephosphorylation of phosphorylated eIF2α and protects cells from ERS-induced apoptosis (Zhang et al., 2015). p-eIF2α expression increased with increasing Sal concentration (**Figures 6A,B**). To investigate

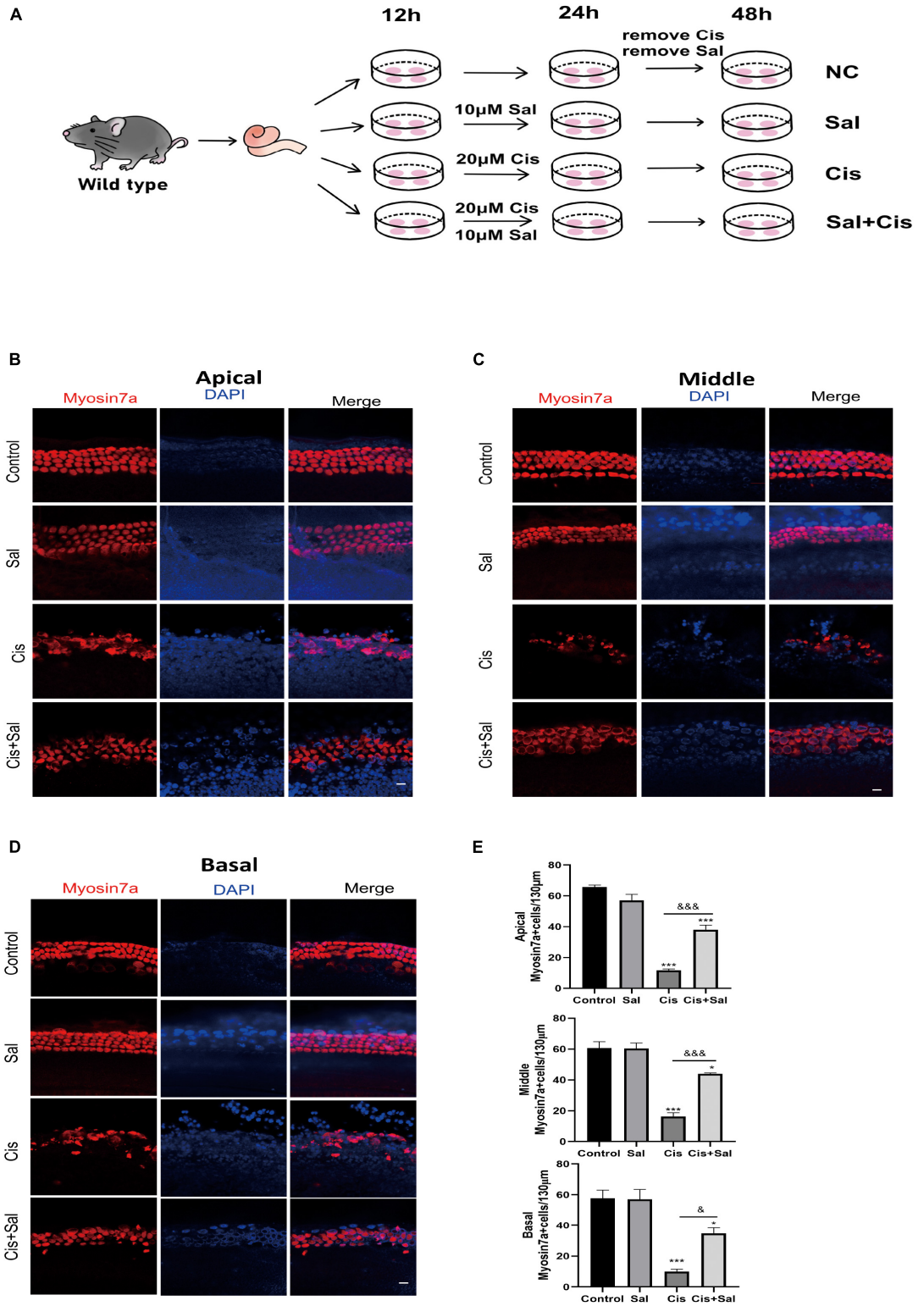

FIGURE 3 | Sal promotes hair cell (HC) survival in the cochlea after cisplatin exposure. **(A)** Schematic diagram of drug addiction in tissue culture. **(B,D)** HCs in the apical **(B)**, middle **(C)**, and basal turns **(D)** of the cochlea were stained with anti-myosin-VIIa antibody and DAPI in the control, 10 μM Sal, 20 μM cisplatin, and 20 μM cisplatin + 10 μM Sal groups. **(E)** Quantification of the number of myosin VIIa-positive cells in the apical, middle, and basal turns of the cochlea. Values are presented as mean ± SEM from independent experiments. $^{*}P < 0.05$ and $^{***}P < 0.001$ vs. the control group; $^{\&}P < 0.05$ and $^{\&\&\&}P < 0.001$ vs. the cisplatin group. Scale bars = 10 μm.

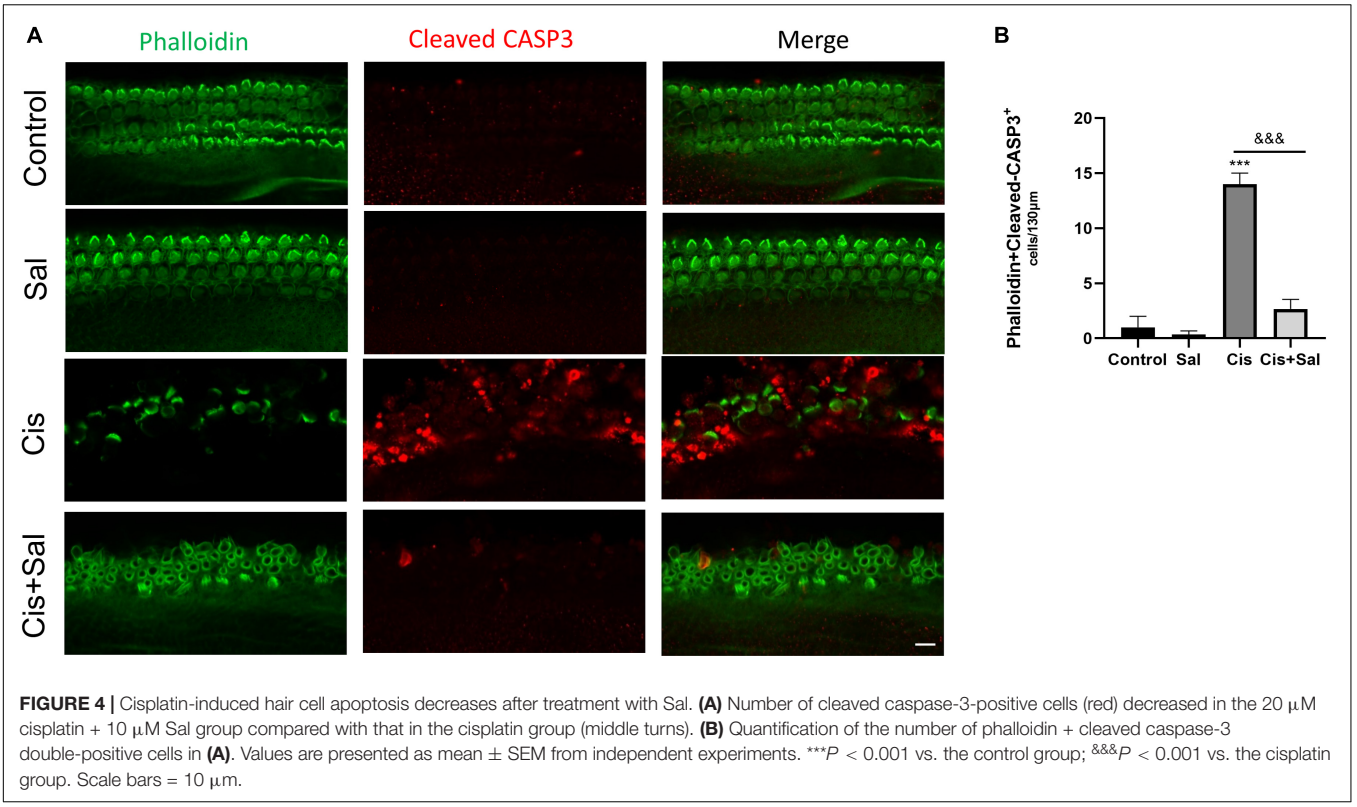

FIGURE 4 | Cisplatin-induced hair cell apoptosis decreases after treatment with Sal. **(A)** Number of cleaved caspase-3-positive cells (red) decreased in the 20 μM cisplatin + 10 μM Sal group compared with that in the cisplatin group (middle turns). **(B)** Quantification of the number of phalloidin + cleaved caspase-3 double-positive cells in **(A)**. Values are presented as mean ± SEM from independent experiments. $^{***}P < 0.001$ vs. the control group; $^{\&\&\&}P < 0.001$ vs. the cisplatin group. Scale bars = 10 μm.

the role of p-eIF2α in cisplatin-induced cytotoxicity, we further analysed p-eIF2α expression after Sal treatment. Western blotting results showed that p-eIF2α expression significantly decreased in the cisplatin group but increased after Sal treatment (**Figures 6C,D**). Furthermore, Sal treatment did not affect the total amount of eIF2α expression (**Figures 6E,F**). These findings suggest that Sal protected HCs from cisplatin-induced apoptosis by activating the eIF2α pathway.

Silencing Eukaryotic Translation Initiation Factor 2α Enhanced Cisplatin-Induced Hair Cell Death

We transfected HEI-OC1 cells with eIF2α-specific or control siRNA to determine whether eIF2α plays a direct role in the Sal-mediated protective effects against cisplatin-induced cell death. The best knockdown effect was observed in HEI-OC1 cells with a Si-eIF2α mixture (**Figure 7A**). After 36-h transfection, cell viability was analysed using the CCK-8 assay, and results showed that Sal significantly enhanced HEI-OC1 cell viability in the presence of cisplatin. However, cell viability was significantly reduced after eIF2α-specific siRNA treatment compared with that in the control siRNA-treated cells (**Figure 7B**). Furthermore, consistent with the CCK-8 results, western blotting results showed that the expression of cleaved caspase-3 was significantly increased in cells treated with eIF2α-specific siRNA (**Figures 7C,D**). These results suggest that eIF2α was responsible for the protective effects of Sal against cisplatin-induced apoptosis in HCs.

The results for both HEI-OC1 cells and cochlear explants showed that the PERK/ATF4/CHOP signalling branch plays an important role in cisplatin-induced ototoxicity (**Figure 8**).

DISCUSSION

Sal attenuated cisplatin-induced HC damage by inhibiting apoptosis. Furthermore, the effect of Sal was attributed to ERS inhibition, which was dependent on p-eIF2α activity. Knockdown of eIF2α reversed the protective effect of Sal against cisplatin-induced injury in HEI-OC1 cells, leading to cisplatin-induced apoptosis. These results demonstrate that cisplatin-induced HC apoptosis was associated with eIF2α signalling, one of the three major pathways of the unfolded protein response (UPR), while Sal could protect against cisplatin-induced ototoxicity in cochlear HC ERS.

Ototoxic chemicals including cisplatin, acetaminophen, and aminoglycoside disrupt the correct folding of protein or induce mistranslation, leading to the aggregation of unfolding or misfolding proteins in the ER of cochleae (Kalinec et al., 2014; Oishi et al., 2015; Qu et al., 2022). Once the excessive accumulation of unfolding or misfolding proteins occurs in the ER, severe ERS results in an inability to maintain ER homeostasis, leading to cell apoptosis and death (Hetz and Papa, 2018). ERS, evoked by misfolding and unfolding proteins in the ER, can activate the UPR to reduce ER workload by increasing the protein folding capacity, removing misfolded/unfolded proteins from the ER, and inhibiting translation to block new protein

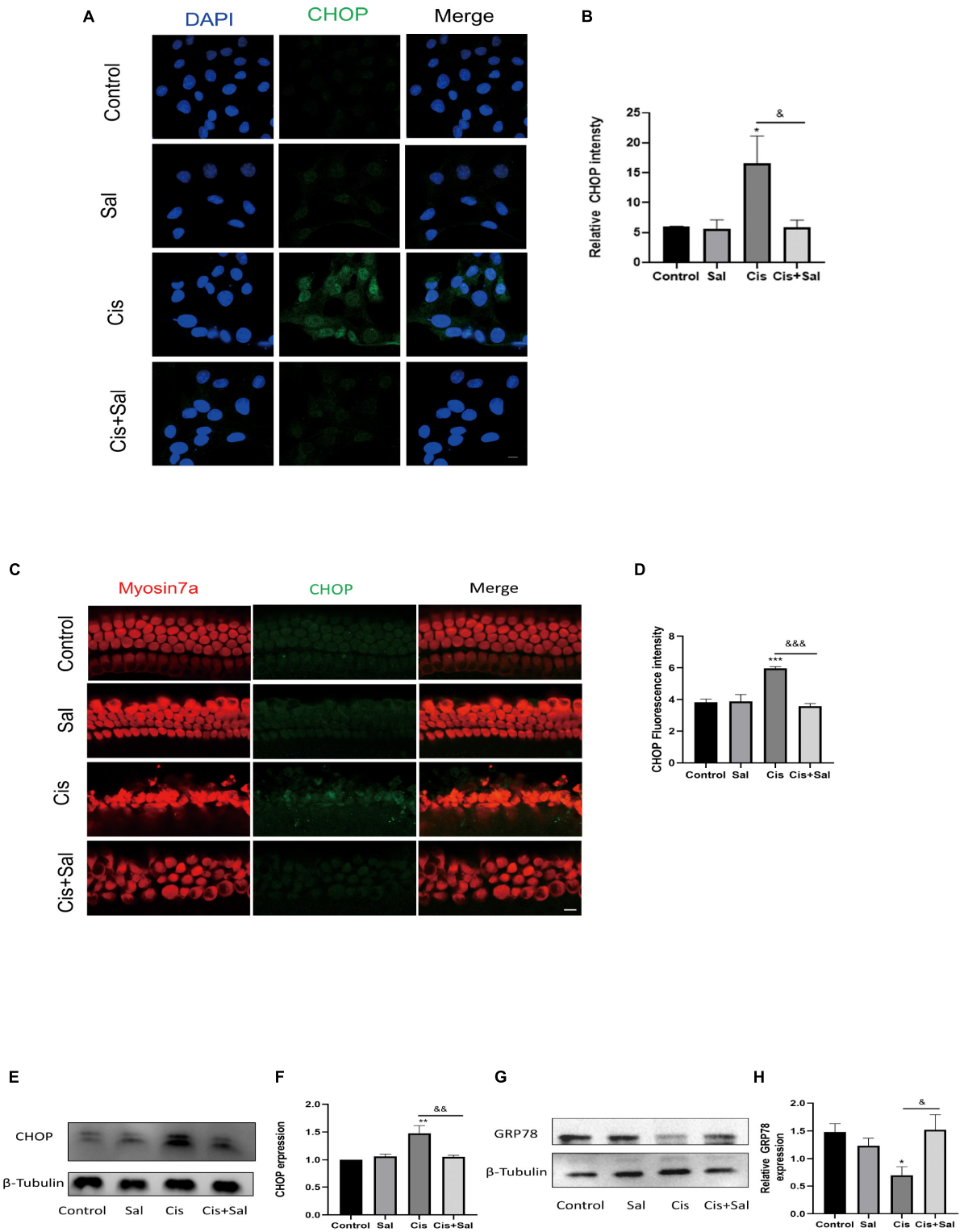

FIGURE 5 | Sal attenuates cisplatin-induced endoplasmic reticulum stress in HEI-OC1 cells. **(A)** HEI-OC1 cells in the different groups were labelled with CHOP ($n = 3$). **(B)** Quantitative analysis of the data shown in **(A)**. **(C)** Cochlear basilar membranes in the different groups were labelled with CHOP ($n = 3$). **(D)** Quantitative analysis of the fluorescence intensity shown in **(C)**. **(E)** Western blotting results showing CHOP expression in HEI-OC1 cells after different treatments ($n = 3$). **(F)** Quantitative analysis of the data shown in **(E)**. **(G)** Western blotting results showing BIP expression in HEI-OC1 cells after different treatments ($n = 3$). **(H)** Quantitative analysis of the data shown in **(G)**. Values are presented as mean ± SEM from independent experiments. $^{*}P < 0.05$, $^{**}P < 0.01$, and $^{***}P < 0.001$ vs. the control group; $^{\&}P < 0.05$, $^{\&\&}P < 0.01$, and $^{\&\&\&}P < 0.001$ vs. the cisplatin group. Scale bars = 10 μm.

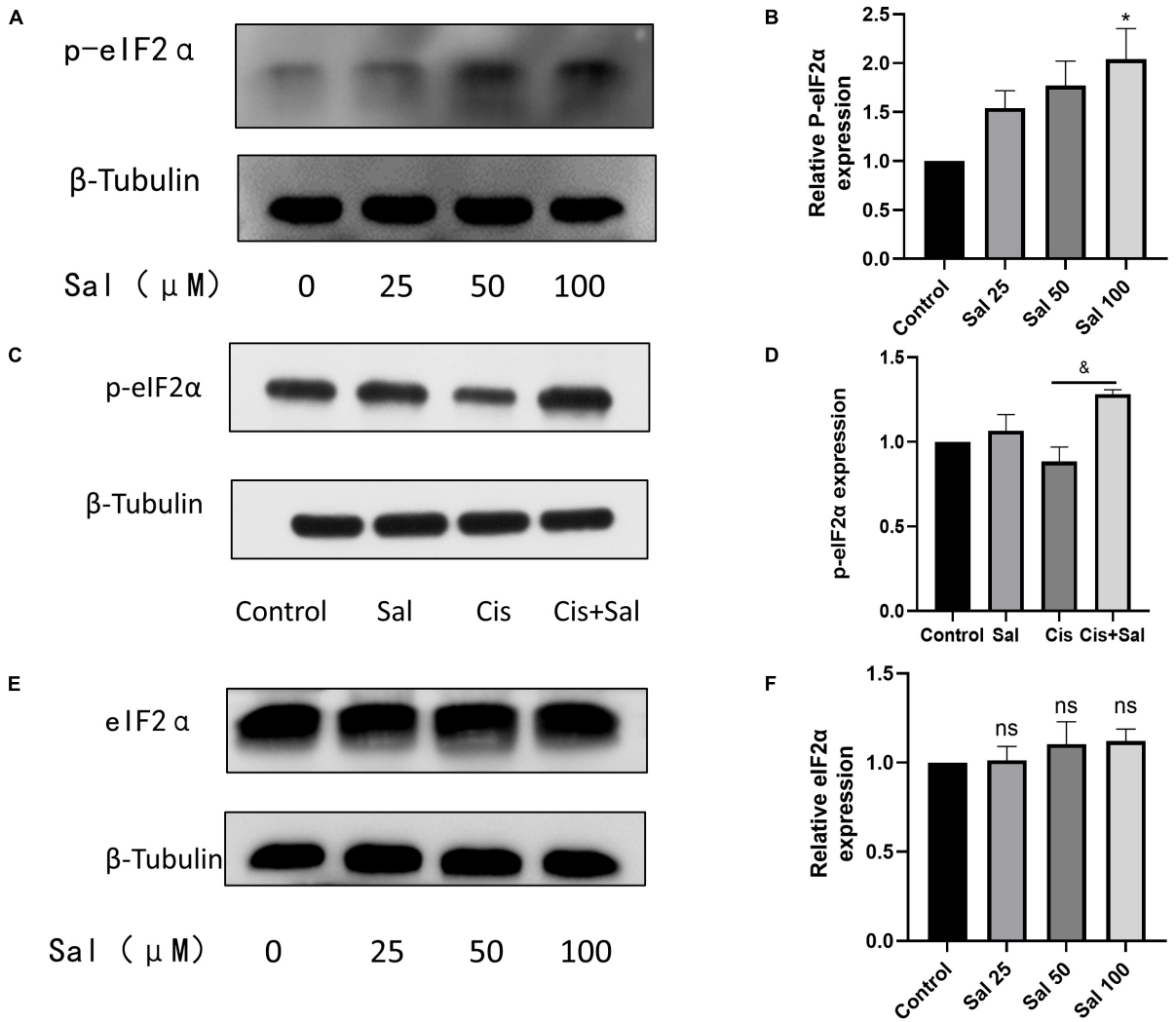

FIGURE 6 | Sal inhibits cisplatin-induced hair cell endoplasmic reticulum stress by inhibiting the dephosphorylation of p-eIF2α. **(A)** As the concentration of Sal increases, p-eIF2α expression increases. **(B)** Quantitative analysis of the data shown in **(A)**. **(C)** Sal increases p-eIF2α expression in hair cell injury after cisplatin exposure. **(D)** Quantitative analysis of the data shown in **(C)**. **(E)** Western blotting results showing the expression of eIF2α after Sal treatment. **(F)** Quantitative analysis of the data shown in **(E)**. Values are presented as mean ± SEM from independent experiments. $^{*}P < 0.05$ vs. the control group; $^{\&}P < 0.05$ vs. the cisplatin group; ns, no statistical difference.

synthesis (Wang et al., 2020). A previous study showed that by inhibiting the accumulation of misfolded/unfolded proteins, upstream of ERS, could effectively attenuate cisplatin-induced damage in auditory HCs (Wen et al., 2021). However, the role of UPR downstream signalling has not been elucidated in HCs. Therefore, whether activating UPR could prevent cisplatin-induced ototoxicity should be further investigated.

UPR mainly consists of three distinct signalling pathways, namely protein kinase R-like endoplasmic reticulum kinase (PERK), activating transcription factor 6 (ATF6), and inositol-requiring kinase 1 (IRE1) (Nakka et al., 2016; Ren et al., 2021). Dysfunction and sustained changes in endoplasmic reticulum function lead to the release of GRP78 PERK, ATF6, and IRE1, which in turn activate associated downstream signalling molecules such as the ERS marker CHOP, ultimately leading to cell death through processes such as apoptosis (Hetz, 2012; Hu et al., 2018). In the current study, we focused on PERK-eIF2α signalling and further investigated the role of eIF2α in cisplatin-induced ototoxicity. The PERK-eIF2α signalling pathway is one of the most critical pathways for the survival of cells exposed to various stressors such as toxic environments, malnutrition, and oxidative stress (Rozpedek et al., 2016). Under ERS, GRP78 is dissociated, and then PERK is activated, which further promotes eIF2α phosphorylation. Phosphorylated eIF2α inhibits general translation, thereby reducing the protein burden of the endoplasmic reticulum and protecting cells from ERS (Godin et al., 2016). Sal has been identified as an inhibitor of eIF2α dephosphorylation (Boyce et al., 2005). Similar to these studies, our results showed that increasing concentrations of Sal increased p-eIF2α expression in HEI-OC1 cells, suggesting

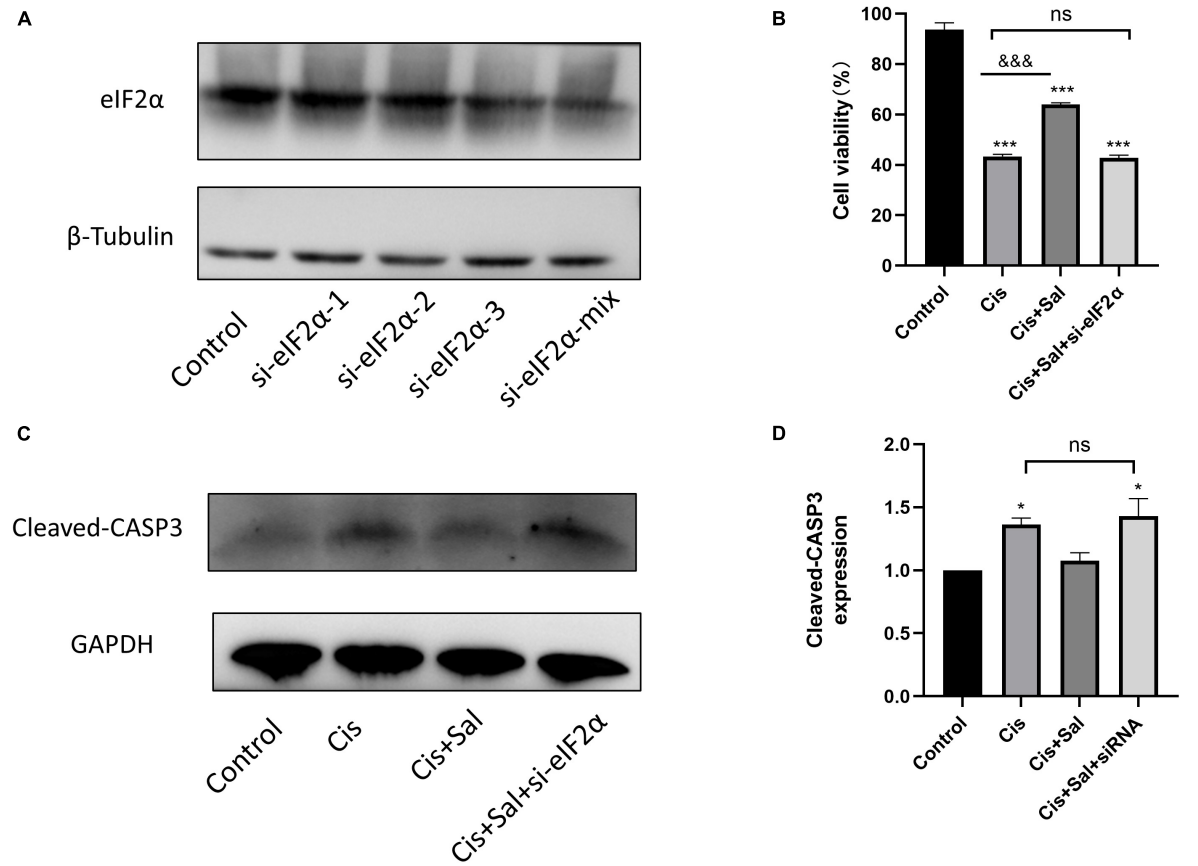

FIGURE 7 | The protective effect of Sal was attributed to eIF2α in HEI-OC1 cells. **(A)** Western blotting results showing the expression of eIF2α transfected with eIF2α-siRNA. **(B)** Effect after eIF2α silencing on cisplatin-induced injury with or without Sal viability in HEI-OC1 cells. **(C,D)** Effects of knocking down eIF2α on cisplatin-induced apoptosis. Western blotting results showing the expression of cleaved caspase in the presence of cisplatin or Sal treatment after eIF2α silencing ($n = 3$). Values are presented as mean ± SEM from three independent experiments. $^{*}P < 0.05$ and $^{***}P < 0.001$ vs. the control group; $^{\&\&\&}P < 0.001$ vs. the cisplatin group. ns, no statistical difference; Sal, salubrinal; Cis, cisplatin.

that Sal inhibited eIF2α dephosphorylation in a dose-dependent manner in auditory HCs. Furthermore, p-eIF2α decreased after cisplatin treatment, but this reduction was inhibited by Sal treatment, suggesting that p-eIF2α is crucial in cisplatin-induced ERS and apoptosis. However, the role of eIF2α is controversial. Although numerous studies support the notion that phosphorylated eIF2α is beneficial in ERS-induced cell death, eIF2α dephosphorylation has also been shown to contribute to cell survival (Novoa et al., 2003; Duan et al., 2014). Our data demonstrated that cisplatin-induced apoptotic cell death was attenuated if eIF2α could be selectively activated, whereas eIF2α knockdown enhanced cisplatin-induced apoptosis. These results further verified our view that the PERK-eIF2α pathway has a protective role in cisplatin-induced ERS in cochlear cells.

ATF4, which is downstream of eIF2α, has dual effects in ERS, including promoting the transcription of ER chaperones such as GRP78 to help ER recovery and increasing CHOP expression to induce apoptosis. CHOP, also known as growth arrest and DNA damage-inducible gene 153, is commonly expressed at very low levels in normal cells (Oyadomari and Mori, 2004). In response to various ERS stimuli, CHOP expression is upregulated and helps regulate cellular redox and cell death. Thus, CHOP upregulation is also a good biomarker of ERS and is a major downstream effector of the PERK pathway, which functions as a pro-apoptotic factor (Hu et al., 2018; Zhao et al., 2021). BIP plays a crucial role in regulating the dynamic homeostasis of the ER and is a sensor of ERS (Elfiky et al., 2020). BIP dissociates from PERK, IRE1, and ATF6 in response to ERS and triggers UPR, which possesses anti-apoptotic and cytoprotective effects (Hetz, 2012). In the current study, BIP expression decreased in the cisplatin-treated group but increased after Sal treatment. Contrastingly, CHOP was upregulated after cisplatin exposure when Sal strongly decreased the expression. Notably, upregulation of BIP/GRP78 is protective against ischemic injury and also against cisplatin-induced damage in HEI-OC1 cells (Ouyang et al., 2011; López-Hernández et al., 2015; Yi et al., 2020). Our results supported this point and further showed that pharmacological activation of eIF2α-BIP could alleviate cisplatin-induced ERS and apoptosis. Moreover, Sal significantly reduced CHOP expression in cisplatin-induced injury in HEI-OC1 cells and cochleae, suggesting that Sal could also regulate the eIF2α-CHOP pathway to inhibit cisplatin-induced ERS in HCs.

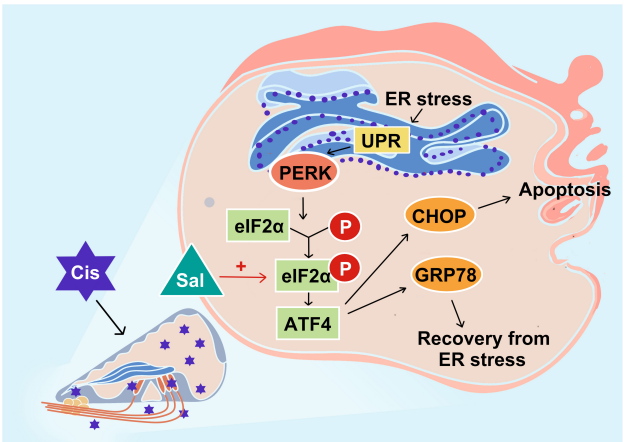

FIGURE 8 | Schematic diagram showing the specific regulatory role of endoplasmic reticulum stress in cisplatin-induced ototoxicity and the main signalling branch exerting a pro-apoptotic effect. PERK and its related PERK/eIF2α/CHOP signalling branch are speculated to play a major role in cisplatin-induced ototoxicity. Sal increases the anti-apoptotic effect of GRP78 by inhibiting the dephosphorylation of eIF2α.

Apoptosis is a positively regulated form of cell death that is mainly involved in cisplatin-induced ototoxicity (Ruhl et al., 2019; Tang et al., 2021). Accumulating evidence indicates that inhibiting apoptosis could effectively protect against cisplatin-induced damage (Wang et al., 2004; Ruhl et al., 2019; Wu et al., 2020). Sal treatment has been proposed to prevent apoptosis in various disease models (López-Hernández et al., 2015; Li et al., 2019, 2020). Consistent with these studies, Sal significantly alleviated cisplatin-induced apoptosis in HEI-OC1 cells and HCs, as evidenced by PARP and caspase-3 levels. In addition, ERS has also been proposed as a potential mechanism for cisplatin-induced ototoxicity. An increasing number of studies have found that ERS plays an important role in drug-induced hearing loss (Gentilin et al., 2019). A previous study found that ERS is involved in spiral ganglion neuron apoptosis after chronic kanamycin-induced deafness (Tu et al., 2019). Moreover, taurine deoxycholic acid attenuates gentamicin-induced cochlear HC death *in vitro* by inhibiting ERS (Hu et al., 2018). In kidney and cancer cell tissues, ERS-induced apoptosis is one of the mechanisms of cisplatin-induced cytotoxicity (Huang et al., 2020; Tham et al., 2020). Our findings are consistent with previous studies showing that Sal effectively inhibits ERS levels, thereby preventing cisplatin-induced apoptosis in HEI-OC1 cells and cochlear HCs. Our results suggest that ERS was hyperactivated in HEI-OC1 cells and HCs after cisplatin exposure, which led to HC apoptosis, and inhibition of ERS could be a promising approach to reduce cisplatin-induced apoptosis. Taken together, our findings suggest that Sal reduces cisplatin-induced apoptosis in HEI-OC1 cells and HCs by attenuating ERS.

This study has several limitations. First, although Sal demonstrates effects associated with preventing cisplatin-induced ototoxicity, it has not been approved by the FDA for clinical application. Second, we demonstrated a protective effect of Sal in cochlear explants and HEI-OC1 cells *in vitro*, but its role *in vivo* was not further explored. Therefore, the role of Sal in protecting against cochlear cisplatin damage and the mechanism involved need to be further investigated and validated in animal models.

CONCLUSION

In conclusion, our findings provide *in vitro* evidence that Sal significantly attenuates ERS in HEI-OC1 and cochlear HCs, subsequently suppressing cisplatin-induced apoptosis. In addition, eIF2α may be an important target for preventing and treating cisplatin ototoxicity. Furthermore, eIF2α plays a crucial role in ERS in HCs, and pharmacological enhancement of eIF2α phosphorylation is a potential therapeutic strategy for cisplatin-induced hearing loss.

DATA AVAILABILITY STATEMENT

The raw data supporting the conclusions of this article will be made available by the authors, without undue reservation.

ETHICS STATEMENT

The animal study was reviewed and approved by the Ethics Committee of Sixth People's Hospital Affiliated with the Shanghai Jiao Tong University.

AUTHOR CONTRIBUTIONS

WL, KN, and ZL performed all the experiments, analysed the data, and wrote the manuscript. JZ and HS conceived and designed all the experiments. WL and ZL acquired and analysed some of the data. LX, YL, and YJ helped with the experimental design and data interpretation. All authors contributed to the article and approved the submitted version.

FUNDING

This work was supported by the International Cooperation and Exchange of the National Natural Science Foundation of China (82020108008), the National Natural Science Foundation of China (82072131), the Shanghai Municipal Education Commission-Gaofeng Clinical Medicine Grant (20191921), and the Interdisciplinary Program of Shanghai Jiao Tong University (YG2022QN084).

ACKNOWLEDGMENTS

We thank Zhen Zhang, Qiang Ma, Qingxiu Yao, Jia Fang, and Chengqi Liu for their help during the experiment.

REFERENCES

Bégin, A. M., Monfette, M. L., Boudrias-Dalle, É, Lavallée, E., Samouelian, V., Soulières, D., et al. (2021). Effect of mannitol on acute kidney injury induced by cisplatin. *Support Care Cancer* 29, 2083–2091. doi: 10.1007/s00520-020-05703-7

Binet, F., and Sapieha, P. (2015). ER stress and angiogenesis. *Cell Metab.* 22, 560–575. doi: 10.1016/j.cmet.2015.07.010

Boyce, M., Bryant, K. F., Jousse, C., Long, K., Harding, H. P., Scheuner, D., et al. (2005). A selective inhibitor of eIF2alpha dephosphorylation protects cells from ER stress. *Science* 307, 935–939. doi: 10.1126/science.1101902

Brock, P. R., Maibach, R., Childs, M., Rajput, K., Roebuck, D., Sullivan, M. J., et al. (2018). Sodium thiosulfate for protection from cisplatin-induced hearing loss. *N. Engl. J. Med.* 378, 2376–2385. doi: 10.1056/NEJMoa1801109

Chadha, S., Kamenov, K., and Cieza, A. (2021). The world report on hearing. *Bull. World Health Organ.* 99, 242A–242A.

Cunningham, L. L., and Tucci, D. L. (2017). Hearing loss in adults. *N. Engl. J. Med.* 377, 2465–2473. doi: 10.1056/NEJMra1616601

Delaunay-Moisan, A., and Appenzeller-Herzog, C. (2015). The antioxidant machinery of the endoplasmic reticulum: protection and signaling. *Free Radic. Biol. Med.* 83, 341–351. doi: 10.1016/j.freeradbiomed.2015.02.019

Duan, Z., Cai, G., Li, J., and Chen, X. (2020). Cisplatin-induced renal toxicity in elderly people. *Ther. Adv. Med. Oncol.* 12:1758835920923430. doi: 10.1177/1758835920923430

Duan, Z., Zhao, J., Fan, X., Tang, C., Liang, L., Nie, X., et al. (2014). The PERK-eIF2α signaling pathway is involved in TCDD-induced ER stress in PC12 cells. *Neurotoxicology* 44, 149–159. doi: 10.1016/j.neuro.2014.06.005

Elfiky, A. A., Baghdady, A. M., Ali, S. A., and Ahmed, M. I. (2020). GRP78 targeting: hitting two birds with a stone. *Life Sci.* 260:118317. doi: 10.1016/j.lfs.2020.118317

Font-Belmonte, E., Ugidos, I. F., Santos-Galdiano, M., González-Rodríguez, P., Anuncibay-Soto, B., Pérez-Rodríguez, D., et al. (2019). Post-ischemic salubrinal administration reduces necroptosis in a rat model of global cerebral ischemia. *J. Neurochem.* 151, 777–794. doi: 10.1111/jnc.14789

Frisina, R. D., Wheeler, H. E., Fossa, S. D., Kerns, S. L., Fung, C., Sesso, H. D., et al. (2016). Comprehensive audiometric analysis of hearing impairment and tinnitus after cisplatin-based chemotherapy in survivors of adult-onset cancer. *J. Clin. Oncol.* 34, 2712–2720. doi: 10.1200/JCO.2016.66.8822

Gentilin, E., Simoni, E., Candito, M., Cazzador, D., and Astolfi, L. (2019). Cisplatin-induced ototoxicity: updates on molecular targets. *Trends Mol. Med.* 25, 1123–1132. doi: 10.1016/j.molmed.2019.08.002

Godin, J. D., Creppe, C., Laguesse, S., and Nguyen, L. (2016). Emerging roles for the unfolded protein response in the developing nervous system. *Trends Neurosci.* 39, 394–404. doi: 10.1016/j.tins.2016.04.002

Hetz, C. (2012). The unfolded protein response: controlling cell fate decisions under ER stress and beyond. *Nat. Rev. Mol. Cell Biol.* 13, 89–102. doi: 10.1038/nrm3270

Hetz, C., and Papa, F. R. (2018). The unfolded protein response and cell fate control. *Mol. Cell* 69, 169–181. doi: 10.1016/j.molcel.2017.06.017

Hetz, C., Zhang, K., and Kaufman, R. J. (2020). Mechanisms, regulation and functions of the unfolded protein response. *Nat. Rev. Mol. Cell Biol.* 21, 421–438. doi: 10.1038/s41580-020-0250-z

Hu, H., Tian, M., Ding, C., and Yu, S. (2018). The C/EBP Homologous Protein (CHOP) transcription factor functions in endoplasmic reticulum stress-induced apoptosis and microbial infection. *Front. Immunol.* 9:3083. doi: 10.3389/fimmu.2018.03083

Huang, Z., Guo, F., Xia, Z., Liang, Y., Lei, S., Tan, Z., et al. (2020). Activation of GPR120 by TUG891 ameliorated cisplatin-induced acute kidney injury via repressing ER stress and apoptosis. *Biomed. Pharmacother.* 126:110056. doi: 10.1016/j.biopha.2020.110056

Jia, Z., He, Q., Shan, C., and Li, F. (2018). Tauroursodeoxycholic acid attenuates gentamicin-induced cochlear hair cell death in vitro. *Toxicol. Lett.* 294, 20–26. doi: 10.1016/j.toxlet.2018.05.007

Kalinec, G. M., Park, C., Thein, P., and Kalinec, F. (2016). Working with Auditory HEI-OC1 cells. *J. Vis. Exp.* 115:54425. doi: 10.3791/54425

Kalinec, G. M., Thein, P., Parsa, A., Yorgason, J., Luxford, W., Urrutia, R., et al. (2014). Acetaminophen and NAPQI are toxic to auditory cells via oxidative and endoplasmic reticulum stress-dependent pathways. *Hear Res.* 313, 26–37. doi: 10.1016/j.heares.2014.04.007

Knight, K. R., Kraemer, D. F., and Neuwelt, E. A. (2005). Ototoxicity in children receiving platinum chemotherapy: underestimating a commonly occurring toxicity that may influence academic and social development. *J. Clin. Oncol.* 23, 8588–8596. doi: 10.1200/JCO.2004.00.5355

Kros, C., and Steyger, P. S. (2019). Aminoglycoside- and cisplatin-induced ototoxicity: mechanisms and otoprotective strategies. *Cold Spring Harb. Perspect. Med.* 9:a033548. doi: 10.1101/cshperspect.a033548

Li, J., Li, X., Liu, D., Hamamura, K., Wan, Q., Na, S., et al. (2019). eIF2α signaling regulates autophagy of osteoblasts and the development of osteoclasts in OVX mice. *Cell Death Dis.* 10:921. doi: 10.1038/s41419-019-2159-z

Li, J., Zhuo, J. Y., Zhou, W., Hong, J. W., Chen, R. G., Xie, H. Y., et al. (2020). Endoplasmic reticulum stress triggers delanzomib-induced apoptosis in HCC cells through the PERK/eIF2α/ATF4/CHOP pathway. *Am. J. Transl. Res.* 12, 2875–2889.

Li, Z., Yao, Q., Tian, Y., Jiang, Y., Xu, M., Wang, H., et al. (2022). Trehalose protects against cisplatin-induced cochlear hair cell damage by activating TFEB-mediated autophagy. *Biochem. Pharmacol.* 197:114904. doi: 10.1016/j.bcp.2021.114904

López-Hernández, B., Ceña, V., and Posadas, I. (2015). The endoplasmic reticulum stress and the HIF-1 signalling pathways are involved in the neuronal damage caused by chemical hypoxia. *Br. J. Pharmacol.* 172, 2838–2851. doi: 10.1111/bph.13095

Luongo, T. S., Lambert, J. P., Gross, P., Nwokedi, M., Lombardi, A. A., Shanmughapriya, S., et al. (2017). The mitochondrial Na(+)/Ca(2+) exchanger is essential for Ca(2+) homeostasis and viability. *Nature* 545, 93–97. doi: 10.1038/nature22082

Matsuoka, M., and Komoike, Y. (2015). Experimental evidence shows salubrinal, an eIF2α dephosphorylation inhibitor, reduces xenotoxicant-induced cellular damage. *Int. J. Mol. Sci.* 16, 16275–16287. doi: 10.3390/ijms160716275

Nakka, V. P., Prakash-Babu, P., and Vemuganti, R. (2016). Crosstalk between endoplasmic reticulum stress, oxidative stress, and autophagy: potential therapeutic targets for acute CNS injuries. *Mol. Neurobiol.* 53, 532–544. doi: 10.1007/s12035-014-9029-6

Novoa, I., Zhang, Y., Zeng, H., Jungreis, R., Harding, H. P., and Ron, D. (2003). Stress-induced gene expression requires programmed recovery from translational repression. *Embo J.* 22, 1180–1187. doi: 10.1093/emboj/cdg112

Oishi, N., Duscha, S., Boukari, H., Meyer, M., Xie, J., Wei, G., et al. (2015). XBP1 mitigates aminoglycoside-induced endoplasmic reticulum stress and neuronal cell death. *Cell Death Dis.* 6:e1763. doi: 10.1038/cddis.2015.108

Ouyang, Y. B., Xu, L. J., Emery, J. F., Lee, A. S., and Giffard, R. G. (2011). Overexpressing GRP78 influences Ca2+ handling and function of mitochondria in astrocytes after ischemia-like stress. *Mitochondrion* 11, 279–286. doi: 10.1016/j.mito.2010.10.007

Oyadomari, S., and Mori, M. (2004). Roles of CHOP/GADD153 in endoplasmic reticulum stress. *Cell Death Differ.* 11, 381–389. doi: 10.1038/sj.cdd.4401373

Qu, Y., Zong, S., Wang, Z., Du, P., Wen, Y., Li, H., et al. (2022). The PERK/ATF4/CHOP signaling branch of the unfolded protein response mediates cisplatin-induced ototoxicity in hair cells. *Drug Chem. Toxicol.* [Online ahead of print] doi: 10.1080/01480545.2022.2039181

Ren, J., Bi, Y., Sowers, J. R., Hetz, C., and Zhang, Y. (2021). Endoplasmic reticulum stress and unfolded protein response in cardiovascular diseases. *Nat. Rev. Cardiol.* 18, 499–521. doi: 10.1038/s41569-021-00511-w

Rozpedek, W., Pytel, D., Mucha, B., Leszczynska, H., Diehl, J. A., and Majsterek, I. J. C. M. M. (2016). The Role of the PERK/eIF2α/ATF4/CHOP signaling pathway in tumor progression during endoplasmic reticulum stress. *Curr. Mol. Med.* 16, 533–544.

Ruhl, D., Du, T. T., Wagner, E. L., Choi, J. H., Li, S., Reed, R., et al. (2019). Necroptosis and apoptosis contribute to cisplatin and aminoglycoside ototoxicity. *J. Neurosci.* 39, 2951–2964. doi: 10.1523/jneurosci.1384-18.2019

Tang, Q., Wang, X., Jin, H., Mi, Y., Liu, L., Dong, M., et al. (2021). Cisplatin-induced ototoxicity: updates on molecular mechanisms and otoprotective strategies. *Eur. J. Pharm. Biopharm.* 163, 60–71. doi: 10.1016/j.ejpb.2021.03.008

Tham, M. J. R., Babak, M. V., and Ang, W. H. (2020). PlatinER: a highly potent anticancer platinum(ii) complex that induces endoplasmic reticulum stress driven immunogenic cell death. *Angew. Chem. Int. Ed. Engl.* 59, 19070–19078. doi: 10.1002/anie.202008604

Tu, Y., Fan, G., Sun, H., Cai, X., and Kong, W. (2019). Endoplasmic reticulum stress is involved in spiral ganglion neuron apoptosis following chronic kanamycin-induced deafness. *Biosci. Rep.* 39:BSR20181749. doi: 10.1042/bsr20181749

Wang, J., Ladrech, S., Pujol, R., Brabet, P., Van De Water, T. R., and Puel, J. L. (2004). Caspase inhibitors, but not c-Jun NH2-terminal kinase inhibitor treatment, prevent cisplatin-induced hearing loss. *Cancer Res.* 64, 9217–9224. doi: 10.1158/0008-5472.Can-04-1581

Wang, Y. C., Li, X., Shen, Y., Lyu, J., Sheng, H., Paschen, W., et al. (2020). PERK (Protein Kinase RNA-Like ER Kinase) branch of the unfolded protein response confers neuroprotection in ischemic stroke by suppressing protein synthesis. *Stroke* 51, 1570–1577. doi: 10.1161/strokeaha.120.029071

Wen, Y., Zong, S., Liu, T., Du, P., Li, H., and Xiao, H. (2021). Tauroursodeoxycholic acid attenuates cisplatin-induced ototoxicity by inhibiting the accumulation and aggregation of unfolded or misfolded proteins in the endoplasmic reticulum. *Toxicology* 453:152736. doi: 10.1016/j.tox.2021.152736

Wilson, B. S., Tucci, D. L., Merson, M. H., and O'Donoghue, G. M. (2017). Global hearing health care: new findings and perspectives. *Lancet* 390, 2503–2515. doi: 10.1016/S0140-6736(17)31073-5

Wu, J., Ye, J., Kong, W., Zhang, S., and Zheng, Y. (2020). Programmed cell death pathways in hearing loss: a review of apoptosis, autophagy and programmed necrosis. *Cell Prolif.* 53:e12915. doi: 10.1111/cpr.12915

Yi, J., Kim, T. S., Pak, J. H., and Chung, J. W. (2020). Protective effects of glucose-related protein 78 and 94 on cisplatin-mediated ototoxicity. *Antioxidants* 9:686. doi: 10.3390/antiox9080686

Zhang, J., Wang, Y., Ju, M., Song, J., Zheng, Y., Lin, S., et al. (2020). Neuroprotective effect of the inhibitor salubrinal after cardiac arrest in a rodent model. *Oxid. Med. Cell Longev.* 2020:7468738. doi: 10.1155/2020/7468738

Zhang, J., Xie, X., Pan, H., Wu, Z., Lu, W., and Yang, G. (2015). Role of endoplasmic reticulum stress in brain damage after cardiopulmonary resuscitation in rats. *Shock* 44, 65–71. doi: 10.1097/SHK.0000000000000367

Zhao, C., Yu, D., He, Z., Bao, L., Feng, L., Chen, L., et al. (2021). Endoplasmic reticulum stress-mediated autophagy activation is involved in cadmium-induced ferroptosis of renal tubular epithelial cells. *Free Radic. Biol. Med.* 175, 236–248. doi: 10.1016/j.freeradbiomed.2021.09.008

Conflict of Interest: The authors declare that the research was conducted in the absence of any commercial or financial relationships that could be construed as a potential conflict of interest.

Publisher's Note: All claims expressed in this article are solely those of the authors and do not necessarily represent those of their affiliated organizations, or those of the publisher, the editors and the reviewers. Any product that may be evaluated in this article, or claim that may be made by its manufacturer, is not guaranteed or endorsed by the publisher.

frontiers | Frontiers in Molecular Neuroscience

ORIGINAL RESEARCH
published: 20 June 2022
doi: 10.3389/fnmol.2022.920528

Hearing Loss in Offspring Exposed to Antiretrovirals During Pregnancy and Breastfeeding

J. Riley DeBacker[1,2]*, *Breanna Langenek*[3] and *Eric C. Bielefeld*[3]

[1]VA RR&D National Center for Rehabilitative Auditory Research, VA Portland Healthcare System, Portland, OR, United States, [2]Oregon Hearing Research Center, Oregon Health and Science University, Portland, OR, United States, [3]Department of Speech and Hearing Science, The Ohio State University, Columbus, OH, United States

Over 27 million people worldwide currently receive daily antiretroviral therapy for the management of HIV/AIDS. In order to prevent the continued spread of HIV, the World Health Organization (WHO) recommends the use of highly active antiretroviral therapy by pregnant and nursing women. There is currently little research into the auditory effects of this therapy on children exposed during pregnancy and breastfeeding, and research to date on the direct effects of antiretroviral exposure on the auditory system is inconclusive. The current study examined the effects of WHO-recommended first-line antiretrovirals in a well-controlled animal model to evaluate the potential for auditory damage and dysfunction following these exposures. Female breeding mice were each exposed to one of four antiretroviral cocktails or a vehicle control once daily during pregnancy and breastfeeding. Offspring of these mice had their auditory status evaluated after weaning using auditory brainstem responses and distortion-product otoacoustic emissions (DPOAEs). Auditory brainstem response thresholds following antiretroviral exposure during gestation and breastfeeding showed elevated thresholds and increased wave latencies in offspring of exposed mice when compared to unexposed controls, but no corresponding decrease in DPOAE amplitude. These differences in threshold were small and so may explain the lack of identified hearing loss in antiretroviral-exposed children during hearing screenings at birth. Minimal degrees of hearing impairment in children have been correlated with decreased academic performance and impaired auditory processing, and so these findings, if also seen in human children, suggest significant implications for children exposed to antiretrovirals during development despite passing hearing screenings at birth.

Keywords: antiretroviral therapy, ototoxicity, HIV, translational model, sensorineural hearing loss, auditory brainstem response

OPEN ACCESS

Edited by:
Peter S. Steyger, Creighton University, United States

Reviewed by:
Ann Anderson Berry, University of Nebraska Medical Center, United States
Allison B. Coffin, Washington State University, United States

***Correspondence:**
J. Riley DeBacker
debacker.2@osu.edu

Specialty section:
This article was submitted to Brain Disease Mechanisms, a section of the journal Frontiers in Molecular Neuroscience

Received: *14 April 2022*
Accepted: *20 May 2022*
Published: *20 June 2022*

Citation:
DeBacker JR, Langenek B and Bielefeld EC (2022) Hearing Loss in Offspring Exposed to Antiretrovirals During Pregnancy and Breastfeeding. Front. Mol. Neurosci. 15:920528. doi: 10.3389/fnmol.2022.920528

Abbreviations: 3TC, lamivudine; ABR, auditory brainstem response; AIDS, acquired immunodeficiency syndrome; ANOVA, analysis of variance; AZT, zidovudine; ARV, antiretroviral; DPOAE, distortion product ototacoustic emissions; EFV, efavirenz; HAART, highly-active antiretroviral therapy; HIV, human immunodeficiency virus; NRTI, nucleoside reverse transcriptase inhibitor; NVP, nevirapine; OHC, outer hair cell; PaB, pregnancy and breastfeeding; TDF, tenofovir disoproxil fumarate; TDT, Tucker Davis Technologies; WHO, World Health Organization.

INTRODUCTION

Human immunodeficiency virus (HIV) is an acquired viral infection that suppresses the immune system and leaves those infected more prone to opportunistic and latent disease. The World Health Organization (WHO) estimates that, at the end of 2020, there were nearly 38 million people living with HIV and that more than 27 million of those individuals were taking lifelong antiretroviral (ARV) therapy for HIV management (WHO, 2020). Highly-active antiretroviral therapy (HAART), also commonly referred to as "combination antiretroviral therapy," has been used since 1996 to manage symptoms of HIV and prevent disease progression and seroconversion to acquired immunodeficiency syndrome (AIDS). HAART typically consists of two nucleoside reverse transcriptase inhibitors (NRTIs) and one or more other drugs that have been shown to be effective not only at disease management but also at lowering disease burden to a point that prevents transmission (Cohen et al., 2011). As the WHO and other public health entities have a goal of preventing HIV transmission, HAART is recommended for all people living with HIV, and special focus has been paid to preventing the spread of HIV from mother to child during pregnancy (vertical transmission). While the use of HAART during pregnancy and breastfeeding has been shown to be effective in preventing the spread of HIV, exposure to HIV and HAART during development has been found to have negative impacts on cognitive development (Blanche et al., 1999; Tardieu et al., 2005; Brogly et al., 2007; Coelho et al., 2017; McHenry et al., 2019), language development (Rice et al., 2013), and auditory function (Poblano et al., 2004; Fasunla et al., 2014; Torre et al., 2017).

Current evidence regarding the auditory effects of HAART on perinatally HIV exposed but uninfected (PHEU) children has been inconclusive. Fasunla et al. (2014) found that *in utero* HIV exposure was more likely to result in failed hearing screening and confirmed hearing loss on a diagnostic auditory brainstem response (ABR), with a significant relationship between maternal viral load during pregnancy and hearing loss, but no relationship between CD4+ cell count and hearing loss. This study suggests that there may be some relationship between pre- and peri-natal HIV exposure and congenital hearing loss, but it did not control for whether or not mothers in the study were taking ARV therapy during pregnancy. Another study found significant delays in the Wave I latency and I-III interpeak latency on the ABR for PHEU infants exposed to the HAART drug zidovudine (AZT) alone or in combination with lamivudine (3TC; Poblano et al., 2004). In contrast, Torre and colleagues found that no specific HAART drug was related to an increased likelihood of hearing screening failure in PHEU children and that exposure to the drug tenofovir disoproxil fumarate (TDF) during the first trimester was associated with a lower odds ratio for a failed hearing screening. The authors also noted that a number of HAART drugs demonstrated an incredibly wide range of variability in auditory outcomes for newborns, even after controlling for factors that often contribute to failed hearing screenings (Torre et al., 2017). Despite the lack of differences in hearing screening results at birth, the Torre group also found that PHEU young adults were more likely to have impaired words-in-noise performance with otherwise normal cognition than young adults with HIV, suggesting an effect of exposure to these drugs during pregnancy and breastfeeding (PaB) not seen from post-natal exposures (Torre et al., 2020).

A prospective controlled human study of the relative contributions of HIV and HAART to hearing loss would be unethical, due to the high efficacy of HAART in preventing vertical HIV transmission, and so this question should first be explored in a well-controlled non-human model. Our group undertook an initial exploration of this modeling by exposing C57BL6/J female mice to AZT and 3TC during PaB (DeBacker et al., 2022). When offspring of these mice underwent ABR threshold testing at three weeks old, they had higher thresholds than control offspring at five of six tested frequencies. This indicates that exposure to AZT+3TC during PaB can lead to auditory dysfunction during development in a mouse model. AZT+3TC alone is not a currently recommended first-line management regimen for HIV, however, and so there is interest in understanding if these effects are seen across different currently-recommended ARV combinations. The current study seeks to expand upon our previous work by evaluating the auditory system of animals exposed to several different currently-recommended ARV combinations.

The current study used a well-characterized model of ototoxicity, the CBA/CaJ mouse, to investigate the auditory effects of HAART exposure during PaB. This model was used due to its stable hearing thresholds over the projected length of the study, in contrast to models with earlier onset of presbycusis like the C57BL6/J used previously. The authors hypothesized that exposure to HAART would lead to increased ABR and distortion product otoacoustic emissions (DPOAE) thresholds at wean in exposed offspring when compared to unexposed controls, with the greatest threshold elevation resulting from exposure to AZT and efavirenz (EFV). This hypothesis was based upon the previously-discussed findings on PHEU children and a study of the effects of ARV compounds on auditory cell (HEI-OC1) lines by Thein et al. (2014). This study found that exposure to moderate- and high-dose EFV resulted in almost 100% cell death and that even low-dose exposures cause significant cell death. While TDF was more toxic than AZT in the Thein et al. (2014) study, Torre et al. (2017) found a decrease in reported hearing screening failures following TDF exposure, and so it was predicted that AZT would have greater auditory effects than TDF. When combined with previous work by Thein et al. (2014) and our lab (DeBacker et al., 2022) on combination ARVs, it was anticipated that this study of WHO-recommended first-line HAART cocktails would result in greater auditory impairment than was observed in our previous study. By using currently-recommended HAART cocktails, this model provides a clinically translatable model of HAART exposure and contributes significant pre-clinical evidence toward the understanding of the auditory effects of HAART exposure during PaB.

METHODS

Subjects

One hundred CBA/CaJ mice were used in this study. Of these mice, 20 were breeding mice obtained from Jackson Labs (Las Vegas, NV) and housed in a vivarium at The Ohio State University. The breeding mice were divided into breeding pairs and then assigned to one of five experimental groups. The other 80 mice were offspring of those pairs. Each experimental group consisted of four breeding mice and 10–16 offspring. In order to exclude confounding variables, the male breeder mice were not exposed to HAART or any other manipulation during the study. Breeding pairs were allowed to generate no more than five litters before removal from the study. The mice were kept in a quiet colony, in which the 24-h dB Leq level never exceeded 45 dB SPL. Animals were acclimatized to the colony for at least 7 days before beginning experiments. All procedures involving the animals were approved by The Ohio State University's Institutional Animal Care and Use Committee.

Antiretroviral Exposures

For all experimental arms and conditions, the following groups were used: one group's (Group 1) breeder females received volume-matched distilled water vehicle; the other four groups' (Groups 2–5) breeder females received 3TC combined with the following drugs: Group (2) TDF and EFV; Group (3) AZT and EFV; Group (4) TDF and nevirapine (NVP); Group (5) AZT and NVP. These drug cocktails correspond to permutations of HAART currently recommended by WHO for first-line therapy for pregnant and nursing women, though emtricitabine is also recommended as an alternative to 3TC, which was used in this study. The combinations were chosen because significant differences were seen in cellular toxicity between EFV and NVP and TDF and AZT, respectively, but no such differences were observed between emtricitabine and 3TC (Thein et al., 2014).

All drugs used in this study were obtained as capsules or tablets through The Ohio State University Wexner Medical Center Pharmacy. AZT and TDF tablets were crushed using a mortar and pestle, and distilled water was added to dissolve them and create stock solutions with a concentration of 10 mg/ml. 3TC tablets were crushed using a mortar and pestle, and distilled water was added to create a stock solution with a concentration of 50 mg/ml. Suspensions were made using the combinations of 3TC with AZT or TDF, depending on the experimental group. For groups receiving NVP, tablets were crushed and added to the suspension. For groups receiving EFV, capsules were emptied directly into the suspension. After adding EFV or NVP, 4 ml of water were added to each suspension, and they were thoroughly mixed to minimize particulate in each jar. All jars were agitated prior to administration to minimize particulate in the suspensions. Suspensions were refrigerated between administrations. Each day, suspensions were monitored for an irregularity in appearance prior to administration. After 28 days, any remaining suspension was discarded, and new suspensions were mixed.

Because the female breeder mice grew in size and weight over the course of the study, the doses of the HAART compounds increased as well. However, best practice standards set the maximum fluid volume that could be delivered to the mice through oral gavage at 0.20 ml. Therefore, in order to deliver the required doses without exceeding the maximum fluid volume, the concentrations in mg/ml of the compounds needed to increase, and so after 3 months, concentrations of the HAART suspensions were recalculated to reflect the higher weight of the animals at that time. After this recalculation, concentrations of AZT and TDF were 13 mg/ml, concentrations of EFV and NVP were 83 mg/ml, and concentration of 3TC was 68.2 mg/ml. Preparations were otherwise unchanged from the above procedure.

Each female breeding mouse was given a once-daily dose *via* oral gavage of one of the four cocktails of antiretroviral agents listed earlier in this section or a matched volume of vehicle solution for control subjects in Group 1. Daily doses were administered beginning after baseline testing and continued until the final group of offspring used for the study was weaned. As such, female mice were exposed during the mating period, pregnancy, and nursing of all offspring. Weights to determine dosing were collected on the first day of each week and were used for the duration of that week unless a mouse gave birth. After giving birth, the previous week's weight was used for the remaining doses during that week. All gavage doses were delivered in a sterile environment under a biosafety hood in the University Laboratory Animal Resource housing vivarium.

Auditory Brainstem Responses

For this study, all animals were anesthetized using an inhaled mixture of gaseous isoflurane (2.5% for induction, 1.2% for maintenance) and oxygen (2 L/min for induction, 1 L/min for maintenance) during both ABR and DPOAE collection. ABR and DPOAE testing was performed in a sound-attenuating booth (Controlled Acoustical Environments, Bronx, NY).

For eliciting the ABRs, tone bursts were presented beginning at 90 dB SPL and in decreasing 5 dB steps to 20 dB SPL or until no repeatable waveform was observed. Test frequencies were 4, 8, 12, 16, 24, and 32 kHz. The stimuli were generated using Tucker Davis Technologies (TDT, Gainesville, FL) SigGen software. Each tone burst was 1 ms in duration and had a 0.5 ms rise/fall time with no plateau. Stimuli were presented at a rate of 19/s. Signals were routed to a speaker (TDT Model MF1) positioned at 90 degrees azimuth (directly next to the right ear), 3 cm from the vertex of each mouse's head. The levels were calibrated with a SoundTrack LxT1 sound level meter (Larson Davis, Depew, NY) with a $\frac{1}{4}$ in condenser microphone (model 7016 and model 4016, ACO Pacific, Inc.), placed at the level of the animal's head. For recording electrical responses from the mice, three 6-mm platinum electrodes (Rochester Electro-Medical, Lutz, FL) were inserted subdermally behind the right pinna (inverting), behind the left pinna (non-inverting), and in the right rear leg (ground) of each anesthetized mouse. The evoked responses of the mice were amplified with a gain of 50,000× using a TDT RA4LI headstage connected to a TDT RA4PA preamplifier. ABRs were averaged across 300 responses at each level. Responses were processed through a 300–3,000 Hz band-pass filter as recommended by the software manufacturer

(TDT). Post-acquisition analyses were performed using TDT BioSig RZ software. ABR P1 latencies were obtained by placing cursors at the positive P1 peak, and P3 latencies were obtained using the same process for the third positive peak.

Distortion-Product Otoacoustic Emissions

While still under the isoflurane anesthesia after the ABR recording, DPOAEs were measured. Prior to recording DPOAEs, all animals were visually inspected for signs of middle ear infection or cerumen buildup within the external auditory canal. DPOAE measurements were collected at the same f_2 frequencies as for ABR (4, 8, 12, 16, 24, and 32 kHz) with a ratio of f_2/f_1 constant at 1.25 and a ratio of L1/L2 constant at 1.2. At each frequency, stimuli began at 80 dB SPL for L1 and decreased in 10-dB steps to 20 dB SPL or until no cubic DPOAE ($2f_1$-f_2) response was observed. A cubic DPOAE was considered to be present if there was a visible spike at $2f_1$-f_2 that exceeded the noise floor at nearby frequencies, as can be seen in the example in **Figure 1**. The lowest intensity at which a visible cubic DPOAE could be detected was recorded at each tested frequency and was defined as the DPOAE threshold for that frequency. The stimuli were generated using TDT SigGen software. Signals were routed to two speakers (TDT Model MF1) in a closed field configuration that were coupled to the microphone tip of the Etymotic Research ER10B+ low noise microphone system (Elk Grove Village, IL) using 1/16" inner diameter, 1/8" outer diameter plastic tubing (McMaster-Carr, Cleveland, OH). The microphone tip was coupled to the ear of each mouse using a pipet tip that was trimmed to fit the ear. For each level, DPOAE recordings were averaged across 128 responses at each level as recommended by the software manufacturer (TDT). Gain for responses was set at 0.00001 so that plot outputs matched dBv for simple conversion to dB SPL and F1, F2, and DP ($2f_1$-f_2) were labeled for all collected responses.

For breeding pairs, ABRs and DPOAEs were recorded prior to assigning each mouse to an experimental group, and then 1, 3, and 6 months after pairing the mice and beginning HAART exposure. For offspring, ABRs and DPOAEs were recorded at 28 days post-birth. Day 28 was selected as the test date because the mice were weaned from their birth cages at 21 days, and then the additional week was given for them to acclimatize to their new cages before undergoing anesthetized auditory testing. All auditory testing was performed during the day (between 9 a.m. and 6 p.m. Eastern time).

Statistical Analyses

For the breeder females', a three-way analysis of variance (ANOVA) comparing group × frequency × test time (0, 3, or 6 months since enrollment) was used. Frequency and test time were treated as within-subjects factors, with the group as the between-subjects factor. ABR and DPOAE thresholds were analyzed for differences by exposure group at wean using a two-factor ANOVA (group*frequency). When significant effects were observed, all *post hoc* analyses for the group used Tukey A pairwise comparisons. Significance was assigned at $p < 0.05$ for all analyses. All statistical analyses were performed using IBM SPSS version 25 (IBM, Armonk, NY) and all associated figures were created using SigmaPlot (Systat Software Inc., San Jose, CA).

RESULTS

Breeding Pairs

At the beginning of the study, the auditory status of all 20 breeding animals was evaluated *via* ABR. No animals were found to have abnormally high baseline ABR thresholds at enrollment, as can be seen in **Figure 2**. For the pre-exposure ABR thresholds, a two-factor ANOVA (frequency*ARV exposure group) was performed to determine differences in baseline hearing between groups' breeder females. There was neither a two-way interaction of frequency and group ($F_{1,20} = 1.106$, $p = 0.401$) nor a main effect of group ($F_{1,4} = 0.608$, $p = 0.675$). This lack of differences between breeding mice across groups indicates that any differences seen in offspring are likely the result of ARV exposures and not the result of obvious inherent differences. While the female breeding mice were being exposed to daily antiretrovirals by gavage, their ABR thresholds were monitored throughout the duration of the study. ABRs were collected at 1, 3, and 6 months (see **Figure 2** for means) after beginning the exposures in order to monitor any auditory changes resulting from HAART. A three-way repeated measures ANOVA (time*frequency*group) was performed to evaluate threshold changes across groups and frequencies over time in the HAART-exposed female breeding animals. There was no three-way interaction of group, frequency, and time ($F_{1,40} = 0.846$, $p = 0.693$) nor any two-way interaction of frequency and group ($F_{1,20} = 0.662$, $p = 0.808$). The only significant interaction was a two-way interaction of time and frequency ($F_{1,10} = 2.734$, $p = 0.016$). Evaluation of this effect showed a significant change in the mean threshold at 16 kHz between the 3-month and 6-month time points across groups. No other significant differences were observed, as can be seen in **Figure 2**. Overall, the results indicate that the daily ARV gavages did not create significant hearing threshold changes and that the mice exhibited generally stable thresholds, consistent with expectations for the CBA/CaJ mouse.

Offspring

The target group size for each exposure group (Groups 1–5) was eight mice. Due to differences in litter sizes, this number served as a target, but the achieved group sizes for each exposure group varied slightly. ABRs and DPOAEs were measured 7 days after wean (28 days of age) for all offspring in the study. This timepoint is referred to as "wean" throughout the rest of this manuscript, and it reflects the auditory status as it was first measured after weaning these animals. Mean ABR and DPOAE thresholds at wean are depicted below in **Figure 3**, and group comparisons are described below.

For the ABR thresholds at this wean time point, a two-factor ANOVA (frequency*group) was performed. There was no two-way interaction ($F_{(1,17.685)} = 1.222$, $p = 0.241$). To account for a lack of sphericity, a Huynh-Feldt correction was run on the reported two-way interaction. A significant main effect was seen for the group ($F_{(1,4)} = 4.749$, $p = 0.002$). When evaluating the

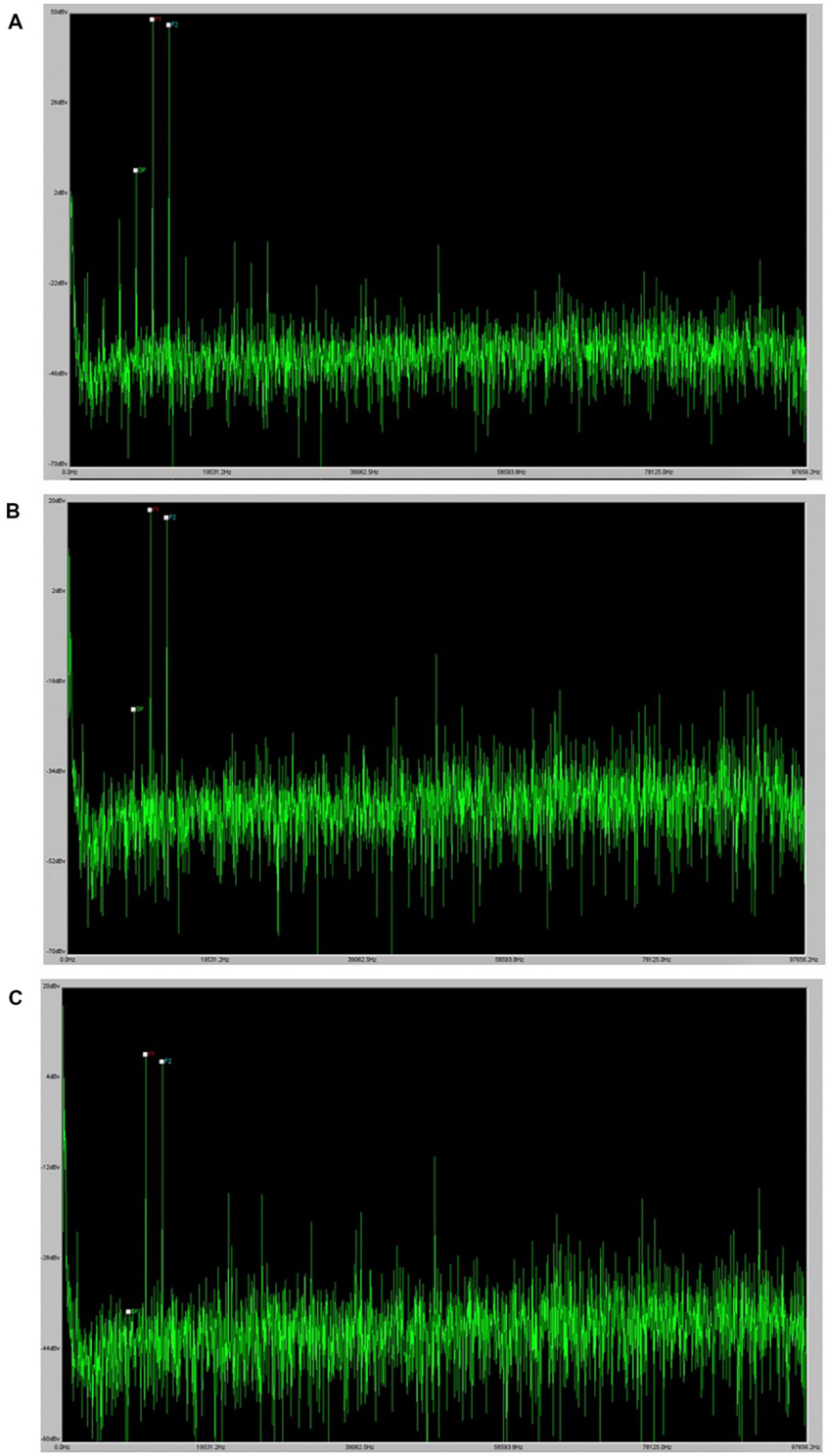

FIGURE 1 | DPOAE example. Panel **(A)** provides an example of a robust DPOAE as it displays in the BioSig software. Panels **(B)** and **(C)** provide examples of the visual indication of a DPOAE at the threshold and the absence of a DPOAE at lower levels.

wean average threshold across frequencies by group with Tukey A *post hoc* comparison, the control group (Group 1) had lower thresholds than Group 2 (5.63 dB mean difference, $p = 0.043$), Group 3 (9.39 dB, $p = 0.001$), and Group 5 (5.83 dB, $p = 0.049$). DPOAE thresholds for this time point were analyzed using a two-factor ANOVA (frequency*group). There was no two-way

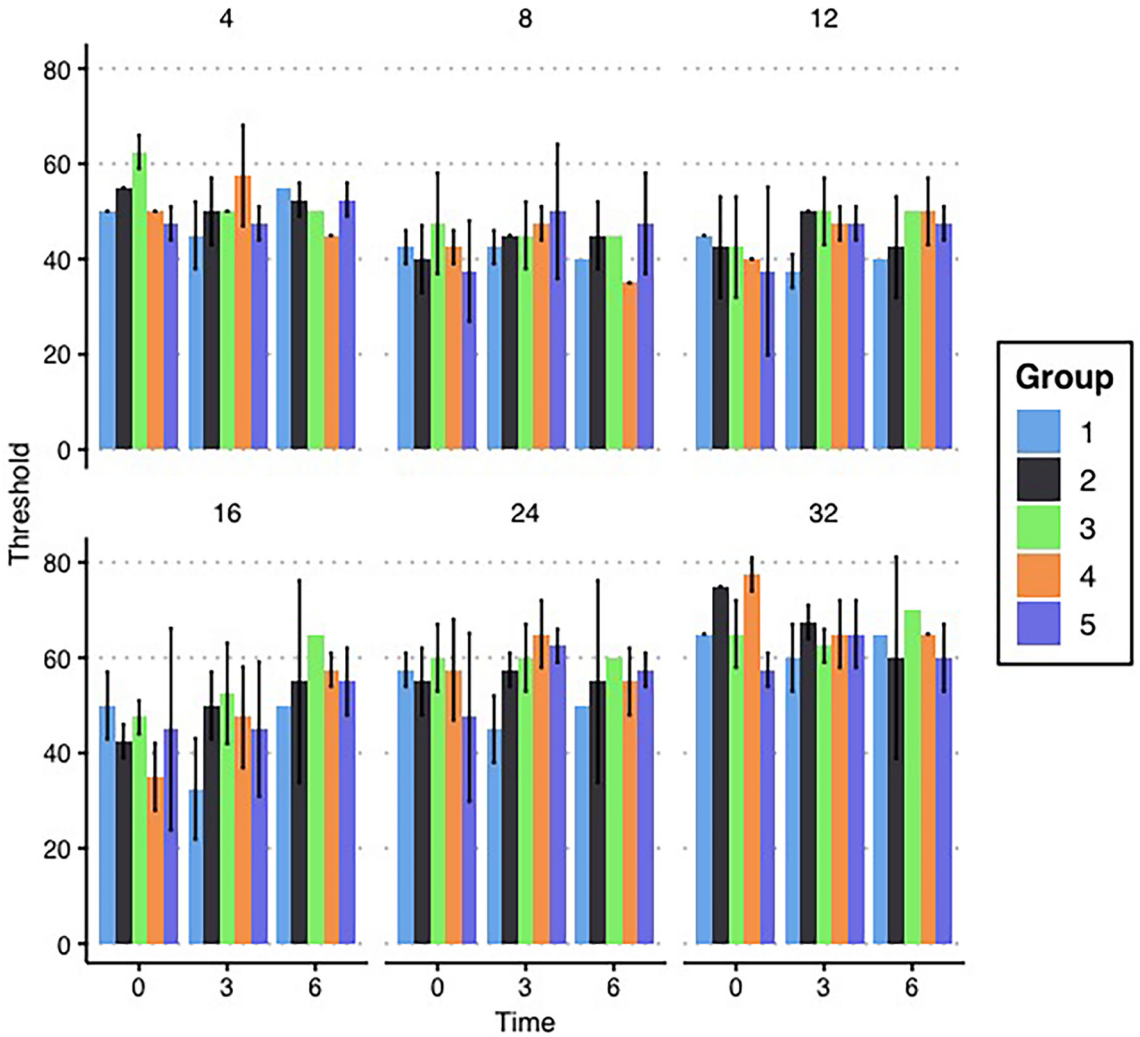

FIGURE 2 | Breeder ABR results. Mean ABR thresholds for each group of female breeding mice are depicted by the bars in each panel. Thresholds are grouped with the first set in each panel depicting mean thresholds before enrollment in the study and the next sets indicating the ABR thresholds at 3 and 6 months, respectively. Each panel represents a tested frequency. No significant differences exist between groups. Error bars represent ±1 standard deviation (SD).

interaction of group and frequency ($F_{(1,13.810)} = 1.1622, p = 0.073$) and there was no significant effect of group ($F_{(1,4)} = 2.363$, $p = 0.059$). To account for a lack of sphericity, a Huynh-Feldt correction was run on the reported two-way interaction with no change in the significance.

To physiologically evaluate the consequences of HAART exposure during PaB on the afferent synaptic pathway and auditory brainstem, P1 and P3 latencies, and P1-P3 interpeak latencies were evaluated for all responses from 70 to 90 dB SPL at 16 kHz for all animals at wean. 16 kHz was chosen for this measure because it had robust responses and low thresholds in all experimental groups, and so was considered likely to indicate if there were any suprathreshold effects across groups. A one-way ANOVA (group) found a significant effect of group for P1 latency at 75 dB SPL ($p = 0.036$) and for P3 latency and P1-P3 interpeak latency at 75 ($p = < 0.001, 0.021$), 80 ($p = 0.001, < 0.001$), and 85 dB SPL ($p = 0.001, .011$). When evaluating these differences using Tukey A *post hoc* analysis, Group 4 had a greater P1 latency than Group 3 at 75 dB SPL, a greater P3 latency than Groups 2, 3, and 5 at 75–85 dB SPL and than Group 1 at 75–80 dB SPL, and a greater P1-P3 interpeak latency than Group 1 at 75 dB SPL, Groups 1, 2, 3, and 5 at 80 dB SPL, and than Groups 3 and 5 at 85 dB SPL. These results can be seen in greater detail in **Figure 4**.

DISCUSSION

Exposure to AZT and EFV During PaB Leads to Elevated ABR Thresholds at Wean

This study represents the first evaluation of the risk associated with exposure to specific controlled antiretrovirals during PaB.

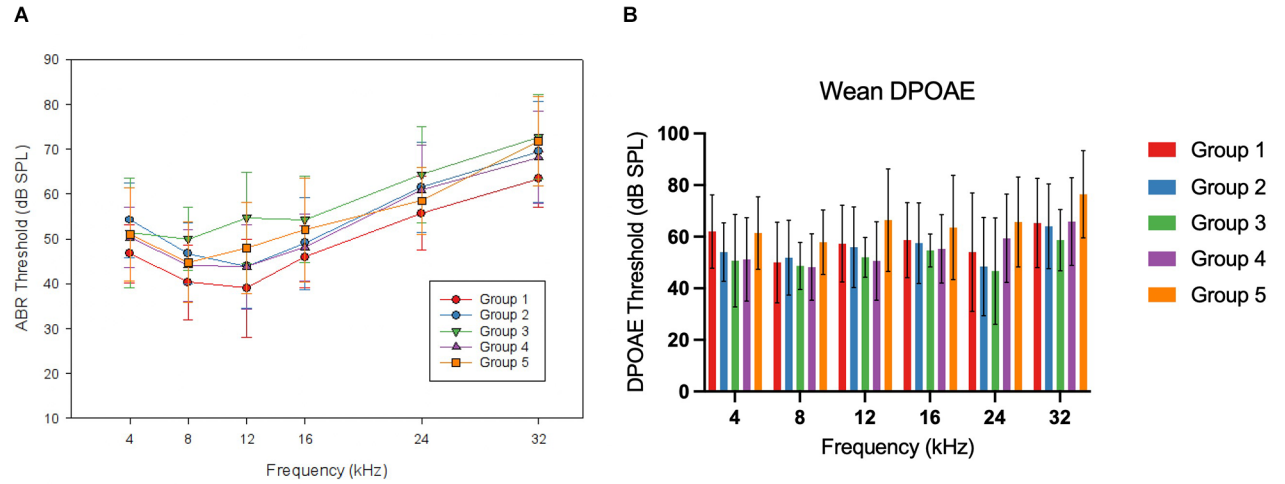

FIGURE 3 | Wean ABR and OAE. Panel **(A)** shows the mean ABR thresholds for each group of offspring mice at wean. No frequency-specific differences were reported at this time point. Mean thresholds for Group 1 were lower than in Groups 2, 3, and 5 ($p < 0.05$). Panel **(B)** shows the mean DPOAE thresholds for each group of offspring mice at wean. No significant differences were seen at this time point. Error bars represent ±1 SD.

The authors hypothesized that antiretroviral exposure during PaB would cause elevated ABR thresholds, with the greatest elevation arising from exposure to AZT and EFV. The results indicate that this hypothesis was correct, as both groups receiving either AZT or EFV had higher thresholds than controls. The group receiving both EFV and AZT saw an additional roughly 4-dB threshold mean increase over the groups receiving only one of those drugs. It is important to acknowledge that while Group 3 (AZT+EFV+3TC) saw higher thresholds than any other group in the study, those thresholds did not reach the level of statistical significance when compared to other ARV-exposed groups. While Group 4 (TDF+NVP+3TC) did not see elevated thresholds when compared to the control group, this group saw increased P3 and interpeak latencies when compared to all other groups. This indicates that different antiretroviral combinations may have different auditory impacts related to exposure during pregnancy and breastfeeding, and the differences across auditory measures may help to distinguish the site of lesion for these exposures.

The hypotheses of this study were largely driven by findings of toxicity to auditory cell lines *in vitro* (Thein et al., 2014). In that study, the authors investigated the mechanisms driving observed ototoxicity and were able to state that auditory cell losses seemed to be caspase 3/7-independent, indicating that those pro-apoptotic pathways did not appear to be the drivers of cell death. They hypothesized that, since EFV did not bind to mitochondrial DNA polymerase-y, EFV-induced damage was likely the result of endoplasmic reticulum stress. Subsequent exploration of the mechanisms of EFV-driven cytotoxicity has found that EFV causes significant cellular instability through the permeabilization of the mitochondrial outer membrane and induces changes in the mitochondrial membrane potential (Ganta et al., 2017). Changes in the mitochondrial membrane potential lead to cytochrome c release and mitochondrial-mediated apoptosis, both known causes of outer hair cell loss (Wang et al., 2004). ARV exposures have also shown toxicity to the placenta (Collier et al., 2003) and other organs throughout the body (Benbrik et al., 1997), which may lead to auditory impacts as a result of this damage. While the current study did not directly evaluate the cellular mechanisms driving threshold elevation, these results when combined with the current literature, suggest that one or more mechanisms may be synergistically combining to damage the auditory system of those exposed to these drugs during PaB.

The lack of significant differences in DPOAE thresholds for this study indicates that the ABR threshold elevations were not the result of damage to the OHCs and were instead the result of damage to the inner hair cells, auditory nerve, and/or auditory brainstem. This is in line with previous work on the auditory impacts of ARVs that found abnormalities in the morphology of the ABR thought to be indicative of central auditory system pathology (Matas et al., 2010) and our previous experiment in the C57Bl6/J mouse (DeBacker et al., 2022). While this contradicts the findings of Thein et al. (2014), it is possible that differences in route of administration, cochlear supporting structures, or *in utero* delivery vs. direct administration to *ex vivo* samples may have caused these differences. This is further supported by the differences in P3 latency and P1-P3 interpeak latency seen in Group 4 when compared to other exposure groups. Especially since Group 4 had no significant differences in ABR threshold at wean, these significant differences in ABR morphology indicate that antiretroviral exposure during PaB may be causing auditory dysfunction that is not detected using conventional hearing screening methods.

Likely the most significant implication of this work is that ARV exposure during PaB causes auditory dysfunction that would not be detected in the most common newborn hearing screenings with ABRs or DPOAEs. This may help to clarify the currently mixed findings in the literature for PHEU children. The Torre group found impaired auditory processing in young

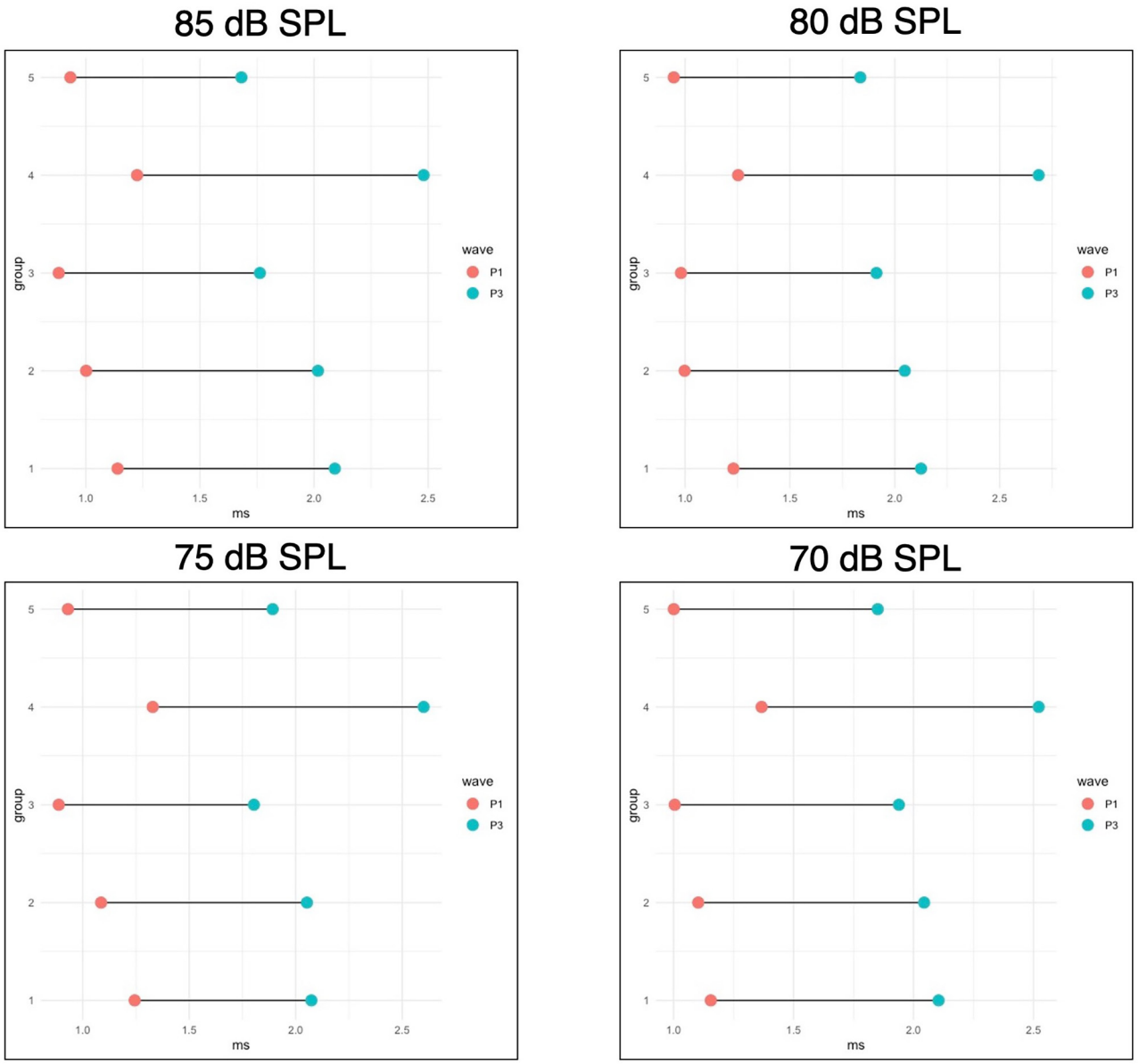

FIGURE 4 | Wean ABR latencies. This figure shows the mean P1 and P3 latencies for offspring measured at wean for four intensities (90 dB SPL is not pictured, but no significant differences were seen at this level). P1-P3 interpeak latencies are represented by the bars connecting the points for each group. Group 4 had a greater P1 latency than Group 3 at 75 dB SPL, a greater P3 latency than groups 2, 3, and 5 at 75–85 dB SPL and than Group 1 at 75–80 dB SPL, and a greater P1-P3 interpeak latency than Group 1 at 75 dB SPL, Groups 1, 2, 3, and 5 at 80 dB SPL, and than Groups 3 and 5 at 85 dB SPL. All significant differences are $p < 0.05$.

adults who had been exposed to HIV and HAART *in utero* (Torre et al., 2020), but did not find an increased rate of failed hearing screenings in children exposed to HIV and HAART *in utero* (Torre et al., 2017). These findings could indicate that children exposed to HAART *in utero* are not at increased risk for clinically-significant hearing loss, but are at risk for other auditory processing difficulties. It is important to note, however, that hearing screening at birth is not as sensitive as other auditory measures, like diagnostic threshold ABRs, and so is likely to miss subtle differences resulting from *in utero* HAART exposure. The small threshold elevations seen in the mice in this study would be unlikely to cause a failed hearing screening, especially given the lack of impact on DPOAEs, which are frequently used in newborn hearing screenings. As such, it is possible that if such minimal hearing losses are also occurring in PHEU children, they are being missed on early hearing evaluations. PHEU children are therefore unable to benefit from the early intervention they would have received had these hearing differences been caught at birth. There is evidence linking short-term minimal hearing losses from otitis media to long-term auditory processing

difficulties (Moore et al., 2020), and so it is possible that persistent minimal hearing losses like those seen in this study could result in the auditory processing difficulties described by Torre et al. (2020).

No Threshold Shifts Were Seen in Adult Mice

No auditory differences were seen in adult mice as a result of ARV exposure during the study. This is in agreement with previous studies of ARV exposure in mice (Bektas et al., 2008), and it is consistent with a model that indicates ARV exposure is causing subtle, even sub-clinical, changes in hearing during development. The CBA/CaJ mouse has "golden ears," a term used to indicate that they develop little age-related hearing loss. Certainly, within the time window of the breeding for the experiments, the female breeder mice would not have been expected to develop age-related hearing loss, and indeed they did not. Our previous work in this area used the C57Bl6/J mouse (DeBacker et al., 2022), which develops age-related hearing loss within weeks of its wean age (Willott et al., 1991). The variability in thresholds of those mice makes it difficult to interpret small mean differences of less than 10 dB. However, the same differences were detected in the CBA/CaJ mouse, which significantly reinforces the earlier finding. There was no reason to expect the HAART-exposed CBA/CaJ mice to be different from the control group unless the HAART exposure during PaB was indeed affecting the auditory system.

Limitations

It is of course important to recognize that the current study was a pre-clinical model of hearing using the CBA/CaJ mouse. While this is a well-studied model of audition and ototoxicity and every effort was made to design this study to be translational in nature, there are limitations inherent to non-human animal studies when applying the results to human populations. As such, further study in humans is required to confirm these findings are applicable across species. Additionally, it should be recognized that this was a model of HAART exposure only and not of the combined effects of HIV and HAART on the developing offspring. As such, differences may exist when introducing the variable of HIV infection alongside these exposures, and future studies should evaluate these exposures concurrently to determine if the addition of HIV impacts the auditory effects seen in this study. Lastly, it should be recognized that the mean threshold elevations seen in this study are small (5–9 dB SPL). Despite the small degree of hearing impairment, the literature on language and cognitive development in children discussed above indicates that even these minimal hearing losses can have significant impacts on outcomes in children. This impact on outcomes is particularly concerning given the fact that minimal hearing losses like those observed in this study are less likely to be detected, even in settings with robust early hearing screening protocols.

CONCLUSIONS

The current study found that exposure to HAART, especially cocktails including AZT and EFV, during PaB was associated with increased ABR thresholds and differences in ABR wave latencies at wean when compared to unexposed offspring. These same threshold elevations were not seen on DPOAEs. Due to the minimal degree of threshold elevation (5–9 dB SPL) and lack of impact on DPOAEs, these hearing losses would be unlikely to be detected with common newborn hearing screenings. This may explain some of the discrepancies in the current literature relating to auditory function at birth in PHEU children (Poblano et al., 2004; Fasunla et al., 2014; Torre et al., 2017). Further study in models of concurrent HIV and HAART exposure and in human subjects is warranted to confirm the clinical relevance of these results.

DATA AVAILABILITY STATEMENT

The raw data supporting the conclusions of this article will be made available by the authors, without undue reservation.

ETHICS STATEMENT

The animal study was reviewed and approved by Ohio State University Institutional Animal Care and Use Committee.

AUTHOR CONTRIBUTIONS

JD and EB contributed to the conception and design of this study. JD and BL performed experiments and collected data. JD performed statistical analyses and wrote the first draft of the manuscript. BL and EB wrote sections of the manuscript. All authors contributed to the article and approved the submitted version.

FUNDING

This work was supported by The Ohio State University Alumni Grants for Graduate Research and Scholarship (JD) and The American Academy of Audiology Foundation's Student Investigator Funds (JD). Work on this manuscript was supported in part by a VA Rehabilitative Research & Development Service Merit Review Award (#C0239R) and with resources and the use of facilities at the NCRAR (Center Award #C2361-C). The content of this manuscript does not represent the views of the Department of Veteran Affairs or the United States Government.

ACKNOWLEDGMENTS

We would like to thank Drs. Christina Roup, Eric Healy, and Ruili Xie for editorial feedback, Dr. Aaron Roman for assistance in generating figures, and Dr. Cara Hollander for sparking this particular line of research.

REFERENCES

Bektas, D., Martin, G. K., Stagner, B. B., and Lonsbury-Martin, B. L. (2008). Noise-induced hearing loss in mice treated with antiretroviral drugs. *Hear. Res.* 239, 69–78. doi: 10.1016/j.heares.2008.01.016

Benbrik, E., Chariot, P., Bonavaud, S., Ammi-Saïd, M., Frisdal, E., Rey, C., et al. (1997). Cellular and mitochondrial toxicity of zidovudine (AZT), didanosine (ddI) and zalcitabine (ddC) on cultured human muscle cells. *J. Neurol. Sci.* 149, 19–25. doi: 10.1016/s0022-510x(97)05376-8

Blanche, S., Tardieu, M., Rustin, P., Slama, A., Barret, B., Firtion, G., et al. (1999). Persistent mitochondrial dysfunction and perinatal exposure to antiretroviral nucleoside analogues. *The Lancet* 354, 1084–1089. doi: 10.1016/S0140-6736(99)07219-0

Brogly, S. B., Ylitalo, N., Mofenson, L. M., Oleske, J., Van Dyke, R., Crain, M. J., et al. (2007). *In utero* nucleoside reverse transcriptase inhibitor exposure and signs of possible mitochondrial dysfunction in HIV-uninfected children. *AIDS* 21, 929–938. doi: 10.1097/QAD.0b013e3280d5a786

Coelho, A., Tricarico, P., Celsi, F., and Crovella, S. (2017). Antiretroviral treatment in HIV-1-positive mothers: neurological implications in virus-free children. *Int. J. Mol. Sci.* 18:423. doi: 10.3390/ijms18020423

Cohen, M. S., Chen, Y. Q., McCauley, M., Hosseinipour, M. C., Kumarasamy, N., Hakim, J. G., et al. (2011). Prevention of HIV-1 infection with early antiretroviral therapy. *N. Engl. J. Med.* 365, 493–505. doi: 10.1056/NEJMoa1105243

Collier, A. C., Helliwell, R. J. A., Keelan, J. A., Paxton, J. W., Mitchell, M. D., Tingle, M. D., et al. (2003). 3'-azido-3'-deoxythymidine (AZT) induces apoptosis and alters metabolic enzyme activity in human placenta. *Toxicol. Appl. Pharmacol.* 192, 164–173. doi: 10.1016/s0041-008x(03)00274-6

DeBacker, J. R., Hu, B. H., and Bielefeld, E. C. (2022). Mild hearing loss in C57BL6/J mice after exposure to antiretroviral compounds during gestation and nursing. *Int. J. Audiol.* 25, 1–7. doi: 10.1080/14992027.2022.2067081

Fasunla, A. J., Ogunbosi, B. O., Odaibo, G. N., Nwaorgu, O. G. B., Taiwo, B., Olaleye, D. O., et al. (2014). Comparison of auditory brainstem response in HIV-1 exposed and unexposed newborns and correlation with the maternal viral load and CD4+ cell counts. *AIDS* 28, 2223–2230. doi: 10.1097/QAD.0000000000000393

Ganta, K. K., Mandal, A., and Chaubey, B. (2017). Depolarization of mitochondrial membrane potential is the initial event in non-nucleoside reverse transcriptase inhibitor efavirenz induced cytotoxicity. *Cell Biol. Toxicol.* 33, 69–82doi: 10.1007/s10565-016-9362-9

Matas, C. G., Silva, S. M., de Almeida Macron, B., and Gonçalves, I. C. (2010). Electrophysiological manifestations in adults with HIV/AIDS submitted and not submitted to antiretroviral therapy. *Pró-Fono R. Atual. Cient.* 22, 107–113. doi: 10.1590/s0104-56872010000200007

McHenry, M. S., Balogun, K. A., McDonald, B. C., Vreeman, R. C., Whipple, E. C., Serghides, L., et al. (2019). *In utero* exposure to HIV and/or antiretroviral therapy: a systematic review of preclinical and clinical evidence of cognitive outcomes. *J. Int. AIDS Soc.* 22:e25275. doi: 10.1002/jia2.25275

Moore, D. R., Zobay, O., and Ferguson, M. A. (2020). Minimal and mild hearing loss in children: association with auditory perception, cognition and communication problems. *Ear Hear.* 41, 720–732. doi: 10.1097/AUD.0000000000000802

Poblano, A., Figueroa, L., Figueroa-Damián, R., and Schnaas, L. (2004). Effects of prenatal exposure to Zidovudine and Lamivudine on brainstem auditory evoked potentials in infants from HIV-infected women. *Proc. West. Pharmacol. Soc.* 47, 46–49.

Rice, M. L., Zeldow, B., Siberry, G. K., Purswani, M., Malee, K., Hoffman, H. J., et al. (2013). Evaluation of risk for late language emergence after *in utero* antiretroviral drug exposure in HIV-exposed uninfected infants. *Pediatr. Infect. Dis. J.* 32, e406–e413. doi: 10.1097/INF.0b013e31829b80ee

Tardieu, M., Brunelle, F., Raybaud, C., Ball, W., Barret, B., Pautard, B., et al. (2005). Cerebral MR imaging in uninfected children born to HIV-seropositive mothers and perinatally exposed to zidovudine. *Am. J. Neuroradiol.* 7, 695–701.

Thein, P., Kalinec, G. M., Park, C., and Kalinec, F. (2014). *In vitro* assessment of antiretroviral drugs demonstrates potential for ototoxicity. *Hear. Res.* 310, 27–35. doi: 10.1016/j.heares.2014.01.005

Torre, P., Russell, J. S., Smith, R., Hoffman, H. J., Lee, S., Williams, P. L., et al. (2020). Words-in-noise test performance in young adults perinatally HIV infected and exposed, uninfected. *Am. J. Audiol.* 29, 68–78. doi: 10.1044/2019_AJA-19-00042

Torre, P., Zeldow, B., Yao, T., Hoffman, H., Siberry, G., Purswani, M., et al. (2017). Newborn hearing screenings in human immunodeficiency virus-exposed uninfected infants. *J. AIDS Immune Res.* 10:102.

Wang, J., Ladrech, S., Pujol, R., Brabet, P., Van De Water, T. R., Puel, J.-L., et al. (2004). Caspase inhibitors, but not c-Jun NH2-terminal kinase inhibitor treatment, prevent cisplatin-induced hearing loss. *Cancer Res* 64, 9217–9224. doi: 10.1158/0008-5472.CAN-04-1581

WHO (2020). *HIV/AIDS Fact Sheet [WWW Document]*. Available online at: http://www.who.int/mediacentre/factsheets/fs360/en/.

Willott, J. F., Parham, K., and Hunter, K. P. (1991). Comparison of the auditory sensitivity of neurons in the cochlear nucleus and inferior colliculus of young and aging C57BL/6J and CBA/J mice. *Hear Res.* 53, 78–94. doi: 10.1016/0378-5955(91)90215-u

Conflict of Interest: The authors declare that the research was conducted in the absence of any commercial or financial relationships that could be construed as a potential conflict of interest.

frontiers | Frontiers in Molecular Neuroscience

ORIGINAL RESEARCH
published: 18 July 2022
doi: 10.3389/fnmol.2022.944846

An *in vivo* Biomarker to Characterize Ototoxic Compounds and Novel Protective Therapeutics

*Joseph A. Bellairs[1], Van A. Redila[1,2], Patricia Wu[2,3], Ling Tong[1,2], Alyssa Webster[4], Julian A. Simon[4], Edwin W. Rubel[1,2] and David W. Raible[1,2,3]**

[1] Department of Otolaryngology-Head and Neck Surgery, University of Washington, Seattle, WA, United States, [2] Virginia Merrill Bloedel Hearing Research Center, University of Washington, Seattle, WA, United States, [3] Department of Biological Structure, University of Washington, Seattle, WA, United States, [4] Fred Hutchinson Cancer Research Center, Seattle, WA, United States

OPEN ACCESS

Edited by:
Peter S. Steyger,
Creighton University, United States

Reviewed by:
Ruili Xie,
The Ohio State University, United States
Samson Jamesdaniel,
Wayne State University, United States

***Correspondence:**
David W. Raible
draible@uw.edu

Specialty section:
This article was submitted to Methods and Model Organisms, a section of the journal Frontiers in Molecular Neuroscience

Received: 15 May 2022
Accepted: 21 June 2022
Published: 18 July 2022

Citation:
Bellairs JA, Redila VA, Wu P, Tong L, Webster A, Simon JA, Rubel EW and Raible DW (2022) An in vivo Biomarker to Characterize Ototoxic Compounds and Novel Protective Therapeutics. Front. Mol. Neurosci. 15:944846. doi: 10.3389/fnmol.2022.944846

There are no approved therapeutics for the prevention of hearing loss and vestibular dysfunction from drugs like aminoglycoside antibiotics. While the mechanisms underlying aminoglycoside ototoxicity remain unresolved, there is considerable evidence that aminoglycosides enter inner ear mechanosensory hair cells through the mechanoelectrical transduction (MET) channel. Inhibition of MET-dependent uptake with small molecules or modified aminoglycosides is a promising otoprotective strategy. To better characterize mammalian ototoxicity and aid in the translation of emerging therapeutics, a biomarker is needed. In the present study we propose that neonatal mice systemically injected with the aminoglycosides G418 conjugated to Texas Red (G418-TR) can be used as a histologic biomarker to characterize *in vivo* aminoglycoside toxicity. We demonstrate that postnatal day 5 mice, like older mice with functional hearing, show uptake and retention of G418-TR in cochlear hair cells following systemic injection. When we compare G418-TR uptake in other tissues, we find that kidney proximal tubule cells show similar retention. Using ORC-13661, an investigational hearing protection drug, we demonstrate *in vivo* inhibition of aminoglycoside uptake in mammalian hair cells. This work establishes how systemically administered fluorescently labeled ototoxins in the neonatal mouse can reveal important details about ototoxic drugs and protective therapeutics.

Keywords: biomarker, ototoxicity, otoprotection, mouse model, aminoglycloside, hair cell

INTRODUCTION

Aminoglycosides are potent, broad-spectrum antibiotics that are clinically employed to treat mycobacterial infections (*Mycobacterium tuberculosis)*, Gram-negative urinary and respiratory infections, and severe neonatal infections (Durante-Mangoni et al., 2009). Despite their wide antibacterial coverage, low cost, and stability at ambient temperatures, use of aminoglycosides in

developed countries is generally limited by dose-dependent damage to the kidney (nephrotoxicity) and inner ear (ototoxicity) (Forge and Schacht, 2000; Rizzi and Hirose, 2007; Van Boeckel et al., 2014). Aminoglycoside nephrotoxicity can be monitored for with regular kidney function screening and injury can be minimized or even reversed with strategies like adjusting dose for kidney function, hydration, limiting therapy duration, and once-daily dosing (Hatala et al., 1996; Munckhof et al., 1996; Bailey et al., 1997; Guo and Nzerue, 2002). To date there are no reliable clinical strategies or therapeutics that are approved or used to prevent or minimize aminoglycoside ototoxicity.

Aminoglycoside ototoxicity targets the mechanosensory hair cells within the inner ear, which convert mechanical energy from sound waves into electrical impulses. These cells are also exceptionally vulnerable to a wide variety of genetic and environmental challenges, including excessive noise exposure and off-target effects from therapeutics such as antineoplastic agents in addition to aminoglycoside antibiotics (Forge and Schacht, 2000; Rizzi and Hirose, 2007). While aminoglycoside antibiotics have been known to cause disabling hearing loss and vestibular disfunction for decades (Rybak et al., 2008), the cellular mechanisms underlying this pathology remain under intensive study. Previous work has implicated a diverse array of cellular insults caused by aminoglycosides, including excessive free radical accumulation (Priuska and Schacht, 1995; Hirose et al., 1997), mitochondrial damage (Qian and Guan, 2009), plasma-membrane interactions (Marche et al., 1983), calcium dysregulation (Esterberg et al., 2014, 2016), and both caspase-dependent (Cheng et al., 2003; Coffin et al., 2013) and caspase-independent (Jiang et al., 2006) cell death pathways. The diverse range of cytotoxic effects attributed to aminoglycosides makes target selection and rational drug design for protective therapeutics challenging. As an alternative approach, previous studies employed drug and compound screens for phenotypic drug discovery using the zebrafish model. Zebrafish lateral line hair cells closely resemble mammalian hair cells, and importantly they demonstrate susceptibility to known ototoxins such as aminoglycosides and the anticancer therapeutic cisplatin (Pickett and Raible, 2019). Utilizing high-throughput chemical screens in zebrafish to assess for hair cell protection from aminoglycosides, several promising protective compounds have been discovered (Owens et al., 2008; Kenyon et al., 2021), optimized (Chowdhury et al., 2018), and advanced to clinical trials (Kitcher et al., 2019).

Despite recent successes, translation of preclinical otoprotective leads to mammals and ultimately human clinical trials remains an immense challenge. Indeed, across numerous biomedical fields a majority of drug discovery pipelines fail to traverse the preclinical and clinical divide (Seyhan, 2019). Many preclinical ototoxicity studies occur in zebrafish and/or mammalian neonatal explant models, and while these models faithfully recapitulate parts of the auditory system (e.g., hair cells), they lack the complex pharmacokinetics and pharmacodynamics of an *in vivo* mammalian model. *In vivo* mammalian studies assessing clinical outcomes such as hearing loss with pre- and post-treatment auditory brainstem response (ABR) thresholds are the gold standard, but these studies in mice and rats are resource-intensive and take weeks to months to complete. Translating *in vitro* exposure conditions to *in vivo* dosing regimens is also a complex endeavor when considering pharmacokinetics of multiple compounds and the assessment of efficacy is limited to the clinical endpoint of ABR threshold shifts. As such, *in vivo* studies are often reserved for only the most promising lead compounds, and even then, finding a safe and effective drug candidate can be likened to the Herculean task akin to finding a needle in a haystack.

A biomarker is a measured characteristic that is an indicator of a normal biologic process, a pathogenic process, or a response to an exposure or intervention (FDA-NIH Biomarker Working Group, 2016). For studies of ototoxicity, there is a clear need for rapid, low-cost predictive biomarkers that can determine the ability of interventions and therapeutics to inhibit the accumulation of ototoxins in mammalian hair cells *in vivo*. Previous studies have used a variety of preparations such as cochlear cultures from neonatal mice (Richardson and Russell, 1991) and derived cell lines such as HEI-OC1 cells (Kalinec et al., 2003), and more recent reports proposed circulating microRNAs (Lee et al., 2018) and proteins such as prestin (Naples et al., 2018) as specific markers of hair cell injury. However, the translational utility of these markers remain to be validated. Here, we propose utilizing *in vivo* hair cell uptake of fluorescently labeled aminoglycosides as a histologic biomarker for ototoxicity. Despite the variety of mechanisms described for aminoglycoside-induced ototoxicity, there is consensus that a fundamental property of susceptible cells is their uptake and retention of aminoglycosides. Previous studies demonstrated that proximal convoluted tubule (PCT) cells within the kidney and inner ear mechanosensory hair cells show aminoglycoside uptake and retention following *in vivo* systemic aminoglycoside administration, and there appears to be good correlation between aminoglycoside uptake and cell death (Imamura and Adams, 2003; Dai et al., 2006; Kim and Ricci, 2022).

We examine intracellular accumulation of the aminoglycoside geneticin (G418) conjugated to the fluorophore Texas red (TR) in neonatal (P5) mouse hair cells following systemic injection. Building off recent studies (Makabe et al., 2020; Qian et al., 2021), we performed experiments in neonatal mice because (I) neonatal mice can be readily obtained in large number and at low costs from a small number of breeding adults and (II) neonatal otic capsules are incompletely ossified, allowing for rapid tissue fixation and easy dissection of sensory epithelium. We demonstrate that neonates, like juvenile mice (P25-30) with mature hearing sensitivity, exhibit dose- and time-dependent uptake and accumulation of G418-TR in hair cells. Using ORC-13661, an orally available small molecule that acts as a high-affinity permeant blocker of the mechanoelectrical transduction (MET) channel (Kitcher et al., 2019) and preserves hearing in rats treated with the aminoglycoside amikacin (Chowdhury et al., 2018), we demonstrate that hair cell uptake of G418-TR is inhibited *in vivo* in mammals. Our results show that neonatal mice injected with G418-TR can be used as a translational tool to better understand *in vivo* mammalian ototoxicity and characterize the efficacy of otoprotective therapeutics that block aminoglycoside uptake. These results also confirm a

mechanism of action for ORC-13661 predicted from zebrafish and mammalian *in vitro* studies (Kitcher et al., 2019).

MATERIALS AND METHODS

Animals

C57BL/6J wild-type mice were used in all experiments. Both male and female mice were used in all experiments. All procedures involving animals were carried out in accordance with the National Institutes of Health guide for care and use of laboratory animals and approved by the Institutional Animal Care and Use Committee of the University of Washington.

Synthesis of G418-TR

A modified synthesis of geneticin (G418) conjugated Texas Red (TR) was performed based on previously published protocols (Liu et al., 2015). TR-NHS ester was dissolved in anhydrous N,N-dimethylformamide and added to a solution of 1.377 mmol G418 disulfate in a 100 mM potassium carbonate solution. The resulting solution was mixed in darkness at 4°C for 48 h. G418-TR was purified by Reverse-phase chromatography connected to a UV-Vis detector monitoring a wavelength at 214 nm. The analyte was gradient eluted from a Waters delta-pak C18 (300 angstrom) 19 mm × 30 cm column using buffers of 0.1% trifluoroacetic acid (by volume in water) for "A" and acetonitrile/0.08% trifluoroacetic acid (by volume) for "B." Fractions were collected every thirty seconds between 15 and 38 min using a gradient as follows: 0 min at 5% "B," followed by a 5-min hold at 5% "B," then ramping up to 20% "B" in 1 min, followed by a linear gradient to 50% "B" in 25 min, followed by another linear ramp to 95% "B" in 2 min and holding at 95% "B" for 5 min, and finally ramping down to 5% "B" in 2 min and column equilibration at 5% "B" over another 5–10 min. Up to 1/3 of the sample volume was loaded onto the column and purified in three successive HPLC runs. Those fractions in which the m/z value corresponding to the analyte of interest were pooled, lyophilized, and stored in the dark at −20°C with a final yield of 68%.

G418-TR Uptake

G418, an aminoglycoside structurally related to gentamicin, was used for all experiments because unlike gentamicin, which is supplied as a variable mixture of aminoglycosides, G418 is a purified single aminoglycoside without batch-to-batch variation (O'Sullivan et al., 2020). G418-TR has previously been used to study aminoglycoside trafficking in zebrafish hair cells and it has been shown to be similar to gentamicin, both in toxicity and intracellular trafficking (Hailey et al., 2017). G418-TR in saline (2 mg/kg), TR-hydrazide (2 mg/kg; Invitrogen, Waltham, MA, United States), or sterilized saline were injected s.c. into P5 neonatal mice and P25-30 adult mice. Neonatal mice were returned to cages with dams and euthanized 30 min to 72 h following injection. At time of euthanasia, whole blood was collected, and otic capsules were isolated in cold PBS. Otic capsules were fixed in 4% paraformaldehyde in PBS for 1 h at room temperature in the dark. Tissue was washed 3× with PBS, and the organ of Corti was dissected in PBS at room temperature. Basal, middle, and apical turns were isolated and transferred to a 48-well plate. The tissues were permeabilized and immunolabeled with anti-myosin VIIa antibodies (1:1000, Proteus Biosciences, Ramona, CA, United States) in 0.1% Triton X-100, 10% normal horse serum, and PBS overnight at 4°C. After washing with PBS 3×, tissues were incubated with goat anti-rabbit Alexa 488 secondary antibody (1:750, Invitrogen, Waltham, MA, United States) and DAPI (1:2500, Thermo Scientific, Waltham, MA, United States) for 90 min at room temperature. Tissues were washed with PBS 3× and mounted in Fluoromount-G (Southern Biotech, Birmingham, AL, United States).

A similar procedure was carried out in adult animals. P25-30 mice were injected subcutaneously G418-TR in saline (2 mg/kg), TR-hydrazide (2 mg/kg), or sterilized saline. Animals were euthanized 6 h after injection and whole blood was collected. Otic capsules were removed and immediately transferred to cold 4% PFA. An insulin syringe with 27 G needle was used to carefully make an apical cochleostomy, the round window was then pierced with the needle, and cold PFA was slowly infused into the cochlea. Otic capsules were then fixed at room temperature for 90 min. Tissues were washed with PBS 3× and then transferred to 500 mM EDTA for overnight decalcification at 4°C. Tissue was washed with PBS, and the organ of Corti was dissected in PBS at room temperature. Immunolabeling and staining was the performed as above for the neonates.

ORC-13661 Uptake Inhibition

ORC-13661 was obtained from Oricula therapeutics. Compound was dissolved in sterile saline immediately prior to use. Animals were injected i.p. with ORC-13661 at 10–100 mg/kg 2 h prior to receiving aminoglycoside treatment. After 2 h, animals were dosed with G418-TR s.c. at 10 mg/kg. Animals were returned to their cages, and then sacrificed at 3 and 6 h after receiving G418-TR. For booster experiments animals received a booster dose of ORC-13661 3 h following G418-TR administration. Animals and tissues were processed as described above.

Cryostat Sectioning

Cochlea, kidneys, and livers were collected for cryostat sectioning. Animals were treated as indicated above, and after sacrifice the otic capsule was dissected in cold PBS and fixed in 4% PFA for 1 h. Kidneys were also removed from animals at the time of sacrifice and immerse in 10% formalin. After washing in PBS, samples were sequentially dehydrated and equilibrated in 30% sucrose, 1:1 sucrose to OCT compound, and OCT compound overnight. Embedded tissue was frozen at −18°C and sectioned at a thickness of 12 μm. Slides were prepared with sectioned tissue. Cochlea, kidneys, and livers were labeled with phalloidin-Alexa 488 (1:200, Invitrogen, Waltham, MA, United States) for 2 h at room temperature and DAPI (1:100) for 45 min at room temperature. Cochlea sections were also immunolabeled with rabbit anti-β3 tubulin (1:1000; clone TUJ1, Biolegend, San Diego, CA, United States) overnight at 4°C followed by goat anti-rabbit Alexa-488 (1:200, Invitrogen, Waltham, MA, United States) for 2 h at room temperature and DAPI (1:100) for 45 min at room

temperature. All dilutions were in 5% normal goat serum and 0.1% Triton X-100 in PBS.

Confocal Imaging

Slides were imaged with a Zeiss LSM 880 microscope (Zeiss, Oberkochen, Germany). For whole mount specimens, a 40× water objective was used to obtain 8-bit 1024 × 1024 pixel images of the mid-basal, mid-middle, and mid-apical turns. Confocal images were obtained using identical imaging parameters to compare fluorescence between images. For cryostat sectioned tissues, a 40× water objective was used to obtain 8-bit 1024 × 1024 pixel images of the organ of Corti, stria vascularis, spiral ganglia, and renal cortex. Identical imaging parameters were used for cochlea tissues, but laser intensity was decreased to avoid oversaturation when imaging renal cortex.

Fluorescence Quantification

For whole mount fluorescence quantification, ImageJ software was used for image processing and fluorescence quantification. For neonatal hair cells, a single 256 × 165 pixel region of interest (ROI) was selected from the stack in the z-plane that captured all three rows of outer hair cells (OHCs) between the nucleus and cuticular plate. A similar ROI measuring 256 × 55 pixels was selected for the inner hair cells, again at a z-plane between the nucleus and cuticular plate. Inner hair cell (IHC) and OHC ROIs were processed with a custom macro based on previously reported image analysis techniques (Makabe et al., 2020). Otsu thresholding was applied to the green channel to obtain a hair cell specific mask. This mask was then applied to the red channel image, and hair cell ROI mean fluorescence was calculated.

For cryostat sectioned tissue Phalloidin was used as a marker for hair cells, pillar cells, and stria vascularis tissue. OHC fluorescence was quantified by manually drawing an ROI for the region between the nucleus and the apical stereocilia. The ROI was then applied to the red channel, and mean fluorescence was quantified. Similarly, a manually segmented ROI for the pillar cells was used to quantify PC mean fluorescence. The stria vascularis ROI was also manually generated, and care was taken not to include acellular regions such as capillary lumens. For spiral ganglia neuron uptake quantification of tissue stained with Tuj1, a custom macro was generated that applied Otsu thresholding to the green channel to generate a mask which was then applied to the red channel to quantify mean fluorescence.

Statistics

Statistical analyses were done using GraphPad Prism 9.1.2. All statistics were performed comparing values from individual animals. When both cochlea were examined a mean value for the animal was calculated and used for analysis. Specific analyses are indicated in the figure legends. ANOVA was used to evaluate dose responses. Two-way ANOVA was used when multiple variables were analyzed for effect. When tissues from the same animal was compared, sample matching and a mixed effects model was used to account for any missing values. *P*-values less than 0.05 were considered significant.

Study Approval

All experiments were approved by the University of Washington Institution Animal Care and Use Committee.

RESULTS

Dose-Dependent Uptake of Systemically Administered G418-TR in Neonatal Mouse Hair Cells

To assess whether mammalian hair cells take up systemically injected geneticin (G418) tagged with Texas Red (TR), neonatal P5 C57/BL6 mice were subcutaneously (SC) injected with G418-TR (2.5–10 mg/kg), Texas Red-hydrazide (10 mg/kg) as a non-ototoxic control, or saline and sacrificed 6 h after injection. The selected doses of G418-TR were not toxic to neonatal mice and hair cell damage was not evident in cochlear whole mount preparations. G418-TR, like gentamicin-TR (GTTR) (Dai et al., 2006; Wang and Steyger, 2009; Makabe et al., 2020), was detectable within neonatal hair cells 6 h following SC injection with confocal microscopy of whole mount preparations (**Figure 1A**). Confocal microscopy demonstrates a dose-dependent increase in hair cell cytoplasmic accumulation of G418-TR. Control animals injected with 10 mg/kg unconjugated TR hydrazide demonstrate no significant hair cell fluorescence (**Supplementary Figure 1A**).

In order to quantify the dose-dependent uptake of G418-TR, we measured TR fluorescence present in mouse sera and cochlear hair cells. At time of euthanasia, blood was collected, serum was separated, and fluorescence was analyzed. A significant dose-dependent increase in serum fluorescence was observed in all treated animals (**Figure 1B**) after 6 h of treatment.

Quantification of IHC and OHC mean fluorescence was performed utilizing myosin VIIa immunolabeling as a hair cell-specific mask. Given the three-dimensional nature of the organ of Corti, regions of interest were calculated from different images within a stack to include the cytoplasm between the nucleus and cuticular plate for OHCs (**Figure 1A**) and IHCs (**Supplementary Figure 2**). Hair cells were analyzed from the apical, middle, and basal turns of each cochlea to assess for tonotopic differences in uptake. Following systemic administration of G418-TR in neonatal mice, both IHCs and OHCs demonstrated dose dependent increases in hair cell fluorescence (**Figures 1C,D**). When evaluating IHCs, all regions of the cochlea demonstrate a dose-dependent increase in uptake. Mixed-effect analysis with matching across tonotopic regions demonstrates a significant dose-effect ($P < 0.0001$), but no significant variation in IHC uptake across tonotopic regions ($P = 0.1090$). OHCs demonstrated dose-dependent uptake across base, middle, and apex. Mixed-effect analysis with matching across tonotopic regions demonstrates significant interaction between dose and tonotopic region ($P < 0.001$). Hair cells from animals treated with TR-hydrazide

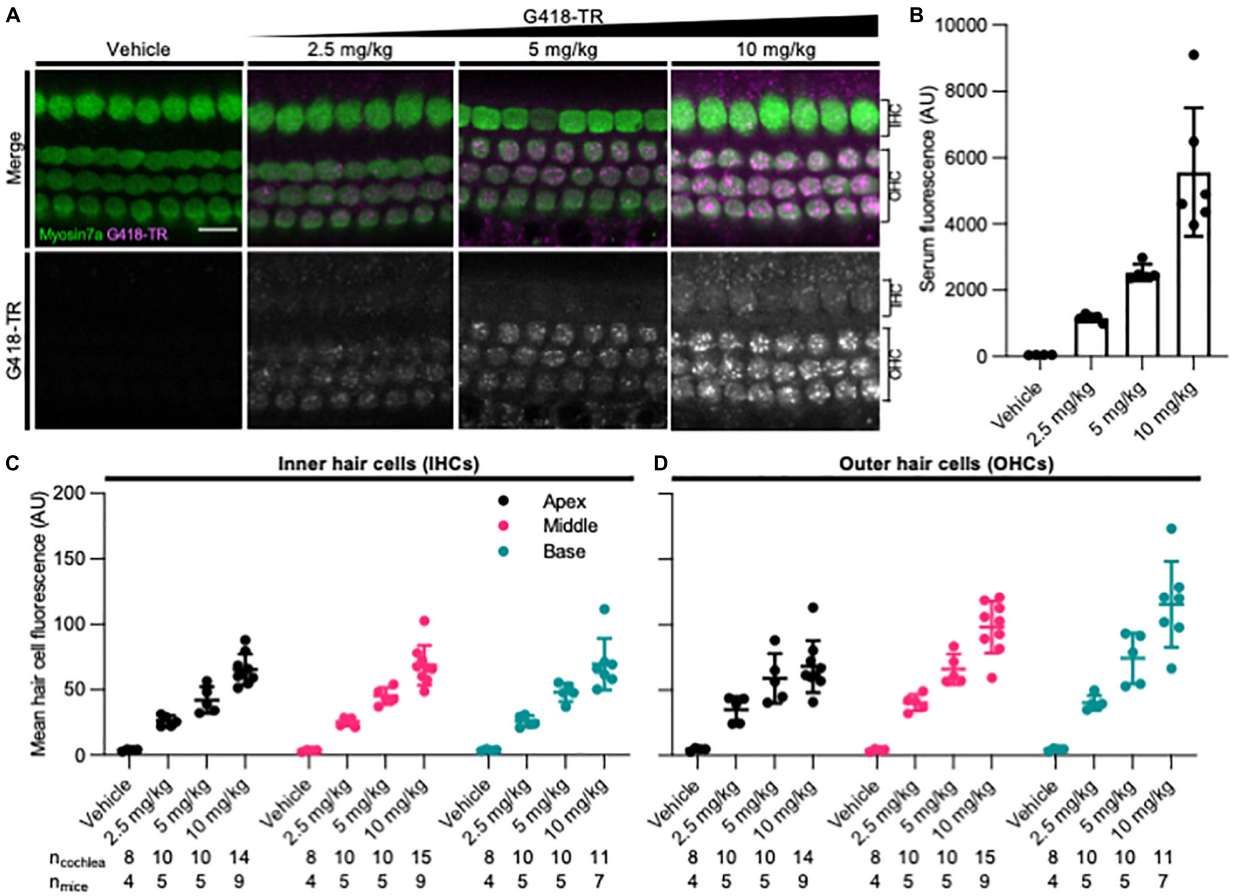

FIGURE 1 | G418-TR is taken up by neonatal mammalian hair cells following systemic administration. **(A)** At 6 h after systemic injection with G418-TR, neonatal mice (P5) were sacrificed, cochlear sensory epithelia was dissected and fixed, and tissue was immunolabeled for myosin VIIa. Representative single z-plane images captured from the middle turn of the cochlea in the region between the cuticular plate and nucleus demonstrate dose-dependent uptake of G418-TR in OHCs. Scale bar = 10 μm. **(B)** 6 h after systemic administration of G418-TR, blood was collected from neonatal mice, serum was extracted, and fluorescence was quantified with a fluorescence plate reader. Increasing doses of G418-TR results in a dose-dependent increase in serum fluorescence [One-way ANOVA; $F_{(3,16)} = 25.02$, $P < 0.0001$]. **(C)** Mean G418-TR fluorescence intensity of IHCs by tonotopic region 6 h after systemic treatment. IHCs demonstrate similar dose-dependent uptake of G418-TR in base, middle, and apex. **(D)** Mean G418-TR fluorescence intensity of OHCs by tonotopic region 6 h after systemic treatment. OHCs demonstrate significant dose-dependent and tonotopic G418-TR uptake [Mixed effects analysis; $F_{(6,36)} = 5.127$, $P = 0.0007$]. $n_{cochlea}$ and n_{mice} represent the number of cochlea and mice examined, respectively. When two cochlea from the same animal were analyzed, the animal mean was calculated and used for all statistics and graphs. Error bars are standard deviations. AU, arbitrary unit.

showed minimal background fluorescence that was not significantly different when compared to vehicle treated animals (**Supplementary Figure 1B**).

Dose-Dependent Uptake of Systemically Administered G418-TR in Mature Mouse Hair Cells Is Similar to Observed Neonatal Hair Cell Uptake

Rodent cochlear hair cells are immature at birth and only begin to acquire the morphological and biophysical specializations characterizing mature hair cells during postnatal development (He et al., 1994; Marcotti and Kros, 1999; Abe et al., 2007; Jeng et al., 2020). Hearing onset in mice is generally thought to begin at approximately P12 and roughly corresponds with maturation of specializations related to hair cell type and location as well as other biophysical properties such as the endocochlear potential. In mice, the cochlea appears fully mature between P25-30 (Rubel, 1978; Kros et al., 1998; Marcotti et al., 2003; Rubel and Fay, 2012). To evaluate whether G418-TR uptake in mature hair cells was similar to that observed in neonatal mouse hair cells, juvenile C57/BL6 mice (25–30 days old) were subcutaneously (SC) injected with G418-TR (5–20 mg/kg), Texas Red-hydrazide (20 mg/kg), or saline and sacrificed 6 h after injection.

Similar to neonatal hair cells, we observed that juvenile mouse hair cells readily take up systemically injected G418-TR (**Figure 2A**). Quantification of fluorescence from serum samples showed a significant dose-dependent increase in serum fluorescence ($P < 0.0001$) (**Figure 2B**). Both juvenile IHCs and OHCs demonstrated a dose-dependent increase in fluorescence across all tonotopic regions examined. Mixed-effect analysis with matching across tonotopic regions demonstrated

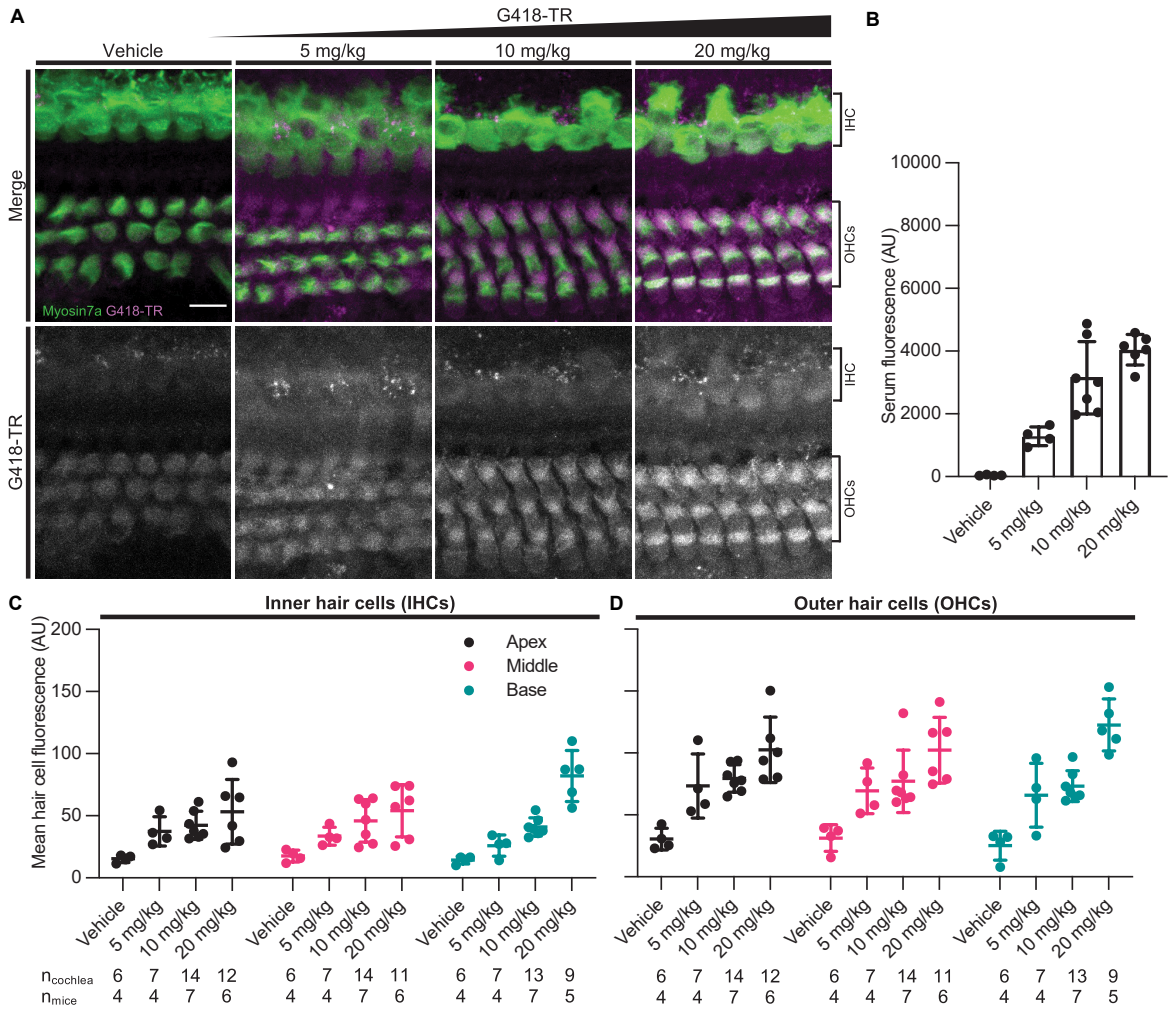

FIGURE 2 | G418-TR is taken up by mature mammalian hair cells following systemic administration. **(A)** At 6 h after systemic injection with G418-TR, juvenile mice (P25-30) were sacrificed, cochlear sensory epithelia was dissected and fixed, and tissue was immunolabeled for myosin VIIa. Representative maximum projection images captured from the middle turn of the cochlea demonstrate dose-dependent uptake of G418-TR in inner and outer hair cells. Scale bar = 10 μm. **(B)** 6 h after systemic administration of G418-TR, blood was collected from juvenile mice, serum was extracted, and fluorescence was quantified with a fluorescence plate reader. Increasing doses of G418-TR results in a dose-dependent increase in serum fluorescence [One-way ANOVA; $F_{(3,17)} = 28.28$, $P < 0.0001$]. **(C)** Mean G418-TR fluorescence intensity of IHCs by tonotopic region 6 h after systemic treatment. IHCs demonstrate low uptake at most doses of G418-TR with no significant tonotopic variation. **(D)** Mean G418-TR fluorescence intensity of OHCs by tonotopic region 6 h after systemic treatment. OHCs demonstrate dose-dependent uptake but not tonotopic variation in G418-TR uptake. $n_{cochlea}$ and n_{mice} represent the number of cochlea and mice examined, respectively. When two cochlea from the same animal were analyzed, the animal mean was calculated and used for all statistics and graphs. Error bars are standard deviations. AU, arbitrary unit.

significant dose-effects for IHCs or OHCs ($P < 0.001$ and $P < 0.0001$, respectively) but no significant variation from by tonotopic region for IHCs or OHCs ($P = 0.5924$ and $P = 9312$). Animals treated with TR-hydrazide demonstrated minimal fluorescence over background, which was similar to that observed in vehicle treated animals (**Supplementary Figures 1C,D**).

Characteristics of G418-TR Hair Cell Accumulation

Aminoglycoside-induced hair cell toxicity typically initially occurs in basal OHCs, and extends apically and to IHCs with increasing cumulative dosing (Forge and Schacht, 2000). We sought to determine whether this pattern of differential toxicity correlated with levels of G418-TR uptake. In P5 neonatal mice treated with 10 mg/kg G418-TR for 6 h, we observed dramatic tonotopic variation in uptake in OHCs, but not IHCs (**Figures 1C,D**). Basal turn OHCs demonstrated nearly twice the mean fluorescence compared to apical OHCs (115.8 and 68.2 AU, respectively). However, IHCs from the basal, middle, and apical turns from the same animals showed similar levels of fluorescence (69.7, 68.8, and 65.5 AU, respectively). In older mice with mature hearing (P25-30) treated with 20 mg/kg G418-TR for 6 h, we observed a much small but significant increase in IHC and OHC fluorescence in the basal turn only (**Figures 2C,D**).

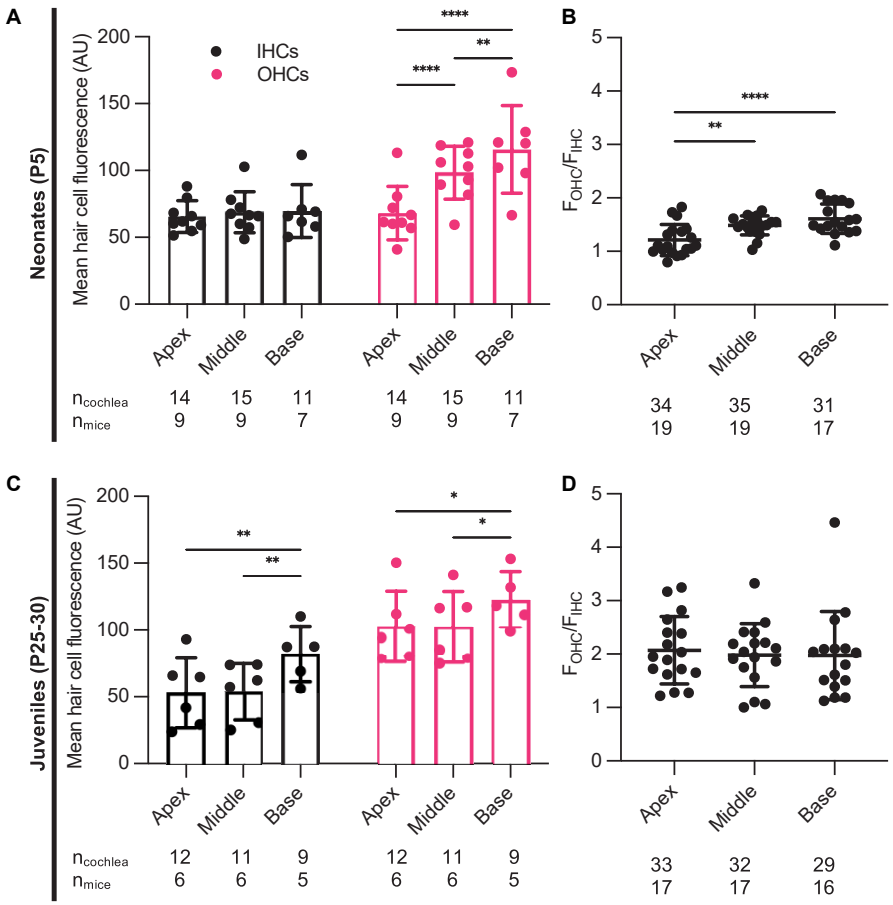

FIGURE 3 | Characteristics of G418-TR uptake in neonatal and juvenile hair cells. **(A)** Pooled analysis of the ratio of OHC to IHC uptake (F_{OHC}/F_{IHC}) was calculated for all neonatal animals treated with G418-TR (2.5, 5, and 10 mg/kg) and sorted by tonotopic region. In neonatal hair cells, there is significant variation in F_{OHC}/F_{IHC} by region [Mixed-effects Analysis; $F_{(2,52)} = 11.81$, $P < 0.0001$]. **(B)** Pooled analysis for all juvenile animals treated with G418-TR (5, 10, and 20 mg/kg) demonstrates no significant tonotopic variation in F_{OHC}/F_{IHC} [Mixed-effects Analysis; $F_{(2,31)} = 0.1442$, $P = 0.8662$]. $n_{cochlea}$ and n_{mice} represent the number of cochlea and mice examined, respectively. When two cochlea from the same animal were analyzed, the animal mean was calculated and used for all statistics and graphs. Error bars are standard deviations. $^{**}P < 0.01$, $^{****}P < 0.0001$; *P*-values generated from multiple comparisons *post hoc* test (Tukey's multiple comparison test).

In each cochlea we directly compared the ratio of OHC fluorescence to IHC fluorescence (F_{OHC}/F_{IHC}) in each tonotopic region. Apical, middle, and basal hair cells demonstrated significantly higher fluorescence in OHCs compared to IHCs (**Figures 3A,B**). When we analyzed data from all neonates treated with G418-TR (2.5–10 mg/kg) for 6 h, the ratio between OHC and IHC uptake increased from a mean of 1.21 at the apex to 1.61 at base. When the same analysis was applied to specimens collected from older animals (P25-30), mean F_{OHC}/F_{IHC} were 2.18, 2.11, and 2.02 in the apex, middle and base, respectively. Note as well that only 5 of 55 neonatal cochlea samples and 0 of the 50 juvenile cochlea samples examined in this way had F_{OHC}/F_{IHC} ratio < 1.0.

Neonatal Hair Cells Accumulate and Retain G418-TR

We also studied the relationship between G418-TR serum kinetics and hair cell uptake. We treated neonatal P5 mice with 10 mg/kg G418-TR and sacrificed cohorts of animals 30 min–72 h after injection. At the time of sacrifice, whole blood was collected from animals and serum was isolated for fluorescence quantification. Serum fluorescence was converted to concentration using a calibration curve of G418-TR diluted in fetal bovine serum. Serum kinetics for G418-TR demonstrate a peak at 3 h post-injection with a $t_{1/2}$ of 2.5 h, resembling the parameters previously reported for gentamicin-TR (Wang and Steyger, 2009; **Figure 4B**).

We also evaluated the kinetics of hair cell uptake and accumulation of G418-TR in hair cells from the same animals over 72 h. After subcutaneous injection with 10 mg/kg G418-TR, both OHCs and IHCs accumulate G418-TR over 6 h, and then retain that fluorescence for at least 72 h post-injection (**Figure 4A**). Quantification of middle turn hair cell fluorescence demonstrates that IHC and OHC fluorescence peaks at 6 h, and then plateaus with no significant decrease from 12 to 72 h post-injection (**Figure 4C**). IHC and OHC fluorescence is similar for the first 3 h, but after 6 h the difference between IHC

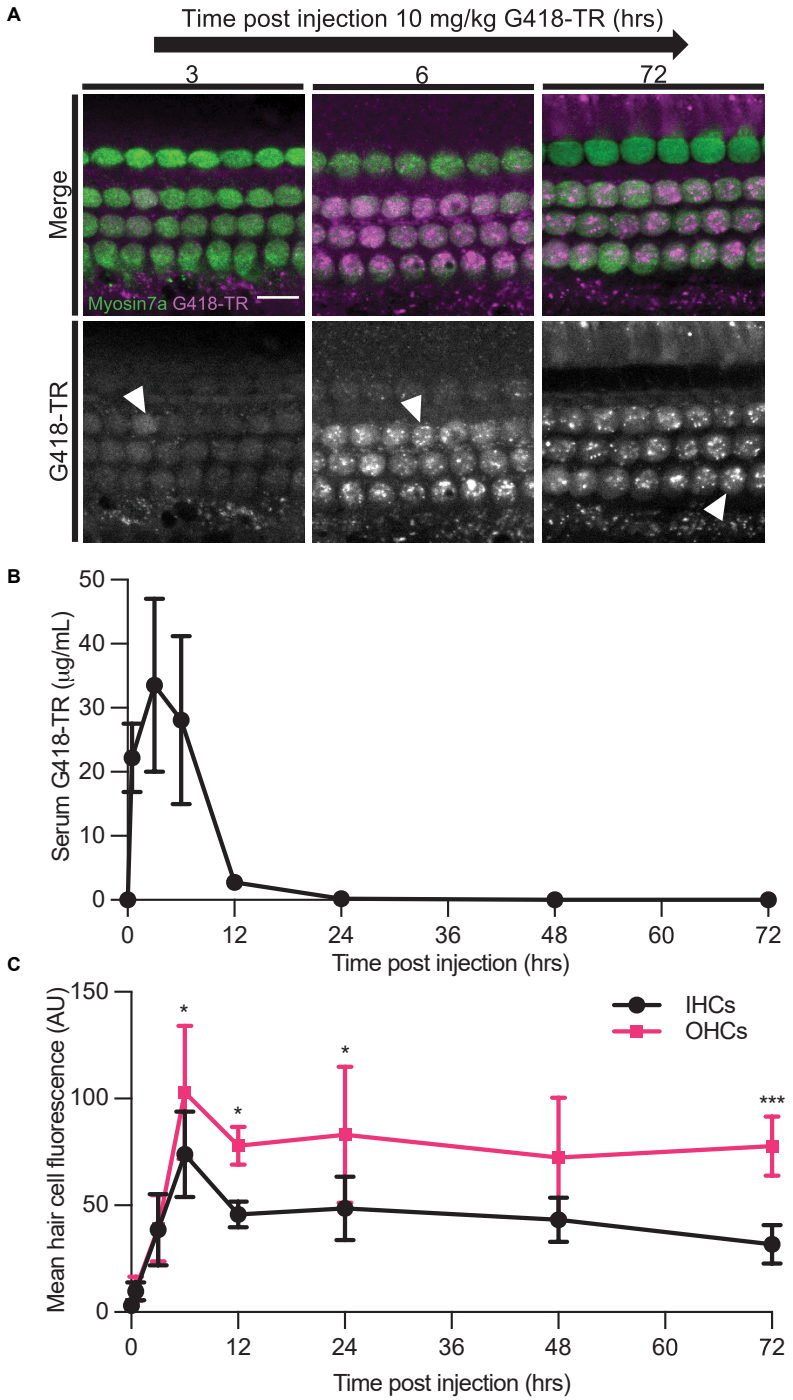

FIGURE 4 | Hair cells accumulate and retain G418-TR after systemic injection. **(A)** 30 min–72 h after systemic injection with 10 mg/kg G418-TR, neonatal mice (P5) were sacrificed, cochlear sensory epithelia was dissected and fixed, and tissue was immunolabeled for myosin VIIa. Representative images captured from the middle turn of the cochlea demonstrate uptake and retention of G418-TR. Images shown are single z-plane images capturing the region between the nucleus and cuticular plate. Arrowhead highlights transition from diffuse G418-TR distribution to accumulation in puncta with time. Scale bar = 10 μm. **(B)** Serum kinetics of G418-TR after systemic injection. After systemic injection with 10 mg/kg G418-TR, neonatal mice were sacrificed at different time points, serum was collected, and fluorescence was quantified. Fluorescence was converted to concentration in μg/mL utilizing a calibration curve of G418-TR diluted in fetal bovine serum. Quantification shows that serum levels of G418-TR peak at 3 h and are undetectable 24 h post-injection. **(C)** Mean hair cell fluorescence from the middle turn of the cochlea was calculated over 72 h. Both IHCs and OHCs show uptake and retention. Animals examined [*t* (hours), *n*] = (0,4), (0.5,4), (3,5), (6,6), (12,5), (24,5), (48,5), (72,5). Error bars are standard deviations. AU, arbitrary unit. Significant differences between IHC and OHCs denoted with: $^{*}P < 0.05$, $^{***}P < 0.001$. *P*-values calculated from multiple comparisons *post hoc* test (Šídák's multiple comparison test).

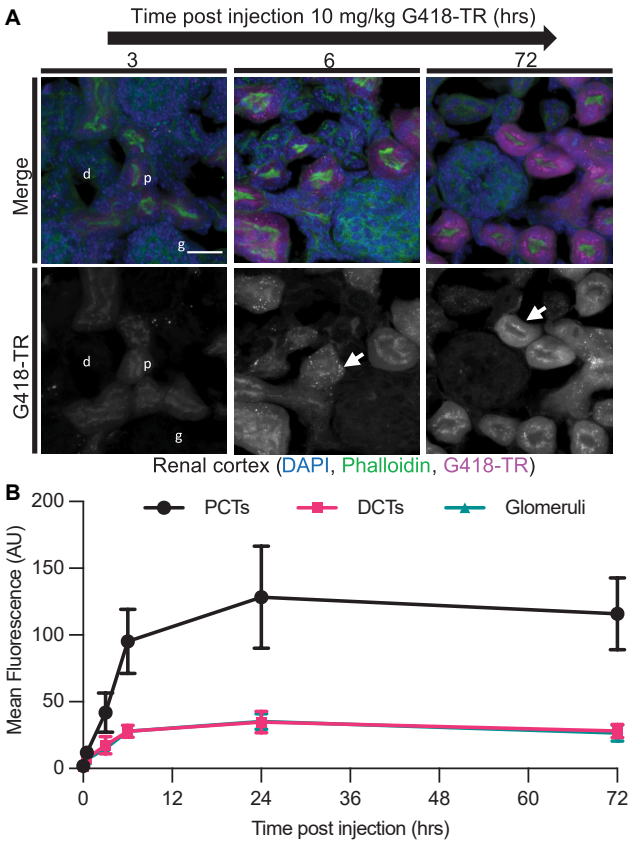

FIGURE 5 | Selective aminoglycoside retention in proximal convoluted tubule cells of the kidney. **(A)** 0 min–72 h after systemic injection with G418-TR, neonatal mice (P5) were sacrificed, and kidneys were removed. Tissues were fixed, embedded and cryostat sectioned at a thickness of 12 μm. Tissue sections were stained with phalloidin and DAPI. Representative maximum projection images from the renal cortex show proximal convoluted tubule (p) uptake and retention, but minimal uptake in the distal convoluted tubule (d) and glomeruli (g). Like hair cells, PCT cells also show apical puncta (arrow) accumulation of G418-TR. Scale bar = 20 μm. **(B)** Mean fluorescence from proximal convoluted tubules (PCTs), distal convoluted tubules (DCTs), and glomeruli was calculated over 72 h. PCTs demonstrate G418-TR uptake and retention like that observed in cochlear hair cells. Animals examined $n = 4$ for each time point. Error bars are standard deviations. AU, arbitrary unit.

and OHC mean fluorescence increases and remains significantly different. Statistical analysis demonstrates significant interaction between time since injection and hair cell population [two-way ANOVA, $F_{(7,62)} = 2.440$; $P < 0.05$]. *Post hoc* testing for multiple comparisons demonstrates significant differences between IHC and OHC values at 6, 12, 24, and 72 h post-injection ($P < 0.05$, $P < 0.05$, $P < 0.05$, and $P < 0.001$, respectively).

G418-TR Accumulation in the Kidney

Aminoglycoside nephrotoxicity is attributed to cytotoxic affects within the tubular epithelium (Lopez-Novoa et al., 2011). Within the nephron, the PCT cells, but not the glomerulus or distal convoluted tubule (DCT) cells, show unique susceptibility to aminoglycosides (Mingeot-Leclercq and Tulkens, 1999). Previous work using GTTR demonstrated that PCT cells rapidly take up aminoglycoside *in vivo* (Dunn et al., 2002; Dai et al., 2006). Kidneys were harvested from animals treated with 10 mg/kg G418-TR in order to evaluate renal aminoglycoside uptake and retention over 72 h (**Figure 5**). Similar to findings for hair cells, PCT epithelial cells rapidly accumulate G418-TR over 24 h and retain that fluorescence for up to 72 h. DCT cells and glomeruli show less accumulation of G418-TR, but it should still be noted that these cell populations demonstrate measurable G418-TR accumulation and retention. Additionally, it is worth noting that the intensity of the G418-TR signal was significantly brighter within the kidney compared to the cochlea, and the excitation laser intensity needed to be decreased in order to prevent over saturation of the detectors used. Because aminoglycosides are renally excreted, the nephrons of the kidney are exposed to significantly more aminoglycoside than the cochlea, accounting for this notable difference in overall fluorescence levels.

Aminoglycoside hepatotoxicity is rare (Aminoglycosides, 2012). Whether this is due to dose limiting toxicity in other organs (e.g., nephrotoxicity) or an intrinsic property of the liver that renders it less susceptible to aminoglycoside toxicity is unknown. When livers from animals treated with G418-TR were examined, we observed low levels of fluorescence analogous to that observed in the DCT and glomeruli of the kidney (**Supplementary Figure 3**). This complements previous analyses that noted low-level aminoglycoside uptake in the liver of animals treated with radioisotope labeled aminoglycosides (Huy et al., 1986).

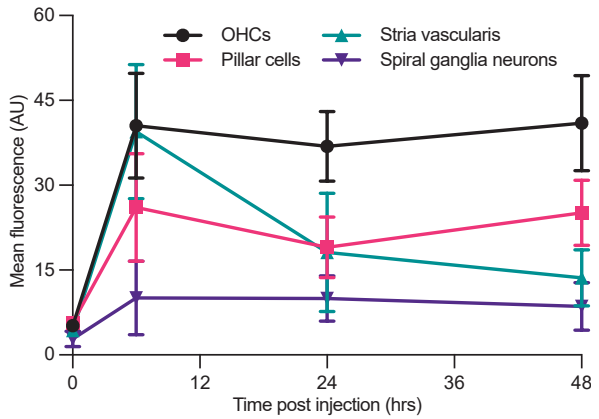

FIGURE 6 | Differential aminoglycoside uptake and retention within the cochlea. Cochlea from neonatal mice treated with G418-TR were fixed, cryostat sectioned, and signed in order to analyze the organ of Corti, stria vascularis, and spiral ganglia neurons. In order to compare relative G418-TR uptake between specific tissue types, fluorescence was quantified for outer hair cells (OHCs), pillar cells, stria vascularis, and spiral ganglia neurons. Note that while OHCs take up and retain G418-TR fluorescence, stria vascularis tissue has an early peak but then declines while SGNs show consistent low level uptake. PCs display an intermediate level of uptake with some retention. Error bars are standard deviations. Animal numbers [time (hours), *n*] = (0,3), (6,4), (24,4), and (48,4).

G418-TR Accumulation in Non-sensory Cochlear Tissues

In addition to hair cells, systemically administered aminoglycosides have been shown to accumulate in the non-sensory tissues of the inner ear (Bareggi et al., 1986; Imamura and Adams, 2003; Kitahara et al., 2005; Wang and Steyger, 2009). In neonatal mice treated with a single dose of 10 mg/kg G418-TR, we observed fluorescence in cryostat sectioned cochlear tissues in the organ of Corti, stria vascularis, and spiral ganglia neurons (**Supplementary Figure 4**).

The organ of Corti includes both the mechanosensory hair cells as well as numerous supporting cell populations and neuronal tissues. Analysis of OHCs in cross section supports the findings reported above for whole mount images; OHCs accumulate G418-TR in a diffuse pattern over 6 h, and at later time points G418-TR fluorescence is sequestered in apical regions (**Supplementary Figure 4A**). In neonatal mice, we observed a transient increase in stria vascularis fluorescence following systemic administration (**Supplementary Figure 4B**). Aminoglycosides have also been localized to spiral ganglia neurons following systemic injection (Imamura and Adams, 2003; Kitahara et al., 2005). Unlike the vascular stria vascularis, spiral ganglia neurons demonstrated consistent low-level fluorescence (**Supplementary Figure 4C**).

To compare the relative uptake of different tissues within the cochlea, we quantified mean tissue fluorescence at 0, 6, 24, and 48 h in each region (**Figure 6**). OHCs show a similar pattern as shown in whole mount imaging and quantification (**Figure 4**), with a peak at 6 h followed by retention of AG at later time points. Stria vascularis fluorescence demonstrated a peak in fluorescence at 6 h post-injection followed by a decrease to near background levels by 48 h. Pillar cells, located between IHCs and OHCs demonstrate relatively low-level uptake and retention of G418-TR, while spiral ganglion neurons demonstrated minimal uptake at all time points.

ORC-13661 Blocks the Uptake of G418-TR *in vivo* in Mammalian Hair Cells

ORC-13661 is a novel therapeutic that protects hair cells from aminoglycoside toxicity in fish and mammals (Chowdhury et al., 2018; Kitcher et al., 2019). Mechanistic studies in zebrafish and mouse cochlear cultures demonstrate that ORC-13661 reversibly blocks MET channel currents and uptake of fluorescently labeled aminoglycosides (Kitcher et al., 2019). To test whether ORC-13661 blocks uptake of aminoglycosides *in vivo* in mice, neonatal mice were pre-treated with saline or ORC-13661 (10–100 mg/kg; i.p.). Two hours after this treatment mice were injected with G418-TR (10 mg/kg; s.c.). Animals were sacrificed at either 3 or 6 h after exposure to G418-TR to test both 3 h ("short") and 6 h ("long") G418-TR exposure paradigms (**Supplementary Figures 5A,B**).

Analysis of the mid-basal turn hair cells demonstrated inhibition of uptake by ORC-13661 in both treatment schemes (**Figures 7A,B**). When animals are pre-treated with vehicle and injected with G418-TR, robust hair cell uptake is observed in both treatment schemes. When pretreated with increasing doses of ORC-13661 followed by injection with G418-TR, the short G418-TR exposure scheme demonstrates significant uptake inhibition at all doses of ORC-13661. Interestingly, the long G418-TR exposure scheme showed uptake inhibition at only the 100 mg/kg ORC-13661 dose.

To compare results between experiments, hair cell fluorescence was normalized to intra-experimental vehicle treated animals. By normalizing within experimental groups, we were able to minimize the variability between experimental groups (as observed in neonates treated with 10 mg/kg G418-TR [**Figures 1C,D**]) and discriminate smaller effects on hair cell uptake. We quantified relative fluorescence for mid-basal turn OHCs and observed a significant dose-dependent inhibition of uptake for increasing doses of ORC-13661 in the short exposure scheme with significant uptake inhibition compared to vehicle treated animals detected at all ORC-13661 dose levels (**Figure 7A**). For animals treated in the long exposure paradigm, significant uptake inhibition was only noted at the highest dose of ORC-13661 (**Figure 7B**). Kidneys from animals in the 100 mg/kg ORC-13661 dose group of the long exposure scheme demonstrated no change in PCT G418-TR uptake (**Supplementary Figure 6**). This supports the hypothesis that ORC-13661 protects hair cells through selective inhibition of MET-dependent aminoglycoside uptake, as opposed to endocytosis.

When comparing the two different treatment schemes with a two-way ANOVA, there is no significant difference in OHC uptake inhibition [$F_{(3,50)} = 1.989$, $P = 0.1276$] however

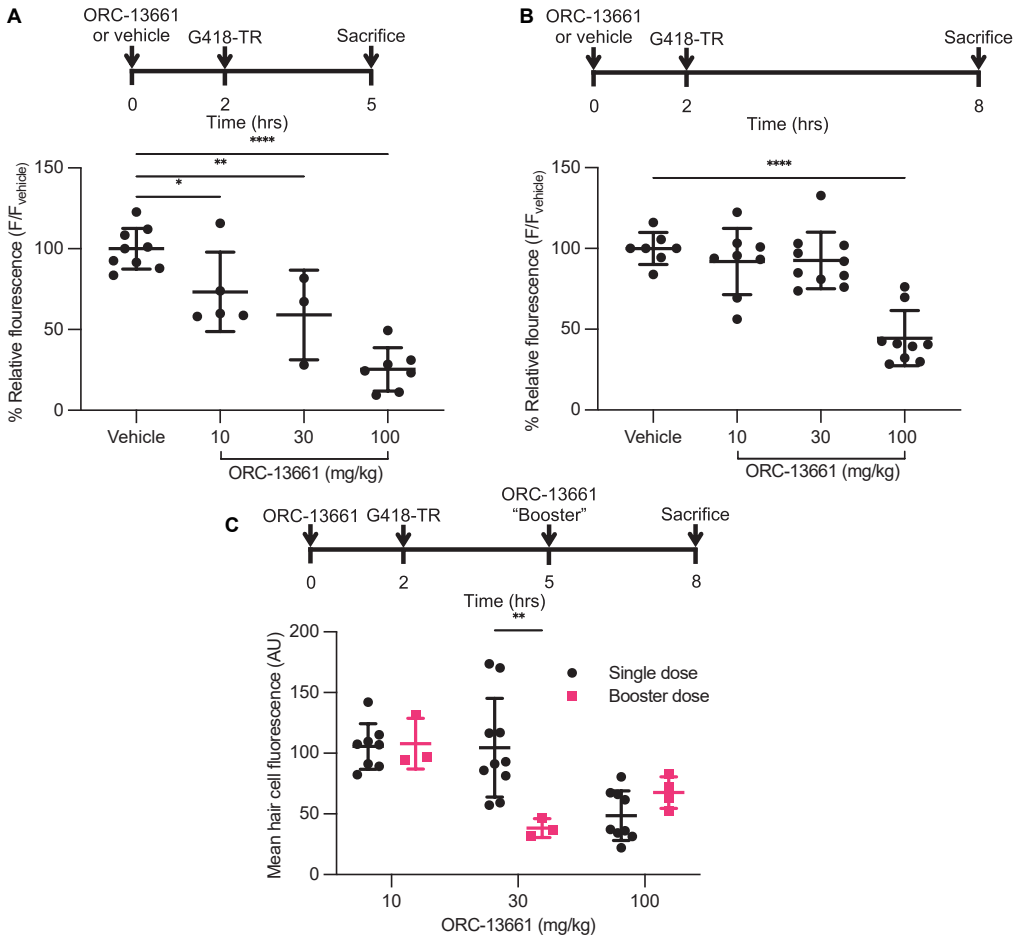

FIGURE 7 | ORC-13661 blocks G418-TR accumulation in mammalian hair cells. **(A)** Short (3 h) G418-TR exposure paradigm. Neonatal mice were pretreated with ORC-13661 or vehicle for 2 h, injected with 10 mg/kg G418-TR, and sacrificed 3 h after aminoglycoside injection. Basal turn OHC mean fluorescence for animals treated with either vehicle or ORC-13661 followed by 10 mg/kg G418-TR. OHC mean fluorescence was quantified and normalized to animals pre-treated with vehicle within each experimental replicate. [One-way ANOVA; $F_{(3,20)} = 23.55$, $P < 0.0001$]. **(B)** Long (6 h) G418-TR exposure paradigm. Neonatal mice were pretreated with ORC-13661 or vehicle for 2 h, injected with 10 mg/kg G418-TR, and sacrificed 6 h after aminoglycoside injection. [One-way ANOVA; $F_{(3,30)} = 19.62$, $P < 0.0001$]. **(C)** Booster dosing strategy with a single pretreatment injection of ORC-13661 followed by a second booster dose 3 h after G418-TR injection. Basal turn OHC mean fluorescence for animals treated with a pretreatment dose ORC-13661 (10–100 mg/kg) followed by 10 mg/kg G418-TR with an additional booster of ORC-13661 (same as pretreatment dose) 3 h after aminoglycoside administration. Note that data for single dose are non-normalized data from part **B**. Error bars are standard deviations. $^{*}P < 0.05$, $^{**}P < 0.01$, $^{***}P < 0.001$, $^{****}P < 0.0001$; *P*-values generated from multiple comparisons *post hoc* test (**A,B**: Dunnett's multiple comparison test; **C:** Šídák's multiple comparison test).

component analysis demonstrates a significant impact from dose [$F_{(3,50)} = 39.75$, $P < 0.0001$] and treatment scheme [$F_{(1,50)} = 13.45$, $P = 0.0006$]. These findings suggest that inhibition of aminoglycoside uptake by ORC-13661 in neonatal mice is both dose- and time-dependent.

We hypothesized that the difference between the short and long exposure paradigms was due to different pharmacokinetics for G418-TR and ORC-13661. At 6 h, we observed high levels or circulating G418-TR (**Figure 4B**). If the elimination kinetics of ORC-13661 in the neonatal mouse are rapid, this might explain the difference between the short and long G418-TR exposure paradigms. To test this hypothesis, we developed a "booster" treatment scheme. Neonatal mice were treated with a single pretreatment of ORC-13661 (10, 30, or 100 mg/kg), then injected with 10 mg/kg G418-TR, and given a booster dose of ORC-13661 (same dose as pretreatment) 3 h after G418-TR (**Figure 7C**). When compared to animals that received a single pretreatment dose of ORC-13661, animals that received 30 mg/kg ORC-13661 pretreatment and a 30 mg/kg ORC-13661 booster showed significantly more uptake inhibition. The 10 mg/kg and 100 mg/kg ORC-1366 booster schemes showed no significant difference when compared to single doses, suggesting that the 10 mg/kg dose is not enough to generate uptake inhibition while the 100 mg/kg dose may be reaching a plateau and an additional booster does not increase uptake inhibition. These findings support our hypothesis and further demonstrating the translational utility of this *in vivo* system.

DISCUSSION

Numerous drugs and therapeutic compounds are known to be toxic to the inner ear and adversely affect hearing and balance, however our understanding of the mechanisms driving ototoxicity remains incomplete. Challenges in studying ototoxicity have led to a paucity of protective therapeutics. The zebrafish lateral line and rodent explants have proven useful in screening and mechanistic studies, but translating these discoveries to adult mammals *in vivo* remains a difficult and costly endeavor. We present the development of low-cost and rapid *in vivo* mammalian model for studying ototoxic compounds and candidate protective therapeutics.

Biomarker

In mammals, diagnosis of ototoxicity is usually limited to functional evaluations such as behavioral paradigms, ABR thresholds, and otoacoustic emissions analysis or post-mortem histologic evaluation. These methods are expensive and time consuming, and they generally only detect ototoxic effects after irreversible damage has occurred. Some *in vivo* mammalian ototoxicity protocols also require cotreatment with loop diuretics, a class of therapeutics that are both independently ototoxic and show synergistic toxicity with other compounds (Rybak, 1993; Ding et al., 2016). While these protocols allow for rapid induction of *in vivo* ototoxicity, the introduction of a second therapeutic agent with independent effects on numerous organ systems confounds analysis and clinical relevance. Indeed, concomitant use of loop diuretics with aminoglycosides or cisplatin in humans is generally cautioned against in all but the most exceptional of circumstances (UpToDate, 2021; Huxel et al., 2021). We hypothesized that by injecting neonatal mice with G418-TR, we could develop a rapid and sensitive technique for evaluating *in vivo* aminoglycoside toxicity. In this study, we demonstrate that systemic injection of G418-TR into neonatal mice results in quantifiable, dose-dependent hair cell uptake of the aminoglycoside. Further evaluation of tonotopic and cell specific uptake patterns demonstrates that basal regions of the cochlea take up more aminoglycoside compared to apical regions, and OHCs take up significantly more aminoglycoside than immediately adjacent IHCs. These findings are consistent with the hypothesis that differential aminoglycoside toxicity within the inner ear is due to differential exposure of the hair cells. Whether this increased exposure is due to characteristics of aminoglycoside trafficking within the cochlea or local hair cell specific properties such as MET channel permeability remains unknown.

Because mice are born with immature cochlear hair cells and functional hearing only develops around P12, we compared neonatal hair cell uptake with that of mature hair cells from juvenile animals P25-30. Slightly higher doses of G418-TR were required in juvenile animals to achieve a similar dose-dependent increase in hair cell aminoglycoside accumulation, however the apicobasal gradient and OHC predilection were again observed. The lower doses required in neonates is consistent with the previously described "sensitive period" during rodent development when neonates are more sensitive to aminoglycosides than older animals (Chen and Saunders, 1983; Nakai et al., 1983; Prieve and Yanz, 1984).

Additionally, it is worth noting that in both neonates and juveniles we observed no animal mortality and no significant hair cell death. This is due to the fact that our studies utilized sublethal dosing of G418-TR (maximum of 10 mg/kg in neonates and 20 mg/kg in juveniles) far lower than previously described aminoglycoside ototoxicity protocols that require multiple sequential doses of 0.5–1 g/kg (Wu et al., 2001; Chowdhury et al., 2018; Horvath et al., 2019).

With similar hair cell uptake patterns observed in neonates and juveniles, albeit requiring slightly different dosing, we elected to pursue the remainder of our experiments in neonates. By using neonates we estimate we saved 80–90% on animal fees (housing only breeding animals), used 1/10th as much reagent (treating 2 g neonates vs. 20 g adults), and decreased our tissue processing time by about 50% (no decalcification required). The significant time and cost savings, coupled with faithful recapitulation of results observed in older animals, makes the neonate an attractive system for rapid and higher throughput translation of preclinical discoveries into mammalian systems designed to evaluate hearing loss and protection.

Characterization of *in vivo* Mammalian Hair Cell Uptake and Retention of G418-TR

In mammalian cochlear explant models there is clear evidence that aminoglycosides act as permeant blockers of MET channels, rapidly gaining entry into hair cells and accumulating without means of egress (Marcotti et al., 2005; Alharazneh et al., 2011; Vu et al., 2013). Aminoglycoside uptake and retention has also been documented *in vivo* (Hiel et al., 1993; Imamura and Adams, 2003; Dai et al., 2006). We sought to quantify the *in vivo* mammalian kinetics of aminoglycoside uptake in hair cells. Neonatal hair cells demonstrate rapid uptake of G418-TR from 0 to 6 h post-injection. Interestingly, we noted differences between IHC and OHC uptake and retention. Between 0 and 3 h, IHCs and OHCs demonstrate nearly identical levels of uptake. From 3 to 6 h post-injection, OHCs demonstrate a greater rate of uptake compared to IHCs which results in a significant difference in peak fluorescence between the two populations at 6 h. After reaching peak hair cell fluorescence levels at 6 h post-injections, OHCs demonstrate no significant loss by 72 h while IHCs show a moderate reduction in fluorescence. When correlated with measured serum fluorescence, we noted that hair cell uptake corresponds to the peak in serum G418-TR levels; when circulating G418-TR is maximal, the hair cells readily accumulate aminoglycoside. Once serum levels of aminoglycoside begin to drop, OHCs retain aminoglycoside while IHCs demonstrate a slow loss of signal. The mechanism of aminoglycoside egress from IHCs is undetermined as these charged molecules are unlikely to cross membranes by passive diffusion.

Our studies are consistent with previous studies using autoradiography and immunolabeling that have established that hair cells rapidly take up aminoglycosides and retain them for extended durations (Portmann et al., 1974; de Groot et al.,

1990; Imamura and Adams, 2003; Dai et al., 2006). Previous studies have noted that aminoglycoside uptake similarly shows a basal OHC predilection using qualitative and semi-quantitative methods of analysis (Hiel et al., 1993; Imamura and Adams, 2003; Dai et al., 2006). An almost universal finding is that outer hair cells are more susceptible to aminoglycoside ototoxicity than IHCs. This difference in ototoxicity remains poorly understood. It is sometimes attributed to the higher metabolic rate of outer hair cells (given their contribution to the active process of the cochlear amplifier), but there is also conflicting evidence for differential aminoglycoside uptake and accumulation in IHCs and OHCs (Lim, 1986; Hiel et al., 1993; Forge and Schacht, 2000; Imamura and Adams, 2003; Taylor et al., 2008; Wang and Steyger, 2009). Our findings support the hypothesis that differential aminoglycoside susceptibility between IHCs and OHCs is in part due to differential exposure. Explant studies have demonstrated differential rates of labeled aminoglycoside uptake in OHCs and IHCs (Alharazneh et al., 2011), but *in vivo* uptake of GTTR previously implied comparable IHC and OHC fluorescence at 3 h post-injection (Wang and Steyger, 2009; Makabe et al., 2020). In agreement with these previous studies, our results demonstrate similar IHC and OHC uptake from 0 to 3 h, but we find that a significant difference between OHCs and IHCs develops at 6 h and persists out to 72 h. We suspect that this difference is due in part to the difference in resting potentials between the hair cell populations, with a more negative OHC resting potential resulting in more favorable electrostatic uptake of positive aminoglycosides (Pickles, 1998). We also demonstrate that IHCs, unlike OHCs, show some level of aminoglycoside egress which could also be contributing to this differential susceptibility. It is worth noting that previous work has also suggested different isoforms of the MET channel could also contribute to differences between OHCs and IHCs (Beurg et al., 2006; Fettiplace, 2009), and certainly these differences could also impact aminoglycoside uptake. Quantification of aminoglycoside levels after an initial peak at 6 h also allowed for evaluation of aminoglycoside retention in hair cells. This process is an ideal application of the neonate system, because hair cell addition and turnover in aquatic vertebrates complicates prolonged analysis and in adult mammals the cost of a cross sectional study with adequate numbers is prohibitive to most research programs. We also observe not only differential accumulation, but also clearance of aminoglycoside. Despite the fact that mechanosensory hair cells and renal proximal tubule cells are known to retain aminoglycoside (Imamura and Adams, 2003; Dai et al., 2006), aminoglycoside clearance at the cellular level has not been well studied. The biologic relevance of this observation is unclear, but certainly warrants additional investigation.

Histologic evaluation of the kidneys from G418-TR treated mice corroborates previous studies which demonstrated rapid and sustained aminoglycoside uptake by the PCT cells (Dunn et al., 2002; Dai et al., 2006). While quantification of fluorescence from the PCT reveals a similar pattern of uptake and retention compared to that observed in cochlear hair cells, qualitatively there are also similarities in the cellular distribution of G418-TR. Both PCTs and hair cells show a pattern of diffuse uptake at early time points, followed by what appears to sequestration in apical puncta. Despite these similarities, hair cells and PCTs are thought to uptake aminoglycosides *via* distinct pathways. Hair cells accumulate aminoglycosides primarily through MET channel transport, with a relatively minor contribution from endocytosis (Huth et al., 2011; Hailey et al., 2017; Makabe et al., 2020). In the nephron, mutation of the PCT endocytic receptor megalin blocks aminoglycoside uptake and protects against nephrotoxicity (Schmitz et al., 2002). Given the differences in uptake mechanisms, the similarities in aminoglycoside uptake and localization in hair cells and PCTs suggest there is convergence of similar mechanisms of intracellular aminoglycoside handling and sequestration. This hypothesis is supported by the observation that aminoglycosides accumulate in lysosomal compartments within both hair cells (Hashino et al., 1997; Hailey et al., 2017) and PCT cells (Silverblatt and Kuehn, 1979). The biologic significance of aminoglycoside sequestration in puncta within hair cells and PCT cells remains to be determined and follow up studies are needed.

Evaluation of non-sensory tissues from the cochlea, including the supporting cells, spiral ganglia neurons, and the stria vascularis further demonstrates the unique pattern of uptake observed in hair cells. Cross sectional analysis of cryostat sections demonstrated once again that hair cells take up G418-TR over 6 h and then retain the aminoglycoside load. Qualitatively, we again observe aminoglycoside entering the hair cells in a diffuse pattern before localizing to puncta toward the apex and cuticular plate at later time points. This is reminiscent of the aminoglycoside loading we observed in zebrafish hair cells, where fluorescently labeled neomycin distributes within hair cells in a diffuse pattern after entry, before becoming sequestered in lysosomes (Hailey et al., 2017). Further characterization of these puncta in mammalian hair cells is needed to better understand their role in aminoglycoside toxicity. Previous *in vivo* evaluations utilizing GTTR demonstrated the intracochlear trafficking pattern of aminoglycosides, including *trans*-strial uptake into the endolymph before entering hair cells (Wang and Steyger, 2009). Indeed a recent study demonstrated *via* real-time imaging using GTTR that aminoglycoside enters the cochlea *via* the stria vascularis (Kim and Ricci, 2022). Consistent with this analysis, we observe a transient increase in stria vascularis fluorescence before fluorescence returns to near baseline levels by 48 h post-injection. Aminoglycoside uptake in spiral ganglia neurons (SGNs) has previously been observed (Bareggi et al., 1986; Imamura and Adams, 2003; Kitahara et al., 2005), however in our study we did not observe significant fluorescence in the cell bodies of the SGNs. It should, however, be noted that the cumulative dose of aminoglycoside used in these prior *in vivo* studies was 75–2000 fold higher than the 10 mg/kg administered in this analysis.

An additional extension of this work is the correlation between hair cell aminoglycoside uptake and circulating, systemic levels of aminoglycoside. Clinically, numerous trials have examined the impact of dosing schemes on aminoglycoside toxicity (Barza et al., 1996; Hatala et al., 1996; Munckhof et al., 1996; Rybak et al., 1999; Contopoulos-Ioannidis et al., 2004). Unfortunately, none of these aminoglycoside administration regimens appear to reduce incidence of ototoxicity. In this analysis, we directly

correlate plasma levels of G418-TR with G418-TR fluorescence in hair cells and non-sensory tissues of the cochlea. After a single subcutaneous injection of G418-TR, hair cells rapidly accumulate the aminoglycoside at all time points that the G418-TR is detected at any significant level in the serum. While not examined closely in this analysis, the relationship between serum aminoglycoside and hair cell accumulation is likely to be of clinical relevance when considering dosing schemes such as bolus dosing, divided doses, and infusions.

ORC-13661 Blocks G418-TR Uptake *in vivo*

Therapeutic inhibition of aminoglycoside uptake is a promising strategy to combat ototoxicity. A recent analysis of gentamicin subtypes demonstrated that chemical modification of the traditional gentamicin mixtures to produce more potent MET channel-blocking analogues can diminishes ototoxicity without compromising antimicrobial activity (O'Sullivan et al., 2020). While aminoglycoside modification remains a promising strategy, multiple previous studies have utilized zebrafish-based screens to identify compounds that inhibit aminoglycoside uptake and protect hair cells (Owens et al., 2008; Kruger et al., 2016; Kirkwood et al., 2017; Chowdhury et al., 2018; Kitcher et al., 2019; Kenyon et al., 2021). Translating preliminary leads from zebrafish to a mammalian model remains challenging given the resources-intensive techniques required for *in vivo* mammalian assessment of ototoxicity. Here, we demonstrate that the drug ORC-13661 blocks aminoglycoside uptake *in vivo* in mammals, and we further highlight the utility of the neonatal mouse system to rapidly evaluate ORC-13661 dosing paradigms.

ORC-13661 is a small molecule therapeutic that protects against aminoglycoside ototoxicity in zebrafish and mammals (Chowdhury et al., 2018; Kitcher et al., 2019). Evidence from zebrafish lateral line hair cells and mammalian cochlear cultures suggests that hair cell protection occurs by blocking MET-dependent aminoglycoside uptake (Kitcher et al., 2019). Here, we extend this conclusion to the mammalian inner ear *in vivo*, demonstrating pharmacologic inhibition of aminoglycoside uptake. We examined two different dosing paradigms and observed a significant dose-dependent reduction in uptake with the short G418-TR exposure paradigm but not the long paradigm. We attribute the observed differences between the two tested schemes to the MET channel block kinetics of ORC-13661. From previous work, we know that ORC-13661 blocks MET-channel currents and MET-dependent aminoglycoside uptake, but this block is readily reversible with washout (Kitcher et al., 2019). Unlike previous *in vitro* experiments, ORC-13661 is subjected to dynamic *in vivo* pharmacokinetics in these studies. If the $t_{1/2}$ for ORC-13661 within the plasma or the endolymph of the neonatal mouse is short, the expected therapeutic window following a single injection would also be of limited duration. To test this hypothesis, we developed an ORC-13661 booster treatment scheme. We found that an additional dose of ORC-13661 rescued G418-TR uptake inhibition for animals treated with 30 mg/kg ORC-13661. Our findings suggest that ORC-13661 blocks the uptake of aminoglycosides through reversible inhibition of MET-dependent uptake, and that multiple doses of ORC-13661 may be needed to provide optimal protection from aminoglycosides.

It is worthwhile noting that the doses of ORC-13661 administered in this study (10–100 mg/kg) were larger than those used previously to protect rats (1–5 mg/kg) from aminoglycoside-induced hearing loss (Chowdhury et al., 2018; Kitcher et al., 2019). While this could be due differences between neonatal mice and adult rats, it also raises the question of how much aminoglycoside uptake inhibition is relevant from a hair cell death perspective and a measurable auditory threshold perspective. The association between aminoglycoside uptake and hair cell death is also poorly understood in mammals, in part because the molecular mechanisms of aminoglycoside-induced hair cell death are not completely understood (Forge and Schacht, 2000; Cheng et al., 2005; Rizzi and Hirose, 2007; Jiang et al., 2017). The developing blood-labyrinth barrier (BLB) is also an important consideration when comparing neonatal animals to mature adults. In particular, the role of the BLB in facilitating aminoglycoside ototoxicity, and its impact on the delivery of otoprotective therapeutics to mechanosensory hair cells are poorly understood but areas of active investigation. The characteristics of uptake inhibition, and specifically whether level of absolute inhibition, manipulation of rate of uptake, and/or altering the subcellular uptake and localization of aminoglycoside are driving protection are also unknown. Further work to begin correlating aminoglycoside uptake and accumulation with hair cell death and hearing threshold shifts, and conversely aminoglycoside uptake inhibition with hair cell survival and hearing protection is needed to better characterize the therapeutic window for uptake inhibition.

Translational Significance

The ability to rapidly evaluate the effects of ototoxins *in vivo* within the mammalian cochlea will not only enable further characterizations of ototoxins and also novel protective therapeutics. Here, we demonstrate that neonatal mice can treated with the aminoglycoside G418-TR and the kinetics of aminoglycoside uptake can be monitored within the cochlea. We find that cochlear hair cells, especially OHCs, uniquely retain G418-TR for days after a single injection without significant efflux or clearance. Further work is needed to better characterize hair cell retention of aminoglycoside in mammals and correlate aminoglycoside uptake and retention with clinical manifestations of ototoxicity. We further demonstrate that mammalian hair cell uptake of G418-TR can be modulated utilizing ORC-13661, a novel otoprotective therapeutic. These findings support the hypothesis that ORC-13661 protects against aminoglycoside ototoxicity by inhibiting MET-dependent uptake without causing any adverse effect on hearing (Kitcher et al., 2019). Finally, we demonstrate the translational utility of this system by testing a novel ORC-13661 dosing scheme which appears to provide significant and sustained aminoglycoside uptake inhibition. Important limitations of this model include the use of neonatal mice as opposed to adult animals with functional hearing and the paucity of data correlating *in vivo* mammalian aminoglycoside uptake with hearing loss, and conversely aminoglycoside uptake

inhibition with hearing protection. In addition, there are likely significant differences in the distribution and metabolism of both aminoglycosides and protective compounds such as ORC-13661 across mammalian species including humans. Caution should be used in directly translating dose and timing of treatments to clinical settings. Utilizing the neonatal mouse, we will continue further characterization of additional ototoxic compounds and optimization of protective therapeutic strategies, with the goal of ultimately translating these findings to human clinical trials.

DATA AVAILABILITY STATEMENT

The raw data supporting the conclusions of this article will be made available by the authors, without undue reservation.

ETHICS STATEMENT

The animal study was reviewed and approved by the University of Washington Institutional Animal Care and Use Committee.

AUTHOR CONTRIBUTIONS

JB, JAS, EWR, and DWR designed the studies. JB, VR, and LT performed the all experiments. AW and JAS provided the reagents. JB and PW acquired the data. JB and DWR analyzed the data and wrote the manuscript. All authors contributed to the article and approved the submitted version.

FUNDING

This work was supported by AAOHNS ASPO CORE grant (JB), University of Washington Cystic Fibrosis Foundation Research Development Program fellowship SINGH19R0 (JB), NIH/NIDCD T32 DC000018 (JB), and NIH/NIDCD R01 DC005987 (DWR).

ACKNOWLEDGMENTS

We are deeply grateful to our laboratory for insightful discussion on the manuscript and T. Linbo for his excellent technical support.

SUPPLEMENTARY MATERIAL

The Supplementary Material for this article can be found online at: https://www.frontiersin.org/articles/10.3389/fnmol.2022.944846/full#supplementary-material

REFERENCES

Abe, T., Kakehata, S., Kitani, R., Maruya, S., Navaratnam, D., Santos-Sacchi, J., et al. (2007). Developmental expression of the outer hair cell motor prestin in the mouse. *J. Membr. Biol.* 215, 49–56. doi: 10.1007/s00232-007-9004-5

Alharazneh, A., Luk, L., Huth, M., Monfared, A., Steyger, P. S., Cheng, A. G., et al. (2011). Functional hair cell mechanotransducer channels are required for aminoglycoside ototoxicity. *PLoS One* 6:e22347. doi: 10.1371/journal.pone.0022347

Aminoglycosides (2012). *LiverTox: Clinical and Research Information on Drug-Induced Liver Injury*. Bethesda, MD: National Institute of Diabetes and Digestive and Kidney Diseases.

Bailey, T. C., Little, J. R., Littenberg, B., Reichley, R. M., and Dunagan, W. C. (1997). A meta-analysis of extended-interval dosing versus multiple daily dosing of aminoglycosides. *Clin. Infect. Dis.* 24, 786–795. doi: 10.1093/clinids/24.5.786

Bareggi, R., Narducci, P., Grill, V., Mallardi, F., Zweyer, M., and Fusaroli, P. (1986). Localization of an aminoglycoside (streptomycin) in the inner ear after its systemic administration. *Histochemistry* 84, 237–240. doi: 10.1007/BF00495788

Barza, M., Ioannidis, J. P., Cappelleri, J. C., and Lau, J. (1996). Single or multiple daily doses of aminoglycosides: a meta- analysis. *BMJ* 312, 338–344. doi: 10.1136/bmj.312.7027.338

Beurg, M., Evans, M. G., Hackney, C. M., and Fettiplace, R. (2006). A large-conductance calcium-selective mechanotransducer channel in mammalian cochlear hair cells. *J. Neurosci.* 26, 10992–11000. doi: 10.1523/JNEUROSCI.2188-06.2006

Chen, C.-S., and Saunders, J. C. (1983). The sensitive period for ototoxicity of kanamycin in mice: morphological evidence. *Arch. Otorhinolaryngol.* 238, 217–223. doi: 10.1007/BF00453932

Cheng, A. G., Cunningham, L. L., and Rubel, E. W. (2003). Hair cell death in the avian basilar papilla: characterization of the in vitro model and caspase activation. *J. Assoc. Res. Otolaryngol.* 4, 91–105. doi: 10.1007/s10162-002-3016-8

Cheng, A. G., Cunningham, L. L., and Rubel, E. W. (2005). Mechanisms of hair cell death and protection. *Curr. Opin. Otolaryngol. Head Neck Surg.* 13, 343–348. doi: 10.1097/01.moo.0000186799.45377.63

Chowdhury, S., Owens, K. N., Herr, R. J., Jiang, Q., Chen, X., Johnson, G., et al. (2018). Phenotypic optimization of urea-thiophene carboxamides to yield potent, well tolerated and orally active protective agents against aminoglycoside-induced hearing loss. *J. Med. Chem.* 61, 84–97. doi: 10.1021/acs.jmedchem.7b00932

Coffin, A. B., Williamson, K. L., Mamiya, A., Raible, D. W., and Rubel, E. W. (2013). Profiling drug-induced cell death pathways in the zebrafish lateral line. *Apoptosis* 18, 393–408. doi: 10.1007/s10495-013-0816-8

Contopoulos-Ioannidis, D. G., Giotis, N. D., Baliatsa, D. V., and Ioannidis, J. P. A. (2004). Extended-interval aminoglycoside administration for children: a meta-analysis. *Pediatrics* 114, e111–e118. doi: 10.1542/peds.114.1.e111

Dai, C. F., Mangiardi, D., Cotanche, D. A., and Steyger, P. S. (2006). Uptake of fluorescent gentamicin by vertebrate sensory cells in vivo. *Hear. Res.* 213, 64–78. doi: 10.1016/j.heares.2005.11.011

de Groot, J. C. M. J., Meeuwsen, F., Ruizendaal, W. E., and Veldman, J. E. (1990). Ultrastructural localization of gentamicin in the cochlea. *Hear. Res.* 50, 35–42. doi: 10.1016/0378-5955(90)90031-J

Ding, D., Liu, H., Qi, W., Jiang, H., Li, Y., Wu, X., et al. (2016). Ototoxic effects and mechanisms of loop diuretics. *J. Otol.* 11, 145–156. doi: 10.1016/j.joto.2016.10.001

Dunn, K. W., Sandoval, R. M., Kelly, K. J., Dagher, P. C., Tanner, G. A., Atkinson, S. J., et al. (2002). Functional studies of the kidney of living animals using multicolor two-photon microscopy. *Am. J. Physiol. Cell Physiol.* 283, C905–C916. doi: 10.1152/ajpcell.00159.2002

Durante-Mangoni, E., Grammatikos, A., Utili, R., and Falagas, M. E. (2009). Do we still need the aminoglycosides? *Int. J. Antimicrob. Agents* 33, 201–205. doi: 10.1016/j.ijantimicag.2008.09.001

Esterberg, R., Hailey, D. W., Rubel, E. W., and Raible, D. W. (2014). ER–mitochondrial calcium flow underlies vulnerability of mechanosensory hair cells to damage. *J. Neurosci.* 34, 9703–9719. doi: 10.1523/JNEUROSCI.0281-14.2014

Esterberg, R., Linbo, T., Pickett, S. B., Wu, P., Ou, H. C., Rubel, E. W., et al. (2016). Mitochondrial calcium uptake underlies ROS generation during aminoglycoside-induced hair cell death. *J. Clin. Invest.* 126, 3556–3566. doi: 10.1172/JCI84939

FDA-NIH Biomarker Working Group (2016). *BEST (Biomarkers, Endpoints, and other Tools) Resource*. Silver Spring, MD: Food and Drug Administration.

Fettiplace, R. (2009). Defining features of the hair cell mechanoelectrical transducer channel. *Pflugers Arch.* 458, 1115–1123. doi: 10.1007/s00424-009-0683-x

Forge, A., and Schacht, J. (2000). Aminoglycoside antibiotics. *Audiol. Neurootol.* 5, 3–22. doi: 10.1159/000013861

UpToDate (2021). *Furosemide: Drug Information*. Available online at: https://www.uptodate.com/contents/furosemide-drug-information [accessed November 22, 2021].

Guo, X., and Nzerue, C. (2002). How to prevent, recognize, and treat drug-induced nephrotoxicity. *Cleve. Clin. J. Med.* 69, 289–290, 293–294, 296–297 passim. doi: 10.3949/ccjm.69.4.289

Hailey, D. W., Esterberg, R., Linbo, T. H., Rubel, E. W., and Raible, D. W. (2017). Fluorescent aminoglycosides reveal intracellular trafficking routes in mechanosensory hair cells. *J. Clin. Invest.* 127, 472–486. doi: 10.1172/JCI85052

Hashino, E., Shero, M., and Salvi, R. J. (1997). Lysosomal targeting and accumulation of aminoglycoside antibiotics in sensory hair cells. *Brain Res.* 777, 75–85. doi: 10.1016/S0006-8993(97)00977-3

Hatala, R., Dinh, T., and Cook, D. J. (1996). Once-daily aminoglycoside dosing in immunocompetent adults. *Ann. Intern. Med.* 124, 717–725. doi: 10.7326/0003-4819-124-8-199604150-00003

He, D. Z., Evans, B. N., and Dallos, P. (1994). First appearance and development of electromotility in neonatal gerbil outer hair cells. *Hear. Res.* 78, 77–90. doi: 10.1016/0378-5955(94)90046-9

Hiel, H., Erre, J.-P., Aurousseau, C., Bouali, R., Dulon, D., and Aran, J.-M. (1993). Gentamicin uptake by cochlear hair cells precedes hearing impairment during chronic treatment. *Audiology* 32, 78–87. doi: 10.3109/00206099309072930

Hirose, K., Hockenbery, D. M., and Rubel, E. W. (1997). Reactive oxygen species in chick hair cells after gentamicin exposure in vitro. *Hear. Res.* 104, 1–14. doi: 10.1016/S0378-5955(96)00169-4

Horvath, L., Bächinger, D., Honegger, T., Bodmer, D., and Monge Naldi, A. (2019). Functional and morphological analysis of different aminoglycoside treatment regimens inducing hearing loss in mice. *Exp. Ther. Med.* 18, 1123–1130. doi: 10.3892/etm.2019.7687

Huth, M. E., Ricci, A. J., and Cheng, A. G. (2011). Mechanisms of aminoglycoside ototoxicity and targets of hair cell protection. *Int. J. Otolaryngol.* 2011:e937861. doi: 10.1155/2011/937861

Huxel, C., Raja, A., and Ollivierre-Lawrence, M. D. (eds). (2021). "Loop diuretics," in *StatPearls* (Treasure Island, FL: StatPearls Publishing).

Huy, P. T. B., Bernard, P., and Schacht, J. (1986). Kinetics of gentamicin uptake and release in the rat. Comparison of inner ear tissues and fluids with other organs. *J. Clin. Invest.* 77, 1492–1500. doi: 10.1172/JCI112463

Imamura, S., and Adams, J. C. (2003). Distribution of gentamicin in the guinea pig inner ear after local or systemic application. *J. Assoc. Res. Otolaryngol.* 4, 176–195. doi: 10.1007/s10162-002-2036-8

Jeng, J., Ceriani, F., Hendry, A., Johnson, S. L., Yen, P., Simmons, D. D., et al. (2020). Hair cell maturation is differentially regulated along the tonotopic axis of the mammalian cochlea. *J. Physiol.* 598, 151–170. doi: 10.1113/JP279012

Jiang, H., Sha, S.-H., Forge, A., and Schacht, J. (2006). Caspase-independent pathways of hair cell death induced by kanamycin in vivo. *Cell Death Differ.* 13, 20–30. doi: 10.1038/sj.cdd.4401706

Jiang, M., Karasawa, T., and Steyger, P. S. (2017). Aminoglycoside-induced cochleotoxicity: a review. *Front. Cell. Neurosci.* 11:308. doi: 10.3389/fncel.2017.00308

Kalinec, G. M., Webster, P., Lim, D. J., and Kalinec, F. (2003). A cochlear cell line as an in vitro system for drug ototoxicity screening. *Audiol. Neurootol.* 8, 177–189. doi: 10.1159/000071059

Kenyon, E. J., Kirkwood, N. K., Kitcher, S. R., Goodyear, R. J., Derudas, M., Cantillon, D. M., et al. (2021). Identification of a series of hair-cell MET channel blockers that protect against aminoglycoside-induced ototoxicity. *JCI Insight* 6:e145704. doi: 10.1172/jci.insight.145704

Kim, J., and Ricci, A. J. (2022). In vivo real-time imaging reveals megalin as the aminoglycoside gentamicin transporter into cochlea whose inhibition is otoprotective. *Proc. Natl. Acad. Sci. U.S.A.* 119:e2117946119. doi: 10.1073/pnas.2117946119

Kirkwood, N. K., O'Reilly, M., Derudas, M., Kenyon, E. J., Huckvale, R., van Netten, S. M., et al. (2017). d-Tubocurarine and berbamine: alkaloids that are permeant blockers of the hair cell's mechano-electrical transducer channel and protect from aminoglycoside toxicity. *Front. Cell. Neurosci.* 11:262. doi: 10.3389/fncel.2017.00262

Kitahara, T., Li, H.-S., and Balaban, C. D. (2005). Changes in transient receptor potential cation channel superfamily V (TRPV) mRNA expression in the mouse inner ear ganglia after kanamycin challenge. *Hear. Res.* 201, 132–144. doi: 10.1016/j.heares.2004.09.007

Kitcher, S. R., Kirkwood, N. K., Camci, E. D., Wu, P., Gibson, R. M., Redila, V. A., et al. (2019). ORC-13661 protects sensory hair cells from aminoglycoside and cisplatin ototoxicity. *JCI Insight* 4:e126764. doi: 10.1172/jci.insight.126764

Kros, C. J., Ruppersberg, J. P., and Rüsch, A. (1998). Expression of a potassium current in inner hair cells during development of hearing in mice. *Nature* 394, 281–284. doi: 10.1038/28401

Kruger, M., Boney, R., Ordoobadi, A. J., Sommers, T. F., Trapani, J. G., and Coffin, A. B. (2016). Natural bizbenzoquinoline derivatives protect zebrafish lateral line sensory hair cells from aminoglycoside toxicity. *Front. Cell. Neurosci.* 10:83. doi: 10.3389/fncel.2016.00083

Lee, S. H., Ju, H. M., Choi, J. S., Ahn, Y., Lee, S., and Seo, Y. J. (2018). Circulating serum miRNA-205 as a diagnostic biomarker for ototoxicity in mice treated with aminoglycoside antibiotics. *Int. J. Mol. Sci.* 19:2836. doi: 10.3390/ijms19092836

Lim, D. J. (1986). Effects of noise and ototoxic drugs at the cellular level in the cochlea: a review. *Am. J. Otolaryngol.* 7, 73–99. doi: 10.1016/S0196-0709(86)80037-0

Liu, J., Kachelmeier, A., Dai, C., Li, H., and Steyger, P. S. (2015). Uptake of fluorescent gentamicin by peripheral vestibular cells after systemic administration. *PLoS One* 10:e0120612. doi: 10.1371/journal.pone.0120612

Lopez-Novoa, J. M., Quiros, Y., Vicente, L., Morales, A. I., and Lopez-Hernandez, F. J. (2011). New insights into the mechanism of aminoglycoside nephrotoxicity: an integrative point of view. *Kidney Int.* 79, 33–45. doi: 10.1038/ki.2010.337

Makabe, A., Kawashima, Y., Sakamaki, Y., Maruyama, A., Fujikawa, T., Ito, T., et al. (2020). Systemic fluorescent gentamicin enters neonatal mouse hair cells predominantly through sensory mechanoelectrical transduction channels. *J. Assoc. Res. Otolaryngol.* 21, 137–149. doi: 10.1007/s10162-020-00746-3

Marche, P., Koutouzov, S., and Girard, A. (1983). Impairment of membrane phosphoinositide metabolism by aminoglycoside antibiotics: streptomycin, amikacin, kanamycin, dibekacin, gentamicin and neomycin. *J. Pharmacol. Exp. Ther.* 227, 415–420.

Marcotti, W., Johnson, S. L., Holley, M. C., and Kros, C. J. (2003). Developmental changes in the expression of potassium currents of embryonic, neonatal and mature mouse inner hair cells. *J. Physiol.* 548, 383–400. doi: 10.1113/jphysiol.2002.034801

Marcotti, W., and Kros, C. J. (1999). Developmental expression of the potassium current IK,n contributes to maturation of mouse outer hair cells. *J. Physiol.* 520, 653–660. doi: 10.1111/j.1469-7793.1999.00653.x

Marcotti, W., Netten, S. M. V., and Kros, C. J. (2005). The aminoglycoside antibiotic dihydrostreptomycin rapidly enters mouse outer hair cells through the mechano -electrical transducer channels. *J. Physiol.* 567, 505–521. doi: 10.1113/jphysiol.2005.085951

Mingeot-Leclercq, M.-P., and Tulkens, P. M. (1999). Aminoglycosides: nephrotoxicity. *Antimicrob. Agents Chemother.* 43, 1003–1012.

Munckhof, W. J., Grayson, M. L., and Turnidge, J. D. (1996). A meta-analysis of studies on the safety and efficacy of aminoglycosides given either once daily or as divided doses. *J. Antimicrob. Chemother.* 37, 645–663. doi: 10.1093/jac/37.4.645

Nakai, Y., Chang, K. C., Ohashi, K., and Morisaki, N. (1983). Ototoxic effect of an aminoglycoside drug on an immature inner ear. *Acta Otolaryngol. Suppl.* 393, 1–5. doi: 10.3109/00016488309129570

Naples, J., Cox, R., Bonaiuto, G., and Parham, K. (2018). Prestin as an otologic biomarker of cisplatin ototoxicity in a guinea pig model. *Otolaryngol. Head Neck Surg.* 158, 541–546. doi: 10.1177/0194599817742093

O'Sullivan, M. E., Song, Y., Greenhouse, R., Lin, R., Perez, A., Atkinson, P. J., et al. (2020). Dissociating antibacterial from ototoxic effects of gentamicin C-subtypes. *Proc. Natl. Acad. Sci. U.S.A.* 117, 32423–32432. doi: 10.1073/pnas.2013065117

Owens, K. N., Santos, F., Roberts, B., Linbo, T., Coffin, A. B., Knisely, A. J., et al. (2008). Identification of genetic and chemical modulators of zebrafish

mechanosensory hair cell death. *PLoS Genet.* 4:e1000020. doi: 10.1371/journal.pgen.1000020

Pickett, S. B., and Raible, D. W. (2019). Water waves to sound waves: using zebrafish to explore hair cell biology. *J. Assoc. Res. Otolaryngol.* 20, 1–19. doi: 10.1007/s10162-018-00711-1

Pickles, J. (1998). *An Introduction to the Physiology of Hearing*, 4th Edn. Leiden: Brill.

Portmann, M., Darrouzet, J., and Coste, C. (1974). Distribution within the cochlea of dihydrostreptomycin injected into the circulation. An autoradiographic and electron microscopic study. *Arch. Otolaryngol.* 100, 473–475. doi: 10.1001/archotol.1974.00780040487014

Prieve, B. A., and Yanz, J. L. (1984). Age-dependent changes in susceptibility to ototoxic hearing loss. *Acta Otolaryngol.* 98, 428–438. doi: 10.3109/00016488409107584

Priuska, E. M., and Schacht, J. (1995). Formation of free radicals by gentamicin and iron and evidence for an iron/gentamicin complex. *Biochem. Pharmacol.* 50, 1749–1752. doi: 10.1016/0006-2952(95)02160-4

Qian, X., He, Z., Wang, Y., Chen, B., Hetrick, A., Dai, C., et al. (2021). Hair cell uptake of gentamicin in the developing mouse utricle. *J. Cell. Physiol.* 236, 5235–5252. doi: 10.1002/jcp.30228

Qian, Y., and Guan, M.-X. (2009). Interaction of aminoglycosides with human mitochondrial 12S rRNA carrying the deafness-associated mutation. *Antimicrob. Agents Chemother.* 53, 4612–4618. doi: 10.1128/AAC.00965-08

Richardson, G. P., and Russell, I. J. (1991). Cochlear cultures as a model system for studying aminoglycoside induced ototoxicity. *Hear. Res.* 53, 293–311. doi: 10.1016/0378-5955(91)90062-e

Rizzi, M. D., and Hirose, K. (2007). Aminoglycoside ototoxicity. *Curr. Opin. Otolaryngol. Head Neck Surg.* 15, 352–357. doi: 10.1097/MOO.0b013e3282ef772d

Rubel, E. W. (1978). "Ontogeny of structure and function in the vertebrate auditory system," in *Development of Sensory Systems Handbook of Sensory Physiology*, eds C. M. Bate, V. M. C. M. Carr, P. P. C. Graziadei, H. V. B. Hirsch, A. Hughes, D. Ingle, et al. (Berlin: Springer), 135–237. doi: 10.1007/978-3-642-66880-7_5

Rubel, E. W., and Fay, R. R. (2012). *Development of the Auditory System*. Berlin: Springer Science & Business Media.

Rybak, L. P. (1993). Ototoxicity of Loop Diuretics#. *Otolaryngol. Clin. North Am.* 26, 829–844. doi: 10.1016/S0030-6665(20)30770-2

Rybak, L. P., Talaska, A. E., and Schacht, J. (2008). "Drug-induced hearing loss," in *Auditory Trauma, Protection, and Repair Springer Handbook of Auditory Research*, eds J. Schacht, A. N. Popper, and R. R. Fay (Boston, MA: Springer), 219–256. doi: 10.1007/978-0-387-72561-1_8

Rybak, M. J., Abate, B. J., Kang, S. L., Ruffing, M. J., Lerner, S. A., and Drusano, G. L. (1999). Prospective evaluation of the effect of an aminoglycoside dosing regimen on rates of observed nephrotoxicity and ototoxicity. *Antimicrob. Agents Chemother.* 43, 1549–1555. doi: 10.1128/AAC.43.7.1549

Schmitz, C., Hilpert, J., Jacobsen, C., Boensch, C., Christensen, E. I., Luft, F. C., et al. (2002). Megalin deficiency offers protection from renal aminoglycoside accumulation *. *J. Biol. Chem.* 277, 618–622. doi: 10.1074/jbc.M109959200

Seyhan, A. A. (2019). Lost in translation: the valley of death across preclinical and clinical divide – identification of problems and overcoming obstacles. *Transl. Med. Commun.* 4:18. doi: 10.1186/s41231-019-0050-7

Silverblatt, F. J., and Kuehn, C. (1979). Autoradiography of gentamicin uptake by the rat proximal tubule cell. *Kidney Int.* 15, 335–345. doi: 10.1038/ki.1979.45

Taylor, R. R., Nevill, G., and Forge, A. (2008). Rapid hair cell loss: a mouse model for cochlear lesions. *J. Assoc. Res. Otolaryngol.* 9, 44–64. doi: 10.1007/s10162-007-0105-8

Van Boeckel, T. P., Gandra, S., Ashok, A., Caudron, Q., Grenfell, B. T., Levin, S. A., et al. (2014). Global antibiotic consumption 2000 to 2010: an analysis of national pharmaceutical sales data. *Lancet Infect. Dis.* 14, 742–750. doi: 10.1016/S1473-3099(14)70780-7

Vu, A. A., Nadaraja, G. S., Huth, M. E., Luk, L., Kim, J., Chai, R., et al. (2013). Integrity and regeneration of mechanotransduction machinery regulate aminoglycoside entry and sensory cell death. *PLoS One* 8:e54794. doi: 10.1371/journal.pone.0054794

Wang, Q., and Steyger, P. S. (2009). Trafficking of systemic fluorescent gentamicin into the cochlea and hair cells. *J. Assoc. Res. Otolaryngol.* 10, 205–219. doi: 10.1007/s10162-009-0160-4

Wu, W.-J., Sha, S.-H., McLaren, J. D., Kawamoto, K., Raphael, Y., and Schacht, J. (2001). Aminoglycoside ototoxicity in adult CBA, C57BL and BALB mice and the Sprague–Dawley rat. *Hear. Res.* 158, 165–178. doi: 10.1016/S0378-5955(01)00303-3

Conflict of Interest: JAS, EWR, and DWR are cofounders of Oricula Therapeutics, which has licensed patents covering ORC-13661 from the University of Washington.

The remaining authors declare that the research was conducted in the absence of any commercial or financial relationships that could be construed as a potential conflict of interest.

Publisher's Note: All claims expressed in this article are solely those of the authors and do not necessarily represent those of their affiliated organizations, or those of the publisher, the editors and the reviewers. Any product that may be evaluated in this article, or claim that may be made by its manufacturer, is not guaranteed or endorsed by the publisher.

frontiers | Frontiers in Molecular Neuroscience

TYPE Original Research
PUBLISHED 27 July 2022
DOI 10.3389/fnmol.2022.934630

OPEN ACCESS

EDITED BY
Peter S. Steyger,
Creighton University, United States

REVIEWED BY
Hongzhe Li,
United States Department of Veterans Affairs, United States
Lavinia Sheets,
Washington University in St. Louis, United States

*CORRESPONDENCE
Samson Jamesdaniel
sjamesdaniel@wayne.edu

SPECIALTY SECTION
This article was submitted to Molecular Signaling and Pathways, a section of the journal Frontiers in Molecular Neuroscience

RECEIVED 02 May 2022
ACCEPTED 04 July 2022
PUBLISHED 27 July 2022

CITATION
Rosati R, Birbeck JA, Westrick J and Jamesdaniel S (2022) Lead exposure induces nitrative stress and disrupts ribbon synapses in the cochlea. *Front. Mol. Neurosci.* 15:934630. doi: 10.3389/fnmol.2022.934630

Lead exposure induces nitrative stress and disrupts ribbon synapses in the cochlea

Rita Rosati[1], Johnna A. Birbeck[2], Judy Westrick[2] and Samson Jamesdaniel[1,3]*

[1]Institute of Environmental Health Sciences, Wayne State University, Detroit, MI, United States, [2]Lumigen Instrument Center, Wayne State University, Detroit, MI, United States, [3]Department of Family Medicine and Public Health Sciences, Wayne State University, Detroit, MI, United States

Environmental exposure to heavy metal lead, a public health hazard in many post-industrial cities, causes hearing impairment upon long-term exposure. Lead-induced cochlear and vestibular dysfunction is well-documented in animal models. Although short-term exposure to lead at concentrations relevant to environmental settings does not cause significant shifts in hearing thresholds in adults, moderate- to low-level lead exposures induce neuronal damage and synaptic dysfunction. We reported that lead exposure induces oxidative stress in the mouse cochlea. However, lead-induced nitrative stress and potential damage to cochlear ribbon synapses are yet to be fully understood. Therefore, this study has evaluated cochlear synaptopathy and nitrative stress in young-adult mice exposed to 2 mM lead acetate for 28 days. Inductively coupled plasma mass spectrometry (ICP-MS) analysis indicated that this exposure significantly increased the blood lead levels. Assessment of hair cell loss by immunohistochemistry analysis and outer hair cell (OHC) activity by recording distortion product otoacoustic emissions (DPOAEs) indicated that the structure and function of the hair cells were not affected by lead exposure. However, this exposure significantly decreased the expression of C-terminal-binding protein-2 (CtBP2) and GluA2, pre- and post-synaptic protein markers in the inner hair cell synapses, particularly in the basal turn of the organ of Corti, suggesting lead-induced disruption of ribbon synapses. In addition, lead exposure significantly increased the nitrotyrosine levels in spiral ganglion cells, suggesting lead-induced nitrative stress in the cochlea. Collectively, these findings suggest that lead exposure even at levels that do not affect the OHCs induces cochlear nitrative stress and causes cochlear synaptopathy.

KEYWORDS

lead exposure, cochlear synaptopathy, nitrative stress, ototoxicity, hidden hearing loss

Introduction

Exposure to lead, a ubiquitous and non-biodegradable environmental toxin (Flora et al., 2012), is a major public health concern. The World Health Organization has reported that lead exposure was associated with 1.06 million deaths worldwide in 2017 and accounted for 63.2% of global developmental intellectual disabilities in 2016. Small amounts of lead are found in the earth's crust (Acharya, 2013) and high concentrations are found in older homes containing lead-based paints, ceramics, pipes and plumbing materials, batteries, ammunition, and cosmetics. Lead is absorbed by the human body through inhalation, ingestion, and dermal contact (Wani et al., 2015) and causes deleterious effects on cardiovascular, renal, skeletal, and nervous systems (Mitra et al., 2017). As a calcium ion substitute, lead can pass through the blood–brain barrier and accumulate in the nervous tissue, which results in the generation of reactive oxygen species (ROS), ultimately interfering with cell signaling and neurotransmission (Sharma et al., 2015). In addition to the well-known neurotoxic effects (Lee et al., 2019; Yang et al., 2019; Zhou et al., 2020), hearing impairment is an important adverse health outcome associated with long-term exposure to lead (Shargorodsky et al., 2011; Choi et al., 2012; Ghiasvand et al., 2016; Rosati and Jamesdaniel, 2020).

Lead exposure disrupts the structure and the function of the auditory system. A blood lead level of $\geq$ 2 μg/dl, which is below the action level (5 μg/dl) recommended by the Centers for Disease Control and Prevention (Rhoads et al., 2012), and bone lead levels of 15 μg/g (in the tibia) were associated with increased odds ratio of hearing loss (Park et al., 2010; Shargorodsky et al., 2011; Ghiasvand et al., 2016). Exposure of mice to even low levels of lead during the early developmental stage decreased the expression of voltage-dependent anion channel proteins and also disrupted the monoaminergic system in the auditory brainstem (Fortune and Lurie, 2009; Prins et al., 2010). Consistent with the observation in other tissues, where increased generation of ROS was detected (Ercal et al., 2001; Vaziri and Khan, 2007; Muthusamy et al., 2016), lead exposure induced oxidative stress in mouse cochlea (Jamesdaniel et al., 2018). Furthermore, animal studies have shown that exposure to lead induced degeneration of cochlear sensory receptor cells, disrupted cochlear blood-labyrinth barrier, affected auditory nerve conduction velocity, and caused vestibular dysfunction (Yamamura et al., 1989; Lasky et al., 1995; Jones et al., 2008; Liu et al., 2013; Klimpel et al., 2017). Despite such compelling evidence, the ototoxic potential of lead is underestimated because short-term exposure to lead at concentrations relevant to environmental settings does not cause significant shifts in hearing thresholds in adults (Carlson and Neitzel, 2018). However, such exposure can cause hidden hearing loss because lead is a potent neurotoxicant that induces synaptic dysfunction (Yang et al., 2019).

Cochlear synaptic transmission is a critical determinant of the quality of auditory perception. It is affected primarily in age-related, noise-induced, and drug-induced (e.g., aminoglycosides) auditory dysfunction long before significant hearing loss is detected (Liberman and Kujawa, 2017). The main target in these otopathologies is the ribbon synapses in the inner hair cells. Even moderate-level ototoxic exposures that do not alter hearing thresholds can damage the ribbon synapses in the inner hair cells, thereby affecting auditory perception (Fernandez et al., 2020). This silencing of subsets of cochlear nerve fibers can contribute to difficulty in hearing speech-in-noise, hyperacusis, and tinnitus, which are among the common hearing disorders caused by ototoxic insults. As the hair cell population is likely to be intact even when there is widespread cochlear synaptopathy, audiograms might not reveal the underlying otopathology. Although the neurotoxic properties of lead imply that environmental exposure can disrupt the cochlear ribbon synapses, lead-induced cochlear synaptopathy has not been studied. The synaptic proteins, which are pivotal for transduction of auditory signals, are highly susceptible to nitration (Bradley and Steinert, 2016). As nitrated proteins are susceptible to degradation, lead-induced cochlear nitrative stress can compromise the transmission and processing of auditory signals. Although we reported that lead exposure induced oxidative stress in the cochlea (Jamesdaniel et al., 2018), lead-induced cochlear nitrative stress, i.e., a sequela of oxidative stress, is yet to be fully understood.

The hypothesis of this study is that environmental exposure to lead at levels that do not affect hair cell viability induces cochlear nitrative stress and causes synaptopathy. To test this hypothesis, we quantified lead-induced cochlear nitrative stress by immunohistochemistry analysis of protein nitration in spiral ganglion cells and evaluated lead-induced disruption of cochlear ribbon synapses by immunohistochemistry analysis of pre- and post-synaptic biomarkers in a mouse model.

Materials and methods

Animals

C57BL6/J mice were purchased from Jackson Laboratories (Bar Harbor, ME, United States) and young-adult male mice (5-week-old) were used in this study. Although the strain C57BL6/J harbors mutations in Cdh23, these mice are considered good models for studying vestibular and cochlear ototoxicity, particularly before the onset of age-related hearing loss (Kane et al., 2012; Jamesdaniel et al., 2018). All animals were allowed to acclimatize for 5 days in a temperature-controlled room with a 12-h light/dark cycle and were housed in the Laboratory Animal Facility of Wayne State University. They had free access to food and water and the ambient noise in the room was maintained below 50 dB sound pressure level (SPL). All animals

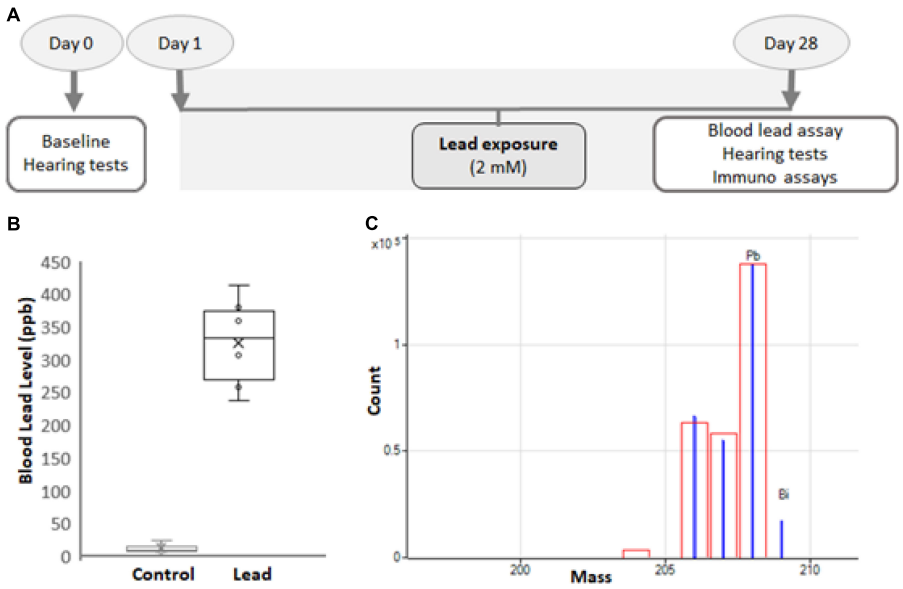

FIGURE 1
Experimental design. **(A)** Five-week-old male C57BL/6 mice were exposed to 2 mM lead acetate in water for 28 days. Hearing thresholds, hair cell loss, ribbon synapse disruption, and nitrotyrosine levels in spiral ganglions were assessed for 1 day after the last exposure. Lead load was analyzed by assessing blood lead levels. **(B)** The blood lead levels in mice that consumed water containing 2 mM lead acetate for 28 days were 326 ± 70 ppb. The results are expressed as mean ± standard deviation, $n = 6$. **(C)** Blood lead levels were analyzed using inductively coupled plasma mass spectrometry (ICP-MS). The mass spectrum (blue) of Pb and Bi (internal) standards used in the ICP-MS analysis is illustrated. The red box indicates the isotopic template.

were handled and treated according to the guidelines established by the National Institutes of Health and every effort was made to minimize pain and discomfort. The experimental protocol (**Figure 1A**) was reviewed and approved by the Institutional Animal Care and Use Committee (#16-01-038).

Lead exposure

The mice were randomly divided into 2 groups and baseline hearing tests were conducted in 5-week-old mice. Only animals with good baseline hearing were used in this study. The mice in the control group were given plain drinking water, while those in the experimental group were exposed to 2 mM lead acetate (Cat # 316512, Sigma-Aldrich, St. Louis, MO, United States) through drinking water for 28 days (**Figure 1A**; Jamesdaniel et al., 2018). The weight, appearance, and behavior of the animals were monitored routinely, and the animals were provided free access to standard mouse chow. To ensure all animals have adequate and similar exposure, three animals were housed in one cage.

Distortion product otoacoustic emissions

Otoacoustic emissions were measured in a soundproof chamber (model AB-4230, ECKEL, Morrisburg, ON, United States). The animals were anesthetized with isoflurane (4% induction, 1.5% maintenance with 1.5 L/min O_2) for measuring the distortion product otoacoustic emissions (DPOAEs). Two primary tones, f1 and f2 at an f2/f1 ratio of 1:2, were used for eliciting the DPOAEs by holding L2–L1 + 10 dB, for L1 levels from 80- to 20-dB SPL in 10-dB increments. The stimulus was generated by using the Tucker-Davis Technology (TDT) RZ6 system, and f1 and f2 were delivered by using multifield magnetic speakers (TDT, Alachua, FL, United States). Frequency f2 varied from 8 to 32 kHz. ER10B_ probe microphone (Etymotic Research, Inc., Elk Grove Village, IL, United States) along with hardware and software from TDTs was used to measure SPLs at the cubic difference frequency (2f1–f2). Distortion product data were collected every 20.971 ms and averaged 512 times. A 100-kHz band surrounding 2f1–f2 was used to measure the noise floor.

Blood and cochleae collection

All animals were euthanized by CO_2 inspiration. After ensuring that there is no response to a toe pinch, blood was collected by cardiac puncture (~100–150 μl) and stored in 1.5 ml Eppendorf tubes containing 10 μl of 0.5 M ethylenediaminetetraacetic acid (EDTA). Then, the mice were sacrificed by cervical dislocation, decapitated,

temporal bone was removed, and the cochlea was dissected out quickly in ice-cold phosphate-buffered saline (PBS). Then, the round and oval windows were opened and immediately perfused with 4% paraformaldehyde in PBS at pH 7.4 by slow injection *via* the round window. The perfused cochlear tissue was fixed overnight in the same solution at room temperature.

Inductively coupled plasma mass spectrometry analysis

A 75-μl sample of blood was diluted with an equal volume of 0.1% Trition X-100. Then, 300 μl of 2% nitric acid was used for further dilution and the samples were incubated for 1–2 h. Samples were centrifuged and 2% nitric acid was used to dilute the samples again for a final 50-fold dilution. A standard curve was generated using standard concentrations of lead ranging from 0.05 to 200 ppb. Lead and bismuth (internal) standards (**Figure 1C**) were purchased from Inorganic Ventures (Christiansburg, VA, United States), and the analysis was performed on an Agilent 7700X Series inductively coupled plasma mass spectrometry (ICP-MS).

Cochlear microdissection

All cochleae were decalcified in 100 mM EDTA solution for 3 days. Then, the organ of Corti was dissected out of the cochlea under a dissecting microscope in a 0.01-mM PBS solution. The basilar membrane from the organ of Corti was further microdissected into 3 major sections, representing the base, middle, and apical turns of the cochlea (Rosati et al., 2021). These sections were used for immunohistochemistry analysis.

Immunohistochemistry

The basal, middle, and apical turns from the cochlear basilar membrane were permeabilized and blocked in a solution containing PBS, 1% v/v Triton X-100, 2% w/v bovine serum albumin, and 10% v/v goat serum (Cat # S26-100 ML, Millipore Sigma, St. Louis, MO, United States) for 1 h at room temperature. Then, the sections were incubated with primary antibodies for 20 h at room temperature. The primary antibodies included mouse anti-C-terminal-binding protein-2 (CtBP2, 1:300, Cat # 612044; BD Biosciences, United States), mouse anti-glutamate receptor 2, clone 6C4 (GluA2, 1:200, Cat # MAB397; Millipore, Germany), rabbit anti-myosin 7a polyclonal (1:500, Cat # 25-6790; Proteus BioSciences, United States), and rabbit anti-nitrotyrosine polyclonal (1:300, Cat # 06-284; Millipore, Germany). CtBP2 and GluA2 antibodies were used together during the immuno-processing for assessing the disruption of ribbon synapses. The following day, the sections were washed in PBS and incubated overnight with the corresponding Alexa Fluor-conjugated secondary antibodies at room temperature. The secondary antibodies included goat anti-mouse Alexa Fluor 568 (IgG1, 1:500), goat anti-mouse Alexa Fluor 488 (IgG2a, 1:500), and Alexa Fluor647 goat anti-rabbit (1:500). Fluorescein-conjugated phalloidin (Cat # F432; Life Technologies, Carlsbad, CA, United States) was used to label F-actin. ProLong Gold antifade reagent containing 4′,6-diamidino-2-phenylindole (DAPI) nuclear stain (Cat # P36935; Invitrogen/Molecular Probes) was used to mount the stained specimens and the slides were kept overnight at 40°C.

Image acquisition and analysis

Images were captured by using the Carl Zeiss Laser Scanning Systems (Zeiss LSM 780, Jena, Germany). The images of synaptic ribbons acquired using a 63X plan apochromatic objective with an effective numerical aperture of 1.4. Z-stacks of 20–25 slices (∼10 μm) were compressed, and 1,024 × 1,024 pixel size (8 bit depth) images were analyzed. At each image field, maximum intensity projection was generated from z-stack for counting the CtBP2 and GluA2 puncta. The area spanning 5 inner hair cells was defined using the freehand selection tool, and the number of puncta in background adjusted images (with a threshold value set to 45 out of 255) was counted using the "analyze particles" tool in the ImageJ/Fiji software (version IJ 1.46r). The images of hair cells and spiral ganglions were acquired using 40X plan apochromatic objective and 1.3 numerical aperture. Z-stacks of 10–15 slices (∼10 μm) were compressed, and 512 × 512 pixel size (8 bit depth) images were analyzed. To quantify the intensity of the immune staining, the pixel values were measured by using the ImageJ/Fiji software (version IJ 1.46r).

Data analyses

Group size was determined statistically by using the data obtained in our previous studies. The G*Power 3.1.9.2 software was used to perform *a priori* power analysis to determine the sample size. Cohen's measures were computed using the mean and standard deviation values obtained in our previous studies, and the actual power was calculated to be 0.95. Two-tailed unpaired *t*-test was used for statistical analysis and p-value of < 0.05 was considered significant. All results are expressed as mean ± standard

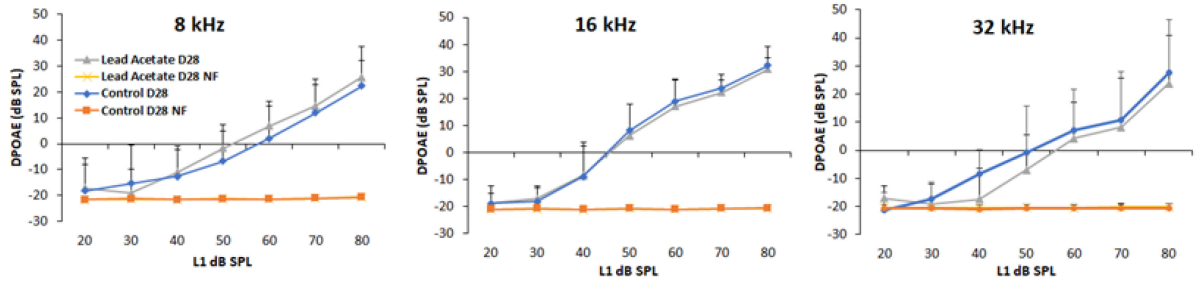

FIGURE 2
Effect of lead exposure on outer hair cell activity. Distortion product otoacoustic emissions (DPOAEs) were recorded in control and lead-exposed mice using 8, 16, and 32 kHz f2 stimuli. The traces labeled NF represent the noise floor of the DPOAE recordings. The distortion product amplitudes of mice with 28-day lead exposure were largely similar to that of unexposed controls. The results are expressed as mean ± standard deviation, n = 4–5.

deviation. Each replicate represents data derived from an individual animal.

Results

Four-week lead exposure increased the blood lead levels in mice

Blood lead levels were assessed by ICP-MS analysis immediately after the 28-day lead exposure. This analysis indicated that the exposure paradigm used in this study significantly increased the lead load (**Figure 1B**), which mimicked lead poisoning levels in most mammals (Dalefield, 2017). Nevertheless, the lead-exposed animals were generally healthy and maintained body weight similar to that of the controls.

Outer hair cell activity was not affected by lead exposure

DPOAE amplitudes were used to assess lead-induced changes in outer hair cell (OHC) activity. The otoacoustic emissions were recorded using 8, 16, and 32 kHz f2 stimuli for 1 day after 28-day lead exposure. Baseline DPOAEs were recorded in all animals prior to lead exposure and only animals with good baseline hearing were used in this study. A comparative analysis of the hearing thresholds recorded in the control and lead-exposed animals indicated that the distortion product amplitudes were largely similar in both groups of mice (**Figure 2**). Although C57BL6 mice have early onset of age-related hearing loss and the vulnerability of the hair cells to ototoxicants in 10-week-old mice is likely to be higher in this strain, these results suggest that lead exposure at this level does not affect the activity of the OHCs.

Lead exposure did not cause hair cell loss

Outer and inner hair cells stained with anti-myosin 7a were examined *via* a confocal microscope (40 × magnification) to detect lead-induced hair cell loss. The confocal images indicated that lead exposure did not induce hair cell loss in the base, mid, and apical regions of the organ of Corti (**Figure 3**). The hair cells in the lead-exposed animals appeared similar to that of controls, suggesting that hair cells are not the primary targets in lead-induced ototoxicity.

Cochlear ribbon synapses were disrupted by lead exposure

Lead-induced loss of ribbon synapses was assessed by immunostaining the inner hair cells with anti-CtBP2 and anti-GluA2. The puncta representing the pre- and post-synaptic markers in the inner hair cells were counted *via* a confocal

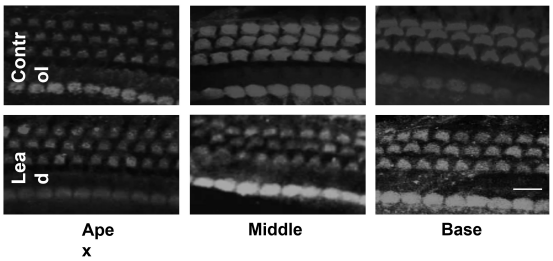

FIGURE 3
Effect of lead exposure on hair cell viability. Surface preparations of organ of Corti stained with anti-myosin 7a are illustrated. The outer and inner hair cells in the lead-exposed mice appear similar to that of controls and no hair cell loss was observed in all three turns of the organ of Corti. Images are representative of six replicates. Scale bar = 20 μm.

microscope (63 × magnification). The count of the stained puncta indicated that lead exposure significantly decreased the expression of CtBP2 and GluA2 in the inner hair cells located in the basal region of the organ of Corti (Figures 4A–D). This suggested that the ribbon synapses in the base of the cochlea were more susceptible to lead-induced disruption than those in the middle and apical regions.

Lead exposure induced nitrative stress in the spiral ganglions

Lead-induced cochlear nitrative stress was evaluated in the spiral ganglion cells located in the basal region of the organ of Corti by immunohistochemistry analysis with anti-nitrotyrosine. We focused on spiral ganglions in the basal region because lead exposure did not affect the ribbon synapses in the middle and apical regions. Moreover, we did not assess the nitrotyrosine levels in the hair cells because hair cells were not affected by lead exposure. The specificity of this immunoreaction was verified in our previous studies (Jamesdaniel et al., 2012). Nitrotyrosine levels were quantified by analyzing the intensity of the fluorescence of anti-nitrotyrosine using the ImageJ software. The fluorescence of DAPI was not quantified. The average intensity of five spiral ganglion cells per cochlear turn was calculated and normalized with corresponding actin intensities. The nitrotyrosine level in lead-exposed animals was significantly higher than that of the controls (Figures 5A,B). This suggested that lead exposure induced nitrative stress in the cochlea.

Discussion

Environmental chemicals pose a significant health risk in urban neighborhoods because of historical contamination from anthropogenic sources, accumulation of multiple pollutants, and harmful interactions. Exposure to lead, one of the most commonly encountered environmental toxicants, is generally unavoidable because it is ubiquitous in air, water, and soil. Residents of inner cities with older infrastructure are exposed to higher levels of lead because most of the houses contain lead paints and/or lead pipes. Hearing impairment, the third most common chronic physical condition (Blackwell et al., 2014) reported by 15% of Americans between the ages of 20 and 69 years (Hoffman et al., 2006), is associated with long-term exposure to lead (Shargorodsky et al., 2011; Choi et al., 2012; Ghiasvand et al., 2016; Rosati and Jamesdaniel, 2020). Since

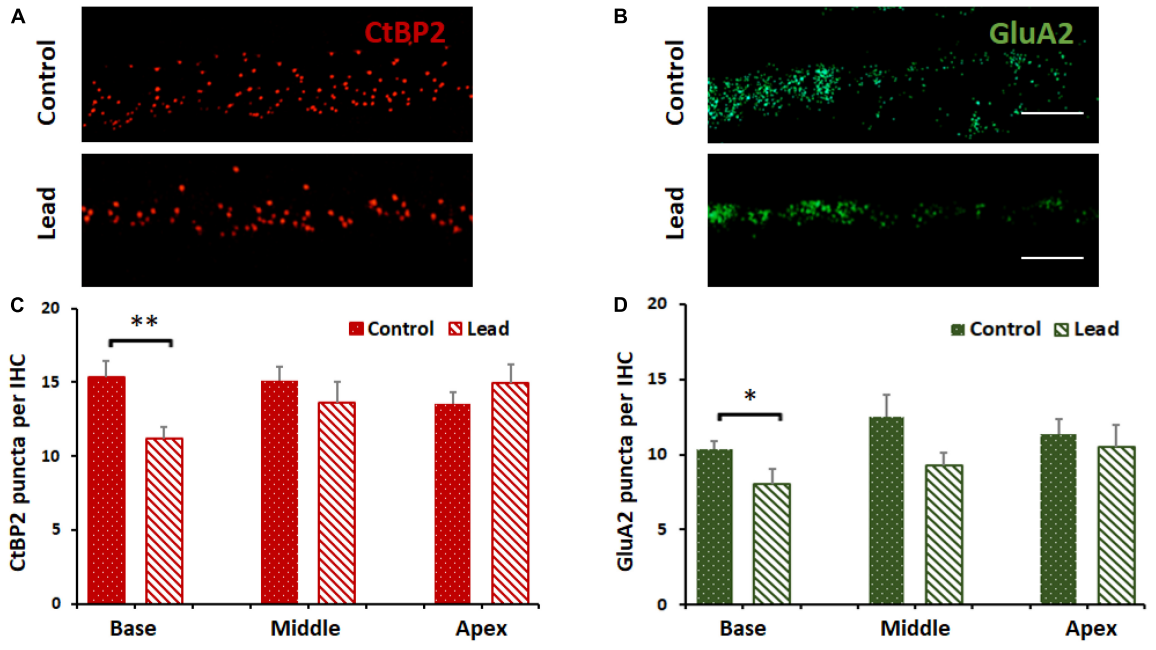

FIGURE 4
Lead-induced disruption of cochlear ribbon synapses. **(A)** Inner hair cells in the basal region of the organ of Corti probed with antibodies against C-terminal binding protein 2 (CtBP2, red stain) are illustrated. Lead exposure decreased the expression of this pre-synaptic marker in the inner hair cell synapses. Images are representative of 5–8 replicates, scale bar = 20 μm. **(B)** Inner hair cells in the basal region of the organ of Corti probed with antibodies against glutamate receptor subunits 2 (GluA2, green stain) are illustrated. Lead exposure decreased the expression of this post-synaptic marker in the inner hair cell synapses. Images are representative of 5–8 replicates, scale bar = 20 μm. **(C,D)** Counts of CtBP2 and GluA2 puncta indicated that lead exposure decreased the counts significantly in the basal region of the inner hair cells (IHC, n = 5–8). *$p < 0.05$, **$p < 0.01$. The results are expressed as mean ± standard error mean, n = 5–8.

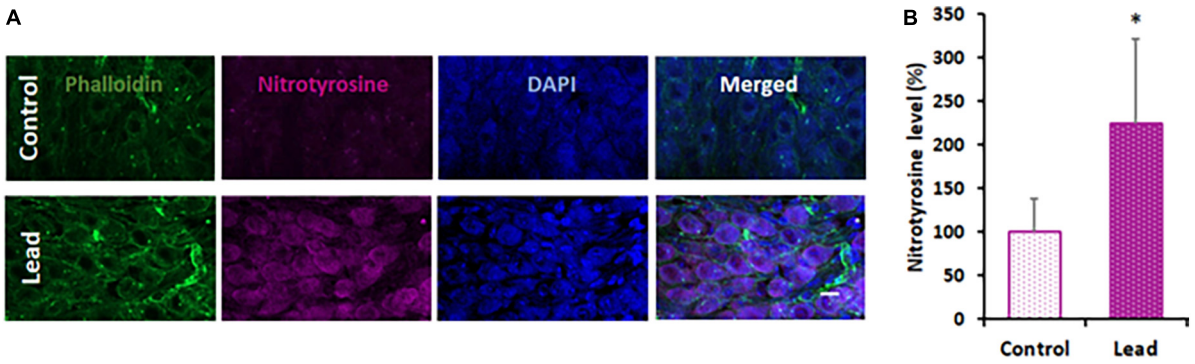

FIGURE 5
Lead-induced cochlear nitrative stress. **(A)** Spiral ganglions probed with anti-nitrotyrosine (magenta stain) indicated an increase in the level of nitrotyrosine after lead exposure. Phalloidin was used to stain actin (green) and DAPI was used to stain the nucleus (blue). Images are representative of 4–5 replicates, scale bar = 10 μm. **(B)** Quantification of nitrotyrosine staining indicated a significant increase in the spiral ganglion cells of lead-exposed mice. The results are expressed as mean ± standard deviation, $*p < 0.05$, $n = 4–5$.

the United Nations projects that 68% of the world population will live in urban areas by 2050, delineating the otopathology associated with lead exposure is important for discovering effective strategies to protect vulnerable communities from lead-induced hearing impairment. This study provides the first evidence indicating lead exposure, even at levels that do not damage OHCs, and disrupts the cochlear ribbon synapses. In addition, this study suggests that nitrative stress may play a role in contributing to this otopathology.

Outer hair cells, the sensory receptor cells in the cochlea, are highly susceptible to damage induced by agents such as noise and ototoxic drugs. In previous studies, lead-induced hearing impairment in rodents was detected by recording auditory brainstem responses (ABRs; Liu et al., 2013; Jamesdaniel et al., 2018). However, the ABRs can reflect ototoxin-induced damage to different regions of the auditory pathway. Therefore, the threshold shifts observed in the ABRs do not always indicate OHC-specific damage. To verify whether lead exposure induces OHC damage, this study employed an exposure paradigm that increased the blood lead levels to ∼32 μg/dl, which mimics lead poisoning levels in most mammals (Dalefield, 2017), and then assessed the DPOAEs, which reflect OHC activity, and OHC loss. Exposure at this level to young-adult mice did not affect the structure and function of the OHCs as reflected by the otoacoustic emissions and immunohistochemistry analysis. Although we did not measure DPOAEs at frequencies higher than 32 kHz, which represents the mid-basal region, the morphological examination indicated that lead exposure did not affect the hair cells in the basal region. These results are consistent with the findings of other studies (Carlson and Neitzel, 2018) and suggest that the OHCs are not the primary targets in lead-induced ototoxicity.

Although OHCs were not damaged, wave 1 latencies were prolonged in ABRs recorded post lead exposure (Liu et al., 2011; Zhang et al., 2019), suggesting interference with the transmission of auditory signals potentially due to cochlear neuropathy. Several studies have reported that lead-induced neuronal damage is facilitated by glutamate excitotoxicity (Lasley and Gilbert, 2002), excessive Ca_2^+ influx (Ferguson et al., 2000; Kern et al., 2000), and oxidative stress (Ding et al., 2000; Patrick, 2006; Antonio-Garcia and Masso-Gonzalez, 2008), which are mechanisms attributed to cochlear synaptopathy and neurodegeneration of the auditory nerve (Liberman and Kujawa, 2017; Sebe et al., 2017). To verify whether lead exposure induces cochlear synaptopathy, pre- and post-synaptic biomarkers of cochlear ribbon synapses were evaluated. Immunohistochemistry analysis indicated that the number of CtBP2 and GluA2 puncta in the ribbon synapses were significantly reduced in the inner hair cells located in the basal region of the organ of Corti after lead exposure. These results suggest that even exposure at levels that do not affect OHC function can disrupt the cochlear ribbon synapses.

The mechanism underlying lead-induced disruption of cochlear ribbon synapses is unknown. Damage to the cochlear ribbon synapses is generally attributed to glutamate excitotoxicity (Liberman and Kujawa, 2017) and excessive Ca^{2+} influx into afferent terminals (Sebe et al., 2017), which can eventually trigger a cascade of reactions resulting in oxidative stress (Maher et al., 2018). As lead-induced neuronal damage is facilitated by glutamate excitotoxicity (Lasley and Gilbert, 2002), excessive Ca2 + influx (Ferguson et al., 2000; Kern et al., 2000), and oxidative stress (Ding et al., 2000; Patrick, 2006; Antonio-Garcia and Masso-Gonzalez, 2008), lead-induced disruption of cochlear ribbon synapses could be mediated by any of these mechanisms. Particularly, redox mechanisms can facilitate cochlear synaptopathy because many synaptic proteins are highly susceptible to nitration (Bradley and Steinert, 2016). Moreover, nitration of synaptic proteins such as SNAP-25, Munc-18, Synaptophysin, Dynamin, and Synaptotagmin, has been reported in other models (Di Stasi et al., 2002;

Vrljic et al., 2011; Mallozzi et al., 2013). In a previous study, lead exposure induced oxidative stress, a precursor of nitrative stress, in the cochlea (Jamesdaniel et al., 2018). The reaction of ROS (e.g., $O_2^{\cdot -}$) with reactive nitrogen species (e.g., NO) leads to the formation of peroxynitrite ($ONOO^-$), which can react with susceptible proteins to form nitrotyrosine, an indicator of nitrative damage to proteins. To verify whether lead exposure induces cochlear nitrative stress, changes in nitrotyrosine levels were evaluated. Immunohistochemistry analysis indicated that the nitrotyrosine levels in the spiral ganglions were significantly increased after lead exposure. As lead exposure induces cochlear nitrative stress, the synaptic proteins in the cochlear ribbon synapses are potential targets for nitration, which could eventually contribute to the disruption of ribbon synapses observed after lead exposure.

Conclusion

This study provides the first evidence for lead-induced disruption of cochlear ribbon synapses and suggests that nitrative stress may play a role in contributing to this otopathology. One of the limitations of this study is the lack of functional data to corroborate lead-induced cochlear synaptic disruption. Nevertheless, the findings of this study are important because they suggest that even exposure at levels that do not damage OHCs can induce cochlear synaptopathy, which in turn can affect the quality of life and productivity. Follow-up studies on cochlear synaptic proteins that are nitrated by lead exposure would provide important insights into the nitrative stress mechanism underlying lead-induced cochlear synaptopathy and identify potential targets for intervention.

Data availability statement

The original contributions presented in this study are included in the article/supplementary material, further inquiries can be directed to the corresponding author.

Ethics statement

The animal study was reviewed and approved by Institutional Animal Care and Use Committee, Wayne State University.

Author contributions

SJ contributed to the study concept and design. RR and JB performed research. SJ, RR, and JW analyzed the data. SJ and RR wrote the manuscript. All authors contributed to the article and approved the submitted version.

Funding

This research was supported by CURES P30 center grant (P30 ES020957) from NIH/NIEHS and K01 grant (K01 ES028750) to SJ from NIH/NIEHS.

Conflict of interest

The authors declare that the research was conducted in the absence of any commercial or financial relationships that could be construed as a potential conflict of interest.

Publisher's note

All claims expressed in this article are solely those of the authors and do not necessarily represent those of their affiliated organizations, or those of the publisher, the editors and the reviewers. Any product that may be evaluated in this article, or claim that may be made by its manufacturer, is not guaranteed or endorsed by the publisher.

References

Acharya, S. (2013). Lead between the lines. *Nat. Chem.* 5:894. doi: 10.1038/nchem.1761

Antonio-Garcia, M. T., and Masso-Gonzalez, E. L. (2008). Toxic effects of perinatal lead exposure on the brain of rats: involvement of oxidative stress and the beneficial role of antioxidants. *Food Chem. Toxicol.* 46, 2089–2095. doi: 10.1016/j.fct.2008.01.053

Blackwell, D. L., Lucas, J. W., and Clarke, T. C. (2014). *Summary Health Statistics for US Adults: National Health Interview Survey, 2012. Vital Health Statistics, Series 10, no. 260*. Atlanta, GA: National Center for Health Statistics, CDC.

Bradley, S. A., and Steinert, J. R. (2016). 'Nitric oxide-mediated posttranslational modifications: impacts at the synapse'. *Oxid. Med. Cell Longev.* 2016:568 1036. doi: 10.1155/2016/5681036

Carlson, K., and Neitzel, R. (2018). Hearing loss, lead (Pb) exposure, and noise: a sound approach to ototoxicity exploration. *J. Toxicol. Environ. Health B Crit. Rev.* 21, 335–355. doi: 10.1080/10937404.2018.1562391

Choi, Y. H., Hu, H., Mukherjee, B., Miller, J., and Park, S. K. (2012). Environmental cadmium and lead exposures and hearing loss in U.S. adults: the National Health and Nutrition Examination Survey, 1999 to 2004. *Environ. Health Perspect.* 120, 1544–1550. doi: 10.1289/ehp.1104863

Dalefield, R. (2017). *Veterinary Toxicology for Australia and New Zealand*. Amsterdam: Elsevier, 233–253. doi: 10.1016/B978-0-12-420227-6.00013-X

Di Stasi, A. M., Mallozzi, C., Macchia, G., Maura, G., Petrucci, T. C., and Minetti, M. (2002). Peroxynitrite affects exocytosis and SNARE complex formation and induces tyrosine nitration of synaptic proteins. *J. Neurochem.* 82, 420–429. doi: 10.1046/j.1471-4159.2002.00980.x

Ding, Y., Gonick, H. C., and Vaziri, N. D. (2000). Lead promotes hydroxyl radical generation and lipid peroxidation in cultured aortic endothelial cells. *Am. J. Hypertens.* 13, 552–555. doi: 10.1016/S0895-7061(99)00226-5

Ercal, N., Gurer-Orhan, H., and Aykin-Burns, N. (2001). Toxic metals and oxidative stress part I: mechanisms involved in metal-induced oxidative damage. *Curr. Top. Med. Chem.* 1, 529–539. doi: 10.2174/1568026013394831

Ferguson, C., Kern, M., and Audesirk, G. (2000). Nanomolar concentrations of inorganic lead increase Ca2+ efflux and decrease intracellular free Ca2+ ion concentrations in cultured rat hippocampal neurons by a calmodulin-dependent mechanism. *Neurotoxicology* 21, 365–378.

Fernandez, K. A., Guo, D., Micucci, S., De Gruttola, V., Liberman, M. C., and Kujawa, S. G. (2020). Noise-induced cochlear synaptopathy with and without sensory cell loss. *Neuroscience* 427, 43–57. doi: 10.1016/j.neuroscience.2019.11.051

Flora, G., Gupta, D., and Tiwari, A. (2012). Toxicity of lead: a review with recent updates. *Interdiscip. Toxicol.* 5, 47–58. doi: 10.2478/v10102-012-0009-2

Fortune, T., and Lurie, D. I. (2009). Chronic low-level lead exposure affects the monoaminergic system in the mouse superior olivary complex. *J. Comp. Neurol.* 513, 542–558. doi: 10.1002/cne.21978

Ghiasvand, M., Mohammadi, S., Roth, B., and Ranjbar, M. (2016). The relationship between occupational exposure to lead and hearing loss in a cross-sectional survey of iranian workers. *Front. Public Health* 4:19. doi: 10.3389/fpubh.2016.00019

Hoffman, H. J., Ko, C.-W., Themann, C. L., Dillon, C. F., and Franks, J. R. (2006). Reducing noise-induced hearing loss (NIHL) in adults to achieve U.S. Healthy People 2010 goals. Abstract. *Am. J. Epidemiol.* 163:S122. doi: 10.1093/aje/163.suppl_11.S122-c

Jamesdaniel, S., Coling, D., Hinduja, S., Ding, D., Li, J., Cassidy, L., et al. (2012). Cisplatin-induced ototoxicity is mediated by nitroxidative modification of cochlear proteins characterized by nitration of Lmo4. *J. Biol. Chem.* 287, 18674–18686. doi: 10.1074/jbc.M111.297960

Jamesdaniel, S., Rosati, R., Westrick, J., and Ruden, D. M. (2018). Chronic lead exposure induces cochlear oxidative stress and potentiates noise-induced hearing loss. *Toxicol. Lett.* 292, 175–180. doi: 10.1016/j.toxlet.2018.05.004

Jones, L. G., Prins, J., Park, S., Walton, J. P., Luebke, A. E., and Lurie, D. I. (2008). Lead exposure during development results in increased neurofilament phosphorylation, neuritic beading, and temporal processing deficits within the murine auditory brainstem. *J. Comp. Neurol.* 506, 1003–1017. doi: 10.1002/cne.21563

Kane, K. L., Longo-Guess, C. M., Gagnon, L. H., Ding, D., Salvi, R. J., and Johnson, K. R. (2012). Genetic background effects on age-related hearing loss associated with Cdh23 variants in mice. *Hear. Res.* 283, 80–88. doi: 10.1016/j.heares.2011.11.007

Kern, M., Wisniewski, M., Cabell, L., and Audesirk, G. (2000). Inorganic lead and calcium interact positively in activation of calmodulin. *Neurotoxicology* 21, 353–363.

Klimpel, K. E., Lee, M. Y., King, W. M., Raphael, Y., Schacht, J., and Neitzel, R. L. (2017). Vestibular dysfunction in the adult CBA/CaJ mouse after lead and cadmium treatment. *Environ. Toxicol.* 32, 869–876. doi: 10.1002/tox.22286

Lasky, R. E., Maier, M. M., Snodgrass, E. B., Hecox, K. E., and Laughlin, N. K. (1995). The effects of lead on otoacoustic emissions and auditory evoked potentials in monkeys. *Neurotoxicol. Teratol.* 17, 633–644. doi: 10.1016/0892-0362(95)02006-3

Lasley, S. M., and Gilbert, M. E. (2002). Rat hippocampal glutamate and GABA release exhibit biphasic effects as a function of chronic lead exposure level. *Toxicol. Sci.* 66, 139–147. doi: 10.1093/toxsci/66.1.139

Lee, J. W., Choi, H., Hwang, U. K., Kang, J. C., Kang, Y. J., Kim, K. I., et al. (2019). Toxic effects of lead exposure on bioaccumulation, oxidative stress, neurotoxicity, and immune responses in fish: a review. *Environ. Toxicol. Pharmacol.* 68, 101–108. doi: 10.1016/j.etap.2019.03.010

Liberman, M. C., and Kujawa, S. G. (2017). Cochlear synaptopathy in acquired sensorineural hearing loss: manifestations and mechanisms. *Hear. Res.* 349, 138–147. doi: 10.1016/j.heares.2017.01.003

Liu, S., Zhang, K., Wu, S., Ji, X., Li, N., Liu, R., et al. (2011). Lead-induced hearing loss in rats and the protective effect of copper. *Biol. Trace Elem. Res.* 144, 1112–1119. doi: 10.1007/s12011-011-9142-6

Liu, X., Zheng, G., Wu, Y., Shen, X., Jing, J., Yu, T., et al. (2013). Lead exposure results in hearing loss and disruption of the cochlear blood-labyrinth barrier and the protective role of iron supplement. *Neurotoxicology* 39, 173–181. doi: 10.1016/j.neuro.2013.10.002

Maher, P., van Leyen, K., Dey, P. N., Honrath, B., Dolga, A., and Methner, A. (2018). The role of Ca(2+) in cell death caused by oxidative glutamate toxicity and ferroptosis. *Cell Calcium* 70, 47–55. doi: 10.1016/j.ceca.2017.05.007

Mallozzi, C., D'Amore, C., Camerini, S., Macchia, G., Crescenzi, M., Petrucci, T. C., et al. (2013). Phosphorylation and nitration of tyrosine residues affect functional properties of Synaptophysin and Dynamin I, two proteins involved in exo-endocytosis of synaptic vesicles. *Biochim. Biophys. Acta* 1833, 110–121. doi: 10.1016/j.bbamcr.2012.10.022

Mitra, P., Sharma, S., Purohit, P., and Sharma, P. (2017). Clinical and molecular aspects of lead toxicity: an update. *Crit. Rev. Clin. Lab. Sci.* 54, 506–528. doi: 10.1080/10408363.2017.1408562

Muthusamy, S., Peng, C., and Ng, J. C. (2016). Effects of binary mixtures of benzo[a]pyrene, arsenic, cadmium, and lead on oxidative stress and toxicity in HepG2 cells. *Chemosphere* 165, 41–51. doi: 10.1016/j.chemosphere.2016.08.137

Park, S. K., Elmarsafawy, S., Mukherjee, B., Spiro, A. III, Vokonas, P. S., Nie, H., et al. (2010). Cumulative lead exposure and age-related hearing loss: the VA Normative Aging Study. *Hear. Res.* 269, 48–55. doi: 10.1016/j.heares.2010.07.004

Patrick, L. (2006). Lead toxicity part II: the role of free radical damage and the use of antioxidants in the pathology and treatment of lead toxicity. *Altern. Med. Rev.* 11, 114–127.

Prins, J. M., Brooks, D. M., Thompson, C. M., and Lurie, D. I. (2010). Chronic low-level Pb exposure during development decreases the expression of the voltage-dependent anion channel in auditory neurons of the brainstem. *Neurotoxicology* 31, 662–673. doi: 10.1016/j.neuro.2010.08.004

Rhoads, G. G., Brown, M. J., Cory-Slechta, D. A., Dietrich, K., Gardner, S, L., Gottesfeld, P., et al. (2012). *Report of the Advisory Committee on Childhood Lead Poisoning Prevention, Centers for Disease Control and Prevention*. Atlanta: CDC.

Rosati, R., and Jamesdaniel, S. (2020). Environmental exposures and hearing loss. *Int. J. Environ. Res. Public Health* 17:4879. doi: 10.3390/ijerph17134879

Rosati, R., Shahab, M., Ramkumar, V., and Jamesdaniel, S. (2021). Lmo4 deficiency enhances susceptibility to cisplatin-induced cochlear apoptosis and hearing loss. *Mol. Neurobiol.* 58, 2019–2029. doi: 10.1007/s12035-020-02226-4

Sebe, J. Y., Cho, S., Sheets, L., Rutherford, M. A., von Gersdorff, H., and Raible, D. W. (2017). Ca2+-permeable AMPARs mediate glutamatergic transmission and excitotoxic damage at the hair cell ribbon synapse. *J. Neurosci.* 37, 6162–6175. doi: 10.1523/JNEUROSCI.3644-16.2017

Shargorodsky, J., Curhan, S. G., Henderson, E., Eavey, R., and Curhan, G. C. (2011). Heavy metals exposure and hearing loss in US adolescents. *Arch. Otolaryngol. Head Neck Surg.* 137, 1183–1189. doi: 10.1001/archoto.2011.202

Sharma, P., Chambial, S., and Shukla, K. K. (2015). Lead and neurotoxicity. *Indian J. Clin. Biochem.* 30, 1–2. doi: 10.1007/s12291-015-0480-6

Vaziri, N. D., and Khan, M. (2007). Interplay of reactive oxygen species and nitric oxide in the pathogenesis of experimental lead-induced hypertension. *Clin. Exp. Pharmacol. Physiol.* 34, 920–925. doi: 10.1111/j.1440-1681.2007.04644.x

Vrljic, M., Strop, P., Hill, R. C., Hansen, K. C., Chu, S., and Brunger, A. T. (2011). 'Post-translational modifications and lipid binding profile of insect cell-expressed full-length mammalian synaptotagmin 1'. *Biochemistry* 50, 9998–10012. doi: 10.1021/bi200998y

Wani, A. L., Ara, A., and Usmani, J. A. (2015). Lead toxicity: a review. *Interdiscip. Toxicol.* 8, 55–64. doi: 10.1515/intox-2015-0009

Yamamura, K., Terayama, K., Yamamoto, N., Kohyama, A., and Kishi, R. (1989). Effects of acute lead acetate exposure on adult guinea pigs: electrophysiological study of the inner ear. *Fundam. Appl. Toxicol.* 13, 509–515. doi: 10.1016/0272-0590(89)90287-X

Yang, W., Tian, Z. K., Yang, H. X., Feng, Z. J., Sun, J. M., Jiang, H., et al. (2019). Fisetin improves lead-induced neuroinflammation, apoptosis and synaptic dysfunction in mice associated with the AMPK/SIRT1 and autophagy pathway. *Food Chem. Toxicol.* 134:110824. doi: 10.1016/j.fct.2019.110824

Zhang, Y., Jiang, Q., Xie, S., Wu, X., Zhou, J., and Sun, H. (2019). Lead induced ototoxicity and neurotoxicity in adult guinea pig. *Biomed. Res. Int.* 2019:3626032. doi: 10.1155/2019/3626032

Zhou, F., Du, G., Xie, J., Gu, J., Jia, Q., Fan, Y., et al. (2020). RyRs mediate lead-induced neurodegenerative disorders through calcium signaling pathways. *Sci. Total Environ.* 701:134901. doi: 10.1016/j.scitotenv.2019.134901

Advantages of publishing in Frontiers

OPEN ACCESS
Articles are free to read for greatest visibility and readership

FAST PUBLICATION
Around 90 days from submission to decision

HIGH QUALITY PEER-REVIEW
Rigorous, collaborative, and constructive peer-review

TRANSPARENT PEER-REVIEW
Editors and reviewers acknowledged by name on published articles

Frontiers
Avenue du Tribunal-Fédéral 34
1005 Lausanne | Switzerland

Visit us: www.frontiersin.org
Contact us: frontiersin.org/about/contact

REPRODUCIBILITY OF RESEARCH
Support open data and methods to enhance research reproducibility

DIGITAL PUBLISHING
Articles designed for optimal readership across devices

FOLLOW US
@frontiersin

IMPACT METRICS
Advanced article metrics track visibility across digital media

EXTENSIVE PROMOTION
Marketing and promotion of impactful research

LOOP RESEARCH NETWORK
Our network increases your article's readership